Top quark pair production cross-section in proton-proton collisions at $\sqrt{s} = 7$ TeV

Menelaos Tsiakiris

FOM

NWO
Netherlands Organisation for Scientific Research

This work is part of the research program of the Foundation for Fundamental Research on Matter (FOM), which is part of the Netherlands Organization for Scientific Research (NWO). The research has been supported by the VICI grant 680-47-309 titled "Beyond the top; a new era in particle physics" of Prof. dr. S.C.M. Bentvelsen.

Top quark pair production cross-section in proton-proton collisions at $\sqrt{s} = 7$ TeV

ACADEMISCH PROEFSCHRIFT

ter verkrijging van de graad van doctor
aan de Universiteit van Amsterdam
op gezag van de Rector Magnificus
prof. dr. D.C. van den Boom
ten overstaan van een door het college van promoties ingestelde
commissie, in het openbaar te verdedigen in de Agnietenkapel
op woensdag 19 september 2012, te 12:00 uur

door

Menelaos Tsiakiris

geboren te Thessaloniki, Griekenland

Promotiecommissie

Promotor:	*Prof. dr. S. C. M. Bentvelsen*
Co-Promotors:	*Dr. P. Ferrari*
	Dr. S. Klous
Overige leden:	*Prof. dr. M. Cobal*
	Prof. dr. ing. B. van Eijk
	Prof. dr. ir. P. J. de Jong
	Prof. dr. P. M. Kooijman
	Prof. dr. P. J. Mulders
	Dr. M. Vreeswijk

Faculteit der Natuurwetenschappen, Wiskunde en Informatica

Στους γονεὶς μου,
Σταμὰτη και Χαροὺλα.

Στην αδερφὴ μου,
Ὀλγα.

Στο Ἀμστερνταμ.
Στο Βερολὶνο.

Contents

Introduction

Physics is about understanding Nature: the characteristics of matter, its constituents and the interactions between them, the underlying processes that lead to the formation of larger objects and finally understanding how all these are manifested in our surrounding environment.

At present times, Modern Physics is based on the idea that matter is built from a few fundamental building blocks, the *elementary particles*. Remarkably, this idea is not new but dates as far back as the 6th century BC and the roots of the *natural philosophy*. The most striking example comes from Leucippus of Miletus (5th century BC.) who, together with Democritus of Abdera (c. 460 - 371 BC.), developed the idea of *atomism*, accepting that matter consists of many different indivisible and everlasting constituents, the *atoms* [1]. Undeniably, however, the main difference between the past and the present is the fact that the science of Physics reaches to conclusions based on the principles of the *Scientific Method*, instead of just following a philosophical reasoning. Consequently, any well-grounded theory must be accompanied by *experimental* observations before being accepted.

The Particle Physics era

The beginning of Particle Physics can be placed with the discovery of the electron in 1897 by Sir J.J. Thomson. From that point on many remarkable discoveries were made, starting with the improvements on the atomic model made by Thomson, Ernest Rutherford and Niels Bohr, and the parallel developments on the field of Quantum Mechanics and Relativity primarily by Max Planck, Albert Einstein, Louis de Broglie, Erwin Schrödinger, Werner Heisenberg and Paul Dirac. By the end of 1940s, physicists had discovered the proton, the neutron, the muon, the positron (anti-particle of electron), the neutrino (the electron and the muon partners) and they had derived a relativistic quantum field theory (QFT) in order to explain the electromagnetic field (Quantum Electrodynamics), mainly thanks to the work of Richard Feynman, Freeman Dyson, Julian Schwinger and Sin-Itiro Tomonaga. Clearly, until then Physics had made important steps forward, however, it still lacked a consistent theory that could explain all of these observations. This was about to change in the coming years.

Before the end of 1950s a number of experiments had already observed a plethora of new sub-atomic particles, collectively called *hadrons*, which indicated that protons and neutrons may not be fundamental particles. In the early 1960s, Murray Gell-Man and George Zweig independently theorized the existence of the quarks, as constituents of the hadrons, and subsequently the existence of the gluon, as the mediator particle of the force that keeps quarks together in the hadron, the *strong force* [2, 3, 4, 5]. The experimental results from the Stanford Linear Collider (SLAC) *deep-inelastic scattering* experiments verified that quarks and gluons are indeed the elementary constituents [6, 7]; the gluon existence was explicitly shown by a number of experiments, namely the TASSO [8], PLUTO [9], MARK-J [10] and JADE [11].

The quantum field theory that nowadays governs the strong interactions is *Quantum Chromodynamics* (QCD). Its final formulation came in 1975 by Hugh Politzer, David Gross and Frank Wilczek after discovering the *asymptotic freedom* property of QCD [12, 13, 14].

At the same period, an effort was made to formulate the *weak nuclear force* as a quantum field theory. Although a description of the force was provided by Enrico Fermi in 1930s, in order to explain beta radiation [15], it was only valid for relatively low energies. The issue was re-visited by Sheldon Glashow, Steven Weinberg and Abdus Salam, and by mid-1960s they had concluded to the *electroweak theory* under which the *electromagnetic* and the *weak interactions* are unified [16, 17, 18]. As an outcome of the theory was the prediction for the existence of a charged massive particle, the $W^{\pm}$, a neutral massive particle, the Z, and a neutral massless particle, the photon. The $W^{\pm}$ and Z particles are the weak force carriers while the photon is the electromagnetic force carrier. In order to accommodate the fact that the weak force carrier particles had mass, the electroweak theory incorporated the electroweak symmetry breaking mechanism proposed by Peter Higgs and others in the mid-1960s (Higgs mechanism) [19, 20, 21]. The outcome from including the Higgs mechanism not only explained the mass of those particles but also suggested the existence of yet another particle, the *Higgs boson*.

Nowadays, the *Standard Model* is the model that describes the strong, the weak and the electromagnetic interactions. It combines the QCD and electroweak theory into a single consistent theory and provides a description on how the elementary particles interact with each other and form the matter. The success of this theory has been outstanding until today, making it a corner-stone for Particle Physics.

In 1973, Makoto Kobayashi and Toshihide Maskawa hypothesized the existence of the bottom and the top quarks as a means to explain CP violation within the Standard Model [22]. Eventually, the bottom quark was discovered in 1977 at the E288 experiment [23], and the top quark was discovered in 1995 at the Tevatron experiments CDF and DØ [24, 25]. Another success of the Standard Model, and the highlight up until recently, was the discovery of the W and Z bosons in 1983 by the UA1 and UA2 experiments with their mass close to the expected values [26, 27]. The most exciting result, however, comes from the two general purpose experiments of the Large Hadron Collider (LHC), ATLAS and CMS, which in July 4 2012 announced the discovery of a new boson which appears to be consistent with the theorized properties of the Higgs boson [28, 29]. If further investigation verifies that is indeed the Higgs boson, this will be a great success for the Standard Model.

The top quark

The top quark is one of the latest discoveries in Particle Physics and the heaviest elementary particle known to date. Due to its large mass, it is the only quark that decays before it hadronizes, therefore allowing to be probed directly by its products. In addition, its mass is at about the same scale of the electroweak symmetry breaking mechanism, indicating that it couples strongly to the proposed Higgs boson.

In proton-proton collisions, the most common production channel for top quarks is through the top quark-pair production ($t\bar{t}$). This thesis is focused in particular on measuring the cross-section of this signature. Since its discovery in 1995, the cross-section of the $t\bar{t}$ production channel has been measured by both the CDF and DØ experiments at the Tevatron collider. However, the Tevatron ran with proton-antiproton collision at $\sqrt{s} = 1.96$ TeV. Therefore the cross-section measurement presented here is a test of QCD, and the Standard Model consistency in general, as it probes a region of the phase space which was previously unexplored.

Additionally, given the facts stated above, precise measurements of the properties of the top quark are very important for gaining a better understanding on the mechanism that gives mass to the particles (the electroweak symmetry breaking). Many of such analyses require a pure sample with enough statistics, therefore a good understanding of the complex topology of the $t\bar{t}$ signature is essential in this case. Last, but not least, many physics processes beyond the Standard Model (e.g. Supersymmetry) take into account that the $t\bar{t}$ might be a potential background which needs to be understood. The cross-section measurement effectively paves the way for those analyses.

This thesis

The analysis we present in this thesis uses the first data recorded by the ATLAS detector at the LHC, collected from March 2010 until November 2011. The total amount corresponds to an integrated luminosity 35.3 pb^{-1}.

In chapter 1 we provide an overview of the theory on which this thesis is based on. We highlight the key aspects of the Standard Model, we discuss the physics related with the top quark and in particular the motivation behind the $t\bar{t}$ cross-section measurement, and we describe the simulation process and the relevant samples that are used for the analysis. In chapter 2 the experimental setup is presented. This includes a brief description of the CERN accelerator complex and a detailed presentation of the different sub-systems of the ATLAS detector. Chapter 3 introduces the muon online reconstruction, which is relevant for selecting events with a muon in the final state, such as in the $t\bar{t}$ single-muon topology. We present the performance of the trigger system using the very first data collected and we discuss the methodology for obtaining the trigger efficiency for the $t\bar{t}$ topology without using simulated events. In chapter 4 we describe the offline reconstruction of the objects that appear in the final state of the $t\bar{t}$ single-lepton topology. We discuss the selection requirements applied for collecting the $t\bar{t}$ sample and we give an introduction to the most important aspects of the cross-section analysis. Chapter 5 deals specifically with the characterization of the background with respect to the observable that is used in the cross-section measurement. We discuss and apply a methodology for deriving the shape of the background directly from data. Lastly, in chapter 6 the cross-section analysis is described in detail. We present the measurement as obtained from each of the two single-lepton channels of interest, $t\bar{t}(\mu)$ and $t\bar{t}(e)$, as well as the result after combining them. The related systematic uncertainties are also discussed.

Chapter 1

Theoretical Overview

"As for me, all I know is that I know nothing."

Socrates
c.469 BC - c. 399 BC

The aim of this thesis is to perform a measurement of the production cross-section of top quark-pairs ($t\bar{t}$) in proton-proton collisions. The analysis that will be presented in the next pages uses the very first data collected by the ATLAS detector at the Large Hadron Collider. In this chapter we discuss the underlying theory that is related with this measurement and we point out its most important aspects.

In section 1.1 a brief overview of the Standard Model of particle physics is given, the theory that governs most of the observed processes in the high-energy regime. Section 1.2 discusses the environment of the hadronic collisions and presents the key elements in the structure of the formula used for estimating theoretically the cross-section. Section 1.3 dives into the top quark physics sector: from production of top quarks with emphasis to $t\bar{t}$ pairs, to the decay channels of the latter. The importance of the cross-section measurement is also highlighted. Lastly, section 1.4 provides an overview of the tools that are used to describe these processes at the simulation level and which are encountered in the rest of this thesis.

1.1 The Standard Model of Particle Physics

The Standard Model is the theory that emerged during the 1960s and 1970s as the result of extensive research in the field of High-Energy Physics [17, 30, 16, 18]. Up until that point, physicists had observed a vast number of sub-atomic particles in many different experiments (the particle "zoo") but without being able to explain their nature. The Standard Model effectively put an end to this by being able to categorize the observed physics based on a few elementary particles and their interactions. The elementary particles are categorized in *fermions* and *bosons*, with the fermions being distinguished into leptons and quarks. The basis of the Standard Model is the symmetry group $SU(3)_C \times SU(2)_L \times U(1)_Y$, where the $SU(3)_C$ group describes the strong interaction and the $SU(2)_L \times U(1)_Y$ group the unified electroweak interaction.

The bosons obey the Bose-Einstein statistics [31, 32] and have integer spin. They act as the force mediators when fermions couple with them and therefore they are considered the respective force carriers. The way a particle will interact depends on its quantum properties, thus particles with an electric charge undergo electromagnetic interactions by coupling to the photons, particles with a *color* charge interact through the strong force of which gluons are the mediators, and lastly those with a *weak isospin* interact with the weak force exchanging a weak boson ($W^{\pm}$ or Z^0). Gravity, although it is hypothesized that is mediated by the graviton, this is yet to be experimentally confirmed and is not described by the Standard Model.

The fermions obey the Fermi-Dirac statistics [33, 34] and therefore are half-integer spin particles. They are the main constituents of matter and can be generally placed into three generations. Each generation contains an *up-type* quark, a *down-type* quark, a charged lepton and its corresponding neutrino. The only difference between corresponding fermions from each generation is their mass.

Figure 1.1 shows the different elementary particles of the Standard Model together with their value of spin, electric charge and mass. The electric charge is shown in units of elementary charge (e) which is equivalent to $1.602176 \cdot 10^{-19}$ C. The mass is shown in units of GeV[1]. For each of the particles in the table, an equivalent anti-particle exists with the same properties but with opposite quantum numbers.

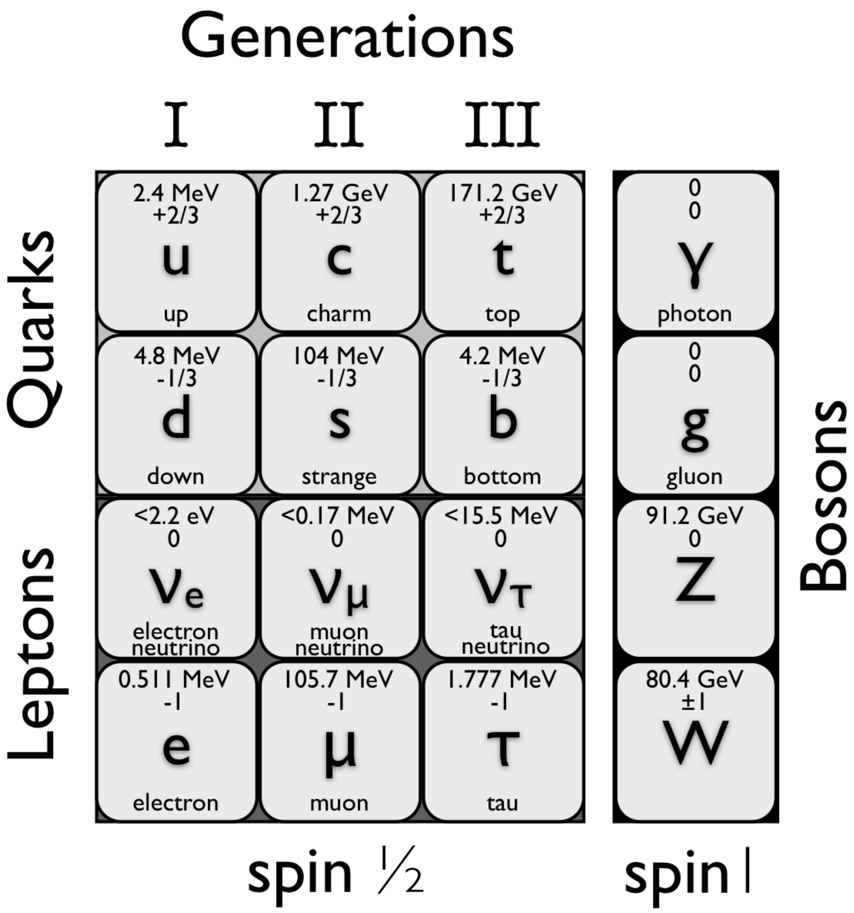

Figure 1.1: *The Standard Model elementary particles: building blocks of matter.*

[1]Throughout this thesis the natural units formalism is used, therefore $\hbar = c = 1$, where $\hbar$ is the reduced Planck constant and c is the speed of light. Consequently, momentum and mass values are given in units of eV (instead of eV$/c$ and eV$/c^2$), unless stated otherwise.

1.1.1 Ingredients of the Standard Model

The Standard Model is defined as a renormalizable relativistic quantum field theory (QFT) which describes the fundamental forces of nature within a single Lagrangian. This definition laconically states a number of key ingredients which are explained in the following.

A quantum field theory

The Standard Model is a QFT, implying that the force fields that it describes are quantized. In practice, this means that a field, when "seen" at an infinite distance, can be described as a particle. Therefore, an immediate connection between the fundamental forces of nature and specific particles is established. On the other hand, it is also an approximate theory, one that is only able to describe the physics up to a certain scale. This is because there exist no widely accepted prescription with which the gravitational field can be quantized. Therefore, within the Standard Model the gravity is completely ignored and only the electromagnetic, the strong and the weak interactions are described by the Standard Model[2]!

A relativistic theory

The Standard Model is a relativistic theory, therefore it is constructed such that the laws of physics are obeyed for every inertial frame of reference. Mathematically, this means that its Lagrangian is a Lorentz scalar, namely it remains invariant under Lorentz transformations.

A renormalizable theory

Within a QFT model, calculations can be performed based on first principles by taking into account all the possible field configurations. However, this is practically impossible and therefore we rely on perturbation theory. Under perturbative calculations we can approximate the result at each order; the higher the order the better the approximation to the real value. However, by expanding to higher orders, the integrals, which generally diverge, lead to infinities. This is an unphysical result. The way that this is dealt with, is to allow the model to absorb the infinities into a finite number of physical quantities. However, an immediate consequence of this method is that the values of the relevant physical quantities may no longer be deduced from first principles. This procedure is called *renormalization* and a theory that is able to absorb all infinities without introducing new ones is called *renormalizable* [30]; the Standard Model is a renormalizable theory.

1.1.2 Symmetries

In order to understand how the fields are formulated within the Standard Model Lagrangian, one must first refer to the notion of symmetry in nature. As Emmy Noether proved in 1915, if an action remains invariant under a group of transformations, therefore implying the existence of a symmetry, then there also exist at least one conserved quantity [35, 36]. In other words, the presence of a symmetry suggests a conservation law (Noether's Theorem).

Symmetries govern the physical world, but, from them all, gauge symmetries have a special role. Gauge symmetries can be categorized in *global*, that remain constant for all space-time points, and *local* that are a function of the space-time coordinates.

[2]It should be mentioned, however, that the gravitational force is by far the weakest of all the fundamental forces. In fact, its relative strength is considered to be many orders of magnitude smaller than the other forces and therefore, in the context of particle physics, ignoring the gravitational force is entirely acceptable.

Global gauge symmetries

As the Noether Theorem suggests, a global gauge transformation leads to a conservation principle. This can be easily demonstrated with the following example of the Lagrangian[3] of the free scalar field with mass m:

$$\mathcal{L} = |\partial^\mu \phi|^2 - m^2|\phi|^2, \tag{1.1.1}$$

which remains invariant under the global gauge transformations ($a \to$ constant):

$$\phi(x) \to e^{iq\alpha}\phi(x) \text{ and} \tag{1.1.2}$$
$$\phi^*(x) \to e^{-iq\alpha}\phi^*(x). \tag{1.1.3}$$

The immediate consequence is that the current:

$$J^\mu = iq(\phi^*\partial^\mu\phi - \phi\partial^\mu\phi^*) \tag{1.1.4}$$

is conserved ($\partial_\mu J^\mu = 0$).

Local gauge symmetries

Taking again the Lagrangian in equation 1.1.1, we impose on it a local gauge transformation similar to the ones from equation 1.1.3, only that now $\alpha = \alpha(x)$. This results to the following:

$$\partial_\mu(\alpha(x)\phi) \neq \alpha(x)(\partial_\mu\phi),$$

which implies that the Lagrangian does not remain invariant. In order to save the invariance we introduce the covariant derivate:

$$D_\mu = \partial_\mu - iqA_\mu(x), \tag{1.1.5}$$

where $A_\mu(x)$ is a vector field, the *gauge field*. By requiring that the gauge field also transforms at the same time:

$$A_\mu(x) \to A_\mu(x) - \partial_\mu\alpha(x), \tag{1.1.6}$$

then the derivative of the ϕ field will give:

$$D_\mu\phi \to e^{iq\alpha(x)}D_\mu\phi \text{ and} \tag{1.1.7}$$
$$D_\mu\phi^* \to e^{-iq\alpha(x)}D_\mu\phi^* \ . \tag{1.1.8}$$

This formulation leads to the following Lagrangian which is invariant under the local gauge transformations:

$$\mathcal{L} = |\partial^\mu\phi|^2 - m^2|\phi|^2 - qJ^\mu A_\mu + q^2A_\mu A^\mu\phi^*\phi - \frac{1}{4}F_{\mu\nu}F^{\mu\nu} \ , \tag{1.1.9}$$

where $F^{\mu\nu} = \partial^\mu A^\nu - \partial^\nu A^\mu$ is called the field strength tensor. It is evident that the first two terms in equation 1.1.9 represent the initial Lagrangian that was invariant under global gauge transformations. The next two terms represent the interaction of the scalar field ϕ with the gauge field A_μ by coupling of the latter to the current J_μ of the former. Lastly, the final term is added explicitly and it represents the contribution of the gauge field to the Lagrangian. It is introduced so that the choice of A_μ remains physical and not entirely arbitrary and it is derived such that the final Lagrangian remains invariant.

The conclusion from this exercise is that in order to have a theory which remains invariant under a local gauge transformation, an extra field is introduced. This extra field, when quantized, becomes the force carrier (gauge boson) that describes the interaction between the matter fields. All fundamental fields that are described by the SM are local gauge invariant.

[3]We refer to the Lagrangian density as the 'Lagrangian'.

1.1.3 Electroweak interactions

The electroweak interaction is built from the unification of the electromagnetic and the weak interaction and its theory was first proposed by S. L. Glashow, S. Weinberg and M. A. Salam. We define the fermionic field ψ_f which can be decomposed into a right-handed and a left-handed component based on the chirality, therefore:

$$\psi_f = \frac{1-\gamma_5}{2}\psi + \frac{1+\gamma_5}{2}\psi = \psi_L + \psi_R \ , \tag{1.1.10}$$

where γ_5 is the fifth gamma matrix of the Dirac matrices (γ^μ) and takes the value $\gamma_5 = i\gamma^0\gamma^1\gamma^2\gamma^3$, while the ψ_L and ψ_R are the left-handed and right-handed projections respectively. Left-handed fermions transform under both the $SU(2)_L$ and $U(1)_Y$ and are represented as weak-isospin doublets:

$$\psi_i = \begin{pmatrix} u_i \\ d_i \end{pmatrix} \text{ or } \begin{pmatrix} \nu_i \\ \ell_i \end{pmatrix} \ , \tag{1.1.11}$$

while right-handed fermions only transform under $U(1)_Y$ and are represented as weak-isospin singlets.

By imposing these symmetries to the Lagrangian of the free fermionic field that describes the spin-1/2 particles ψ_f (Dirac equation):

$$\mathcal{L} = i\sum_f \overline{\psi}_f \gamma_\mu \partial^\mu \psi_f \ , \tag{1.1.12}$$

the covariant derivative must take the following form in order to retain the invariance:

$$D^\mu = \partial^\mu + \frac{1}{2}ig\tau^i W_i^\mu + \frac{1}{2}ig'YB^\mu \ , \tag{1.1.13}$$

where g and g' are coupling constants, τ^i are the Pauli matrices, generators of the $SU(2)_L$, Y is the hypercharge, generator of the $U(1)_Y$, and W_i^μ ($i = 1, 2, 3$) and B^μ are the vector fields that are introduced respectively for each symmetry group. The conserved quantities for the $SU(2)_L$ and the $U(1)_Y$ are the third component of the weak isospin (T_3) and the hypercharge respectively. They are connected via the Gell-Mann - Nishijima formula:

$$Q = T_3 + \frac{Y}{2} \ , \tag{1.1.14}$$

where Q is the conserved quantity (electric charge) of the original $U(1)_{EM}$ symmetry group that describes quantum electrodynamics (QED). As before, the vector fields that are introduced by each group must also be transformed:

$$B^\mu = B^\mu - \partial^\mu \alpha(x) \ , \tag{1.1.15}$$
$$W_i^\mu = W_i^\mu - \partial^\mu \beta_i(x) - g\varepsilon_{ijk}\beta_j(x)W_k^\mu \ , \tag{1.1.16}$$

where ε_{ijk} is the Levi-Civita symbol, and the $\alpha(x)$ and $\beta_j(x)$ are phases. In the end the electroweak Lagrangian consists of the following terms:

$$\mathcal{L} = \mathcal{L}_{fermion} + \mathcal{L}_{interaction} + \mathcal{L}_{gauge} \ , \tag{1.1.17}$$

where:

$$\mathcal{L}_{fermion} = i\sum_f \overline{\psi}_f \gamma_\mu \partial^\mu \psi_f = i\overline{L}\gamma^\mu \partial_\mu L + i\overline{R}\gamma^\mu \partial_\mu R \ , \tag{1.1.18}$$

$$\mathcal{L}_{interaction} = \overline{L}\gamma^\mu(-\frac{g}{2}\tau^i W_\mu^i - \frac{g'}{2}YB_\mu)L + \overline{R}\gamma^\mu(-\frac{g'}{2}YB_\mu)R \ , \tag{1.1.19}$$

$$\mathcal{L}_{gauge} = -\frac{1}{4}W_{\mu\nu}^i W^{i,\mu\nu} - \frac{1}{4}B_{\mu\nu}B^{\mu\nu} \ . \tag{1.1.20}$$

The parameters L and R denote the left-handed doublets and right-handed singlets for the fermions, while the $W^i_{\mu\nu}$ and $B_{\mu\nu}$ correspond to the field strength tensors. Similarly to the example showed in section 1.1.2, the first term corresponds to the fermion field with its left-handed and right-handed components, the second term represents the interaction of the fermions with the gauge bosons, and the last term provides the contribution and self-interactions of the vector fields. Rewriting the interaction term, we can separate it into two categories:

$$\mathcal{L}_{charged} = -\frac{g}{2}\overline{L}\gamma^{\mu}(\tau^1 W^1_{\mu} + \tau^2 W^2_{\mu})L \text{ and} \tag{1.1.21}$$

$$\mathcal{L}_{neutral} = -\frac{g}{2}\overline{L}\gamma_{\mu}\tau^3 W^3_{\mu}L - \frac{g'}{2}\overline{L}\gamma^{\mu}YB_{\mu}L - \frac{g'}{2}\overline{R}\gamma^{\mu}YB_{\mu}R. \tag{1.1.22}$$

$\mathcal{L}_{charged}$ evidently contains only left-handed components, therefore it can be written in the following form:

$$\mathcal{L}_{charged} = -\frac{g}{2}\overline{L}\gamma^{\mu}\begin{pmatrix} 0 & W^1_{\mu} - iW^2_{\mu} \\ W^1_{\mu} + iW^2_{\mu} & 0 \end{pmatrix}, \tag{1.1.23}$$

where it is possible to extract the definition of the charged gauge boson as the linear combination of the vector fields, namely:

$$W^{\pm}_{\mu} = \frac{1}{\sqrt{2}}(W^1_{\mu} \mp W^2_{\mu}). \tag{1.1.24}$$

The fact that left-handed fermions do not undergo charged current interactions is incorporated through the vector (V) and axial-vector (A) components that are introduced and is in accordance to the experimental observation of parity violating processes. Equivalently, from the $\mathcal{L}_{neutral}$, which contains both left-handed and right-handed components, we can redefine the fields in the following way:

$$\begin{pmatrix} A_{\mu} \\ Z_{\mu} \end{pmatrix} = \begin{pmatrix} \cos\theta_W & \sin\theta_W \\ -\sin\theta_W & \cos\theta_W \end{pmatrix}\begin{pmatrix} B_{\mu} \\ W^3_{\mu} \end{pmatrix}, \tag{1.1.25}$$

which gives the neutral gauge bosons as a combination of the introduced vector fields. The parameter θ_W is called the Weinberg angle and it relates with the coupling constants in the following way:

$$\sin\theta_W = \frac{g'}{\sqrt{g^2 + g'^2}}, \tag{1.1.26}$$

$$\cos\theta_W = \frac{g}{\sqrt{g^2 + g'^2}}. \tag{1.1.27}$$

In conclusion, the introduced vector fields which are required to retain the invariance of the electroweak Lagrangian, give rise to gauge bosons that act as mediators of the electroweak interaction. However, in the initial formalism these gauge bosons are expected to be massless. This contradicts the experimental observations since the $W^{\pm}$ and Z^0 have a mass. If those masses are put in by hand then the invariance of the Lagrangian breaks. As a result, an additional mechanism is required.

1.1.4 The Higgs mechanism

The Higgs mechanism [19, 20, 21] is the proposed theory with which the mass of the gauge bosons, evident in the weak interactions, is explained. The theory suggests to introduce a complex scalar field doublet:

$$\phi = \begin{pmatrix} \phi^+ \\ \phi^0 \end{pmatrix} , \tag{1.1.28}$$

which remains invariant under $SU(2)_L$ transformations. We write the Lagrangian of the system:

$$\mathcal{L}_{Higgs} = (D_\mu \phi)^\dagger (D^\mu \phi) - V(\phi) , \tag{1.1.29}$$

where $V(\phi)$ is the potential of the field (Higgs potential) and is given by:

$$V(\phi) = -\mu^2 |\phi|^2 + \lambda^2 |\phi|^4. \tag{1.1.30}$$

The covariant derivative in the Lagrangian is also chosen such that it remains invariant under the $SU(2)_L \times U(1)_Y$ transformations. In the notation in equation 1.1.30, λ is a positive constant, while μ^2 denotes the mass term of the field. When $\mu^2 > 0$, the Lagrangian transforms to the QED equivalent of a charged scalar particle with mass μ and ϕ^4 self-interactions. However, if $\mu^2 < 0$ then the minimum of the potential is given by:

$$|\phi_0|^2 = -\frac{\mu^2}{2\lambda} \tag{1.1.31}$$

and not zero as one might have expected. This value, referred to as the vacuum expectation value, defines in fact a circle of minima and therefore an infinite number of ground states for the Higgs potential. We can choose an arbitrary value without loss of generality:

$$\phi_0 = \begin{pmatrix} 0 \\ u/\sqrt{2} \end{pmatrix} , \tag{1.1.32}$$

where $u = \sqrt{-\mu^2/\lambda}$. This, however, breaks the invariance under $SU(2)_L \times U(1)_Y$ transformations (spontaneous symmetry breaking) but retains it for the $U(1)_{EM}$ symmetry group. By perturbing the system and by an appropriate choice of gauge, we can write:

$$\phi(x) = \frac{1}{\sqrt{2}} \begin{pmatrix} 0 \\ u + h(x) \end{pmatrix} , \tag{1.1.33}$$

and the Lagrangian now becomes:

$$\begin{aligned} \mathcal{L}_{Higgs} = & \frac{1}{8} \left[g^2 (W_1^2 + W_2^2) + (-gW_3 + g' Y B_\mu)^2 \right] (u + h(x))^2 \\ & + \frac{1}{2} (\partial h(x))^2 - \mu^2 (h(x))^2 - u\lambda (h(x))^3 - \frac{1}{4} \lambda (h(x))^4 , \end{aligned} \tag{1.1.34}$$

where, using the equations 1.1.23 and 1.1.25, the first two terms can be written as:

$$\mathcal{L}_{Higgs} = \frac{1}{2} g^2 W^+ W^- (u + h(x))^2 + \frac{1}{8} (g^2 + g'^2) Z^2 (u + h(x))^2 + 0 \cdot A_\mu^2 + \dots \tag{1.1.35}$$

Evidently, under this formulation mass terms have been included in the Lagrangian and consequently in the Standard Model; they are given by:

$$M_W = \frac{1}{2} u g \text{ and} \tag{1.1.36}$$

$$M_Z = \frac{1}{2} u \sqrt{g^2 + g'^2} , \tag{1.1.37}$$

while for gauge field A_μ the mass term is zero, pointing to the massless photon. The vacuum expectation value (u) is approximated to $u \approx 246$ GeV and the theoretically expected values of the W and Z bosons are in good agreement with the experimental results.

The emergence of these masses comes as a result of the Goldstone theorem. Once the symmetry was broken, due to the choice of a ground state value for the potential, three massless bosons appear (Goldstone's theorem). These are subsequently absorbed by the gauge fields as their longitudinal polarization, hence giving a mass to the gauge bosons. The massless field (photon), that still remains, preserves the $U(1)_{EM}$ symmetry. From the initial four degrees of freedom of the Higgs doublet, however, one more remains and it corresponds to the physical Higgs field, which has a mass term provided by:

$$M_{Higgs} = \sqrt{2\lambda u} \; . \tag{1.1.38}$$

This is the so-called Higgs boson. Since the λ parameter is entirely arbitrary, there is no prediction on the expected mass of this particle and thus it can only be probed experimentally. Discovering this new particle, which is well motivated by the theory, is one of the major goals of the physics program of the Large Hadron Collider.

Yukawa interactions

The Higgs mechanism, as presented so far, does not offer an answer on the mass of the fermions. In fact, in the Lagrangian the fermions remain massless contradicting the experimental observations. To tackle this problem an extra term is introduced which allows the fermions to interact with the Higgs field; the Yukawa interaction. The Lagrangian term is of the form:

$$\mathcal{L} = -\lambda_f \overline{L}\phi R - \lambda_f \overline{R}\phi^\dagger L \; , \tag{1.1.39}$$

where λ_f is the coupling between the fermion and the Higgs field. As before, when the symmetry breaks, the fermions acquire mass which is given by:

$$M_f = \frac{\lambda_f}{\sqrt{2}} u \; . \tag{1.1.40}$$

Like for the case of the Higgs boson, the parameter λ_f is not predicted by the theory and as a result it can only be probed experimentally.

1.1.5 Strong interactions

The description of the strong interactions arises from the need to explain why quarks form mesons ($q\overline{q}$) and baryons (qqq or $\overline{qqq}$). A particularly interesting example is the pion-proton resonance Δ^{++}, which consists of three up-quarks (uuu) thus having the following quantum numbers: charge $Q = 2$ and isospin $I = 3/2$. The resonance with the known terms is symmetric under permutation of two quarks, something that contradicts the Pauli principle; no two identical fermions (half-integer spin particles) are allowed to occupy the same quantum state simultaneously. To accommodate the reasoning of Pauli the notion of *color* charge was introduced by O. W. Greenberg in 1965, an arbitrary quantum number that leaves the state antisymmetric. The values of the color charge are *red, blue* and *green*. Under this definition all hadrons are color-neutral, with the baryons carrying all three colors and the mesons, which are made from a quark-antiquark pair, carrying a color and its complimentary color (anti-color) charge.

The symmetry group $SU(3)_C$ is introduced in the Standard Model in order to describe the strong interactions. The color C is the conserved quantity and the generators of the group are given by the eight Gell-Mann matrices λ_i (3-dimensional equivalent to the Pauli matrices). The Lagrangian is given by:

$$\mathcal{L}_{QCD} = \sum_{flavors} \overline{\psi}_q (i\gamma^\mu D_\mu - m)\psi_q - \frac{1}{4} G^a_{\mu\nu} G^{a,\mu\nu} \ , \tag{1.1.41}$$

where as ψ_q are the Dirac four-spinors corresponding to the quark fields, D_μ is the covariant derivative, and $G^a_{\mu\nu}$ is the field strength tensor. The index a corresponds to the gluon-color index $a = 1, \ldots, 8$. The number of flavors in the Lagrangian runs up to six, to account for all the known quarks, while also they appear in three color charges (not shown in the notation). The covariant derivative is given by:

$$D_\mu = \partial_\mu + i g_s \lambda_a A^a_\mu \ , \tag{1.1.42}$$

where g_s corresponds to the coupling constant of the strong interaction while A^a_μ denotes the gluon fields. The field strength tensor is also given by:

$$G^a_{\mu\nu} = \partial_\mu A^a_\nu - \partial_\nu A^a_\mu - g_s f^{ABC} A^B_\mu A^C_\nu \ . \tag{1.1.43}$$

The gluons which have been referred up to this point, are naturally the carriers of the strong force. They are massless, spin-1 particles with no electric charge, no hypercharge and no isospin. However, they do hold color charge which allows them to also couple with themselves. The coupling of the strong interaction is given by the following relation:

$$\alpha_s = \frac{g_s^2}{4\pi} \ . \tag{1.1.44}$$

This coupling, however, depends on the momentum scale of the interaction, denoted as Q^2; it is a ‘running coupling’. This is understood after including higher order corrections in the strong interactions. Taking into account fermion loops (virtual fermion-antifermion pairs), vacuum polarization terms are included which pronounce the effect of *screening* of the color charge[4]. However, gluon contributions have a different effect as they also have a color charge but in addition an anti-color magnetic moment. Eventually, the gluon correction acts in the opposite direction of screening (*anti-screening*). The overall effect results in a prevailing anti-screening effect. The renormalized coupling constant - where the renormalization is required in the process of higher order corrections to avoid ultraviolet divergencies - is given by:

$$\alpha_s(Q^2) = \frac{\alpha_s(\mu_r^2)}{1 + \frac{1}{12\pi}\alpha_s(\mu_r^2) \cdot (11N_C - 2N_f) \ln\left(\frac{Q^2}{\mu_r^2}\right)} \ , \tag{1.1.45}$$

where N_C is the number of color charges ($N_C = 3$) and N_f is the number of fermions and depends on the scale Q^2 ($N_f = 6$ when $Q > M_{top}$, while $N_f < 6$ for lower energies). The parameter μ_r^2 is a reference mass parameter directly related with the choice of the renormalization scale. We can introduce a mass scale Λ_{QCD}; a scale for which the strong coupling constant is infinite:

$$\ln(\Lambda^2_{QCD}) = \ln(\mu_r^2) - \frac{12\pi}{11N_C - 2N_f \alpha_s(\mu_r^2)} \ , \tag{1.1.46}$$

and the equation 1.1.45 then takes the form:

$$\alpha_s(Q^2) = \frac{12\pi}{(11N_C - 2N_f)\ln\left(\frac{Q^2}{\Lambda^2_{QCD}}\right)} \ . \tag{1.1.47}$$

[4]Analogously to QED where electron-positron pairs emerging in higher-orders act as dipoles around the real charge inducing a partial screening effect.

It is evident that when $Q^2 \to \infty$, namely the distance of the interaction shrinks, the coupling goes to zero suggesting that quarks behave as free particles. This is the *asymptotic freedom* effect and it allows us to use perturbation theory in QCD at high energies. On the other hand, it is by definition that when Q^2 is low, namely $Q^2 \to \Lambda^2_{QCD}$, the coupling goes to infinity and all perturbative computations fail. This effect describes the *color confinement* which suggests that no free quarks can be directly observed by experiments. The value of the Λ_{QCD} scale can be extracted experimentally after choosing a renormalization scheme, its value for the modified minimal subtraction scheme ($\overline{MS}$) and for $N_f = 5$ is approximately ~ 200 MeV.

1.2 Cross-section in hadronic collisions

At the LHC, proton beams are used as the colliding particles[5]. The proton is a baryon consisting of two up-quarks and one down-quark (valence quarks), each carrying a different color-charge thus forming a bound neutral-color state. In addition, gluons as well as pairs of quark-antiquarks (sea-quarks) emerge briefly due to quantum fluctuations. The interesting collisions, namely collisions where new particles appear, occur when the constituents of the two opposite-moving protons interact with each other (inelastic process). Such a process is rather complex but it can be separated into the following parts:

- The *parton*[6] *distribution function (PDF)*: when constituents of the protons interact with each other, each carries a fraction of the total momentum of the initial particle ($x \in (0, 1)$). This fraction is modeled by the PDF, which is defined as the probability density for having a particle with momentum fraction x at a given scale Q^2. Clearly, PDFs are not an inherent part of the inelastic collisions but are rather a parametrization that facilitates calculations. It should be noted that PDFs cannot be estimated with perturbative QCD and therefore are extracted from experimental data, typically involving global fits to the data of deep-inelastic scattering experiments e.g. from the HERA *ep* collider experiments H1 [37, 38, 39, 40] and ZEUS [41, 42], as well as fixed target experiments e.g. NuTeV [43], including results from Drell-Yan [44] and jet production processes [45, 46, 47] . Figure 1.2 shows an example of a PDF for two different Q^2 values. It uses the parametrization of the MSTW group, which stands for A.D. Martin, W.J. Stirling, R.S. Thorne and G. Watt. The complete list of data included in this fit can be found in [48].
- *The hard-process*: the interaction between two partons from each of the colliding protons, when it happens at sufficiently high energy, has the result to break their confinement and lead to the appearance of other particles. The products of the hard-process are usually the signature of interest.
- The *initial state radiation (ISR)*: incoming partons may radiate quarks or gluons due to quantum fluctuations, therefore losing part of the parton's initial momentum fraction.
- The *final state radiation (FSR)*: outgoing partons, similarly to what happens in the case of ISR, radiate quarks or gluons. Although, the definition between ISR and FSR is very similar, kinematically they differ substantially.
- The *underlying event*: proton remnants, namely everything but the hard-process partons, also contribute to the overall process as they hold a color charge. Usually, the underlying event manifests itself through soft scatterings. The ISR/FSR processes can also be regarded as part of the underlying event.

[5] The LHC can also collide heavy ion beams but these collisions are out of the scope of this thesis.
[6] Quarks and gluons are collectively referred to as partons.

- The *hadronization*: outgoing partons from any of the previous processes eventually form hadrons as a result of the color confinement.
- The *decay*: formed hadrons or other unstable particles that may be formed during the hard-process eventually decay into more stable particles. Oftentimes, extensive radiating effects from a single parton may lead to a spray of particles towards the same direction. This formation is typically referred to as a jet.

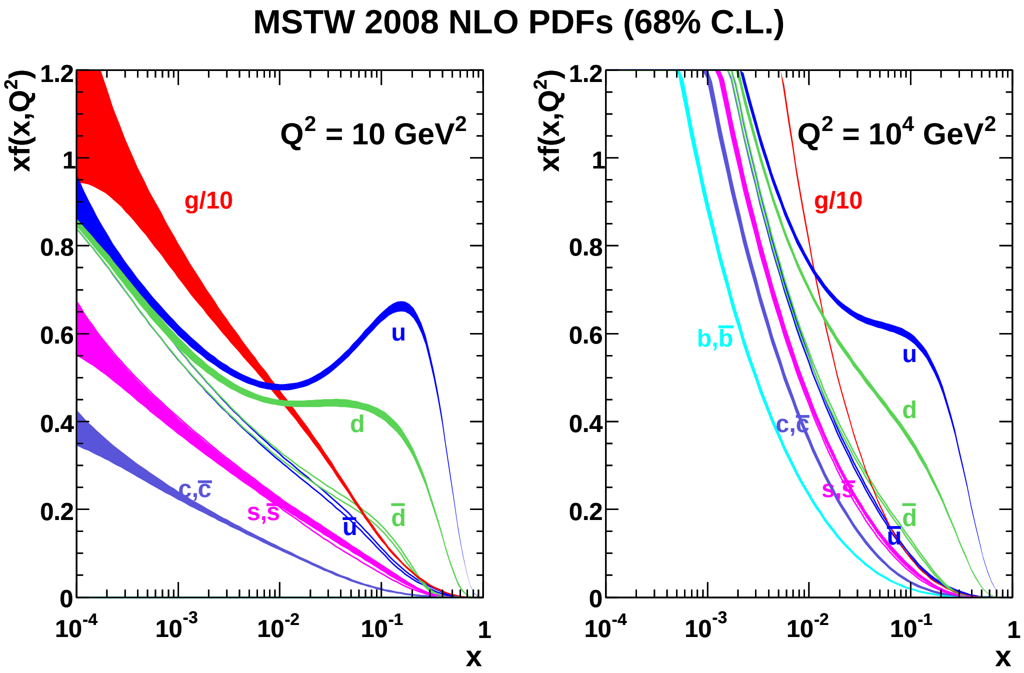

Figure 1.2: *The* `MSTW2008NLO` *PDF of protons for two different scales (Q^2) and as function of the parton momentum fraction x. The letter g is given for the gluons while u, d, s, c denote the corresponding quarks, with the anti-quarks given with as e.g. $\bar{u}$; see also figure 1.1. It should be noted that the estimate for gluons is divided by an order of magnitude, hence shown as $g/10$. Plots taken from [48].*

Calculating the cross-section of a process based on the original incoming and outgoing particles is an unfeasible task. The main reason is that we cannot have knowledge of the momentum carried by each parton since they are constituents of the proton. Instead, we calculate the cross-section at the hadronic level. Consider the process depicted in figure 1.3 where the two incoming protons have momenta P_1 and P_2 and their interacting partons have momenta that are given by $p_1 = x_1 P_1$ and $p_2 = x_2 P_1$, respectively. The hadronic cross-section is formulated as follows:

$$\sigma(P_1, P_2) = \sum_{i,j} \int dx_i dx_j f_i(x_1, \mu_f^2) f_j(x_2, \mu_f^2) \hat{\sigma}_{ij} \left(p_1, p_2, \alpha_s(\mu_r^2), \frac{Q^2}{\mu_r^2}, \mu_f^2 \right) , \qquad (1.2.1)$$

where Q is the scale of interaction and the functions $f_i(x_1, \mu_f^2)$ and $f_j(x_2, \mu_f^2)$ are the corresponding PDFs at a certain *factorization scale* μ_f. The $\hat{\sigma}_{ij}$ denotes the cross-section of partons i and j at short-distance physics[7] and therefore can be calculated using perturbation theory.

[7] We refer to *short-distance* physics the regime within which we can perform perturbative calculations (due to asymptotic freedom). Likewise, long-distance physics suggests the opposite.

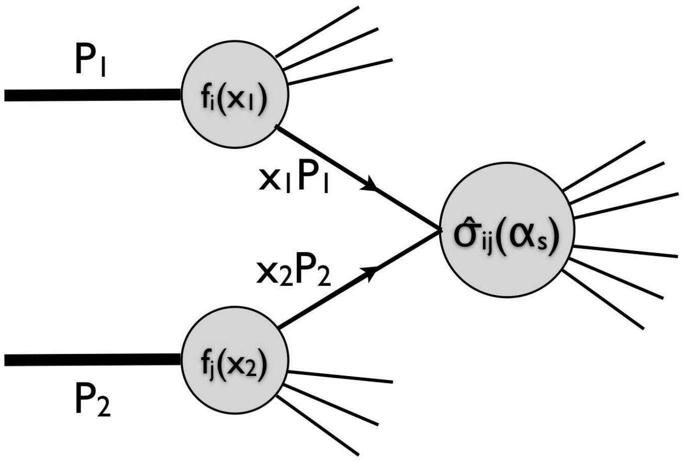

Figure 1.3: *An example of a hard-process interaction.*

Thus, it is given by:

$$\hat{\sigma} = \alpha_s^k \sum_{m=0}^{n} c_m \alpha_s^m \ , \tag{1.2.2}$$

where c_m are functions with kinematic variables and k gives the leading power of the interaction. It is important to note that with this formulation, when including higher orders, the cross-section formula may show terms which cause divergencies. These naturally break the calculation but can effectively be factored out by including them in the PDFs in equation 1.2.1; the PDFs are experimentally estimated. The factorization scale, shown above, is similar to the renormalization scale in the sense that it is pre-defined and somewhat arbitrary. It is set such that it defines the threshold between long-range and short-range physics so that a radiating parton with momentum less than the given scale becomes part of the PDF, else it contributes to the short-distance cross-section. Typically, the factorization scale and the renormalization scales are set to be equivalent to the interaction scale Q. For a calculation of the cross-section at infinite order the result is entirely independent on the chosen renormalization and factorization scales, however, as this is computationally unfeasible, a residual dependence always exists at the theoretical level that depends on the non-included higher orders.

Figure 1.4 shows the cross-section evolution for various processes in proton-antiproton (Tevatron) and proton-proton collisions (LHC) as a function of the center-of-mass energy $(\sqrt{s})$[8].

1.3 Top-quark physics

From all the particles of the Standard Model this thesis focuses on the top quark. In 1973, the existence of the top quark was implied theoretically by the prediction of M. Kobayashi and T. Maskawa on the existence of at third generation of quarks as a mean to explain CP-violation in kaon decays [22]. As their theory was heavily relying on the GIM mechanism (by S.L. Glashow, J. Iliopoulos and L. Maiani) [50] it was not until the discovery of the J/ψ meson ($c\bar{c}$) in 1974 [51, 52], which verified the existence of charm quark based on the same mechanism, that it was actually believed as a plausible theory. The prediction was further solidified with

[8]The center-of-mass energy is given by: $\sqrt{s} = \sqrt{(E_1 + E_2)^2 - (\mathbf{p}_1 + \mathbf{p}_2)^2}$, where E and $\mathbf{p}$ denote the energy and the momentum vector of the particle respectively.

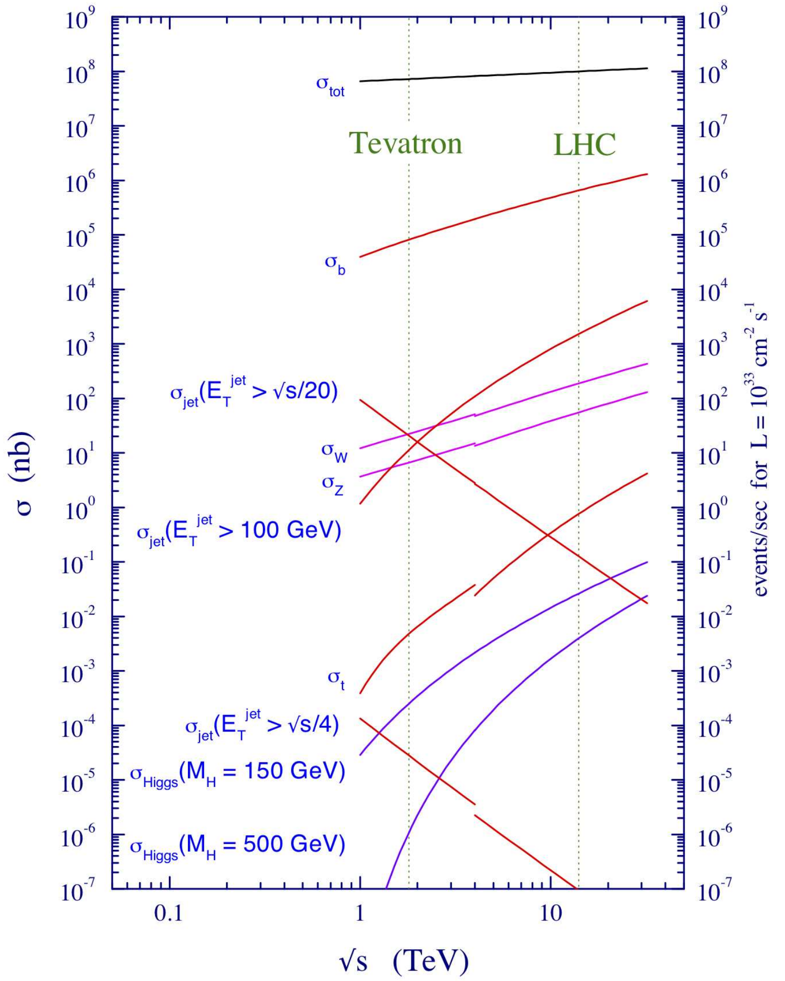

Figure 1.4: *Evolution of cross-section for proton-antiproton (Tevatron) and proton-proton (LHC) collisions. Plot taken from [49].*

the discovery of the bottom quark by the E288 experiment at Stanford's Linear Collider in 1977 [23]. Eventually, the top quark was first observed at the Tevatron proton-antiproton collider in 1995 by both the CDF [24] and DØ [25] experiments. As it stands today, it is by far the heaviest of all experimentally known elementary particles with a mass estimated at $M_t = 172.9$ GeV [53].

1.3.1 Production of top quarks in hadronic collisions

Top-quarks can be produced via both electroweak and strong interactions. In the first case, a single quark is produced. Three distinct channels exist: the Wt-channel where the top quark is produced in association with a W boson; the t-channel where a virtual W boson transforms a bottom quark into a top quark (t-channel); the s-channel where a time-like off-shell W boson decays into a top and a bottom quark.

In the second case, which is also the focus of this thesis, the top quark is produced in pairs of a top and an anti-top quark ($t\bar{t}$). It is interesting to see what is the momentum fraction threshold for the production of a $t\bar{t}$ signature. Considering the $t\bar{t}$ as a single-particle system with invariant mass $M = 2M_{top}$, we can write the rapidity of the system with the following terms:

$$y = \frac{1}{2} \ln \frac{E + p_z}{E - p_z} \ , \tag{1.3.1}$$

with E and p_z the total energy and the longitudinal momentum of the system as measured in the lab-frame. The momentum fractions carried by the incoming partons are given by:

$$x_1 = \frac{M}{\sqrt{s}} e^{+y} \ , \text{ and} \tag{1.3.2}$$

$$x_2 = \frac{M}{\sqrt{s}} e^{-y} \ . \tag{1.3.3}$$

If $p_z = 0$, no boost is experienced in the system and the rapidity is $y = 0$. Consequently, the momentum fractions of the partons are equal, $x_1 = x_2$. For this system, we can define the threshold, x_{thr}, for each of the partons momentum fraction by simply substituting M with 346 GeV (assuming a top quark invariant mass of 173 GeV) and with $\sqrt{s}$ given by the energy of the collision. Thus, it will be $x_{thr} \sim 0.18$ and $x_{thr} \sim 0.05$ for the energies of the Tevatron (1.96 TeV) and the LHC (7 TeV) respectively. This clearly suggests that at the LHC, in comparison to the Tevatron, also partons with much lower momentum fraction will be contributing thus increasing greatly the cross-section. In addition, with the help of figure 1.2 is evident that at the LHC energies the probability of gluons to have the necessary momentum fraction is greatly increased. As as result, the primary contribution in $t\bar{t}$ production comes from gluon-gluon fusion. In fact, for the LHC 2010-2011 data-taking, the collision energy of $\sqrt{s} = 7$ TeV gives a $\sim 75\%$ contribution for $gg \to t\bar{t}$, at leading order, whereas for the nominal, $\sqrt{s}$ of 14 TeV, the contribution rises to $\sim 86\%$. Instead, for the Tevatron the most dominant production channel was via quark-antiquark annihilation with a contribution of approximately $\sim 91\%$. Figure 1.5 shows the leading-order Feynman diagrams of $t\bar{t}$ production, namely quark-antiquark annihilation ($q\bar{q} \to t\bar{t}$) and gluon-gluon fusion ($gg \to t\bar{t}$). It should be noted that at the next-to-leading order quark-gluon ($qg \to t\bar{t}$) contributions also appear.

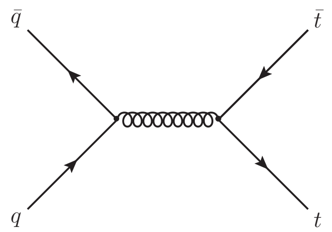

(a) Quark - antiquark annihilation.

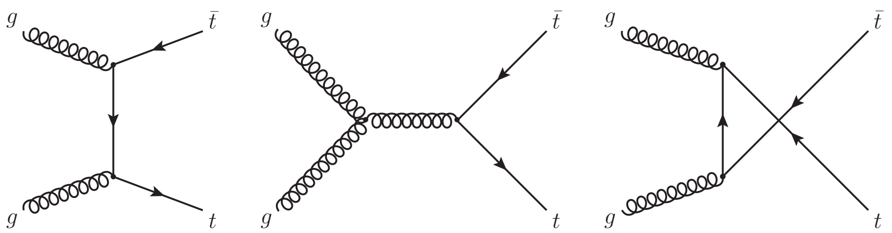

(b) Gluon-gluon fusion.

Figure 1.5: *The leading order diagrams for $t\bar{t}$ production.*

At the theoretical level, for estimating the top quark-pair production cross-section we can set the scale of the interaction to be equal to the mass of the top quark. As the top quark mass is much larger than the QCD scale, the strong coupling constant will give a value of $\alpha_s(M_{top}) \sim 0.1$, thus allowing us to perform perturbation theory and estimate the short-distance cross-section. We can write the cross-section with the following form (stemming from expanding equation 1.2.2):

$$\hat{\sigma}_{t\bar{t}}(\hat{s}, M_{top}^2, \alpha_s(\mu^2), \mu^2) = \frac{\alpha_s^2(\mu^2)}{M_{top}^2} \mathcal{F}_{t\bar{t}}(\rho, M_{top}^2, \alpha_s(\mu^2), \mu^2) \ , \tag{1.3.4}$$

where $\hat{s} = x_1 x_2 s$, corresponding to the squared center-of-mass energy of the colliding partons, $\rho = 4M_{top}^2/\hat{s}$, and $\mathcal{F}_{t\bar{t}}$ is the perturbative series of dimensionless scaling functions which correspond to the order of calculation. It is therefore written as:

$$\mathcal{F}_{t\bar{t}}(\rho, M_{top}^2, \alpha_s(\mu^2), \mu^2) = \mathcal{F}_{t\bar{t}}^{(0)}(\rho) + 4\pi\alpha_s(\mu^2) \left[\mathcal{F}_{t\bar{t}}^{(1)}(\rho) + \overline{\mathcal{F}}_{t\bar{t}}^{(1)}(\rho) \ln \frac{\mu^2}{M_{top}^2} \right] + \mathcal{O}(\alpha_s^2) \ , \tag{1.3.5}$$

where the first term corresponds to the leading-order estimate, the second term to the next-to-leading order and so on. At each order, the necessary Feynman diagrams that contribute are taken into account and are integrated in the whole momentum phase-space. For leading-order the tree-level gluon-gluon fusion and quark-antiquark annihilation diagrams are important and the result is proportional to α_s^2.

One may assume that higher order corrections corrections are not necessary, given the small value of α_s, however, when considering the coefficients of those terms, significant contributions may arise. Moreover, as mentioned earlier, the dependence of the leading-order estimate from the renormalization/factorization scale is significant and with including higher order corrections we can reduce this effect. These highlight the importance of implementing higher order corrections. At the next-to-leading order ($\mathcal{O}(\alpha_s^3)$), both virtual and real contributions are taken into account. The virtual corrections arise from interference of the tree-level amplitude with one-loop virtual amplitudes, resulting in ultra-violet and infra-red divergencies. The ultra-violet divergencies are handled by the renormalization scheme while infra-red effects are eventually cancelled by the factorization. On the other hand, the real corrections appear from amplitudes due to flavor excitation, gluon splitting or direct gluon emissions. These, also give rise to contributions to the $t\bar{t}$ production cross-section from the qg and $g\overline{q}$ channels. In this case, soft (low-energy) or collinear effects may emerge which cannot be calculated with perturbation, instead they are isolated through factorization. Typical examples of next-to-leading order virtual and real corrections to $t\bar{t}$ production are shown in figure 1.6. It should be mentioned that the actual contribution of the $gg \to t\bar{t}$ channel rises at the next-to-leading order to $\sim 83\%$, for LHC collisions at $\sqrt{s} = 7$ TeV, and $\sim 90\%$ for the LHC at $\sqrt{s} = 14$ TeV, which is significantly higher than the leading-order expectation, thus emphasizing the need for higher-order corrections in the theoretical predictions.

An exact calculation at the next-to-next-to-leading order ($\mathcal{O}(\alpha_s^4)$) does not exist. Instead, approximate methods are applied where the appearing logarithmic terms at next-to-leading order, which result after factoring collinear divergencies into the PDFs, are re-summed to the perturbative expansion at a given α_s order. The most up-to-date theoretical cross-section estimate[9] for the inclusive $t\bar{t}$ production for proton-proton collisions at $\sqrt{s} = 7$ TeV is taken at this approximate next-to-next-to-leading order and is given at [54, 55]:

$$\sigma_{t\bar{t}} = 164.57^{+4.30}_{-9.27}(\text{scale})^{+7.15}_{-6.51}(\text{PDF}) \text{ pb.} \tag{1.3.6}$$

This calculation assumes a mass of $M_t = 172.5$ GeV and uses the `CTEQ6.6` next-to-leading order PDF [56]. For the analysis performed in this thesis these numbers are used as reference.

[9] Cross-sections are given in units of barn. 1 barn $= 10^{-28}\ m^2$

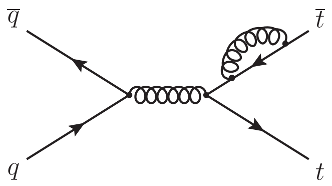

(a)

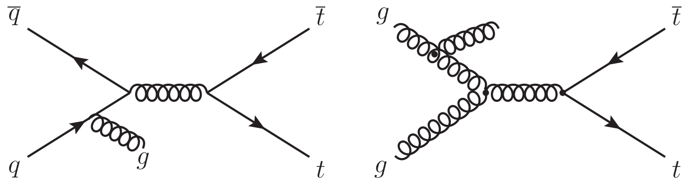

(b)

Figure 1.6: *Next-to-leading order ($\mathcal{O}(\alpha_s^3)$) virtual (a) and real (b) corrections to $t\bar{t}$ production in proton-proton collisions.*

1.3.2 Top quark final state topology

The top quark decays predominantly into a W boson and a b-quark, $t \to Wb$. The decay width of this process can be written at leading order in the following form [57]:

$$\Gamma_{LO}(t \to Wb) = \frac{G_F m_t^3}{8\pi\sqrt{2}}|V_{tb}|^2 \left(1 - \frac{M_W^2}{M_t^2}\right)^2 \left(1 + 2\frac{M_W^2}{M_t^2}\right) , \tag{1.3.7}$$

where G_F is the Fermi constant and $|V_{tb}|$ the CKM matrix element. Assuming three quark generations and unitarity of the CKM matrix, the value of the V_{tb} is found to be [53]:

$$V_{tb} = 0.999152^{+0.000030}_{-0.000045} , \tag{1.3.8}$$

which justifies the initial expectation, $\Gamma_{t\to Wb} \approx \Gamma_t$. After including higher order QCD corrections the decay width becomes:

$$\Gamma(t \to Wb) = \Gamma_{LO}\left[1 - \frac{2\alpha_s}{3\pi} f\,(y)\right] , \tag{1.3.9}$$

where the function $f(y)$ is defined as:

$$\begin{aligned} f(y) &= \frac{2\pi^2}{3} - 2.5 - 3y + 4.5y^2 - 3^2 \ln y \text{ , and} \\ y &= \frac{M_W^2}{M_t^2} . \end{aligned}$$

Using $M_W = 80.4$ GeV and $M_t = 173$ GeV, we have $\Gamma_t = 1.34$ GeV which corresponds to a lifetime of roughly $5 \cdot 10^{-25}$ seconds [58]. This is the most striking characteristic of the top quark, since its lifetime is about an order of magnitude smaller than the hadronization timescale. As a result, it decays via the weak interaction long before it hadronizes and therefore its properties can be directly probed through its decay products.

The final topology of a $t\bar{t}$ event depends entirely on the decay of the W bosons. The W boson decays either leptonically, $W \to \ell\nu_\ell$, or hadronically, $W \to q\bar{q}'$. Naturally, this gives three distinct channels:

- The *di-leptonic* channel: when both W bosons decay leptonically, the final state consists of two high-p_{T} charge leptons and two high-p_{T} neutrinos, and two jets from b-quark hadronization (b-jets).
- The *single-lepton* channel: when one W boson decays leptonically and the other hadronically. The signal consists of one high-p_{T} charged lepton, its corresponding neutrino, the two b-jets and two jets from light-quark hadronization (light-jets).
- The *fully-hadronic* channel: when both W bosons decay hadronically. The signature consists exclusively of jets, namely the two b-jets and four light-jets.

The leptonically decaying W boson can result in any of the three flavors ($e\nu_e$, $\mu\nu_\mu$ or $\tau\nu_\tau$). The analysis presented in this thesis focuses on the single-lepton $t\bar{t}$ channel with an electron, $t\bar{t}(e)$, or a muon, $t\bar{t}(\mu)$, in their final state. The reason for making the distinction for the channels with τ-leptons in their final state, is because the τ decays fast, either hadronically ($\sim 65\%$) producing jets, or leptonically via $\tau \to e\nu_e\nu_\tau$ ($\sim 17.8\%$) or $\tau \to \mu\nu_\mu\nu_\tau$ ($\sim 17.2\%$). In the first case, it is difficult to distinguish the τ from a jet at the experimental level, while in the second case it is almost impossible to distinguish it from the original W boson decay. Figure 1.7 shows schematically the different decay channels of the $t\bar{t}$. The contributions, assuming a branching ratio for the hadronically decaying W boson of 67.6% [53], are 43.8% from single-lepton with about 1/3 having a τ-lepton in the final state, 10.5% from di-leptonic events with roughly half having at least one τ-lepton, and 45.7% are fully-hadronic decays.

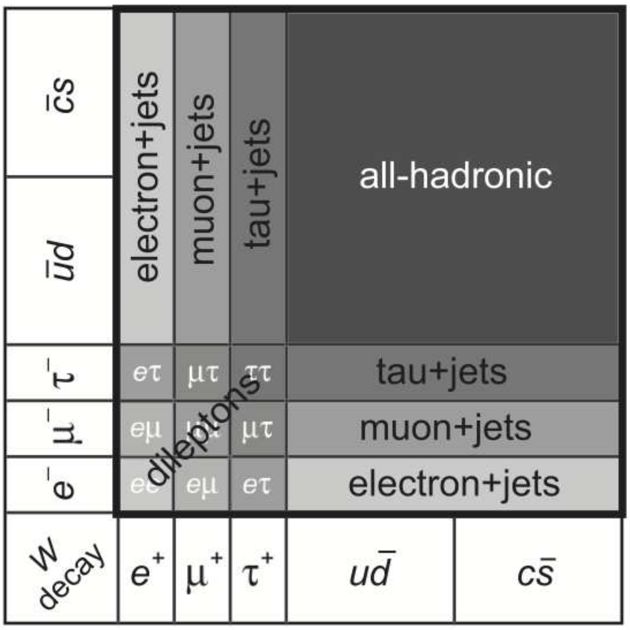

__Figure 1.7:__ Overview of the different decay channels of a $t\bar{t}$ event. Plot taken from [59].

1.3.3 Backgrounds to single-lepton $t\bar{t}$ events

As discussed in the previous section, the single-lepton topology, that is of interest for this thesis, consists of a rather complex signature that involves a charged lepton, a neutrino and at least[10] four jets from which two are b-jets. Additionally, the charged lepton is expected

[10] If we consider the radiating effects, such as ISR/FSR, the final number of jet in the final state may be significantly higher than four.

to have a high-p_{T}, as it is the decay product of a massive object (W boson), but also be quite *isolated*, namely without much activity around its trajectory. Despite the distinctive characteristics of the single-lepton $t\bar{t}$ events, other processes may still resemble the final state of our *signal*[11]. These processes are typically the *background* and for the analysis we perform in this thesis the following are relevant:

- QCD multi-jet events[12].
- Events with a vector-boson (W or Z bosons) produced with associated jets.
- Single-top events.
- Diboson events.

We discuss each of these backgrounds in the next paragraphs.

QCD multi-jets

The LHC environment is swamped by the large background of QCD events having a total cross-section at the order of $\mathcal{O}(1mb)$. Most of these events are the result of $2 \to 2$ processes, such as $q\bar{q} \to gg$, $gg \to gg$, $qg \to qg$, where, due to hadronization, quarks and gluons result in energetic jets. Higher order processes ($2 \to 3, 4, 5$) are also very probable, resulting in higher jet multiplicities. In these cases, extra jets are produced from initial and final state radiation through parton branching; examples of such processes are shown in figure 1.8.

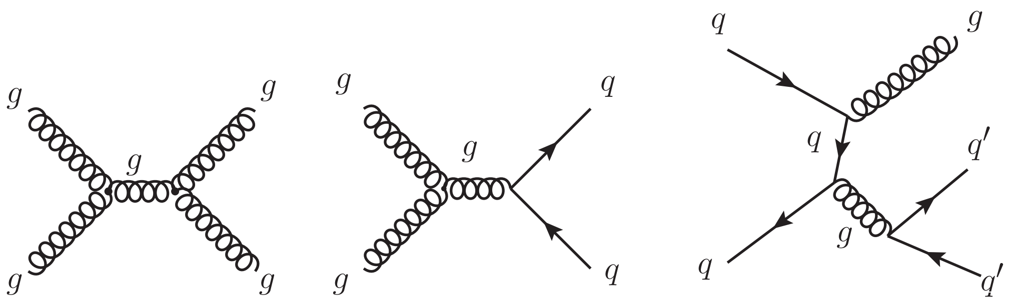

(a) QCD $2 \to 2$ (b) QCD $2 \to 3$

Figure 1.8: *Example Feynman diagrams for different QCD processes.*

For the QCD multi-jet events to be considered as background to the single-lepton $t\bar{t}$ channels, a lepton must be present while also the energy balance of the event must show significant missing energy due to the neutrino requirement. Experimentally, QCD events are considered as background only if the lepton, originating from decays inside the jets (non-prompt), passes the identification criteria that an analysis has set. Additionally, for the electron final state, a jet may be misidentified as an electron ('fake') increasing the probability for the event to be seen as signal. The overall probability for a QCD event to satisfy the necessary requirements is very small. However, this is balanced by the extremely large cross-section of the QCD multi-jet processes and therefore a significant fraction of events will still be mistaken as signal. Requiring the presence of b-jets further reduces the contribution of this background, however a considerable amount of QCD events still comes with associated heavy-quark production.

Theoretically, predicting the cross-section of QCD multi-jet processes is difficult. Although for typical di-jet $2 \to 2$ processes this is fairly simple, when considering leading-order $2 \to N$ processes (where $N > 2$) every extra outgoing parton must take into account an additional

[11] We will be using the term 'signal' to refer to the $t\bar{t}$ events of interest for this analysis.

[12] Hereafter called simply as QCD events.

factor of α_s. As the scale of the interaction is typically set to the scale of the produced particle or jet, for radiating partons this scale is at the limit of the perturbative region and therefore, unlike the $t\bar{t}$ production, the α_s is not small. Due to the strong scale dependence, the added uncertainty with every α_s factor is quite large and each outgoing parton further increases the uncertainty in the inclusive production cross-section. Including higher-order corrections can reduce this uncertainty, however, this is practically unfeasible. At leading order the $2 \to 2$ processes are described by no less than ten Feynman diagrams and when considering higher order corrections this number increases dramatically. In addition to the above, the low-energy showers and hadronization processes, that occur at certain stages of the above events, also introduce a significant uncertainty as they cannot be calculated exactly. Generally, the theoretical prediction on the normalization of QCD multi-jet events cannot be trusted a priori at the LHC and therefore it poses a great challenge for the related analyses.

Vector-boson production with associated jets

In high-energy hadron collisions, W and Z bosons can be produced directly from the hard-process via quark-antiquark annihilations. At the LHC, because the reaction involves only protons (uud), the process requires at least one sea-antiquark to emerge from the one colliding particle and interact with a quark from the other. For W boson production, a change of the third component of the weak isospin (T_3) happens with an up-type quark interacting with a down-type quark and the emitted boson has $T_3 = +1$ (for W^+) or $T_3 = -1$ (for W^-). Instead, the Z boson production does not involve a change of T_3, therefore both quarks have to be up-type or down-type and the resulting boson's T_3 is zero.

The W bosons decay to either a charged lepton and its neutrino (leptonic decay) or to a pair of an up-type and a down-type quark (hadronic decay). In approximately one-third of the times, the produced W boson will undergo a leptonic decay and often associated jets due to initial or final state radiation ($2 \to N$ processes) may emerge (W+jets). When the number of jets is sufficiently large, namely at least four jets are identified, these events constitute an important background for $t\bar{t}$ single-lepton decays. Naturally, if the performed analyses requires b-jets to be identified, the contribution is reduced significantly. However, W+jets events with associated heavy quark production ($b\bar{b}$, c or $c\bar{c}$) are also possible. Example Feynman diagrams of W+jets are shown in figure 1.9, the $W + 1$ parton is a clear example of a $2 \to 2$ process where in one case (left) one of the two quarks radiates a gluon before interacting with the other quark, while in the second case (right) a gluon is emitted from one of the protons and then splits into a quark-antiquark pair, and one of which interacts with the second incoming quark.

On the other hand, the Z bosons decay into a fermion and its anti-particle. Therefore, the final state may result into jets (hadronic) when decaying into quarks, into a pair of neutrinos (invisible) or into two charged leptons (leptonic). Similarly to W boson events, the Z boson events may also contain jets due to initial or final state radiation, including processes where heavy quarks are produced. However, due to the existence of the second charged lepton, their contribution as background to the single-lepton $t\bar{t}$ is not expected to be of significant amount as they can be vetoed easily with a multiplicity requirement.

For the same reasons as in the case of QCD multi-jet events, the prediction of the W+jets and Z+jets cross-sections becomes more difficult when extra outgoing partons are added. In fact, the precise next-to-leading order estimate of the W+4 jets and Z+4 jets productions at the LHC has only recently became available [60, 61]. At leading order the cross-sections of these processes have been estimated up to the order of six associated jets, naturally involving large uncertainties as in the case of the multi-jet events.

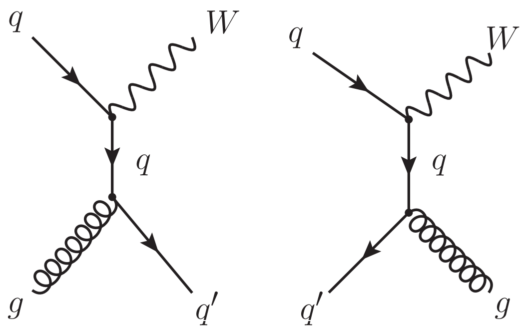

(a) W+1 parton

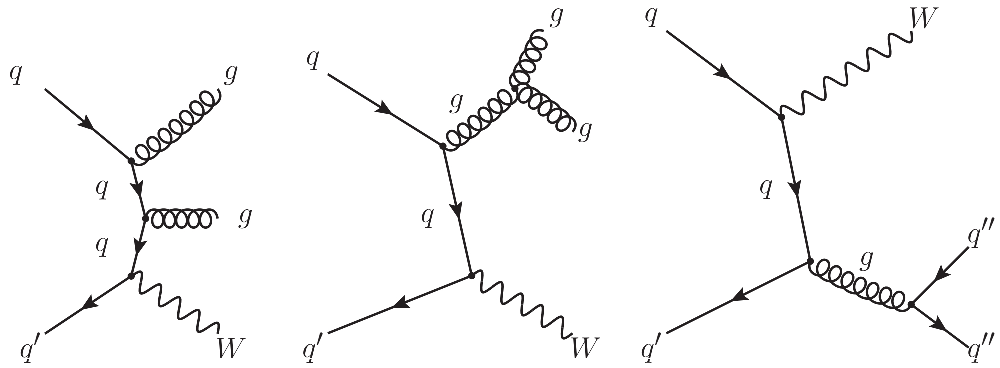

(b) W+2 partons

Figure 1.9: *Feynman diagrams for the W+1 parton with $qg \to Wq$ (a-left) and $q\bar{q} \to Wg$ (a-right), and W+2 parton processes.*

Single-top production

The production of single-top events was briefly introduced in section 1.3.1. The highest cross-section at the LHC comes from the t-channel with $\sigma_t = 64.2 \pm 2.6$ pb [62], while the Wt-channel gives a considerable contribution with $\sigma_{Wt} = 15.6 \pm 1.3$ pb[63]. The s-channel, on the other hand, has the smallest cross-section of all, $\sigma_s = 4.6 \pm 0.2$ pb [64]. In all of the cases, the cross-section is estimated theoretically at the approximate next-to-next-to-leading order.

The final state of all channels, when produced in association with jets, may easily resemble the signature of the signal events in many ways e.g. if the top quark results to a leptonic final state, or if the associated W decays leptonically and the top quark hadronically etc. However, the overall cross-section for this process is lower than the one of the $t\bar{t}$ signal and it only becomes a sizable background when requiring b-jet identification, which are present in this topology. Figure 1.10 shows example Feynman diagrams for each single-top production channel.

Diboson production

The vector-boson production in association with jets, that was presented earlier, referred to a single boson being produced. However, associated production of two bosons is also possible, namely with WW, WZ and ZZ. An example Feynman diagram is shown in figure 1.11. The production cross-section for these processes are in general quite low, when compared to the cross-section of signal events. In particular at next-to-leading order, the inclusive cross-sections are for the WW production, $\sigma_{WW} = 44.9$ pb, for the WZ production, $\sigma_{WZ} = 18.0$ pb and for the ZZ production channel only $\sigma_{ZZ} = 9.2$ pb [65].

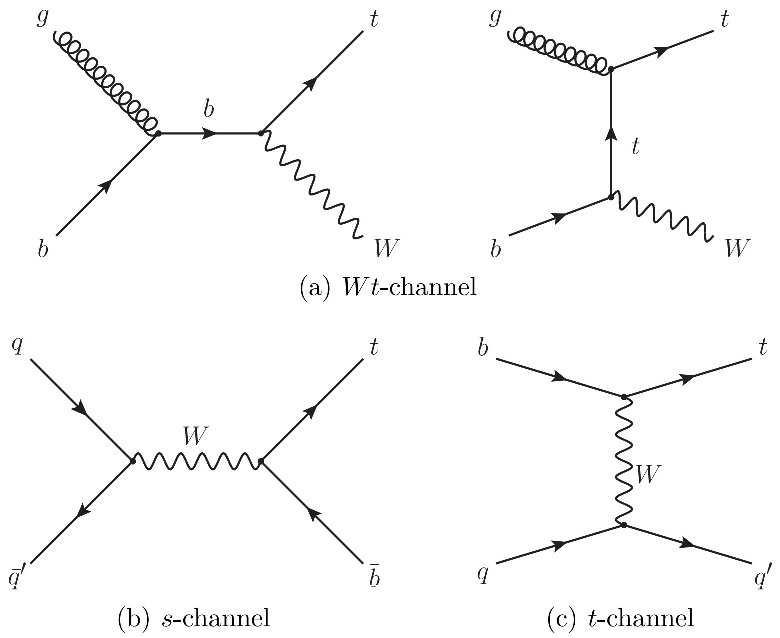

Figure 1.10: *The leading order single-top diagrams for the three different production channels.*

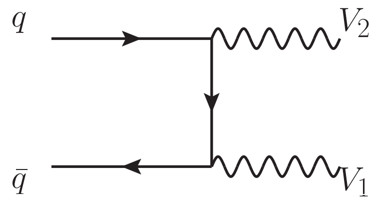

Figure 1.11: *An example of di-boson production where V stands for either W or Z bosons.*

1.3.4 Importance of top quark-pair cross-section measurement

Understanding the physics related with the top quark is of significant importance for the Standard Model. This argument is easily justified by simply considering equation 1.1.40 where, taking the experimentally measured values of the top quark mass and the vacuum expectation value for the Higgs field, the resulting coupling between the top quark and Higgs is close to unity. This indicates that the top quark may play an important role in the mechanism of electroweak symmetry breaking.

The first step in performing precise measurements of the properties of the top quark is to understand its production mechanism. As the LHC enters a previously unexplored energy region for particle physics, our current knowledge of QCD will be put to test. Therefore, it is necessary to establish that the theoretical and experimental agreement of the $t\bar{t}$ production cross-section estimate, initially shown at the Tevatron, also holds in this environment. Possible deviations from expectation may indicate the presence of physics that has not yet been observed. A particular example is the possibility of resonances in the $t\bar{t}$ system which are not expected by the Standard Model. Considering the nominal running parameters of the LHC, the expected rate of $t\bar{t}$ events is so greatly improved (approximately one $t\bar{t}$ pair per second) that the cross-section measurement not only is feasible but it can also be made with a great accuracy, thus being more sensitive to such new physics effects.

Except from establishing the validity of the production mechanisms of $t\bar{t}$ events at the LHC, an accurate cross-section determination lays the road to the measurement of many of the top quark's properties. The most striking example, which is also directly related with the search for the Higgs boson, is the measurement of the top quark mass which is directly related with the $t\bar{t}$ cross-section (see equation 1.3.4). Figure 1.12 shows this dependence, estimated at both next-to-leading and approximate next-to-next-to-leading orders for LHC at $\sqrt{s} = 14$ TeV.

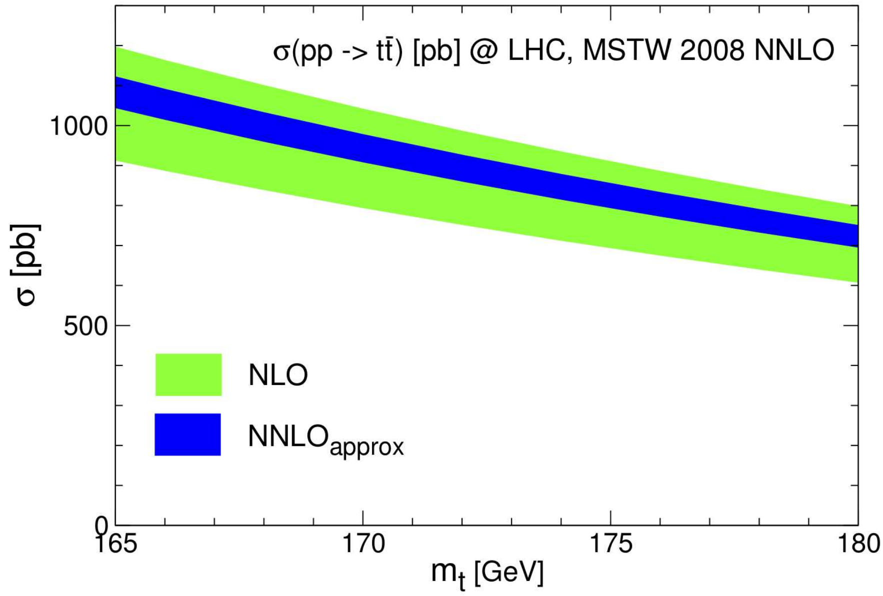

Figure 1.12: *Dependence of the top quarks cross-section from its mass at next-to-leading and the approximate next-to-next-to-leading order, estimated for proton-proton collisions at the LHC ($\sqrt{s} = 7$ TeV). The `MSTW2008NLO` is used as a PDF. Figure taken from [66].*

A precise determination of the top quark mass can provide, together with the measurement of the W mass, constraints on the mass of the Standard Model Higgs. This evident when considering radiative (one-loop) corrections in the Standard Model Lagrangian [67], in which case the mass term for the W boson (initially shown in equation 1.1.36) can be re-written in the following form:

$$M_W^2 = \frac{\alpha\pi}{\sqrt{2}G_F} \cdot \frac{1 + \Delta r/2}{\sin^2\theta_W} \ , \tag{1.3.10}$$

where G_F is the Fermi constant, α is the QED coupling constant, θ_W is the Weinberg angle, which can be written as $\sin^2\theta_W = 1 - M_W^2/M_Z^2$, and Δr corresponds to the radiative corrections applied. Using the measurements of the Z mass [68], the QED coupling constant [69] and the Fermi constant [70], the W mass is left to depend only on the radiative corrections. When considering the top quark loops, we have:

$$\Delta r_{top} \approx \frac{3G_F M_{top}^2}{8\sqrt{2}\pi^2 \tan^2\theta_W} \ , \tag{1.3.11}$$

which suggests a strong dependence between the mass of the W boson and the top quark. For the case of the Standard Model Higgs corrections, we have the following form:

$$\Delta r_{Higgs} \approx \frac{3G_F M_W^2}{8\sqrt{2}\pi^2} \left(\ln \frac{M_{Higgs}^2}{M_Z^2} - \frac{5}{6} \right) \ . \tag{1.3.12}$$

Clearly, from the relation between the masses of the top quark and the W boson, the mass of the Standard Model Higgs can be constrained. It should be noted however, that since the dependence between the W mass and the Higgs mass evolves logarithmically, only a loose constraint can be placed. Figure 1.13 shows the relationship between the three masses as estimated using direct (LEP2, Tevatron) and indirect (LEP1, SLD) measurements of the W and top quark masses.

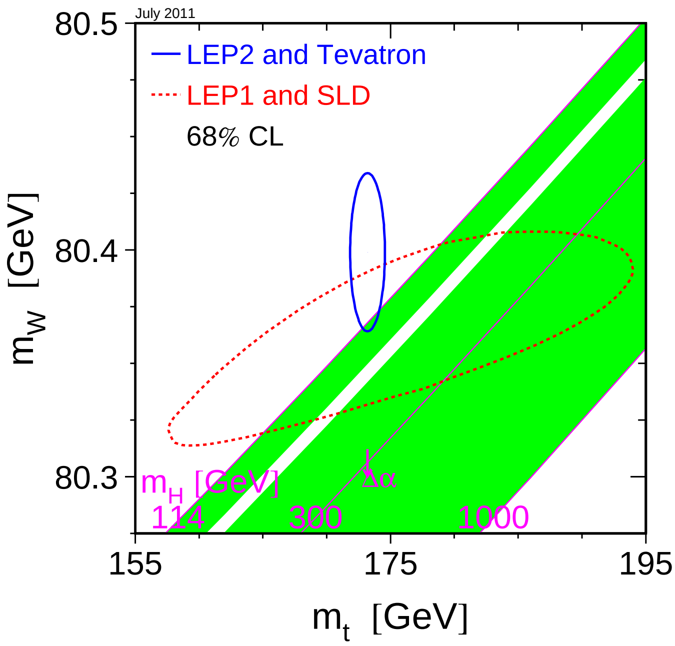

Figure 1.13: *Dependance between the W boson and the top quark mass and their relation with the Higgs mass. Contours shown at 68% confidence level. Figure taken from [71], version of summer 2011.*

Lastly, the $t\bar{t}$ events, and in particular the single-lepton final states, have a distinctive complex signature which involves the presence of a charged lepton, its neutrino and a high multiplicity of jets, including jets induced by b-quark. Effectively, for the detection of such events almost all detector parts, as will be shown in chapters 2, 3 and 4, are used. Therefore, a largely pure $t\bar{t}$ sample can effectively be used to commission and calibrate the experimental apparatus even from the beginning of the data-taking. The determination of cross-section naturally provides a road towards such sample.

1.4 Event generation and Monte Carlo samples

An important part of a physics analysis is the simulation of the processes that are expected to be observed. The software we use for this task, wrap the theoretical and experimental knowledge of the physics of interest and provide events randomly but within the allowed kinematic phase-space (*event generation*). Subsequently, generated events are interfaced with the simulation of the detector in order to provide a representation of a real physics signal. These are the Monte Carlo simulations and they allows us to perform feasibility studies, systematic studies and to a certain extend compare the theoretical expectations with the real data.

1.4.1 Generators

The various sub-processes which take place during a proton-proton collision have been briefly described in section 1.3.1. Certain generators are able to simulate the complete process from the initial interaction up to the hadronization and decay level. Other generators are more specialized in a certain process. Often a combination of different packages is used in order to improve the accuracy of the simulation. The general purpose generators that are used in this thesis are: `Pythia` [72], `Herwig` [73] and `Sherpa` [74]. The main specialized generators that are used are: `MCatNLO` [75, 76, 77, 78], `AcerMC` [79], `AlpGen` [80], `POWHEG` [81] and `Jimmy` [82].

Hard-process

The hard-process takes place at the high-Q^2 regime of the simulation, where perturbation theory can be applied. Taking into account all the contributing Feynman diagrams of a process, and at a certain order α_s, the simulation estimates the matrix element at each phase-space point. Subsequently, it integrates over the complete phase-space, taking into account possible cuts that might be applied, in order to determine the cross-section. Naturally, with including higher-order corrections, virtual and real, the simulation of the hard-process becomes more challenging. All but the `Jimmy` generator can perform matrix element calculations, while the rest are described in the following:

- *`Pythia`* and *`Herwig`*: Both of these general purpose generators contain a large number of built-in processes which are generated at the lowest QCD order, therefore they are at fixed leading-order. However, they provide reduced accuracy in multi-parton final states as they handle QCD and QED radiations only at the parton shower evolution (see next paragraphs). Therefore, they are not the primary choice for the generation of events. In the analysis presented here `Herwig` is used only for the generation of di-boson events.
- *`AlpGen`*: The `AlpGen` generator is a leading-order matrix element generator specialized for multi-parton final states ($2 \to N$). In contrast to `Pythia` and `Herwig`, it provides a more accurate description by using perturbation theory on all the relevant tree-level Feynman diagrams with a fixed number of outgoing partons. The result is bare partons and therefore an additional simulation package must be interfaced to handle subsequent processes. This generator is used to simulate the background W+jets, Z+jets and QCD multi-jet processes up to five outgoing partons.
- *`Sherpa`*: Similarly to `AlpGen` it provides a more accurate description of multi-parton final states based on matrix element calculation. However, it can also handle internally the rest of the processes without needing to couple with an external package. In this thesis, W+jets events generated with this generator are used for systematic studies.
- *`AcerMC`*: Also a leading-order generator, the `AcerMC` provides a library of matrix-element calculation of a number of built-in processes. Primarily aimed for background processes with a large number of partons in the final state, such as W+jets and Z+jets, it can also be used for the simulation of $t\bar{t}$ events. Simulated $t\bar{t}$ events using `AcerMC` are used for the systematic studies of ISR/FSR effects.
- *`MCatNLO` and `POWHEG`*: The only generators in this thesis that provide both real and virtual corrections in the generation process at next-to-leading order. Primarily used for the production of top quark events. The `MCatNLO` is used to generate the signal events for the $t\bar{t}$ cross-section analysis, while `POWHEG` is used for systematic studies. The `MCatNLO` is also used for generation of the single-top events.

Parton shower

The parton shower is the process which describes the splitting of the partons, namely ISR and FSR effects. These interaction evolve at lower Q^2 and until the hadronization effects take over. For the leading-order matrix element generators including these processes implies practically a correction to higher-order calculation. However, since these calculations involve also collinear ($\theta_{qg} \downarrow 0$) and low-energy ($E_g \downarrow$) effects they cannot be handled by the matrix element as they lead to infinities. Most leading-order generators use leading-order DGLAP splitting functions [83, 84, 85, 86] with Sudakov form factors [87] to include these regimes.

Underlying event

Description of the underlying event in simulations is distinct from the ISR/FSR effects as it mainly involves the proton remnants. These processes are semi-hard with low-transverse momentum and evolve mainly in the forward directions. However, they affect also the hard-process due to color connection. It is not unlikely that jets from the underlying event are present in more central region and in the vicinity of the hard-process products. Generators describe this process as a $2 \rightarrow 2$ QCD interaction. The underlying event can be described by both `Pythia` and `Herwig` packages although the latter is usually interfaced with `Jimmy` which is dedicated for this task.

Hadronization

At the hadronization scale perturbative calculations cannot be followed anymore. Instead generators model the related physics to produce results and then tune these models with respect to the observed data. In this thesis, the generator mainly implement the two following models: the *cluster fragmentation* and the *string fragmentation*. The cluster fragmentation splits all gluon into $q\bar{q}$ pairs and forms neutral color clusters from the available quarks. The cluster subsequently decay into lighter clusters of hadrons. On the other hand, the string fragmentation 'sees' field lines between color charges. With increasing distance between quark-antiquark pairs the potential energy of the field increases and causes new quarks to emerge. Hadrons are formed from the available quarks. In this view, gluons are seen as kinks which in the end affect the angular distribution of the hadrons.

For the MC samples in our analysis, almost all use the `Herwig` package for the hadronization. Alternatively, `Pythia` is used together with the `AcerMC` generator and the `POWHEG` generator for parton shower systematic studies on the signal sample.

Decay

The decay process takes over after the hadronization step. Generators simply use experimental data, namely branching ratios, to determine the final state of the events. All particles with a decay length below 10mm are allowed to decay, while the rest are treated in the detector simulation.

Matrix element to parton shower matching

Combining the matrix element result with the parton showers simulation has the consequence of double counting. This is because the same Feynman diagram can describe both a higher order matrix element calculation for an e.g. $2 \rightarrow 3$ event, and an matrix element calculation of the same process $2 \rightarrow 2$ but where the parton shower splits an outgoing gluon to emit a soft or collinear parton. Even though the two processes occur at different energy scales they may still give overlap kinematically. The goal then becomes clear that a specific separation point must be given which will define up to which level the processes are handled by the matrix element while leaving the rest for the parton shower scheme.

The AlpGen generator, which is used for most background processes, implements such a matching method named MLM [88, 89]. With this procedure, the jets produced from the parton shower are matched to the matrix element partons. Naturally, an algorithm which reconstructs the hadronized partons is required. The matching is simply done based on the distance between the jet and the parton in the pseudo-rapidity (η) versus azimuthal angle (ϕ) space. If every hard parton is matched to a jet the event is kept, otherwise it is rejected.

1.4.2 Monte Carlo samples

A large number of Monte Carlo samples were used for the analysis presented hereafter. This section provides some details on certain technical aspects that are of interest.

Top-quark samples

Both the top quark pair sample (signal) and the single-top use the MCatNLO generator (v3.41) with the CTEQ6.6 PDFs [56]. The top quark mass, for all cases, is taken to be 172.5 GeV which is accordance with the current world average. The $t\bar{t}$ sample is inclusive for the leptonic states, namely containing both single-lepton and di-lepton events in all flavors. A distinct, but with the same generation parameters, sample is used for the fully-hadronic $t\bar{t}$ events. On the other hand, the single-top processes are produced exclusively for each of the three channels. For the Wt-channel an overlap removal scheme is applied [90] to avoid double counting with $t\bar{t}$ final states. These diagrams happen on higher order correction of the Wt-channel and can effectively be interpreted as $t\bar{t}$ at leading-order with a decay of the anti-quark into a Wb pair. In all cases, the Herwig and Jimmy combination is used for the parton shower, hadronization and underlying event processes.

Also, as mentioned earlier, the POWHEG samples are used for the systematic checks. These are produced with both Herwig and Pythia for the hadronization process in order to accommodate relevant systematic studies. Lastly, the AcerMC leading-order samples, interfaced with Pythia for hadronization, are used in order to estimate the ISR/FSR systematic uncertainty.

W+jets and Z+jets samples

As mentioned in the previous section, the vector-boson samples are generated using the AlpGen (v2.13) package with the CTEQ6L1 PDF [91], while their hadronization and underlying event physics is handled by Herwig and Jimmy. For the MLM matching the minimum p_{T} that is used to define the parton shower jet is 20 GeV, every jet below that value is not considered for the matching. Also, the matching distance is set to be 0.7. For the W+jets samples, four individual processes are used: the W+light jets, the $Wb\bar{b}$+jets, the $Wc\bar{c}$+jets and the $Wc(\bar{c})$+jets. The W+light jets sample has a significant overlap with the other three samples and therefore, an appropriate removal of the duplicate events is performed. The Z+jets events are not considered in their full phase-space but are restricted to the region where $M_{\ell^+\ell^-} > 40$ GeV.

QCD multi-jet samples

The QCD multi-jet samples use the same configuration as the W+jets samples. However, in order to facilitate their production and usage for the $t\bar{t}$ analysis certain requirements are placed. The following apply for these samples:

- **QCD Slicing:** The samples are separated into transverse momentum slices and each event is categorized according to the highest jet p_{T}(leading-jet). The jets are considered at the truth level, namely after applying a reconstruction algorithm on the stable particles after hadronization of the event. With this classification, the lowest leading-jet threshold available in the simulation is $p_T^{leading} \geq 17$ GeV, thus any event with leading-jet p_{T} lower than that value is not saved.
- **QCD Filtering:** For the lower p_{T} slices, which contain all events with leading-jet p_{T} of less than 140 GeV, the true cross-section is very large and it is practically difficult to generate enough events that correspond to a reasonable integrated luminosity. Therefore, filters are applied that register only events which are likely to pass the requirement of the nominal $t\bar{t}$ analysis. For analyses that look at the leptonic decay channels, and specifically the ones where a muon or an electron exists in the final state, two filters are used for QCD events with increased probability of passing the default cuts. The muon filter which requires all events to contain a true muon with $p_{\mathrm{T}} \geq 10$ GeV and $|\eta| \leq 2.8$, and the jet filter where all events must have at least three jets with $p_{\mathrm{T}} \geq 25$ GeV and at least one more jet with $p_{\mathrm{T}} \geq 17$ GeV , with all jets within $|\eta| \leq 5.0$. The muon filtered samples are, typically, used for the analysis with $t\bar{t}$ events with a muon in the final state, while the jet-filtered sample is used when an electron exists in the $t\bar{t}$ final state.

1.5 Summary

We introduced in this chapter the theoretical context upon which we base our cross-section measurement. The implementation of the Standard Model has been very successful in the past decades providing physicists with an important predictive tool. The most striking example is the prediction and subsequent discovery of the vector bosons, W and Z, as a result of the unification of the electromagnetic and the weak force and the imposition of the Higgs mechanism as the means for them to gain mass. In addition, the categorization of the elementary particles into generations, although not fully understood, led to the discovery of the top quark, a milestone for modern physics.

The top quark was also presented. Measuring the cross-section of the top quark pair production is an important first goal for the experiments at the LHC. The measurement provides an excellent first test for QCD and for the first time at the energy regimes that the LHC explores; deviations may surely give a hint for the existence of new physics. In addition, the cross-section measurement opens up the door for precision measurements of the different top quark's properties. In the following chapters, we present one of the first $t\bar{t}$ cross-section measurements performed with the ATLAS detector using the very first collision data delivered by the LHC.

Chapter 2

The experimental setup

"Give me a lever long enough and a place to stand on, and I will move the Earth."

Archimedes of Syracuse
c. 287 BC - c. 212 BC

The essence of the Scientific Method is to perform experimental measurements that will verify or refute the theoretical predictions. Consequently, constructing and understanding the necessary tools that will make the measurements possible is an important step in research. This chapter describes the accelerator, the Large Hadron Collider (LHC) [92], which provides the proton-proton collisions, and the ATLAS[1] detector [93] which identifies the products of the collisions.

Section 2.1 gives a description of the accelerator system and its basic parameters. Section 2.2 discusses the layout of ATLAS with its different sub-detector systems, addresses the particle identification principles and provides an overview of the performance with real data. In the last section, insight is given in the triggering and data-acquisition system of the detector that allows for recording of events.

2.1 The Large Hadron Collider

The LHC is a circular accelerator with a circumference of 27 km. It is located in an underground tunnel, 100 m beneath the surface, near the border region between France and Switzerland and close to the city of Geneva. It is operating since Autumn 2009. The machine accelerates either protons or lead ions ($_{82}$Pb) with two beams traveling in opposite directions. Four crossing points exist, the interaction points, where the two beams meet and collide with each other. Each interaction point houses one of the four major particle detectors ALICE [94], ATLAS, CMS [95] and LHCb [96]. Only proton-proton collisions are of interest for this thesis.

2.1.1 Injection chain

The LHC is at the end of an injection chain, a series of accelerators and other devices that contribute in bringing the necessary proton beams into collision. The injection chain is shown in figure 2.1.

[1]The ATLAS acronym stands for: A Toroidal LHC ApparatuS.

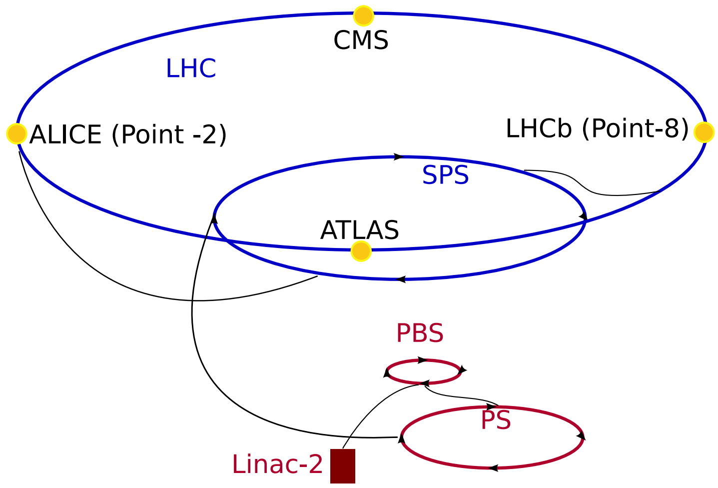

Figure 2.1: *The LHC's injection chain. The two beam insertion points, Point-2 and Point-8 are located near the ALICE and LHCb detectors.*

The first step of the process requires the protons to be produced. This is achieved by introducing hydrogen gas into a Duoplasmatron device [97]. In this device, the gas is held in a vacuum chamber and is bombarded with electrons. The result is to ionize the gas leaving it in a state of plasma. This plasma is accelerated inside the device to a maximum of 100 keV forming a beam that is then sent to the Radio-Frequency Quadrupole (RFQ). The RFQ's main purpose is to focus the beam and further speed it up to a maximum of 750 keV before it enters into a linear accelerator, the Linac-2. In the Linac-2 the beam is accelerated to an energy of 50 MeV.

The proton beam is introduced into the Proton Synchrotron Booster (PSB) through a transfer line that consists of quadrupole magnets that focus the beam and several other multipole magnets that guide it. The PSB is the first circular accelerator in the injection chain with a circumference of 157 m and it consists of four superimposed synchrotron rings. The protons enter the accelerator's rings and in each ring a bunch of $1.8 \cdot 10^{12}$ protons is formed. They are subsequently accelerated to an energy of 1.4 GeV.

The next machine in line is the Proton Synchrotron (PS) circular accelerator with a circumference of 628 m. After every PSB cycle four proton bunches enter the PS. A total of two PSB cycles are required in order to fill the PS. Once the PS is filled, the beam is accelerated to 26 GeV. Subsequently, the protons are de-bunched and then recaptured with the help of 40 MHz radio-frequency cavities. In the end, a total of 81 bunches with a spacing of 25 ns between them and with 1.15×10^{11} protons each are inserted into the next machine[2].

The last step before the beam enters the LHC requires the protons to reach an energy of 450 GeV, which is the nominal LHC injection energy. This is achieved in the Super Proton Synchrotron (SPS) circular accelerator which has a circumference of approximately 7 km. The SPS requires three PS cycles to be completely filled. The insertion in the LHC takes place into two separate points: in the arc between Point-1 and Point-2 (where the ALICE detector is located), and Point-1 and Point-8 (where the LHCb detector is located). Bunches entering in Point-2 follow a clock-wise trajectory while bunches entering in Point-8 travel in the opposite direction. A nominal number of 2808 bunches are inserted for each beam, thus requiring a total of 12 SPS cycles.

[2]These numbers refer to the nominal values which were gradually achieved with the machine from the beginning of its operation in Autumn 2009 and throughout 2010.

For the results in this thesis the configuration of the bunches did not reach the nominal values. Instead, as the machine was gradually commissioned, the proton bunches evolved from an initial of 2 bunches per beam up to a total of 295 bunches at the end of 2010. Also, the proton density of the bunches did not reach immediately the nominal value but was gradually increased.

2.1.2 Characteristics of the LHC

The LHC is designed such that it can accelerate the proton beams to a nominal energy of 7 TeV per beam, hence providing collisions at a center-of-mass energy of 14 TeV. This is significantly larger than the previous hadron collider experiment, the Tevatron, which produced proton-antiproton collisions at an energy of 1.96 TeV of energy in the center-of-mass frame. In addition, LHC is designed to achieve an instantaneous luminosity ($\mathcal{L}$) of the order of 10^{34} $\mathrm{cm}^{-2}\mathrm{s}^{-1}$, thus allowing the experiments to record a large statistics sample. In fact, assuming collisions take place at $\sqrt{s} = 14$ TeV, the inelastic proton-proton scattering has a cross-section of 60 mbarn [98], resulting in an average of 600 million events per second. The disadvantage of the high luminosity is that, since collisions are delivered in bunches of many protons, remnants from many inelastic scatterings may simultaneously be present during an interesting event. This effect, which is named *pile-up*, poses a great challenge for the detectors.

Once the protons are inside the LHC, they travel inside the beam-pipe which is kept at an ultra-high vacuum in order to avoid interactions with gas molecules. The acceleration process takes place in Radio-Frequency (RF) cavities. A total of eight super-conducting cavities per beam are used which have a nominal operational temperature of 4.5 K and a frequency of 400 MHz, achieving an accelerating field of 5 MV/m. A total of 20 minutes is required for the protons to be brought from an energy of 450 GeV to 7 TeV. An equally important task of the RF cavities is to protect the bunch structure of the beam thus ensuring the maximum possible luminosity. This is achieved by keeping the operating frequency of the RF cavities as an integer multiple of the revolution frequency of the bunches.

For the protons to remain on their trajectory inside the beam pipe, a magnetic field vertical to their plane of motion must be applied. A total of 1232 super-conducting dipole magnets are employed for this purpose operating at a temperature of 1.9 K and providing a maximum magnetic field of 8.33 Tesla. During the acceleration process the field must be adjusted as the energy of the protons ramps up. An additional 858 quadrupole magnets ensure the focusing of the beam while a number of other types (such as sextuples, octuples etc.) are used for making various corrections.

On September 2008 the first proton beams successfully circulated the LHCs beam pipes at a minimum energy of 450 GeV per beam. However, just nine days after the beginning of operation a technical failure lead to extensive damage of several components of the accelerator, consequently stalling the physics program. The machine became operational again in November 2009. As of March 2010 the LHC is providing proton beams at an energy of 3.5 TeV, hence collisions take place at $\sqrt{s} = 7$ TeV with the prospect to achieve 13 TeV collisions in 2014. Although the 3.5 TeV per beam is only half-way from the design specifications of the machine, it still makes it the world's most powerful accelerator to date. By the end of 2010, the LHC reached a peak instantaneous luminosity of $2.1 \cdot 10^{32}$ $\mathrm{cm}^{-2}\mathrm{s}^{-1}$. A considerable amount of data were delivered to the detectors by that time allowing them to perform the very first physics measurements of proton collisions in the multi-TeV region. Figure 2.2 shows the total integrated luminosity ($\int \mathcal{L}dt$) delivered by the LHC at the ATLAS interaction point during 2010 as well as the amount that was successfully recorded by the detector (45 pb^{-1}).

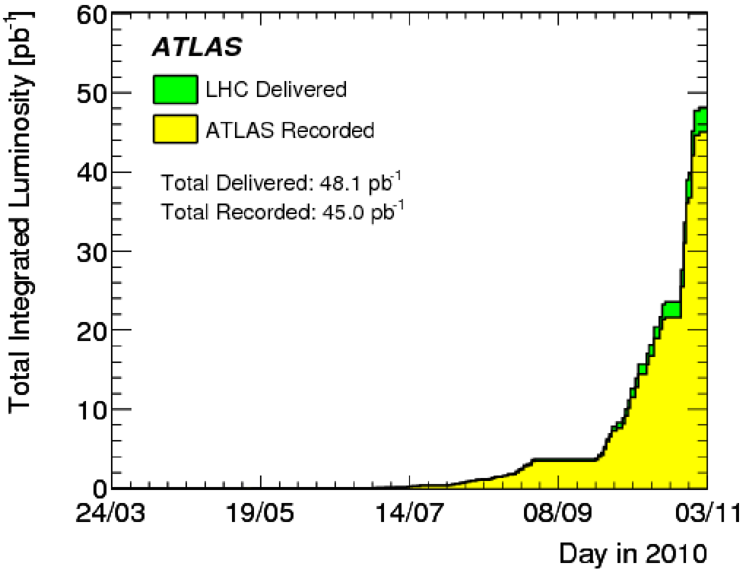

Figure 2.2: The evolution of the total integrated luminosity delivered by the LHC to the ATLAS experiment during the 2010 physics run. Also the total amount that was actually recorded by ATLAS is shown. Plot taken from [99].

2.2 ATLAS - A Toroidal LHC ApparatuS

The ATLAS detector is a cylindrical construction of 7000 tonnes, 42 m in length and 25 m in height, centered on one of the interaction points of the LHC (Point-1). It consists of three main areas, the central area or barrel, of cylindrical shape, and the two outer areas which are perpendicular to the axis of the cylinder and are commonly referred to as the end-caps. It is designed as a general purpose experiment with many different physics goals, such as:

- Discovery of the Higgs boson.
- Search for Supersymmetry (SUSY) and other physics beyond the Standard Model (e.g. extra dimensions, microscopic black-holes etc.).
- Standard model precision measurements including W-boson and top quark properties.
- CP-violation and B-hadron physics.
- Study of QCD at the quark-gluon state with lead-ion collisions (heavy-ion physics).

For the detector to achieve its goals an excellent ability to identify particles in almost all possible directions and in a wide energy spectrum is required. A number of different detection techniques are employed and as a result many different sub-detector systems are used; a representation of the ATLAS detector with all the different sub-detectors and magnets is shown in figure 2.3. The sub-detectors can be categorized in three major layers. Firstly, the Inner Detector (ID) which is located close to the beam-pipe and is mainly dedicated to the reconstruction of the trajectory of charged particles. Secondly, the Calorimeters which are placed around the ID and are assigned the task to determine the energy of most of the traversing particles. They are separated in an electromagnetic part which is designed to identify mainly electrons and photons and a hadronic part which is designed to absorb hadrons. Lastly, the Muon Spectrometer (MS) surrounds the calorimeters and is dedicated to the reconstruction of the trajectories of muons. The sub-detectors are complemented by a hybrid magnet system consisting of a central solenoid magnet, surrounding the ID, and an outer toroid magnet that is placed such that it provides magnetic field for the MS. Table 2.1 shows the general performance goals set for the various ATLAS detector layers in terms of energy or momentum resolution.

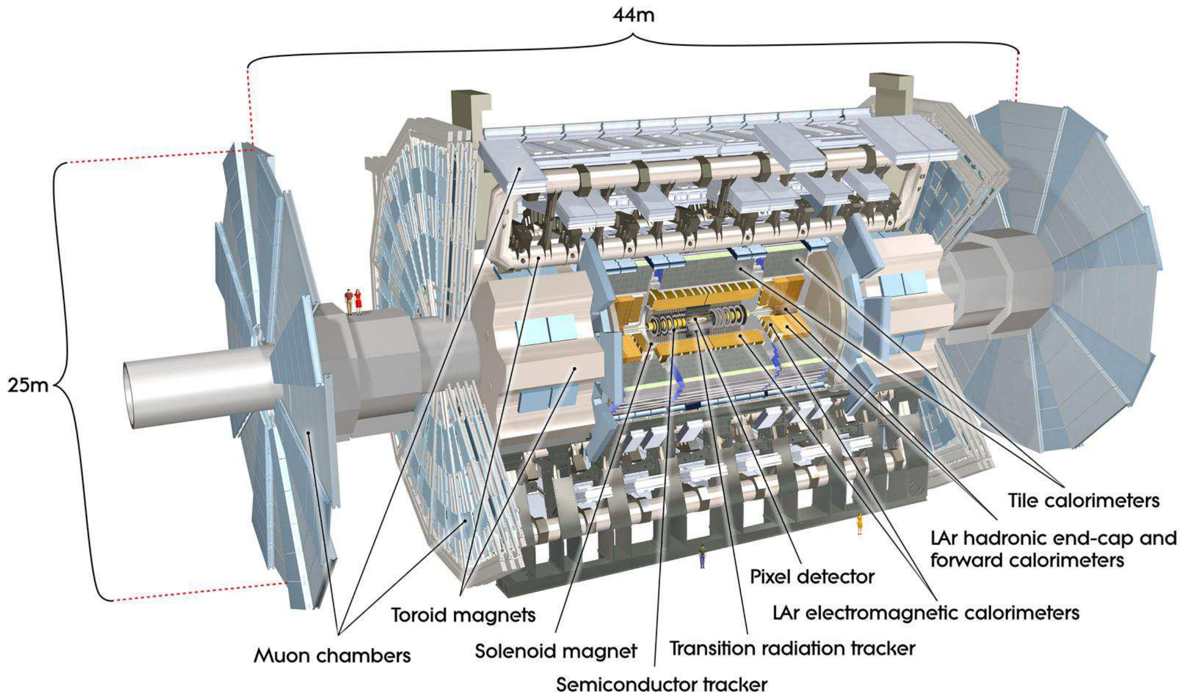

Figure 2.3: *The general layout of the ATLAS detector.*

Detector layer	Required resolution	η coverage Offline Reco.	Trigger
Tracking	$\sigma_{p_T}/p_T = 0.05\% \times p_T \oplus 1\%$	± 2.5	± 2.5
EM calorimeter	$\sigma_E/E = 10\%/\sqrt{E} \oplus 0.7\%$	± 3.2	± 2.5
Had. calorimeter			
Barrel/End-cap	$\sigma_E/E = 50\%/\sqrt{E} \oplus 3\%$	± 3.2	± 3.2
Forward	$\sigma_E/E = 100\%/\sqrt{E} \oplus 10\%$	$3.1 < \lvert\eta\rvert < 4.9$	$3.1 < \lvert\eta\rvert < 4.9$
Muon Spec.	$\sigma_{p_T}/p_T = 10\%,\ p_T = 1$ TeV	± 2.7	± 2.4

Table 2.1: *The general performance goals for the ATLAS detector separated in the major components. Units of E and p_T are in GeV. Table taken from [93].*

An essential part of ATLAS is its trigger and data-acquisition system (T/DAQ). The T/DAQ is responsible for retrieving the information (e.g. electric signals) from the detector parts, and decide in 'quasi-real' time whether it should be kept for physics analysis or not. The T/DAQ is not a detector itself, but it is still a fundamental part since if it fails the data are lost. It is designed such that it deals with the immense amount of collisions provided by the LHC, an approximate 40 MHz input rate, and ensures the free flowing of data to the analyzers. It consists of three main layers the Level-1, the Level-2 and the Event Filter.

2.2.1 Coordinate system

A right-handed coordinate system is used in ATLAS with its center coinciding with the nominal LHC interaction point. The positive x-axis of the system points towards the center of the LHC while the positive y-axis points upwards towards the surface. The xy-plane is usually referred to as the transverse plane. The z-axis of the system runs parallel to the beam taking positive values in the counter clock-wise direction. The side of the detector on the positive z-axis is called A-side and on the negative z-axis C-side.

Given the cylindrical structure of the detector it is convenient to use polar coordinates instead of the $x-y-z$ set. For this reason, the radial distance $R=\sqrt{x^2+y^2}$, the azimuthal angle $\phi \in [-\pi,\pi]$ and the polar angle $\theta \in [0,\pi]$ are defined. The azimuthal angle runs on the transverse plane, having $\phi = 0$ when on the positive x-axis and taking positive (negative) values when moving (counter) clockwise facing the positive z-axis. The polar angle runs on the xz-plane having $\theta = 0$ when on the positive z-axis. Typically, we replace the polar angle with the pseudo-rapidity (η) which is defined by:

$$\eta = -\ln\left(\tan\frac{\theta}{2}\right).$$

Thus, zero pseudo-rapidity corresponds to the transverse plane while it goes to positive (negative) infinity when closing the beam direction towards the A-side (C-side) of the detector. It is common to refer objects with low $|\eta|$ as 'central' and with high $|\eta|$ as 'forward'.

The choice of pseudo-rapidity stems from its relation with the rapidity of a particle[3]. In fact, for massless particles or particles with energy much larger than their mass the pseudo-rapidity equals the rapidity. For the latter, the particle multiplicity distribution remains constant while it is also invariant under Lorentz transformations along the beam axis.

With the η and ϕ coordinates of the particles given, we can defined a 'distance' measure for two particles on the detector, the ΔR:

$$\Delta R = \sqrt{(\Delta\phi)^2 + (\Delta\eta)^2}\ , \tag{2.2.1}$$

for which small values suggest that particles are located close to each other.

2.2.2 Magnet system

The magnet system is an integral part of the ATLAS detector which is necessary for allowing identification and momentum measurement of the charged particles. A depiction of the coils of the magnet system of ATLAS is shown in figure 2.4. A total of four super-conducting magnets are used, a single solenoid magnet, a toroid magnet in the barrel region and two toroid magnets in the two end-caps of the detector.

The solenoid magnet

The solenoid magnet is a 5.8 m long cylinder with an inner diameter of approximately 2.5 m, surrounding the ID and inside of the calorimeter structure. It is constructed as a single-layer coil magnet made from super-conducting material and is able to provide an axial magnetic field of approximately 2 T. The coil is made from 1154 windings and in order to achieve its operational current of 7.7 kA it must remain at a temperature of approximately 4.5 K. Its aim is to force charged particles to make a circular motion on the bending (ϕ) plane that will help determine their charge, mass and momentum.

One of the main consideration for the construction of the solenoid magnet was to keep the amount of un-instrumented material, between the calorimeters and the interaction point, as

[3]The pseudo-rapidity of a particle can be expressed as $\eta = \frac{1}{2}\log\frac{|\mathbf{p}|+p_z}{|\mathbf{p}|-p_z}$ and depends only on the polar angle of its trajectory while rapidity which is given by $y = \frac{1}{2}\log\frac{E+p_z}{E-p_z}$ depends on its energy.

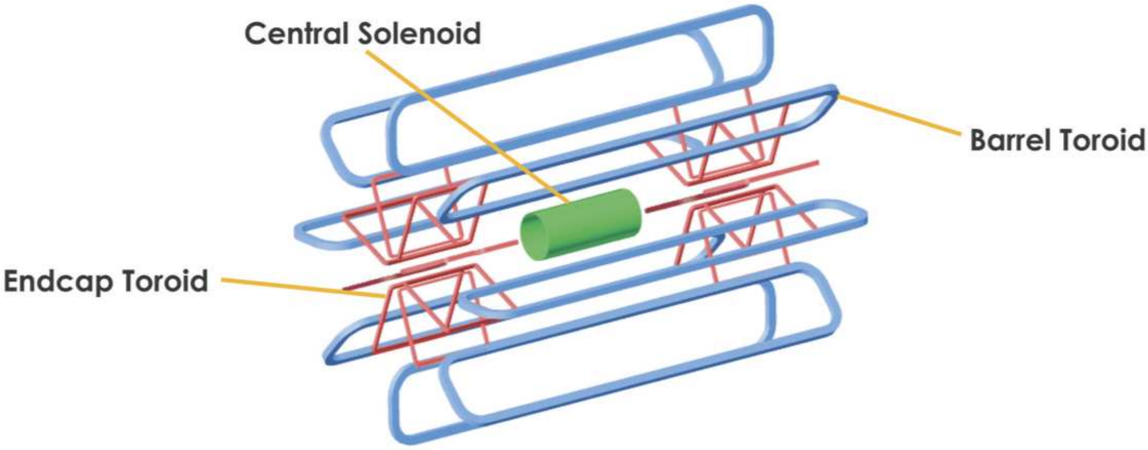

Figure 2.4: *Schematic view of the configuration of the coils for the magnet system of ATLAS.*

low as possible. For this reason the magnet's windings and the electromagnetic calorimeter share a common vacuum vessel while only an aluminum heat shield of 2 mm separates the two structures. A total of 0.66 radiation lengths at normal incidence angles was eventually achieved.

The toroid magnets

The toroid magnet system consists of three individual parts: the barrel toroid, which is situated in the central part of the detector forming a cylindrical volume with an axis that coincides with the beam axis, and the two end-cap toroids, each at one end of the detector. All parts are located behind the calorimeters and are placed such that a magnetic field penetrates all sections of the Muon Spectrometer. The η-plane is bending plane of the toroid.

The barrel toroid is 25.3 m in length and has an inner diameter of 9.4 m and an outer diameter of 20.1 m. It consists of eight super-conducting coils of rectangular shape each sealed in a stainless steel vacuum vessel. Each coil has 120 windings and operates at a nominal temperature of 4.6 K with a nominal current of 20.5 kA. The toroidal magnetic field that is achieved in the center of the toroid magnet reaches 0.5 T.

The end-cap toroids complement the magnetic field of the barrel toroid in the forward regions of the detector. Each end-cap toroid consists of eight super-conducting coils of square shape and are all housed inside a single vacuum vessel. The specifications are very similar to the barrel toroid with 116 windings, 20 kA operational current at 4.6 K temperature. The magnetic field that is achieved at each end-cap reaches 1 T.

2.2.3 Inner Detector

The Inner Detector consists of three separate sub-detector devices: the Pixel detector, the Semi-Conductor Tracker (SCT) and the Transition Radiation Tracker (TRT). It is 6.2 m in length and its cylindrical structure has an approximate diameter of 2.1 m. It resides at a distance of only 45.5 mm from the beam-pipe and and it is submerged in the 2 T axial magnetic field of the solenoid super-conducting magnet that surrounds it.

The ID aims to identify tracks of charged particles in the range of $|\eta| < 2.5$, with momenta of at least 0.1 GeV. It is designed to achieve pattern recognition, high momentum resolution and full reconstruction of primary and secondary vertices. As it sits closest to the interaction

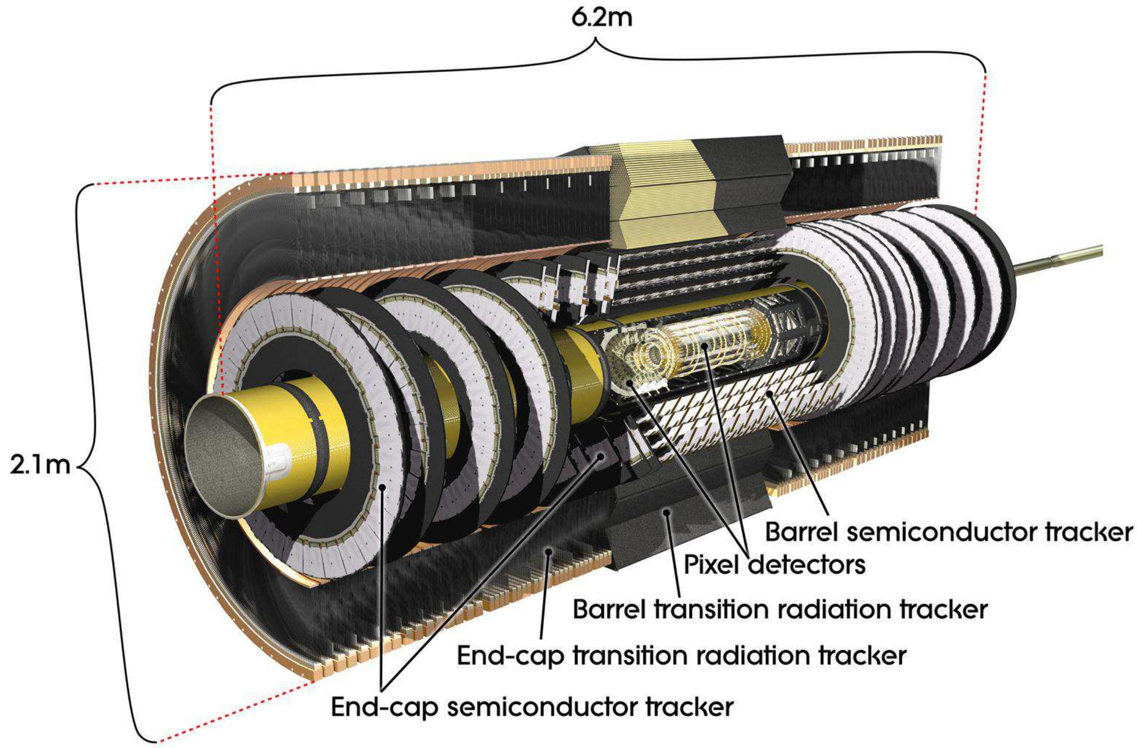

Figure 2.5: *Schematic view of the ATLAS Inner Detector consisting of the Pixel, the Semi-Conductor Tracker and the Transition Radiation Tracker sub-detectors.*

point special care was taken to ensure its ability to cope with the very large track multiplicity and the significant radiation that it is exposed to, even at the highest LHC luminosity. Figure 2.5 shows the different parts of the ID.

Pixel detector

The Pixel detector is the closest to the interaction point of all the sub-detector systems of ATLAS. Its goal is to provide excellent precision measurements of the position of the particle tracks that fall within the region of $|\eta| < 2.5$, hence assisting significantly in the identification of primary and secondary vertices.

The basic element of this detector is the silicon pixel sensor, a 62.4×21.4 mm^2 silicon wafer comprised by 46080 pixels segmented in $R - \phi$ and z and of size $R - \phi \times z = 50 \times 400$ μm^2 each. A total of 1744 wafers make up the full Pixel detector, which translates to approximately 80.4 million read-out channels. A total of 1456 of the wafers are mounted on three concentric cylindrical layers centered around the interaction point in the barrel region of the detector. They are arranged at different distances from the beam pipe, namely 50.5, 88.5 and 122.5 mm, with the innermost often referred to as the B-layer since it provides the most critical information for the secondary vertex identification. The coverage of the barrel layers is up to $|\eta| < 2.5$ for the B-layer and $|\eta| \geq 1.7$ for the other two layers. The remaining 288 wafers are distributed in the six end-cap disks, three on each side) which effectively cover the region $1.7 < |\eta| < 2.5$. Typically, three space points per particle are provided by the Pixel detector.

The detection principle of the pixel sensors is based on the creation of electron-hole pairs on the charge-depleted layer of silicon once a charged particle traverses it. Since a single particle may traverse and ionize silicon in a number of close-by pixels, a cluster is formed and the hit position is determined by the center of this cluster. Consequently, the precision to the measurements is partially determined by the pixel granularity.

Semi-Conductor Tracker

The Semi-Conductor Tracker (SCT) is the second in line of the Inner Detector's sub-systems. The purpose of the SCT is to assist in the track determination of charged particles in the region of $|\eta| < 2.5$, especially for those particles with a high p_{T}.

The SCT is using silicon sensors, just as the Pixel detector. Each sensor of the SCT consists of 768 strips with a pitch of 80 μm. Two sensors are glued back-to-back to form a module for a total of 4088 SCT modules. The strips of the two sensors on each module have a relative stereo angle of 40 mrad, used for a position measurement along the strip length by finding the intersection of the two strips hit by the traversing particle. A total of 2112 modules are distributed in the four co-axial layers in the barrel, located in distances of 299, 371, 443, 514 mm from the beam pipe and covering the $|\eta| \leq 1.4$ region. The remaining modules are placed on nine disks in each end-cap side covering the $1.4 < |\eta| < 2.5$ region. Four space points are typically detected for each particle.

The detection of particles with the SCT is performed in a similar way as with the Pixel detector. The main difference is that instead of a pixel configuration the SCT modules follow a strip segmentation. The granularity is reduced however this does not affect the tracking performance because it resides further away from the interaction point covering a larger area, hence a lower particle density is expected. An important advantage of the strip segmentation, compared to the pixels, is that the number of read-out channels is limited to a total of 6.2 million.

Transition Radiation Tracker

The Transition Radiation Tracker (TRT) is the last sub-detector of the ID ensemble that a particle traverses. It is designed to help the track reconstruction in the region of $|\eta| \leq 2$ by providing a large number of space points in addition to the silicon hits from the Pixel and the SCT. Moreover, it provides the capability to discriminate between electrons and pions through transition radiation emission.

The TRT consists of a large number of thin-walled proportional drift tubes, the straws. Each tube has a 4 mm radius and a length of up to 144 cm in the barrel, or 37 cm in the end-caps. A gold-plated tungsten anode wire of 31 μm diameter is in the middle of each straw while the tube is filled with a gas mixture of Xe, CO_2 and O_2. A total of 52544 straws are deployed in the barrel region, placed parallel to the beam axis and at a distance of 544 mm up to 1082 mm. The pseudo-rapidity coverage is $|\eta| \leq 0.7$. In each of the end-cap regions 122880 straw are used, placed radially around the beam axis, covering the pseudo-rapidity range of $0.7 < |\eta| \leq 2$. The total number of read-out channels is approximately 351000. Unlike the Pixel and SCT detectors, the TRT provides measurement only on the $R - \phi$ coordinate.

The detection is based on the ionization of the gas once a charged particle traverses it. Due to the voltage applied between the wall of the tube and the anode wire, the electrons produced from the ionization drift towards the wire. The drift time of the electrons is used to determine the exact incident point of the particle with the tube. A large number of ionizing hits with the gas are typically expected ranging from 30-36 hits per traversing particle.

For the electron identification the TRT straws are placed inside polypropylene fibers with different refraction indices. Traversing particles emit transition radiation at X-ray wave length due to the crossing between two mediums. The intensity of the radiation is proportional to

$\gamma = E/m$ and given that electrons have a much smaller mass than pions, it is possible to make a distinction. Discriminating between the transition radiation and the ionization processes is rather simple as the former is efficiently absorbed by the Xenon gas resulting in energy deposition of several keV in contrast to an average of 200 eV that relate with the ionization process.

Alignment and performance

The position of the detector modules have to be known with an accuracy comparable to their intrinsic resolution (see table 2.2) for precision position and momentum measurements. This is achieved by the following alignment procedure.

Detector	**Section**	**Intrinsic Resolution (μm)**
Pixel	Barrel	$R-\phi: 10,\ z: 115$
	End-cap	$R-\phi: 10,\ R: 115$
SCT	Barrel	$R-\phi: 17,\ z: 580$
	End-cap	$R-\phi: 17,\ R: 580$
TRT	Barrel	$R-\phi: 170$
	End-cap	$R-\phi: 170$

Table 2.2: *The intrinsic resolution accuracy for each part of the Inner Detector. Number taken from [93].*

The Inner Detector employs a track-based alignment algorithm. The algorithm makes use of track-hit residuals[4] where their squared-sum over a large number of reconstructed tracks must be minimal for the aligned geometry. This is formulated as chi-squared minimization problem and is further explained in [100].

Two alignment campaigns were performed: one prior to the first LHC collisions in autumn 2009 which includes only cosmic-rays (Pre-Collisions), and one after the first LHC commissioning collisions were made in $\sqrt{s} = 900$ GeV (Post-Collisions). The alignment constants obtained from each of the two campaigns were tested on 7 TeV collision data. Figure 2.6 shows as an example the residuals on the local x coordinate, namely the projection of the residual on the module's local x direction, for the three sub-detector systems and compared with perfectly aligned Monte Carlo samples. As the distributions follow the form of a gaussian the σ = FWHM/2.35 of each is also shown. The post-collisions calibration results in better agreement with the ideal Monte Carlo distribution. In particular, a significant improvement is observed at the SCT end-caps (figure 2.6(b)), their vertical orientation results in reduced effectiveness of calibration with cosmic data (due to the topology of the atmospheric events).

The performance of the Inner Detector can be inferred from the performance of the reconstruction algorithms when comparing basic track observables. With the 7 TeV data, the transverse (d_0) and longitudinal (z_0) impact parameters were taken for a large number of events. The former is defined as the point of closest approach in the transverse plane while the latter, which is usually taken multiplied by $\sin\theta$ with θ being the scattering angle, represents the point of closest approach in the longitudinal plane. The parameters are derived from the initial track seeds of the track algorithm which require only silicon hits (Pixel and SCT), more details can be obtained from [101]. Figure 2.7 shows the comparison of d_0 and $z_0 \sin\theta$ as taken from data with `Pythia` generated non-diffractive minimum-bias events for which the

[4]A track-hit residual is defined as the distance between the extrapolated track position after the track reconstruction in the given module and the actual hit recorded by the module.

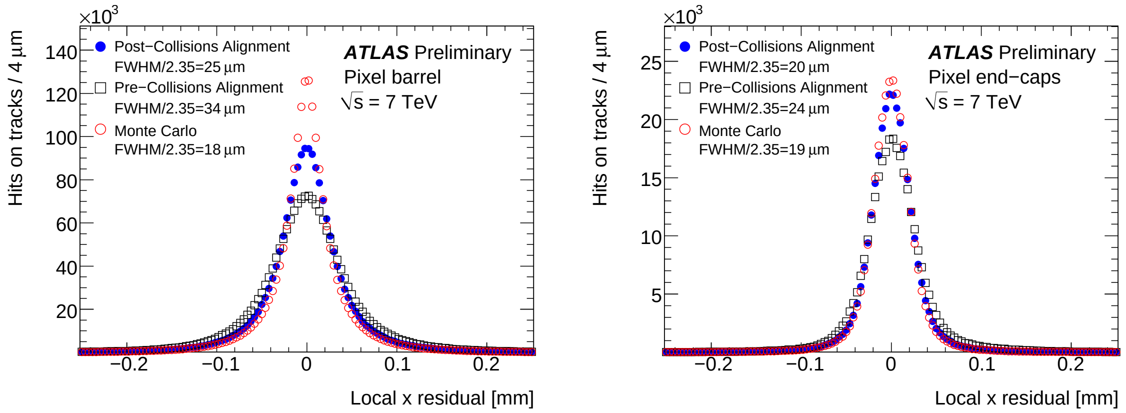

(a) *Pixel local x residual distributions for the barrel (left) and the end-caps (right).*

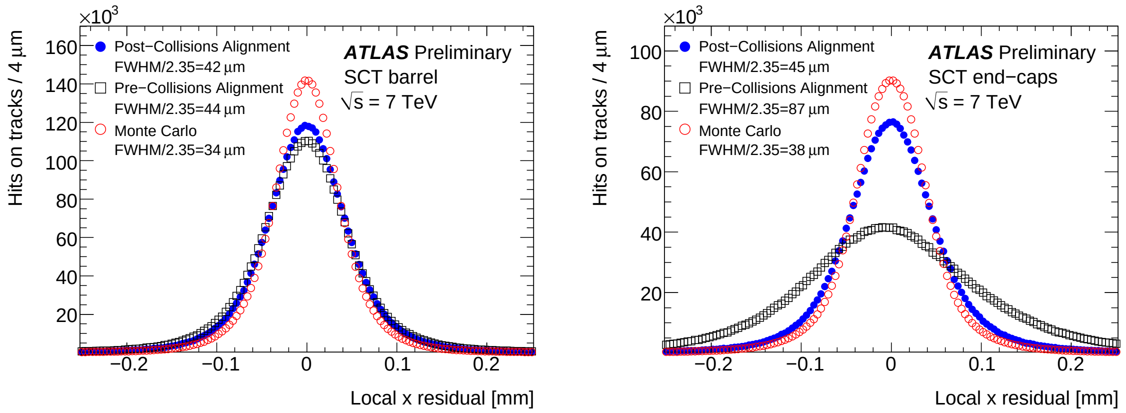

(b) *SCT local x residual distributions for the barrel (left) and the end-caps (right).*

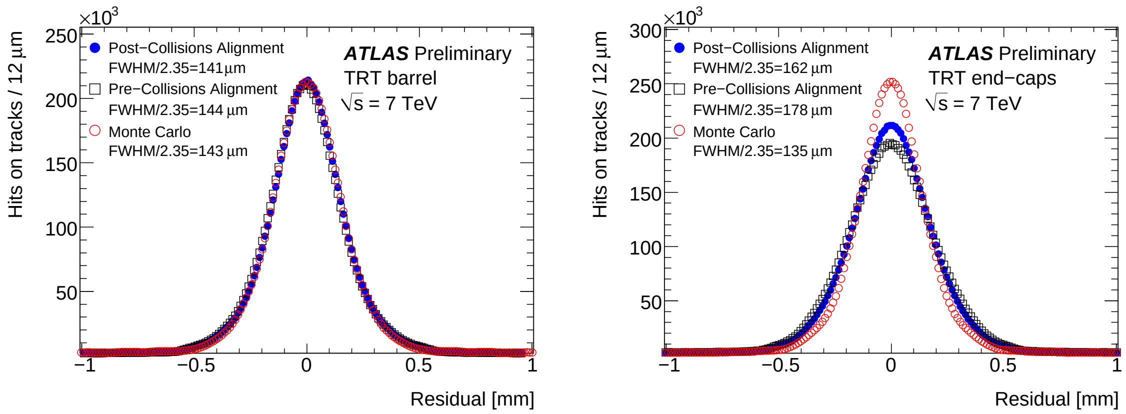

(c) *TRT residual distributions for the barrel (left) and the end-caps (right)*

Figure 2.6: *Residual distributions over all the hits on tracks calculated using the Pre-Collisions and Post-Collisions alignment constants on $\sqrt{s}$ = 7 TeV data and compared with perfectly aligned Monte Carlo samples. Plots taken from [100].*

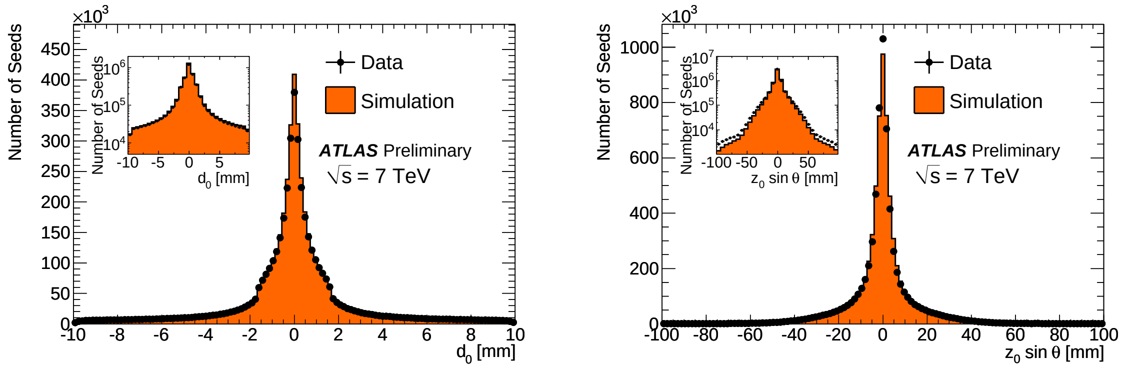

(a) (b)

Figure 2.7: *Comparison of the transverse (a) and the longitudinal (b) impact parameters as obtained from track seeds, between 7 TeV collision data and Monte Carlo. Plots taken from [101].*

p_{T} spectrum was smeared to agree with the data. The agreement is very good with the only exception the discrepancy in the tails of the $z_0 sin\theta$ which is due to a crude estimate of the θ angle.

2.2.4 Calorimetry

The calorimetry system of ATLAS consists of three individual sub-detectors: the electromagnetic calorimeter, the hadronic calorimeter, and the forward calorimeter (FCal). The electromagnetic calorimeter consists of the barrel and the two end-cap components, the hadronic calorimeter has the barrel, the two extended barrels and the two end-cap components, and the FCal consists of just two elements both placed in the very forward region. The whole system is symmetric around the beam axis and has full coverage in the ϕ direction. The pseudo-rapidity coverage is up to $|\eta| < 4.9$. A schematic view of the calorimeters is shown in figure 2.8.

The detector can measure, through complete absorption, both charged and neutral particles from a few GeV up to the TeV scale with high resolution for energy and position measurements and good signal linearity. The construction follows a sampling principle where layers of absorber material are separated by layers of active material. Particles entering the absorber develop into a shower and the energy of the shower is then measured by the active material. The measured value of the energy is proportional to the real energy. Weakly interacting particles such as muons or neutrinos do not get stopped by the detector. However, muons do leave a measurable trace that can be used in conjunction with information from the Inner Detector or the Muon Spectrometer while the energy and direction of neutrinos in the transverse plane can be inferred from momentum conservation (see later section 4.1.5 for details).

Electromagnetic calorimeter

The electromagnetic calorimeter is the most inner sub-detector of the calorimetry system of ATLAS. It is placed right behind the solenoid magnet, surrounding the Inner Detector and it has the task to precisely measure the energy and position of photons and electrons. Its barrel part covers the $|\eta| < 1.475$ region and it is separated in two halves by a small gap of 4 mm at $z = 0$. Each of the end-cap parts covers the $1.375 < |\eta| < 3.2$ region and is separated in two coaxial wheels, the outer one covering the $1.375 < |\eta| < 2.5$ region and the inner one covering

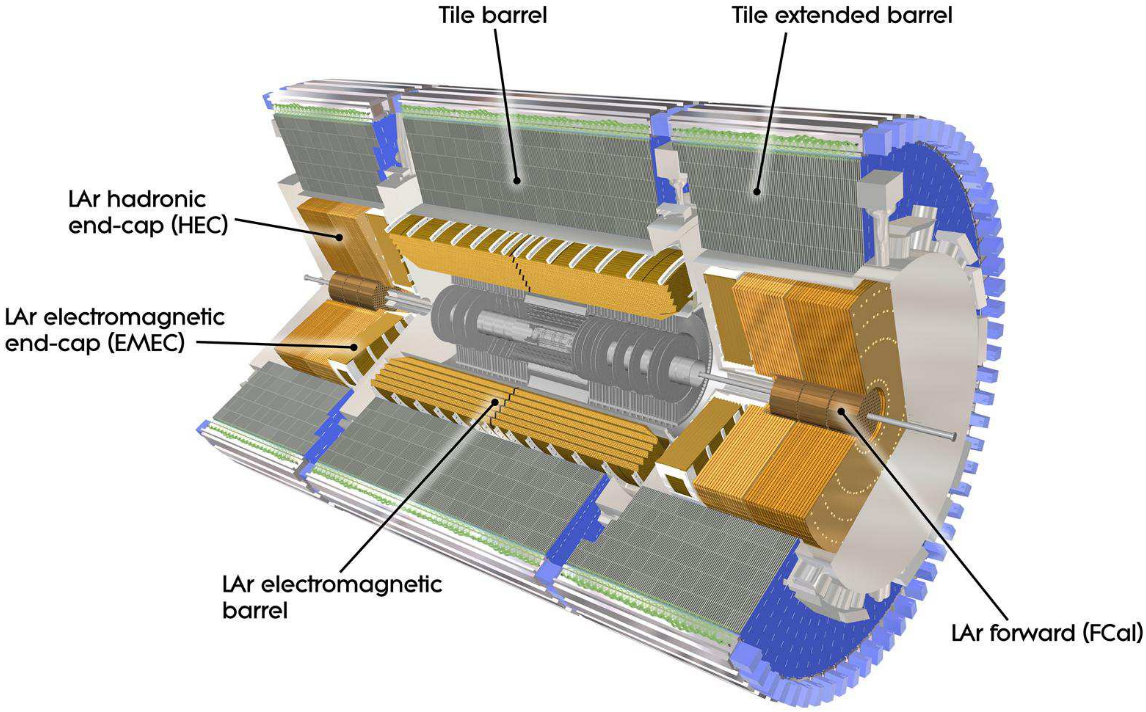

Figure 2.8: *Schematic view of the ATLAS Calorimetry system comprises the electromagnetic, the hadronic and the forward calorimeter sub-detectors.*

the $2.5 \leq |\eta| < 3.2$ region. Lastly, a small unit, the pre-sampler covering the $|\eta| < 1.8$ region, is placed in front of the main calorimeter.

The main part of the calorimeter is constructed with an accordion-shape geometry, thus ensuring a complete ϕ coverage without cracks, and consists of several interchanging layers of absorber and active materials. The absorber material is made from lead plates covered with stainless steel while the active medium is liquid argon. The pre-sampler part, located before the main calorimeter, consists only of active material with the sole purpose of correcting the energy loss electrons and photons suffer before entering the calorimeter. The total depth of the detector translates to more than 22 radiation lengths (X_0) in the barrel and more than $24X_0$ in the end-caps. Within the precision measurement range of $|\eta| < 2.5$ (barrel and outer-wheel), which also coincides with the Inner Detector coverage, the calorimeter is separated in three sections. In the first section, which is only $4.3X_0$ in depth, a fine granularity in terms of pseudo-rapidity is used ($\Delta\eta \times \Delta\phi = 0.003 \times 0.1$ in the barrel) for improved identification of γ/e or e/π_0. The second section has a more coarse granularity ($\Delta\eta \times \Delta\phi = 0.025 \times 0.025$ in the barrel) and receives most of the shower's energy with $16X_0$ depth. The last section, which is even coarser ($\Delta\eta \times \Delta\phi = 0.050 \times 0.025$ in the barrel) has about $2X_0$ depth and measures the tails of electromagnetic showers or distinguishing them from hadronic ones which develop further away and into the hadronic calorimeter. The energy deposition is measured with ionization of the LAr by the shower particles where the charges created are collected by high-voltage electrodes.

Hadronic calorimeter

The hadronic calorimeter sits just behind the electromagnetic calorimeter and its purpose is to measure the hadronic showers that develop due to interactions of the particles with the nuclei of the calorimeter's material. Typically, such particles are the result of the hadronization of quark and gluons, or of the hadronic decay of τ-leptons The barrel part of the calorimeter covers the $|\eta| < 1$ region with a central part, and the $0.8 < |\eta| < 1.7$ region with two extended parts. Each end-cap part covers the $1.5 < |\eta| < 3.2$ region and consists of two wheels.

The calorimeter is designed with interchanging layers of absorber and active materials. For the central and the extended parts of the barrel, steel plates are used as an absorber and scintillating tiles as the active medium. The structure is segmented in three layers with granularity of $\Delta\eta \times \Delta\phi = 0.1 \times 0.1$ for the first two layers and 0.2×0.1 in the last layer. The first layer of the central barrel has a total depth of 1.5 interaction lengths (λ), the second has 4.1λ and the third 1.8λ. The respective values for the extended parts are 1.5, 2.6 and 3.3λ. For the end-cap, the applied technology is different with the absorber being copper and the active medium consisting of liquid argon (similar to the electromagnetic calorimeter). The liquid argon can easily be replaced, possibly a necessity given the high radiation levels. The total depth of each end-cap is about 10λ and the granularity is $\Delta\eta \times \Delta\phi = 0.1 \times 0.1$ for the $1.5 < |\eta| < 2.5$ region, and 0.2×0.2 for the $2.5 < |\eta| < 3.5$ region.

The energy deposition in the barrel part of the calorimeter is measured from the light created in the scintillator material by the traversing shower particles. Subsequently, the light is collected by wavelength-shifter fibers which are grouped together and read-out by photo-multiplier tubes. In the end-caps the signal extraction method is the same as in the electromagnetic calorimeter.

Forward calorimeter

The forward calorimeter completes the calorimetry system of ATLAS. Covering the forward pseudo-rapidity region of $3.1 < |\eta| < 4.9$ it for ensures an almost hermetically closed calorimetry which is necessary for the determination of the missing transverse energy (see section 4.1.5 for details).

The forward calorimeters that serve both for electromagnetic and hadronic calorimetry. They are segmented in three modules: the FCal1 which uses copper plates as absorber and is dedicated to the detection of electromagnetic showers, and the FCal2 and FCal3 with tungsten plates dedicated to the detection of hadronic showers. The modules consist of a metal matrix (copper or tungsten) in which cylindrical copper tubes are placed with equal spacing between them and with their direction parallel to he beam axis. Inside the tubes, rods made of copper (FCal1) or tungsten (FCal2 and FCal3) are inserted, leaving a very small gap in between filled with liquid argon which serves as the active medium. The tube-rod construction acts as the electrode which collects the signal. The total depth of the FCal is about 10λ. In terms of radiation length FCal1 has $27.6X_0$, FCal2 has $91.3X_0$ and FCal3 $89.2X_0$.

Performance

With the first 7 TeV of data recorded by the ATLAS detector it is possible to determine the performance of the calorimetric system from the reconstruction of basic observables. One such observable is the $E_{\mathrm{T}}^{\mathrm{miss}}$ which is calculated from the energy imbalance on the transverse plane and is typically due to particles that escape detection. Events with neutrinos in their final state are characterized by missing energy, but a significant fraction can also be accounted to mis-measurements of the visible energy, hence $E_{\mathrm{T}}^{\mathrm{miss}}$ maybe non-zero even for events with no neutrinos. A more detailed description on the reconstruction of $E_{\mathrm{T}}^{\mathrm{miss}}$ is discussed in section

4.1.5.

In [102] the transverse missing energy reconstruction performance was examined. Figure 2.9 shows the x and y component of the $E_{\mathrm{T}}^{\mathrm{miss}}$, as well as the total of the $E_{\mathrm{T}}^{\mathrm{miss}}$ vector in minimum-bias data compared with the Monte Carlo simulation (`Pythia` generated events). As expected, for minimum-bias events, the distributions of the x and y components are centered around zero. All the plots show very good agreement between data and Monte Carlo.

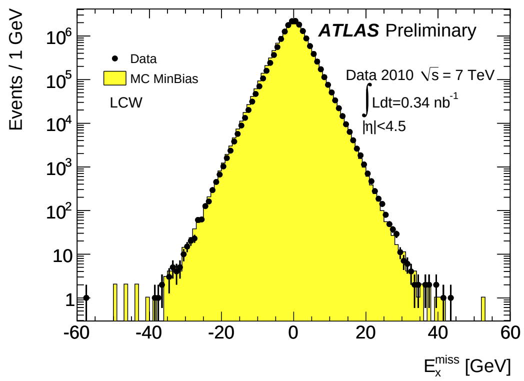

(a) *The x component of $E_{\mathrm{T}}^{\mathrm{miss}}$.*

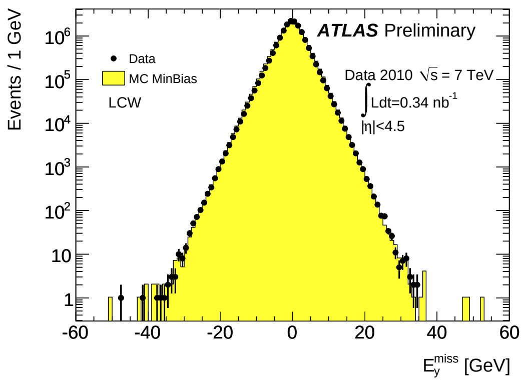

(b) *The y component of $E_{\mathrm{T}}^{\mathrm{miss}}$.*

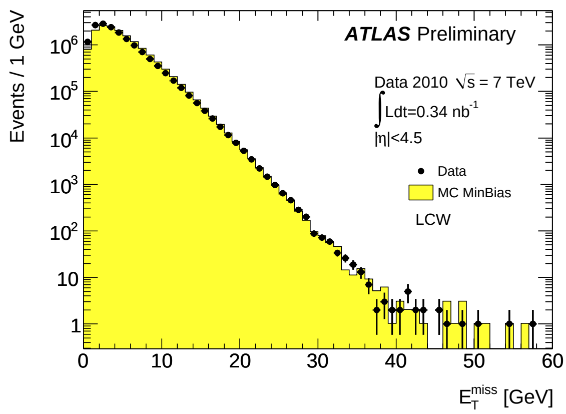

(c) *The total $E_{\mathrm{T}}^{\mathrm{miss}}$ vector.*

Figure 2.9: *Comparison of missing transverse energy as measured for minimum-bias events in the first 7 TeV data and compared with Monte Carlo. Plots taken from [102].*

Another test of the performance of ATLAS calorimetry, and in particular of the electromagnetic calorimeter, is the reconstruction of the J/ψ meson and the Z boson when they decay into two electrons. The details of the study are presented in [103]. Figure 2.10 shows the reconstructed invariant masses of the two particles compared with the Monte Carlo expectation.

2.2.5 Muon Spectrometer

The Muon Spectrometer is the last sub-detector that a particle may traverse in ATLAS as it is located in the outermost part of the detector. Its purpose is to precisely measure the momenta of muons by reconstructing their track and also to trigger on events when a muon is detected. For this reason, it is assisted by the magnetic field of the toroid magnet, which

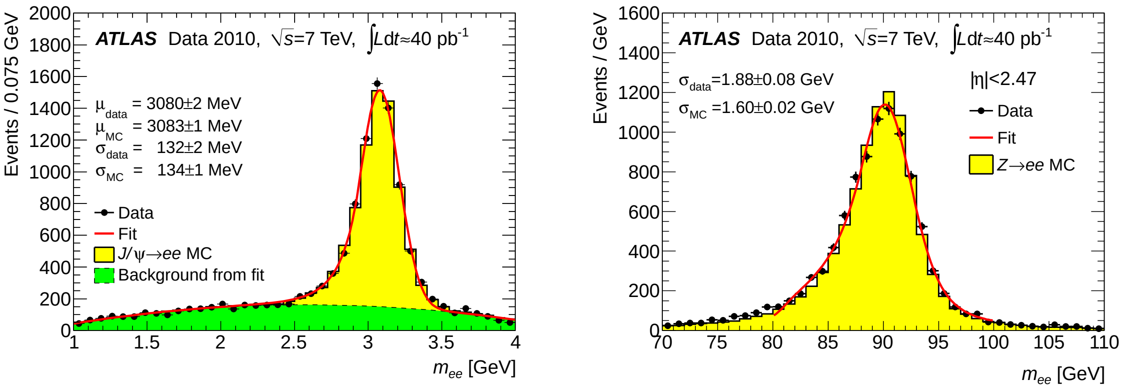

(a) $J/\psi \to ee$ (b) $Z \to ee$

Figure 2.10: *Reconstructed invariant mass of the J/ψ meson (a) and the Z boson (b) in the di-electron final state. Plots taken from [103].*

bends traversing muons, while often its information is combined with information from the Inner Detector or the calorimeters.

The coverage of the Muon Spectrometer is in the range of $|\eta| < 2.7$ and consists of the central barrel part and the two end-caps. The main detection instrument are the Monitored Drift Tubes . The MDTs are also assisted in the forward region ($2 < |\eta| < 2.7$) by the Cathode Strip Chambers (CSCs). Together the MDTs and the CSCs form the tracking system of the Muon Spectrometer. Two separate systems are used for the triggering task: the Resistive Plate Chambers (RPCs) in the barrel part ($|\eta| < 1.05$) and the Thin Gap Chambers (TGCs) in the end-caps ($1.05 < |\eta| < 2.4$), both providing coarse tracking information but fast enough to handle the nominal LHC rates. Figure 2.11 shows the layout of the Muon Spectrometer.

The measurement of the muon momentum is based on identifying the trajectory of the muon. Three space points are typically needed to reconstruct a track. Because of the magnetic field, the trajectory does not follow a straight line but it is bent, hence by calculating the curvature of the track the momentum of the muon can be estimated. However, in the ATLAS design, the sagitta[5](s) is used instead of the curvature and the transverse momentum is then given by:

$$p_T = \frac{L^2 B}{8s} \, , \tag{2.2.2}$$

where B is the integrated strength of the magnetic field and L is the distance between the two outer space points. The achieved resolution on the transverse momentum measurement ranges from $1 - 10\%$ for muons with p_{T} of $10 - 1000$ GeV respectively.

Monitored drift tube chambers

The MDTs are the main instrument of the Muon Spectrometer for measuring the trajectory of the muons. They are arranged in three layers, the inner, the middle and the outer layer.

The main element of the MDTs is an aluminum tube with a diameter of 30 mm which is filled with a gas mixture of $Ar(97\%) : CO_2(3\%)$ at a pressure of 3 bar. The choice of material for the tube is made such that it has minimal interaction with the magnetic field. In the middle of the tube an anode wire of 50 μm is placed which is made of gold plated tungsten and between the tube and the wire a constant voltage is applied. The tubes are arranged in

[5] The sagitta is defined as the depth of an arc.

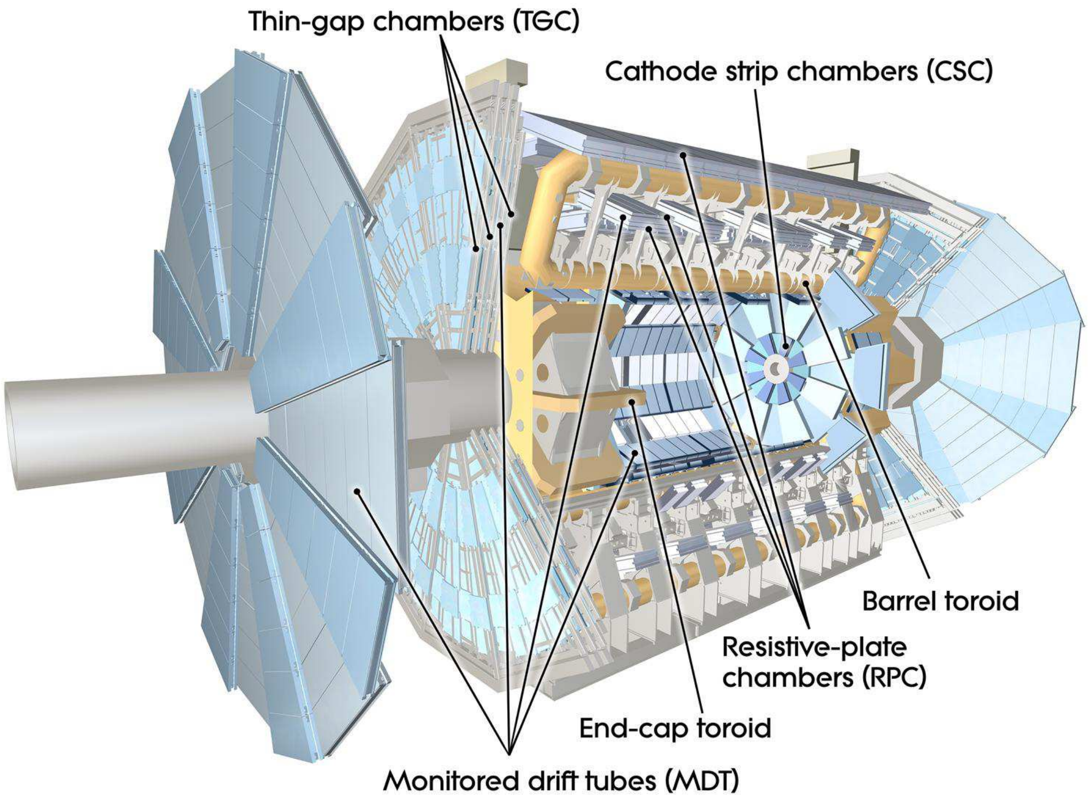

Figure 2.11: *Schematic view of the ATLAS Muon Spectrometer, comprised of the Monitored Drift Tube, the Cathode Strip Chambers, the Thin Gap Chambers and the Resistive Plate Chambers.*

chambers, a total of 1150, where each chamber consists of two multilayers of drift tubes. Each multilayer has typically three drift tube layers placed consecutively and parallel to each other, except for the inner chambers which are deployed with four drift tube layers per multilayer. The MDT chambers are also distinguished in small and large ones. The positioning of the MDTs is such that it allows precision measurement in the plane parallel to the beam axis (bending plane of the toroid). A total of 20 measurements per track for the bending plane are made but no information is provided in the non-bending plane (ϕ). The average resolution per chamber is shown in table 2.3.

The detection of particles in the MDTs is based on the ionization of the gas medium by the traversing particles. The voltage applied between the wire and the tube will drive the electron clusters towards the anode creating an avalanche of charges. The distance of the traversing particle from the wire is calculated by measuring the arrival time of the first cluster that passes a certain threshold. The time is transformed into a drift radius via an rt-relation[6]. The rt-relation is sensitive to a number of factors including temperature and magnetic field strength, so continuous monitoring is necessary.

Cathode strip chambers

The CSCs complement the tracking capability of the Muon Spectrometer in the forward region ($2 < |\eta| < 2.7$). In this region, particle rates exceed the 150 Hz/cm^2 limit of the MDTs and

[6]The rt-relation effectively connects the drift distance(r) with the drift time(t) and is an important element for accurate track reconstruction

Detector	Chamber Resolution	
	z/R	ϕ
MDT	35 μm in z	N/A
CSC	60 μm in R	5 mm
RPC	10 mm in z	10 mm
TGC	2-6 mm in R	3-7 mm

Table 2.3: *The chamber resolutions for each sub-detector element of the Muon Spectrometer. Alignment uncertainties are not taken into account.*

different technology must be applied. The CSCs are capable of handling the high occupancy up to a level of 1000 Hz/cm^2.

The CSCs are constructed from multi-wire proportional chambers filled with an $Ar(80\%)$: $CO_2(20\%)$ gas mixture. A total of two disks are placed on each side of the detector. Each disk consists of eight CSC chambers resulting in a total of 32 chambers for the entire system. The anode wires inside the chambers are placed radially while cathode strips are oriented either perpendicular (η direction) or parallel to them (ϕ direction). The detection principle is the same as in the MDTs with ionization of the gas creating an avalanche of electrons to the anode wire. The coordinates (in $\eta - \phi$) are measured by interpolation of the charge distribution over the neighboring cathode strips. A total of four modules in each chamber are constructed providing four independent measurements in η and ϕ for each track. This gives a significant advantage as it can resolve ambiguities when multiple tracks are present, which is common in the forward region. The intrinsic resolution of the CSCs is shown in table 2.3.

Resistive plate chambers

The RPCs are the dedicated system of the Muon Spectrometer for triggering on muons in the barrel region ($|\eta| < 1.05$). Three layers of RPCs exist. Two are placed at each side of the middle layer MDTs and one on, either the outermost side of the outer large MDTs, or the innermost side of the outer small MDTs. The system has a total of 606 chambers. A full complement of an MDT chamber plus the RPC layer is called a "station". An additional task assigned to the RPCs is to provide the coordinate of the tracks on the plane perpendicular to the beam axis (non-bending plane), hence complementing the MDT measurement which is only in the bending plane. However, due to its technology it is not optimal for precision tracking and the achieved resolution is much coarser than in the MDTs (see table 2.3).

The actual RPC detector consists of two parallel resistive plates separated by a gap of 2 mm. The gap is filled with a gas mixture of $C_2H_2F_4(94.7\%)$: Iso$-C_4H_{10}(5\%)$: $SF_6(0.3\%)$ and a high voltage is applied between the plates. Similarly to the MDTs and CSCs, a traversing muon ionizes the gas and an electron avalanche is created towards the anode. Read-out strips are placed on the outer side of the plates and they are optimized to measure in both η and ϕ directions. As a result, two measurements are made, one in each direction. A complete RPC unit consists of two independent detectors, each with a gas gap and a rectangular pair of strips, adding up to a total of at least four read-out outputs per RPC layer. RPC units are connected to neighboring units with a small overlap in order to avoid un-instrumented gaps. A pair of units forms a the trigger station. Given the layout of the RPC trigger chambers on the detector, a total of six measurements in η and ϕ are made in the barrel, providing redundancy for the determination of tracks.

Thin gap chambers

The TGCs are the muon triggering instruments of the Muon Spectrometer in end-cap region ($1.05 < |\eta| < 2.4$). Similarly to what happens in the barrel region, TGCs are used in conjunction with MDTs in the end-caps. A total of four layers of TGCs are arranged: one in front of the middle layer MDTs, two behind the middle MDTs and one in front of the inner MDTs. However, the inner TGCs were not used during the 2010 run. As in the RPC case, the TGCs are also responsible for providing the ϕ coordinate (non-bending plane) of the tracks.

The TGC detector is similar to the CSCs having multi-wire proportional chambers which operate with a gas mixture of $CO_2(55\%) : n - C_5H_{12}(45\%)$. The wires are oriented in the η direction and operate on a high voltage while the pick-up strips are placed perpendicular to them. The main characteristic of the TGCs is that both the wire and the strips are provided with readout and as a result a measurement can be made of both the η and ϕ directions. For the TGCs used at the middle MDT layer, the one on the inner side consists of a triplet of detectors and the two layers on the outer side each consists of a doublet of detectors. Similarly a doublet is used for the inner TGC layer. A maximum of nine measurements per track can be made and similar to the RPCs the intrinsic resolution is coarser in the bending plane than the resolution of the MDTs or CSCs (see table 2.3).

Alignment and performance

As with the Inner Detector, the Muon Spectrometer must also be geometrically calibrated before providing measurements for physics analyses. This is particularly important for the precision tracking measurements made by the MDTs and the CSCs. The design specifications for momentum resolution require that the locations of the chambers is known with a 30 μm precision. This is much more accurate than the position precision achieved after installation which is at best 5 mm and 2 mrad with respect to the nominal positions.

Given the size of the Muon Spectrometer of ATLAS occasional movement of its elements may occur. Hence, ATLAS uses an optical alignment system which provides a continuous precision measurement of the relative positions of MDT chambers with respect to their neighboring chambers. The alignment principle is based on a three point straightness monitor where an optoelectronic image sensor (CCD or CMOS) continuously monitors the position of an illuminated target with the help of a lens. The image is then analyzed and its deviation from the nominal distribution is translated in four parameters. The optical system effectively detects misplacements within an MDT layer (inner, middle or outer) and along the $R - z$ direction and passes the information to the offline reconstruction algorithms that apply corrections. A similar system is used for the CSCs. In addition to the optical system, track-based algorithms are also used, similarly to what happens for the Inner Detector alignment. The main reason is because the optical system itself is not enough to determine the absolute position of the MDT chambers with respect to the interaction point. Naturally, this approach requires for the tracks to be reconstructed; a more detailed explanation of the muon reconstruction is given later in section 4.1.2.

The alignment of the Muon Spectrometer has been tested with a large amount of cosmic ray data in the years prior the LHC collisions. Once proton-proton collisions took place more data were obtained in order to refine the alignment especially in the end-caps. These data were recorded with the toroid magnet switched off. This way the straight line muon tracks, which should have a zero sagitta, determined the initial spectrometer geometry. Once this was established, the magnet started to ramp-up and the displacements of the chambers were measured with the optical alignment system, thus providing further refinement of the alignment constants. Figure 2.12 shows the comparison of 7 TeV data recorded with the toroid

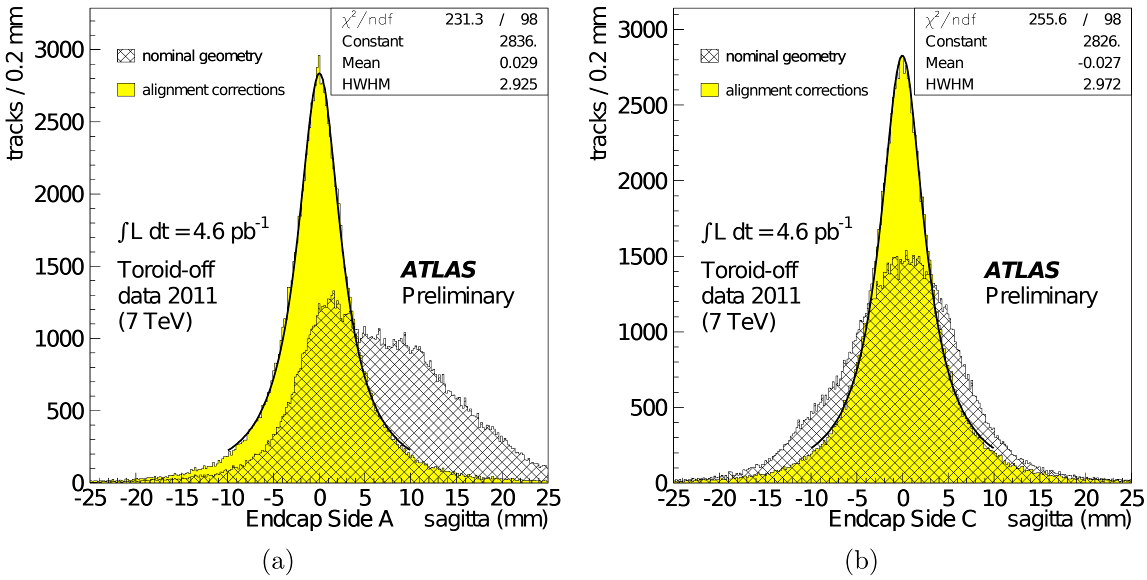

Figure 2.12: *Sagitta distributions of muon tracks at the end-caps (left: side-A, right: side-C) before and after alignment corrections are applied. Recorded in 7 TeV data with the toroid magnet off. Plots taken from [104].*

magnet off with and without application of the alignment corrections obtained with the above method.

The general performance of the Muon Spectrometer can be inferred from the results on the reconstruction performance for muons, in a similar way as was shown for the calorimeters and the Inner Detector. Figure 2.13 shows the relative momentum scale and resolution for the Muon Spectrometer up to $|\eta| \leq 2.5$. The relative momentum scale and resolution are provided by fitting the distribution of the function:

$$\frac{\Delta p}{p} = \frac{p_{ID} - p_{MS}}{p_{ID}}, \tag{2.2.3}$$

where p_{ID} is the muon momentum measurement provided by the Inner Detector and p_{MS} is the momentum of the track measured by the Muon Spectrometer and extrapolated to the primary vertex. The 7 TeV collision data are compared with the results from the cosmic ray events and the QCD Monte Carlo. More details on this analysis can be obtained from [105]. Also, in figure 2.14 the invariant mass of a di-muon system is plotted. The muons are selected based on information from the Muon Spectrometer combined with information of tracks from the Inner Detector. The resonances of several known particles is observed. More details can be found in [106].

2.3 Triggering and Data Acquisition in ATLAS

After a collision takes place at the interaction point, the resulting particles cause an electrical signal in the read-out modules of the various sub-detectors. These signals must then be transferred from the read-out systems to an environment where physicists will be able to analyze them. In ATLAS this task is assigned to the Data Acquisition System (DAQ) [107].

With the specifications of the LHC as given earlier (see section 2.1.2) an immense rate of events, of the order of 1 GHz, is expected at the interaction point of ATLAS. Not all of these events can be recorded since they constitute a huge amount of data (1 PByte per second) which

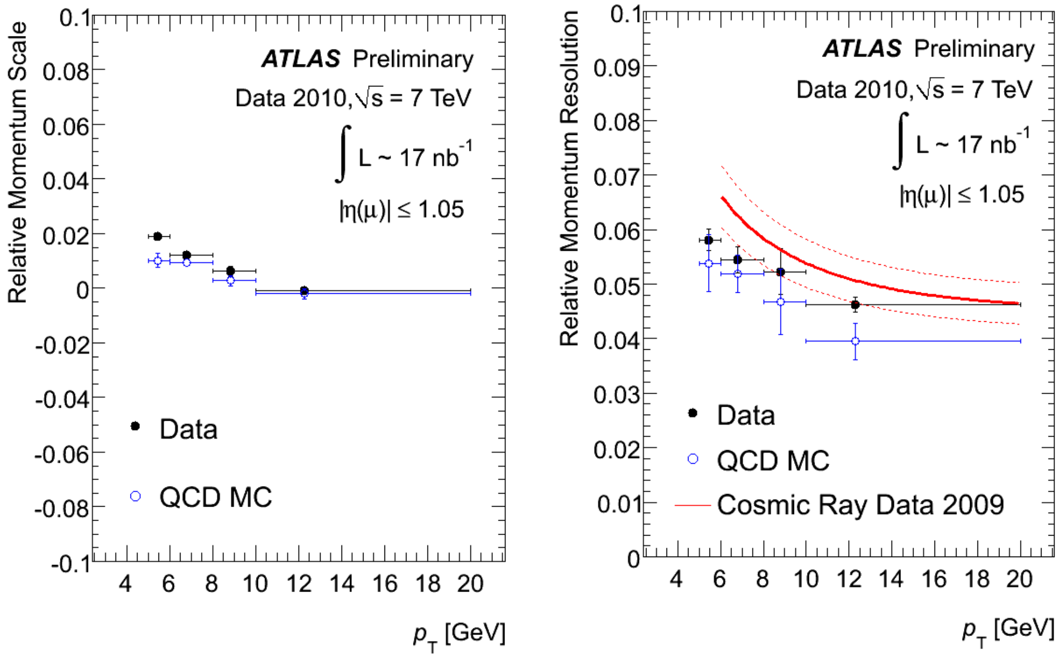

Figure 2.13: *The relative momentum scale (left) and resolution (right) for the barrel* ($|\eta| < 1.05$) *region of the Muon Spectrometer. The 7 TeV collision data are compared with the Monte Carlo QCD and the cosmic ray data (resolution measurement only). The cosmic ray data are shown in the form of the fit (solid-line) with a* $\pm 1\sigma$ *uncertainty band (dashed-lines). Plots taken from [105].*

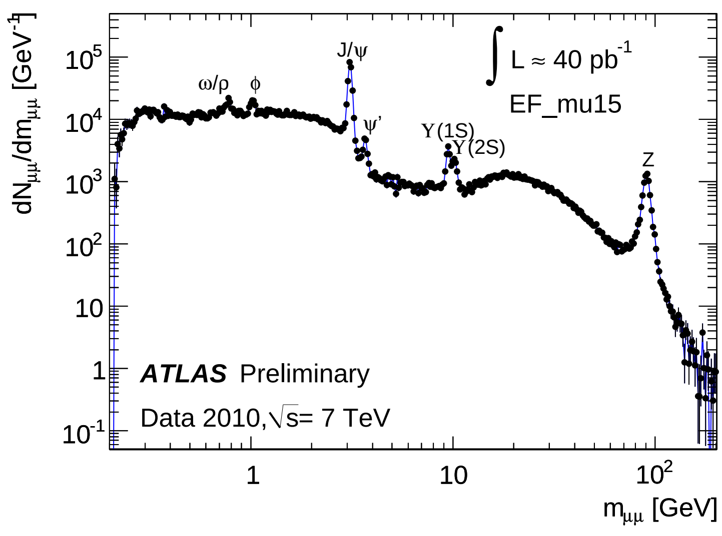

Figure 2.14: *The di-muon invariant spectrum from 7 TeV data. The plot is an updated version with more data of the one found in [106].*

exceeds by far the technical possibilities and the budget of the experiment. However, not all of the events need to be recorded since only a very small fraction is expected to contain interesting physics with respect to the goals of the experiment. Hence, the Data-Acquisition system of ATLAS has a Trigger system that filters about 99.9995% of the events and allows only the rest to be written to disk. Since the trigger is integrated in the general DAQ infrastructure the whole system is commonly referred to as the Trigger and Data-Acquisition of ATLAS (T/DAQ).

The T/DAQ system of ATLAS can be broken down into: the Level-1 (L1), Level-2 (L2) and the Event Filter (EF) trigger layers, which handle the event selection procedure, and the Read-Out System (ROS) and the Event Builder (EB) layers that handle additional tasks in the data flow between the trigger layers. The L1 is a hardware based trigger consisting of custom-made electronics that are located on the detector. The L2 and the EF, referred to as the High-Level Trigger (HLT), are both software-based, running sophisticated and highly efficient reconstruction algorithms before reaching a decision. At each level an event may be rejected in which case it gets deleted, else it continues to the next level until it is eventually accepted by the EF and is written to disk. The main consideration in the implementation of each trigger level is to reduce the incoming event rate by a certain factor, without throwing away the interesting events and such that the output is acceptable as input to the next level.

2.3.1 The Level-1 Trigger

The L1 works at the input rate of the bunch-crossing (40 MHz) and it needs to be synchronized at all times with the LHC clock, it eventually reduces the rate down to to 75 kHz (upgradeable to 100 kHz). The time envelope allowed for the L1 to make a decision is only 2.5 μs from the time of its associated bunch-crossing.

The L1 trigger is implemented such that it measures the multiplicity of hits on the detector that pass a certain pre-programmed threshold. Information is only obtained from the calorimetry system (L1Calo) and the Muon Spectrometer (L1 muon); no Inner Detector information is used. The overall decision is made by the Central Trigger Processor (CTP) after combining the information from all the relevant detector parts. The timing signals, needed for synchronization with the LHC bunch-crossing and the trigger information are handled by the Timing, Trigger and Control (TTC) which makes them available to the detector's front-end and read-out electronics. A block diagram of the L1 trigger is shown in figure 2.15.

L1Calo

The L1 Calorimeter trigger is responsible for identifying objects with high transverse energy (E_T) in the calorimeters (e.g. photons, electrons, jets) as well as events with large energy imbalance ($E_{\mathrm{T}}^{\mathrm{miss}}$), typically caused by the unidentified neutrinos, or large total transverse energy ($\sum E_T$). An exact measurement of the energy deposition is not made, instead the decision of the L1 is based on the multiplicity of hits that exceed a certain E_T threshold. Determining the isolation of certain objects is also possible by deducing the angular separation of the hits from other significant energy depositions in the calorimeter, during the same bunch-crossing. This is possible since the angular coordinates of the energy depositions are known with the accuracy of the detector's granularity (see section 2.2.4). For the $E_{\mathrm{T}}^{\mathrm{miss}}$ and the $\sum E_T$ measurements, global sums are made from the total deposit of the hits.

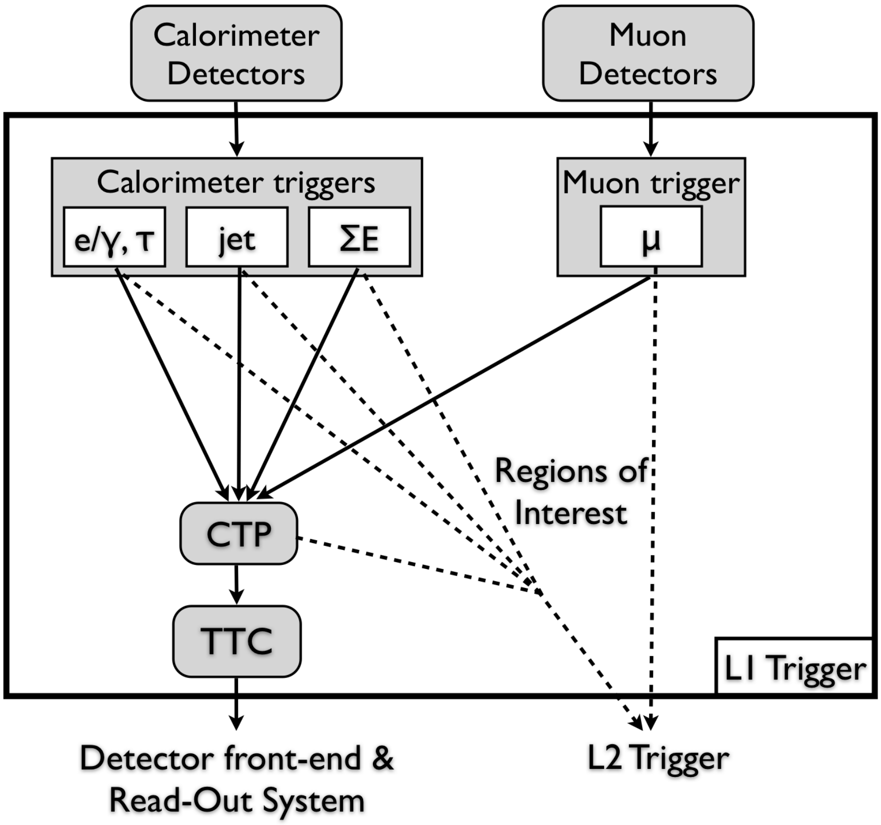

Figure 2.15: *Schematic block diagram of the L1 trigger of ATLAS.*

L1 muon

The L1 muon trigger is based only on signal from the muon trigger chambers (RPCs and TGCs). Similarly to the L1Calo, the decision of the trigger is based on the multiplicity of pattern hits that are assigned to a given prescribed threshold; a total of six threshold exist, three for low-p_{T} (6-9 GeV) muons and three for high-p_{T} (9-35 GeV) muons. More details on the muon trigger are given in chapter 3.

The CTP

The Central Trigger Processor is the receiver of all L1 trigger information from the calorimeter and the muon trigger processors. The CTP subsequently uses look-up tables to build the trigger conditions from the input signals and then the trigger conditions are used to check each of the 256 predefined trigger items (e.g. checking for at least two muons of threshold XX and one jet of threshold YY). A L1-accept signal (L1A) is generated by the CTP as the logical OR of all trigger items.

In addition, the CTP provides the luminosity block (LB) number to the read-out system. The LB is the shortest time interval for which the integrated luminosity can be determined. The use of LBs allows to reject part of the data where failures on the detector systems where observed. For this reason the LBs are kept as small as possible but at the same time must be large enough to contain enough data such that the uncertainty on the luminosity value is not driven by the statistics. At each LB change the CTP holds the trigger for a brief instance and increases the number. The LB interval during the 2010 run was 2 minutes.

Data flow

When the collision remnants reach the detector, the number of hits that exceed certain thresholds is counted by the relevant electronics. Based on this information the L1 identifies regions in $\eta - \phi$ which are considered to contain interesting features, the so-called Regions-of-Interest (RoI). A RoI includes information on the type of features as well as the accepting criteria. Four types of RoIs are recognized by the L1 trigger: muon, electron/photon, τ-lepton and jets, with the last three based on the calorimeters.

During the decision-making process, the L1 trigger stores all signals from the detector in pipeline memories and they remain there until a L1A is given, if this does not happen within the time-envelope defined for L1 the data are eventually lost from the pipelines. Once a L1A is transmitted by the CTP the signals are moved to the Read-Out Drivers (RODs), where they are transformed to a raw data format pre-defined by ATLAS. Subsequently, with the help of point-to-point optical read-out links (ROLs) the raw data fragments are transferred to the Read-Out buffers (ROBs) of the Read-Out System (ROS). In addition, the information of the RoIs is transferred by dedicated ROLs to the Region-of-Interest Builder system (RoIB) of the L2 trigger.

2.3.2 The Read-Out System

The ROS is the system that temporarily stores the event-fragments of an event if it has been accepted by the L1 trigger. The complete system consists of 151 PCs most of them housing 4 of the so-called ROBIN cards. The ROBIN is a custom-made Peripheral Component Interconnect (PCI) card that consists of three optical-link inputs for the ROLs, allowing data to be transferred with a rate of 160 MB/s per card. Each input has a dedicated Read-Out Buffer (ROB) of 64 MB memory size available where the event-fragments are stored.

The ROS PC controls and monitors the ROBIN cards via the Read-Out Application. It receives messages from the L2 trigger (section 2.3.3) or the Event Builder (section 2.3.4) to either send the requested data from its buffers via the data-collection network or delete them completely. The Read-Out Application is also responsible for detecting possible errors in the event-fragments (e.g. corrupted or missing event-fragments). This information is later on added in the event status and helps to monitor the quality of the data.

As each PC is mapped to a region of the detector, it makes the ROS a cornerstone element within the T/DAQ infrastructure. Consequently, a failure in a ROS PC may lead to a loss of the event-fragments related to that region.

2.3.3 The Level-2 trigger

With the L1A given, the event will be processed by the L2 trigger. The L2 trigger processes events at a rate equal to the output rate of the L1. The nominal output rate of the L2 system is 3.5 kHz although it can go as high as 5 kHz. The average process time available for a decision by the L2 is 40 ms.

Unlike the L1 trigger, the L2 is a software-based trigger which runs dedicated algorithms on the collected event-fragments in order to reach a decision for the event. The L2 is typically seeded by the RoIs which contain only 2% of the total event size. This is a significant advantage that assists in the fast processing of events, but mainly it reduces the bandwidth needed for processing the events. However, it has access to an increased granularity of the data inside the RoIs including information from the Inner Detector.

The L2 system consists of the Region-of-Interest Builder (RoIB), a few L2 Supervisors

(L2SV) running on dedicated nodes, a small number of L2 Result Handlers (L2RH) which are similar to the ROS PCs, and the processing farm of 750 nodes which run the L2 Processing Unit applications (L2PUs). See figure 2.16.

Data flow

Upon transmission of a L1A, the position information of the RoIs along with the L1 trigger decision is sent to the RoIB. The RoIB is responsible for merging this information into a single event record and forwarding the record to one of the L2SVs via a ROL. The L2SV assigns the event to an L2PU application and simultaneously transmits to it the relevant RoI information. The L2PU will execute the necessary algorithms and with the given RoI information will request the necessary event-fragments from the ROS PCs. Once the L2PU reaches a decision it is transmitted to the same L2SV that initially assigned the event. In case the event is accepted it will proceed to the Event Builder and subsequently to the Event Filter (see figure 2.16).

During the execution of the L2 algorithms a complete record of their process is kept. This record is written out in the buffer of the L2RH, which acts similarly to a ROS machine, and remains there until it is cleared.

2.3.4 The Event Builder

The Event Builder is the layer preceding the Event Filter trigger. Its purpose is to collect all the event-fragments of an event and assemble them into a single unit. Essentially, it works on the output rate of the L2 trigger. It consists of the Data-Flow Manager (DFM) and the Sub-Farm Input (SFI) nodes. To accomplish its tasks the Even Builder is made up of a total of 12 DFM nodes and 48 SFI nodes. Each SFI node however is able to run two event building applications for a total of 96.

The DFM is the receiver of the L2 event decision, transmitted by the L2SV. In case the event is rejected it will ask the ROS PCs and the L2RH to delete the relevant event-fragments and the L2 trigger result respectively from their memories. In the opposite case it acts as a supervisor by deciding, depending on a load-balancing round-robin method, which SFI will receive the event information.

The SFI assigned with an event will request and receive the necessary event-fragments via the data-collection network from the ROS and will build the complete event. The L2 trigger record will be obtained from the L2RH and become part of the event as well. After completion of the event building the SFI transfers the event, via the back-end network, to one of the EF nodes. It will then be cleared from the SFI buffer and a message will be sent to inform the DFM. In turn, the DFM will request from the ROS and the L2RH to delete the relevant event-fragments. At that moment the EF node becomes the holder of the event. Figure 2.16 shows a block diagram with the message exchange between the elements of the L2 trigger layer and the Event Builder layer.

2.3.5 The Event Filter

The last trigger level of the ATLAS online selection system is the Event Filter.The EF receives the events from the Event Builder and writes them to a shared memory buffer (Shared-Heap) while keeping a back-up on the local disk as well. Similarly to the L2 trigger, the EF is software-based, seeded by the RoI (which may have been updated by the L2), and runs dedicated algorithms for selecting events. However, in contrast to the L2 it has access to full granularity

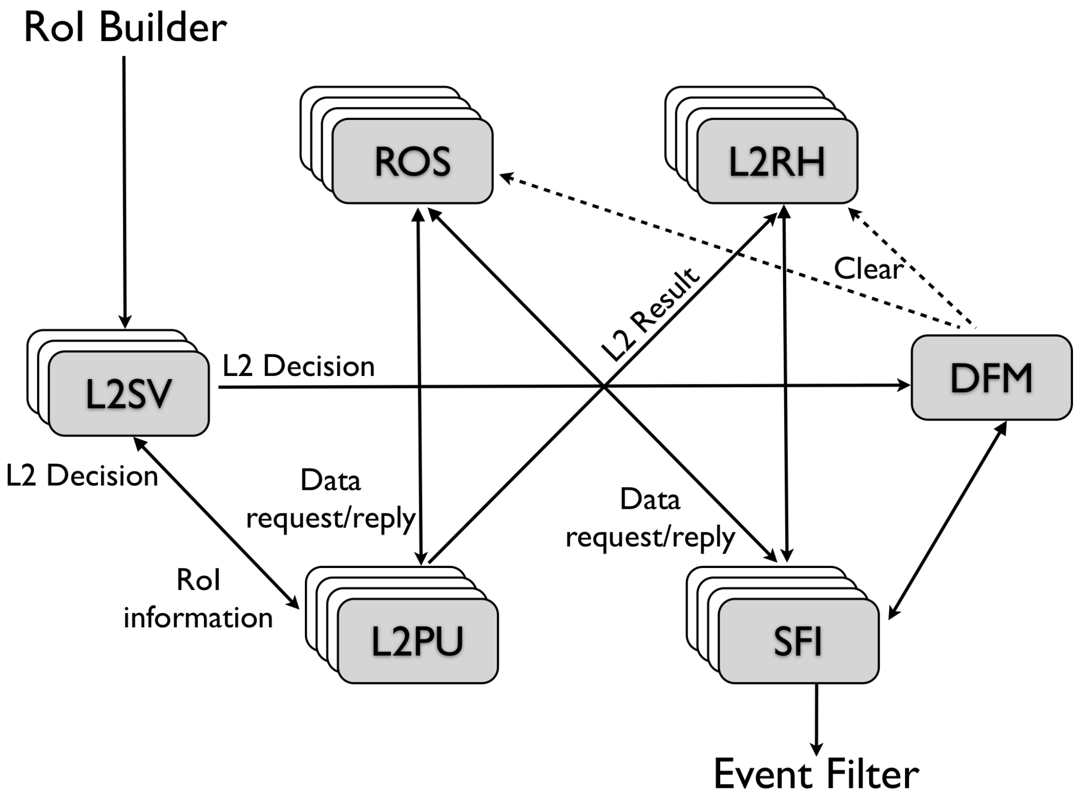

Figure 2.16: *Block diagram depicting the components of the L2 trigger and the Event Builder as well as the message exchange between them.*

of the complete event and it employs, to a large extend, the same reconstruction algorithms as the offline ATLAS reconstruction. The complete system consists of a processing farm of about 600 nodes where each node contains multi-core CPUs. Each node runs a single Event Filter Data-flow (EFD) application and multiple EF Processing Unit applications, typically equal to the number of cores in a node. The EFD is responsible for communicating with and transferring the data between the Sub-Farm Inputs (SFI). and the Sub-Farm Output (SFO), which is the receiving end that stores the accepted events. The EF Processing Unit (EFPU) is the application that runs the EF selection algorithms, similar to the L2PU.

The EF nominal output is designed at 300 MB/s, which, for a size of 1.5 MB per event, translates to a rate of 200 Hz. However, the actual capability of the system can sustain higher rates up to the level of 600 Hz, for the same event size. It should be noted that the limitation of the 200 Hz is not because of the design of the EF system itself, but rather due to the capability of the offline reconstruction to keep up with the incoming events for a long period.

2.3.6 Trigger menus and event streaming

A trigger menu is a description of the complete trigger logic throughout all trigger levels. It consists of a list of L1 trigger items (see section 2.3.1) and, L2 and EF *trigger chains.* The trigger chain is the sequence of algorithms which are ran on the events by the L2PUs or the EFPUs. Two types of such algorithms are defined:

- The Feature Extraction (FEX) algorithms reconstruct comprehensive parts of the event, identify objects and extract their specific features such as tracks, energy clusters etc.

- The Hypothesis (HYPO) algorithms compare the information obtained by the FEXs with certain pre-defined criteria and decide whether the specific object satisfies these criteria.

Both algorithms are executed in steps and they are usually interleaved, typically with one FEX being followed by one HYPO. The choice of the trigger chains inside the trigger menu defines which algorithms will be used. For an event to be accepted by the trigger at least one of the defined trigger chains must be valid.

Depending on the chains that are satisfied by an event will be classified into *streams*. Four major stream categories exist:

- **Physics streams:** Contain fully built events that were successfully processed by the T/DAQ system and are targeted to physics analysis.
- **Calibration streams:** These are based on calibration triggers. Events that end up in calibration streams are stripped down to 1-100 kB keeping only the information that is necessary for the calibration task.
- **Express stream:** This stream consists only of a small subset of physics events. These events are used for fast monitoring and for verifying the overall data quality of the data-taking. They are not used for physics analysis.
- **Debug stream:** Events ending-up in this stream are subject to a failure during their processing by the T/DAQ e.g. algorithm time-out. The failure does not necessarily imply a malfunction of the system and these events are re-processed offline for debugging.

All but the debug stream are inclusive, meaning that events may duplicate between streams. Especially for the physics analyses, in case multiple physics streams are used, extra care must be taken to avoid double counting of events. For most of the data during 2010 the main physics streams were: `Egamma` for events accepted by the electron or photon chain triggers, `Muon` for events accepted by muon chain triggers and `JetTauEtMiss` for events accepted by jet, τ-lepton, $E_{\mathrm{T}}^{\mathrm{miss}}$ or $\sum E_T$ trigger chains.

The assignment of the event to the various streams takes place within the SFO, the last component of the T/DAQ system. The SFO stores the events and organizes them over different data files that will make up the streamed events. In the final step, these data files are transferred asynchronously to the mass storage facilities outside of the T/DAQ environment.

2.3.7 Performance of the T/DAQ system

The excellent data-taking capability of the detector is evident from the results that were presented in the previous section for each of the detector's components. However, the very good performance of the Trigger system can be best illustrated by its success to sustain the expected, or even higher, trigger rates. This is depicted in figure 2.17 where the rates for each trigger level is shown for the run with the highest peak of instantaneous luminosity in 2010. It is interesting to note that, during this run, the EF was stable at an output rate of approximately 500 Hz.

In order to quantify the overall performance of the T/DAQ system one can compare the running time of the detector during *stable beams*[7] with the total time of stable beams. This

[7] As 'stable beams' is defined the state in which the configuration of the proton beams at the LHC is at the expected conditions for the experiments to begin data-taking.

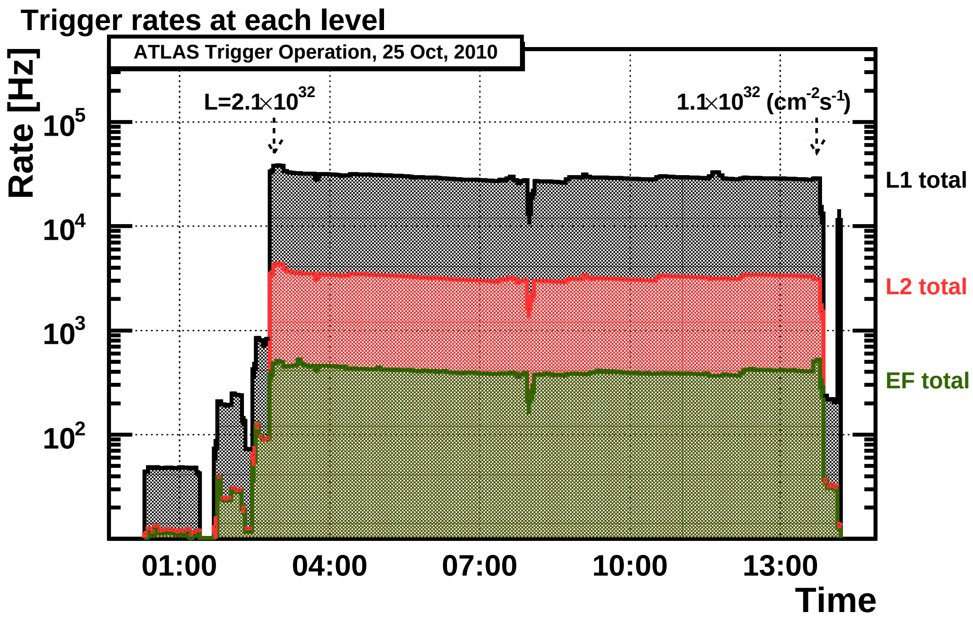

Figure 2.17: *Trigger rates for the highest luminosity run during the 2010 data-taking period. Figure taken from [108].*

ratio, which defines the *Run Efficiency*, is shown as a per-week average for the 2010 data-taking in figure 2.18(a). The 'Beam Time' histogram corresponds to the total time (in hours) during which stable beams are given. The 'Run Eff.' histogram corresponds to the Run Efficiency as defined above, however, this definition includes data-taking time in which not all detector components are at their nominal state e.g. data-taking runs for which the toroid magnet was switched off for calibration purposes. The averaged Run Efficiency is 96.5%. The histogram 'Run Eff. Ready', on the other hand, is defined as the time in which the detector was running with all detector component at their nominal states. In this case, the averaged Run Efficiency is found to be 93.0%. The reasons for the lower efficiency are due to the start of data-taking runs after stable beams are declared, or due to stopping or holding a run during beam time in order to work on a malfunctioning sub-system or adjust the trigger configuration. In figure 2.18(b) the total time is shown for stable beams (Beam), for ATLAS running (Run) and for ATLAS running under nominal conditions (Ready). The total time of stable beams is estimated at approximately 752.7 hours.

2.4 Summary

In this chapter we provided an overview of the Large Hadron Collider and the ATLAS detector. We presented in more detail the layout of ATLAS together with the most important considerations in its design and with the first data collected, during 2010, we presented examples of measurements in order to illustrate the excellent performance of each of the sub-detector systems. In addition, we described thoroughly the Trigger and Data Acquisition system of ATLAS which allows the data to flow from the sub-detector to the offline storage system. With the first data, the performance of the system is shown to be outstanding.

In conclusion, both the accelerator and the detector perform admirably. The combination of these two machines allows us to move from the theoretical predictions to the experimental measurements. In the next chapters, we will focus on the experimental results we obtained

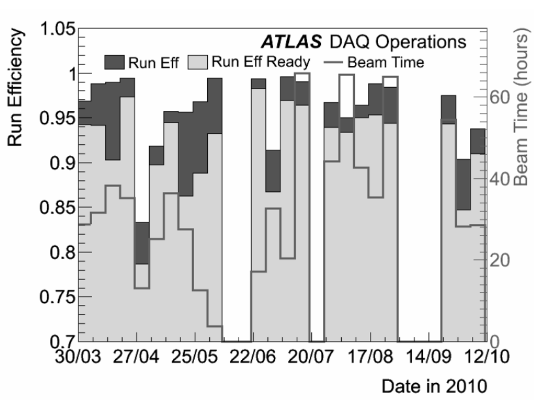

(a)

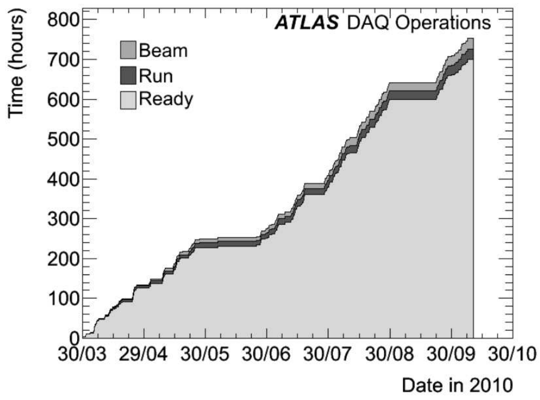

(b)

Figure 2.18: *The Run Efficiency (a) and the total running time (b) of the ATLAS detector for 2010. The Run Efficiency is also shown based on the total time in which the detector was running under nominal conditions, namely with all sub-systems operational, denoted as 'Run Eff. Ready' in (a) and as 'Ready' in (b). Figures taken from [109].*

with the first proton-proton $\sqrt{s} = 7$ TeV collisions and are related with the measurement of the $t\bar{t}$ production cross-section.

Chapter 3

Triggering on muons

*"Physics is, hopefully, simple.
Physicists are not."*

Edward Teller
1908 - 2003

The real-time selection of events is an essential step for the ATLAS experiment. As discussed in section 2.3, this task is assigned to the three-level trigger system with the main consideration of bringing the initial collision rate down to an acceptable write-out level, of typically 200 Hz, without throwing away interesting events. The T/DAQ system, ultimately, should ensure the stable and efficient selection of the interesting physics signatures and storing of the data for later (offline) analysis

In this chapter, we present the part of the trigger that is responsible for the identification of muons. In section 3.1 an overview of the reconstruction of muons at the trigger level is given. In section 3.2 we show the performance of the muon trigger system by analyzing the very first 7 TeV proton-proton collision data provided by the LHC. Lastly, we discuss in section 3.3 the possibility of measuring the trigger efficiency directly from data. We provide a feasibility study using the so-called *tag-and-probe* method, based on part of the collected data, and we show how the extracted result can be applied to the $t\bar{t}$ cross-section measurement.

3.1 Muon online reconstruction

Online reconstruction refers to the reconstruction and identification of objects that takes place within the TDAQ system. The main priority at this level is to be robust and efficient within tight time intervals and at the same time provide accurate measurements of the kinematics of the traversing objects. The three trigger layers (L1, L2 and EF) have different input rate tolerance and output rate requirements. So, different techniques are required at each level. Muon reconstruction at the trigger level depends mainly on information from the Muon Spectrometer and the Inner Detector, with the latter available only at the High Level Trigger (HLT).

3.1.1 The L1 Muon Trigger

At the L1 trigger [110] the muon selection depends solely on the information acquired by the RPCs and TGCs; a brief description of the technical details of the two technologies is already given in 2.2.5. As discussed in section 2.3.1, the small time window available for the L1 trigger to make a decision does not allow a complete reconstruction of a muon track. Instead, it uses the hits seen by the chambers to translate them into trajectories based on their topology. We explain the method in detail in the following:

- Firstly, an infinite momentum trajectory is defined, i.e. a trajectory that starts from the nominal interaction point and traverses the Muon Spectrometer in a straight line by passing through a reference point. The reference point is determined based on the collected hits on one of the detector's layer, the *pivot*.
- Secondly, the deviations between all the observed hits and the straight line trajectory are measured.
- Lastly, the calculated deviations are compared with Look-Up Tables (LUT), obtained from Monte Carlo, which map the result to certain p_{T} intervals.

Eventually, all track candidates are collected and counted according to their assigned p_{T} intervals. This information is subsequently sent to the CTP where the L1 items are formed (see section 2.3.1).

RPC trigger

As discussed in section 2.2.5, the RPCs trigger on muons that traverse the barrel region of the Muon Spectrometer ($|\eta| \leq 1.05$). They are arranged in three layers and they are capable of measuring in both the η and the ϕ planes. An illustration of the RPC trigger can be seen in figure 3.1.

The low-p_{T} triggers begin with a hit at the middle RPC (pivot) which acts as the reference point for the infinite momentum trajectory. Further hits are then searched in the other RPC planes but within a specified region of certain width along each of the η and ϕ planes; this is called the *road*. The center of the road coincides with the infinite momentum trajectory while the size of the width depends on the evaluated p_{T} threshold; the higher the threshold, the smaller the width. For low-p_{T} triggers only the inner layer (RPC1) and the pivot is used and a coincidence of 3-out-of-4 hits per direction is required for the track to be considered. Depending on the size of the width that is used for including the track coincidence hits, the p_{T} is assigned. As mentioned earlier, the correlation between the road widths and different p_{T} thresholds is pre-computed from Monte Carlo and is placed in LUTs

The procedure for the high-p_{T} trigger is almost identical as for low-p_{T}, with the only exception that also hits in the outer plane (RPC3) are searched for. Furthermore, the coincidence of hits is 1-out-of-2 per direction for the outer layer, in addition to the requirement for the low-p_{T} trigger.

TGC trigger

The TGCs are responsible for triggering on muon candidates at the end-caps of the Muon Spectrometer. They are assembled in four layers and can measure both in the radial (R) and the azimuthal (ϕ) directions. Their acceptance limit, of $|\eta| \leq 2.4$, also defines the acceptance of the muon trigger for the ATLAS detector. A more detailed technical description of the layout is given in section 2.2.5. An illustration of the TGC trigger is shown in figure 3.2.

The triggering procedure on TGCs follows the same steps as in the RPC case. The pivot plane is now taken to be the outermost layer of TGCs (TGC3). Once a hit is found in the pivot plane, the algorithm searches for hits in the other TGC layers. For low-p_{T} thresholds only the two outermost layers (TGC2 and TGC3) are used and a coincidence of 3-out-of-4 is required in both directions, else the track is not considered. The p_{T} assigned to the track

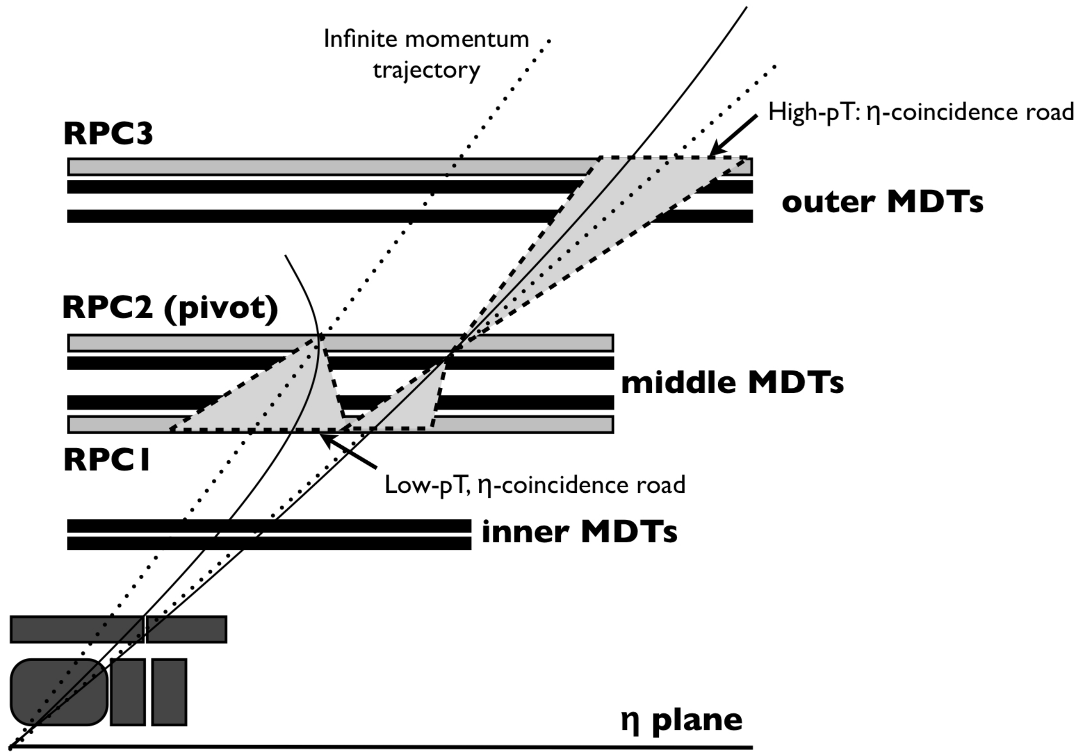

Figure 3.1: *Illustration of the RPC trigger at L1 identifying low-p_T and high-p_T tracks at the η (bending) plane.*

works in the same way as for the RPCs.

For the high-p_T thresholds, hits on the TGC layer right before the middle MDTs (TGC1) are also required. In this case a coincidence of hits of 2-out-of-3 in the radial plane and 1-out-of-2 in the azimuthal plane in TGC1 is required on top of the low-p_T coincidences. Note that the innermost TGC layer (inner TGC) has not been used throughout the 2010 data-taking period.

3.1.2 The L2 Muon Trigger

Starting from the L2, the Trigger is able to run software-based feature extraction algorithms (FEX) on the Regions-of-Interest (RoI), selected by the L1, and reconstruct the tracks of the traversing muons partially or completely. At this level, information from the Inner Detector becomes available allowing for a more accurate estimation of the p_T of the muons and an increased rejection rate of fakes. Also, information from the MDTs precision chambers become available at this level. The main FEX algorithms are: `muFast` [111, 112] and `muComb` [113]. These will be discussed below.

Additional algorithms are also implemented, oriented to more specific event signatures, usually employed in parallel to the main algorithms. Such examples are the `muIso` [113, 114], which can determine the isolation around a muon track by accessing calorimetry information, or the `muTile` [113, 115], which utilizes hadronic calorimeter information to determine the presence of low-energy muons, typically interesting for B-physics searches. These algorithms are not discussed further on.

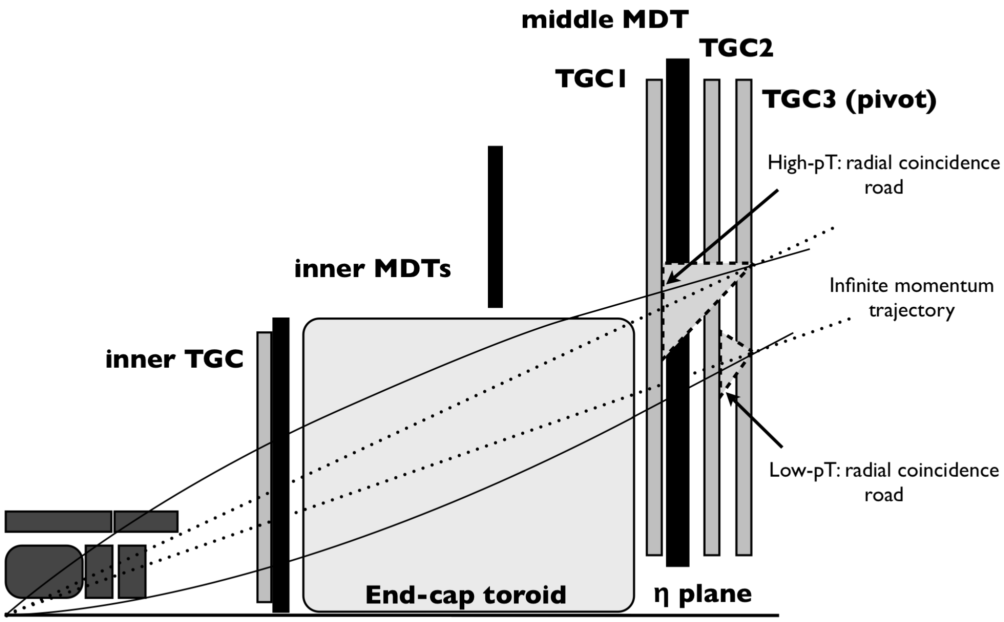

Figure 3.2: *Illustration of the TGC trigger at L1 identifying low-p_{T} and high-p_{T} tracks at the radial (bending) plane.*

The standalone track algorithm **-** `muFast`

Among the various algorithms at L2, `muFast` [111, 112] is the first algorithm that is invoke and only uses hit information obtained from the Muon Spectrometer, specifically from the RPCs, TGCs and the MDTs. For the barrel region the reconstruction steps are the following:

- **Pattern recognition:** Based on the Region-of-Interest found by the L1 trigger, a pattern recognition algorithm is ran. At first the pattern recognition is applied on RPC hits and determines a road around the candidate muon trajectory. This result serves as input to the MDT pattern recognition where hits not associated with the muon trajectory are rejected (background hits).
- **Straight line fit:** At each MDT station, a straight-line track fit is performed based on the tubes that were selected by the pattern recognition. The drift-time measurements are exploited and the independent fits provide up to three precision points, one at each MDT layer, taken from the middle of the straight-line tracks. The curvature of the track and its sagitta (s) is estimated based on these precision points.
- p_{T} **assignment:** Following the sagitta measurement, the p_{T} of the track is found with pre-computed LUTs, hence avoiding time-consuming fit methods. The LUTs are basically an $\eta - \phi$ map which, assuming that tracks originate from the nominal interaction point, follows the relation:

$$\frac{1}{s} = A_0 \cdot p_{\mathrm{T}} + A_1 \ , \tag{3.1.1}$$

  where A_0 depends on the Muon Spectrometer alignment and the magnetic field of the toroid, and A_1 corrects for the energy loss in the calorimeters. Both parameters are estimated from Monte Carlo and can, naturally, vary for different $\eta - \phi$regions.

A modified approach is followed for the end-cap regions with the main difference being in the computation of the track's p_{T}. Equation 3.1.1 is only valid in case of a homogeneous field where the trajectory in the plane perpendicular to the field can be considered circular. This is not the case for magnetic field in the end-caps, i.e. the trajectory is not a helix. Two angles are defined for estimating the p_{T}. The angle α for low-p_{T} tracks, which is defined as the angle between the direction of the muon track (slope) in the middle layer MDTs and the direction of an infinite momentum track. The angle β for high-p_{T} tracks, which is defined as the angle formed by the inner MDT track and the middle MDT track. In each case, the p_{T} is obtained from LUTs which are based on the following linear relation:

$$\frac{1}{p_{\mathrm{T}}} = A_x \cdot x + B_x, \ , \tag{3.1.2}$$

where x is either α or β. The parameters A_x and B_x depend on the position of the track and are extracted from Monte Carlo. Finally, the output of `muFast` is a list of features including the track's coordinates and its transverse momentum. These are then used by hypothesis algorithms which form a decision (accept or reject) for the event (see section 2.3.6).

***The combined track algorithm* - `muComb`**

The `muComb` algorithm combines the tracks found in the Muon Spectrometer with the ones found by the Inner Detector. This gives good rejection power on muons that originate from decaying-in-flight particles (e.g. $\pi^+ \to \mu\nu$ or $K^+ \to \mu\nu$) and reduces the amount of fakes that originate from cavern background.

The reconstruction procedure of `muComb` requires that both a Muon Spectrometer and an Inner Detector track exist. For the former, the track is already calculated by the `muFast` algorithm that precedes, while for the latter the result is obtained from the `IDSCAN` algorithm [113]. The `IDSCAN` algorithm receives the three-dimensional space points from the Pixel and the SCT detectors as input and performs the following tasks:

- **z-finder:** Initially, the algorithm estimates the z-position of the primary vertex. This is done in three steps. Firstly, the observed hits are divided in ϕ-windows and hit pairs are made for each window. Secondly, the hit pairs are extrapolated to the beam line and their z-position is put in a histogram. Finally, the z value is extracted from the histogram by integrating the region with the most entries over all the ϕ windows.
- **Hit Filter:** The algorithm identifies clusters of hits (groups) in an $\eta - \phi$ grid by considering all those that are related with tracks originating from the estimated z-position. During this process, hits that may originate from pile-up or noise are effectively filtered out. For a group to be considered, hits must be found in multiple layers of the SCT and Pixel detectors.
- **Group Cleaner:** At this stage the groups are cleaned from duplicated hits and possible noise. Subsequently, track candidates are formed. Each triplet of hits is considered as a candidate and an initial estimate of its p_{T}, ϕ_0 and d_0 is made. After applying certain quality cuts groups of candidates are made.
- **Track Fitter:** The last step is to run the fitting algorithm on the track candidates. The fit is performed by the Kalman-filter fitter [116, 117, 118] and returns the space points of the track, the relevant track parameters and the error matrix.

The `muComb` algorithm combines the information obtained from the Muon Spectrometer and the Inner Detector. It first extrapolates tracks, from each of the two sub-detectors, to a common virtual surface: a cylinder around the beam-line at the entrance of the Muon Spectrometer. Initially, a pre-selection is performed on the Inner Detector tracks based on spatial matching with the `muFast` tracks. The matching windows are optimized with the help of Monte Carlo simulated samples. Subsequently, each pre-selected track is combined with the standalone track and a p_{T} estimate is made. The p_{T} is in fact a resolution-weighted average. For each combination a χ^2 of the fit is obtained and the one with the minimum value is considered to be the best candidate.

3.1.3 The EF Muon Trigger

At the EF level the trigger is able to run a complete track reconstruction within the time window available for a decision. As a result, the algorithms are in fact wrappers of the actual offline reconstruction software, modified to be able to run on the Trigger system. Two main algorithms exist: the `TrigMuonEF` and the `TrigMuGirl` [113, 119].

The outside-in algorithm - `TrigMuonEF`

The `TrigMuonEF` algorithm provides complete track reconstruction by running four sequential steps: the `SegmentFinder`, the `TrackBuilder`, the `Extrapolator` and the `Combiner`. At each step, the corresponding offline reconstruction algorithm runs based on either the `MOORE` [120] or the `MuID` [121] reconstruction software.

`MOORE` is responsible for reconstructing the tracks in the Muon Spectrometer. It identifies regions with hit activity in both MDTs and trigger chambers and applies a pattern recognition algorithm. Subsequently a track fitting procedure is performed on the selected hits. In addition, it takes energy losses from traversing the calorimeter, as well as Coulomb scattering effects into account. The final reconstructed track is expressed with respect to its entry point in the Muon Spectrometer. Within the `TrigMuonEF` implementation the above tasks are performed by the `SegmentFinder` and the `TrackBuilder`.

On the other hand, `MuID` is responsible for associating tracks found by `MOORE` with tracks found in the Inner Detector. Calorimeter information is used as well. At first, the algorithm refits the Muon Spectrometer track such that it is expressed with respect to the production vertex. These tracks are then matched with Inner Detector tracks and a combined fit is performed to all successful matches. The `TrigMuonEF` implementation wraps the above functionality in the `Extrapolator` and the `Combiner` steps.

An important advantage of the `TrigMuonEF` is its ability to run in both “full scan” and “seeded” mode. The first is practically the same as the offline reconstruction where the complete detector information is available. In the second mode, the EF algorithms are only ran on identified RoIs that seed the EF. The seeding typically comes from the L2 trigger, however for debugging purposes it may also be provided by the L1 trigger. Due to the step-wise procedure that begins at the Muon Spectrometer and extrapolates to the Inner Detector, the `TrigMuonEF` can be seen as an “outside-in” reconstruction strategy.

The inside-out algorithm - `TrigMuGirl`

Similar to the `TrigMuonEF`, the `TrigMuGirl` algorithm is also based on the offline reconstruction software of `MuGirl`. The algorithm begins with track candidates found in the Inner Detector. Those tracks are then extrapolated to the Muon Spectrometer and the algorithm searches for hits in the vicinity of the estimated trajectory. Segments are constructed from the found hits and are then used to improve the extrapolated track. The final muon track is estimated by a global fit on the initial Inner Detector track and the respective Muon Spectrometer hits. The `TrigMuGirl` algorithm is seeded by Inner Detector tracks and as a result it must be based on the result of the L2 combined algorithm. This implementation of the Event Filter, although initially considered for first analyses, is not used in this thesis and thus not discussed further on.

3.2 Performance of the muon trigger with the first data

The first proton-proton collisions at a 7 TeV center-of-mass energy were delivered by the LHC to the ATLAS detector in early 2010. Up until the end of July 2010, the luminosity of the beams was low enough, reaching a peak of just $3 \cdot 10^{30} cm^{-2} s^{-1}$, to allow the trigger system to apply only a minimal rejection of events. This had the advantage of establishing an inclusive muon sample with minimum kinematic biases, which is well suited for testing the performance of the trigger.

3.2.1 Data sample and selection of muons

In order to accommodate the changes that may take place during the data-taking, each run in ATLAS belongs to a period (A through I, for 2010) and a sub-period (numerically defined within a period). Each period corresponds to a number of data-taking runs in which the accelerator, the trigger of the detector and the detector as a whole were left in the same configuration. The data used in this section of the thesis are obtained from period B up to period D1. The selected events are required to be recorded with all the Muon Spectrometer and Inner Detector components in operation and in addition with the magnetic fields of both the solenoid and the toroid magnets at their nominal values. The total integrated luminosity under these conditions is estimated at about 50 nb^{-1}, as shown in table 3.1.

Period	$\int \mathcal{L}dt$ (nb^{-1})	**Date (in 2010)**
B (1-2)	9.2	23^{rd} April - 17^{th} May
C (1-2)	9.6	17^{th} May - 5^{th} June
D1	30.9	27^{th} June - 1^{st} July
All Periods	49.70	

Table 3.1: *Total integrated luminosity registered by ATLAS for the data periods of interest.*

Event selection

The performance of the trigger is tested on a muon enriched sample that is collected with minimal kinematic biases introduced. At the trigger level, events are selected based on a muon "full-scan" trigger that follows the chain:

$$\texttt{L1\_MBTS\_2} \rightarrow \texttt{EF\_mu4\_MSonly\_MB2\_noL2\_EFFS}\,.$$

The `L1_MBTS_2` item is a Minimum Bias trigger based on sets of scintillators that are placed next to the cryostats of the Liquid Argon calorimeter end-caps, covering the region of $2.0 \leq |\eta| \leq 3.8$. The only requirement for acceptance is to have at least two independent signals in each end-cap scintillator set. Effectively, this trigger fires when collision events take place at the time of an expected bunch-crossing, thus it reduces the rate of non-collision background events. After the acceptance of the L1 item, the event is evaluated by the Event Filter, entirely bypassing L2 processing. At the EF level, the `TrigMuonEF` algorithm is applied to find candidate muon tracks within the full coverage of the Muon Spectrometer. Thus, it is not seeded by an RoI and it doesn't try to combine tracks with the Inner Detector. Kinematically, the EF algorithm introduces as little bias as possible with no directional cuts applied and with the p_{T} thresholds adjusted at the lowest expected transverse momenta for muons originating from the interaction point[1]; the actual η dependent thresholds are shown in table 3.2.

$\lvert\eta\rvert$ **bin**	p_{T} **threshold (GeV)**
$[0.00, 1.05]$	3.0
$(1.05, 2.50]$	2.5

Table 3.2: *Event Filter p_{T} thresholds for the trigger used in the selection of the muon-rich sample. Numbers taken from [122].*

In order to reject possible cosmic contamination, further refinement is done by requesting the reconstruction of a primary vertex. In addition, this vertex must have its z-position within 150 mm from the nominal interaction point ($z_{PV} < 150mm$) and at least three tracks must be associated with it ($N_{tracks} \geq 3$).

Muon selection

Offline reconstructed muons which are considered for the final event sample must be successfully combined from a Muon Spectrometer and an Inner Detector track, i.e. those muons defined as "combined" by the `MuID` reconstruction software are used. In addition, for a combined muon to be included it must satisfy all the following requirements:

- $p > 4$ GeV and $p_{\mathrm{T}} > 2.5$ GeV, which is the minimum requirement for a muon that has successfully traversed the calorimeters and has reached the Muon Spectrometer. This way possible contamination with fakes, originating by combining an Inner Detector track with a fake Muon Spectrometer track, is reduced.
- Number of hits in the SCT and Pixel layers: $N_{SCT} > 5$ and $N_{Pixel} > 0$, respectively. With these requirements we establish that the track is built from information from all the silicon detectors, assuring a good Inner Detector track quality.
- The matching between the Muon Spectrometer track and the Inner Detector track gives $\chi^2 < 50$, minimizing the ambiguity on the compatibility of the Inner Detector and Muon Spectrometer track components. The large threshold is justified by the fact that this is the beginning of the data-taking period and therefore large deviations may occur due to uncalibrated algorithms.

3.2.2 Performance measurements

The performance of both the L1 trigger and the HLT is examined primarily on their selection efficiency. For the purpose of this analysis the efficiency is defined as the ratio of muons accepted by the trigger (n_{trig}) over the total number of muons (n_{tot}). The n_{tot} is taken as all the muons passing the selection explained in the previous section and n_{trig} is taken as those that have are matched to a trigger object satisfying the respective trigger requirements; the n_{trig} is a subset of n_{tot}. Hence the following holds:

$$\epsilon = \frac{n_{trig}}{n_{tot}} \ . \tag{3.2.1}$$

[1] Muons produced at the interaction point, able to traverse the calorimeters and reach the Muon Spectrometer must have $p \geq 3$ GeV at $\eta \approx 0$ [93].

The efficiency depends on the selection requirements applied at the trigger level. The usual implementation is to simply accept or reject events based on their transverse momentum compared to a given threshold. The distribution of the efficiency with respect to the transverse momentum is usually referred to as the *turn-on curve* of a trigger. The transverse momentum used, is typically taken from the offline reconstruction as this is considered to be closer to the "true" value.

For a hypothetical trigger that fires above a certain p_{T} threshold (p_{T}^{thres}), the efficiency described in relation 3.2.1, in an ideal case, will follow a step-function, namely it will return an efficiency of 1 for $p_{\mathrm{T}} \geq p_{\mathrm{T}}^{thres}$ and 0 for $p_{\mathrm{T}} < p_{\mathrm{T}}^{thres}$. However, due to resolution effects the measured p_{T} at the trigger level may be smeared with respect to the offline reconstructed p_{T}, therefore altering the turn-on curve. Assuming that the resolution effects induce a gaussian behavior, the expected distribution would be of the following form:

$$f(x) = 0.5\alpha \left(1 + Erf\left(\frac{x-\beta}{\sqrt{2}\gamma}\right)\right) \ , \qquad (3.2.2)$$

where x is the selection parameter (p_{T}) and $Erf(y)$ is a gaussian error function:

$$Erf(y) = \frac{2}{\sqrt{\pi}} \int_0^y e^{-t^2} dt \ . \qquad (3.2.3)$$

The constant parameters are: α, which provides a measure of the plateau of the efficiency, namely the efficiency at value of the p_{T} well above the trigger threshold; β, the actual threshold of the trigger; γ, the slope in the turn-on region which is gives a measure of the smearing as it is equivalent to the gaussian σ. Naturally, additional effects that are not simply described by a gaussian resolution may still be present and often they may not be described simply by the above equation. In the following, we focus mainly on the result of the plateau measurement to illustrate the performance of trigger.

Level-1 efficiency

The efficiency of the L1 trigger is evaluated, with the muon sample selected as described in section 3.2.1, for the following trigger items: the `L1_MU0` which is configured with a low-p_{T} logic but with an 'open' road, the latter does not specify a road width in which coincidences are counted but it takes into account all the hits that fall within the same trigger tower ($\eta \times \phi \approx 0.1 \times 0.1$) thus maximizing acceptance and minimizing the p_{T} bias; the `L1_MU6` configured with a low-p_{T} logic accepting muons with p_{T} of at least 6 GeV; the `L1_MU10` configured also with a low-p_{T} logic and accepting muons with p_{T} of at least 10 GeV.

For establishing the connection between an offline reconstructed object and the trigger decision, the former is required to be matched to a corresponding trigger-level object. Only if such a match is successful and the trigger-level object has satisfied the trigger threshold requirements, the offline muon is considered a triggered muon. The matching itself is based on a $\Delta R = \sqrt{\Delta\eta^2 + \Delta\phi^2}$ metric with a cut threshold of $\Delta R \leq 0.3$. At L1, the decision is based only on Muon Spectrometer information, thus the kinematic variables of the offline reconstructed muon are taken from the Muon Spectrometer track. The turn-on curves for L1 are also created with respect to the p_{T} as measured by the Muon Spectrometer. In figure 3.3 we plot the results for the three trigger items separated in the barrel (RPC) and the end-cap (TGC) regions. Minimum Bias Monte Carlo events and single-muon Monte Carlo[2] events are also overlaid with the data, with the single-muon sample being generated with muons of

[2]The single-muon Monte Carlo events are simply muons that are generated from the nominal interaction point, distributed uniformly in $\eta - \phi$ and at different p_{T} intervals.

Trigger Item	Data (%)		MC (%)	
	RPC	TGC	RPC	TGC
`L1_MU0`	75.3 ± 0.2	94.2 ± 0.2	79.2 ± 0.8	96.4 ± 0.3
`L1_MU6`	75.8 ± 0.3	73.2 ± 0.4	78.7 ± 1.1	91.8 ± 1.1
`L1_MU10`	74.2 ± 0.5	75.4 ± 0.9	74.7 ± 1.9	93.5 ± 1.7

Table 3.3: *Plateau efficiencies for L1 trigger items as estimated by fitting the function 3.2.2 on the turn-on distributions. All uncertainties are statistical only and are obtained from the fit.*

$p_{\mathrm{T}} > 6$ GeV. With the function described in equation 3.2.2, each of the curves provides an estimate of the efficiency plateau at each trigger item; the results are shown in table 3.3.

A number of observations can be made. First of all, the generally lower efficiency observed in the RPCs, compared to ones in the TGCs, is because of the reduced geometrical acceptance of the former. In the barrel region, primarily due to the cabling hole at approximately $\eta \approx 0$, the acceptance is estimated to be about 80%, while in the end-cap regions it is 95%. The reason why the offline reconstruction still finds these muons is because of optimized reconstruction which includes extensive information, by taking into account the Inner Detector or even in certain cases the Calorimeters, and can successfully reconstruct their tracks. Secondly, all the RPC triggers and the TGC open-road trigger show to be very close to the expected plateau limits with only a maximum of 4% difference which is accounted as detector inefficiencies. However, for the TGCs, when a road width is applied (triggers `L1_MU6` and `L1_MU10`), a large deviation from the expected acceptance is observed, an effect that is only present in the data sample. The reason for this was found to be the TGC chamber cross-talk at the direction of the strips, namely hits that could also be found in strips neighboring the actual muon track. If such a hit is found, its position may be used instead of the real track hit for defining the coincidence window in ϕ and naturally the result after counting the coincidences may differ significantly. As this effect worsens the ϕ resolution, it also has an effect in the counting of n_{sel} which depend on the matching between trigger and offline. In the end, the solution, which was also incorporated for subsequent data-taking periods, is to increase the road width in the ϕ direction, thus increasing the acceptance of the trigger. The reason that this effect does not appear in the Monte Carlo events is because the simulation is modeled with a lower cross-talk probability A detailed description of the effect along with the proposed solution and the results after the optimization of the road is presented in [123].

HLT efficiency - Standalone triggers

The performance of the HLT is first tested at the Muon Spectrometer only, i.e. the standalone triggers. We examine the efficiency of the L2 Muon Spectrometer algorithm with respect to the seeding L1 trigger item and subsequently the equivalent Event Filter algorithm with respect to the L2 selection. The L2 algorithms under consideration are: the `L2_mu4_MSonly` which is seeded by `L1_MU0`, the `L2_mu6_MSonly` seeded by `L1_MU6` and the `L2_mu10_MSonly` seeded by `L1_MU10`. Respectively for the Event Filter the `EF_mu4_MSonly`, `EF_mu6_MSonly` and `EF_mu10_MSonly` are examined. The applied thresholds for the above triggers are shown in table 3.4. Similar to what happens with the L1, the offline muons are matched with the L2 `muFast` or EF `TrigMuonEF` objects that satisfy the hypothesis criteria of the trigger algorithms and the sample of trigger-selected muons is obtained. As these algorithms are based on Muon Spectrometer information their efficiency is given with respect to the track p_{T} estimated by this sub-detector. In figure 3.4 we plot the L2 result separated in the RPC and TGC regions,

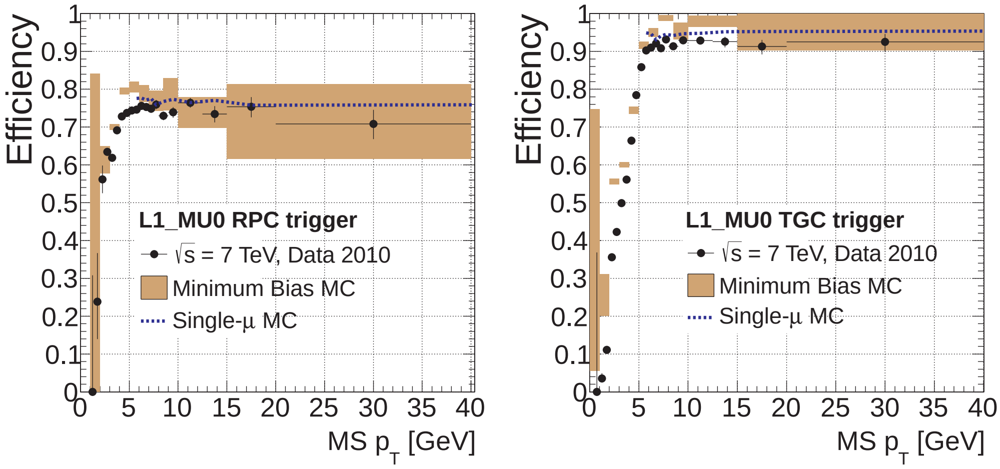

(a) *The `L1_MU0` trigger configured with a low-p_{T} logic and an 'open' road.*

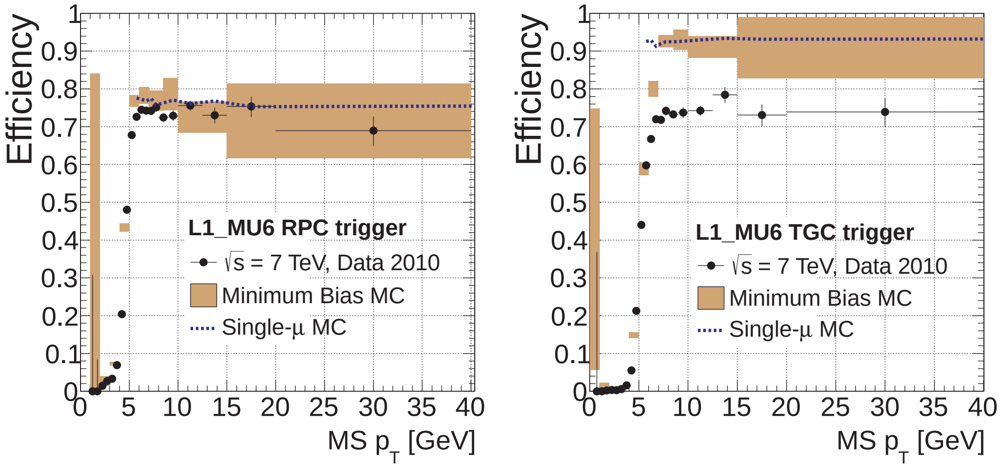

(b) *The `L1_MU6` trigger with a low-p_{T} logic applied.*

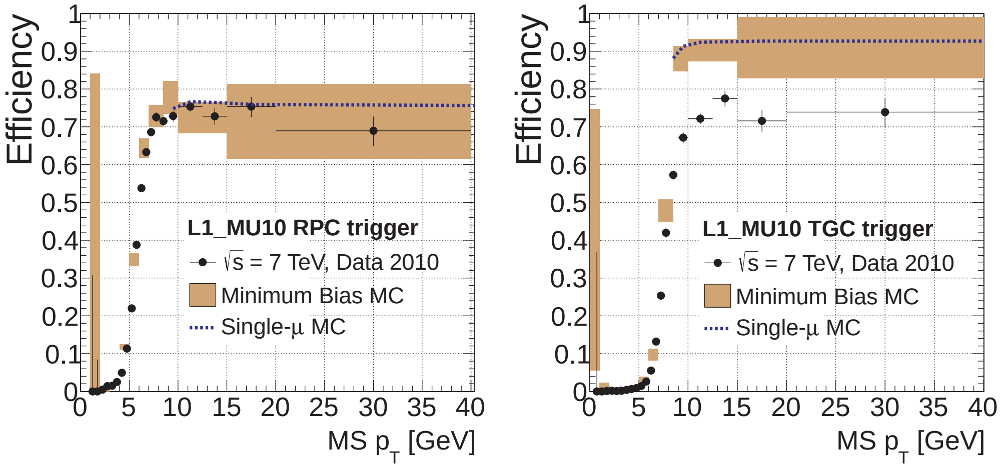

(c) *The `L1_MU10` trigger with a low-p_{T} logic applied.*

Figure 3.3: *The L1 turn-on curves for three different trigger items with a low-p_{T} configuration. The efficiency is shown with respect to the p_{T} of the offline reconstructed Muon Spectrometer track and is separated in the RPC, $|\eta| < 1.05$ region (left), and the TGC, $|\eta| > 1.05$ region (right).*

$\lvert\eta\rvert$ bin	p_{T} thresholds for L2 and EF (GeV)		
	mu4_MSonly	mu6_MSonly	mu10_MSonly
$[0.00, 1.05]$	3.0	5.4	8.9
$(1.05, 1.50]$	2.5	4.5	9.0
$(1.50, 2.00]$	2.5	4.9	8.4
$(2.00, 2.50]$	2.5	5.3	9.2

Table 3.4: *The L2 and Event Filter p_{T} thresholds applied for the three Muon Spectrometer-only triggers that are tested. Numbers taken from [122].*

since small differences between them exist especially in the estimated track p_{T}. In figure 3.5 we plot the EF results for the full detector coverage. The reason for not separating in RPC and TGC in this case is because the same algorithm is applied throughout, irrespectively of the muon's η coordinate, while in the case of the L2, differences exist in the determination of the p_{T}.

As the L2 efficiency is estimated based on the L1 selected sample, the geometrical effects are absent and the expected efficiency is closer to 100%. The same applies for the Event Filter when examined with respect to the L2. For the L2, the plateau efficiency of the turn-on curves is between 90% and 100%. The agreement between data and Monte Carlo is in general good although the data exhibit a slightly lower plateau efficiency than what the Monte Carlo anticipate. This difference is attributed to the non-optimized LUTs that were used in the early data due to the lack of knowledge with respect to the alignment of the Muon Spectrometer [124]. Another effect that is observed is that a fraction of muons below the threshold are successfully passing the `L2_mu6_MSonly` and `L2_mu10_MSonly` trigger requirements. For the TGCs, where the effect is more pronounced, it is attributed to the complex and inhomogeneous magnetic field in the end-caps, especially in the transition regions which worsens the p_{T} resolution [124]. Additionally, and what is mainly the case for the RPCs, mis-matching of muons may lead to such effects.

For the Event Filter, the first important observation is that the turn-on builds faster that in the case of the L2 as a result of the better resolution that can be achieved. Additionally, the plateau efficiency is reaching the expected 100% and is well in agreement with the Monte Carlo. Lastly, the effect with the lower-than-threshold muons is again observed although less severe in terms of efficiency and with lower statistics, practically indicating the better rejection power at the Event Filter.

HLT efficiency - Combined triggers

At the next step, we test the performance of the algorithms that are based on combination of the Inner Detector and Muon Spectrometer track. Namely, the `L2_mu4`, `L2_mu6` and `L2_mu10` at the L2, and the `EF_mu4`, `EF_mu6` and `EF_mu10` at the Event Filter. In each case, the relevant L2 algorithm (`muComb`) is tested with respect to its seed, the L2 Muon Spectrometer algorithm (`muFast`) and then the Event Filter combined algorithm is tested with respect to the L2 combined algorithm. As these algorithms are based on the combined track the turn-on curves are estimated with respect to the offline reconstructed combined track. The thresholds applied in each case by the hypothesis algorithms are shown in table 3.5.

Figure 3.6 shows the resulting efficiency plots for the L2 and the Event Filter. Given that the reconstruction procedure is equivalent for both RPC and TGC regions no distinction is made. It is evident from the plots that the L2 achieves the expected plateau very close to

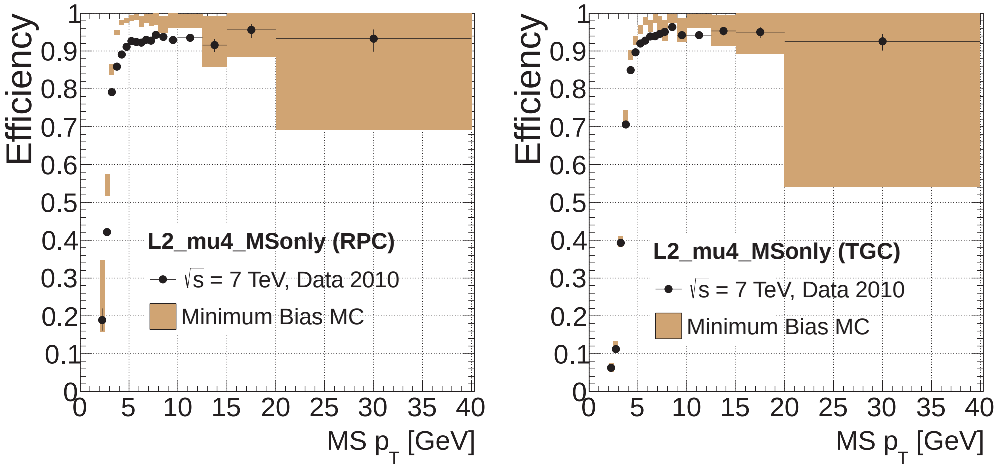

(a) *The* `L2_mu4_MSonly` *trigger seeded by* `L1_MU0`*.*

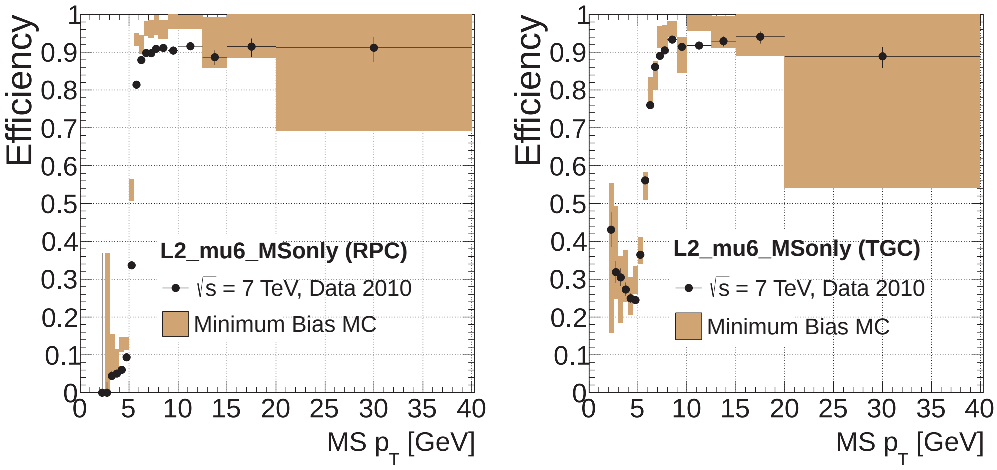

(b) *The* `L2_mu6_MSonly` *trigger seeded by* `L1_MU6`*.*

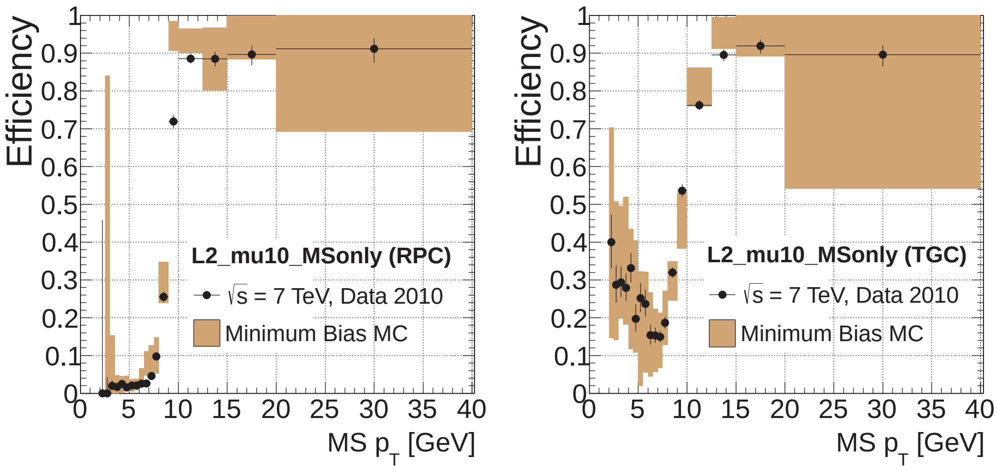

(c) *The* `L2_mu10_MSonly` *trigger seeded by* `L1_MU10`*.*

Figure 3.4: *The L2 RPC (left) and TGC (right) turn-on curves for* `L2_mu4_MSonly`*,* `L2_mu6_MSonly` *and* `L2_mu10_MSonly`*. The efficiency is estimated relative to the L1 trigger items and with respect to the offline Muon Spectrometer track* p_T*.*

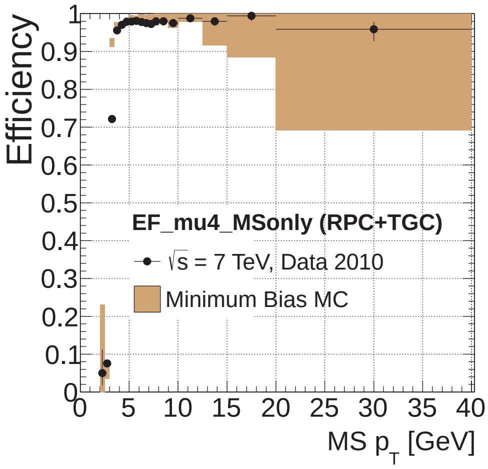

(a) *The EF_mu4_MSonly trigger.*

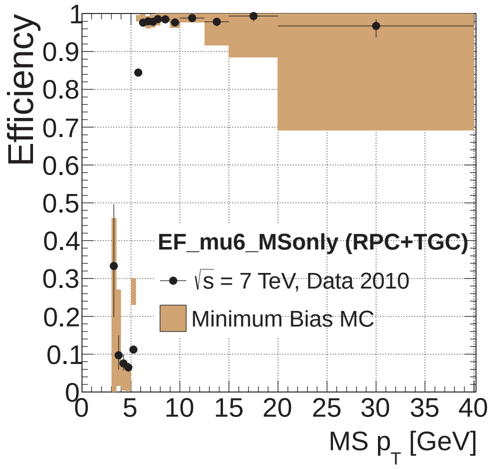

(b) *The EF_mu6_MSonly trigger.*

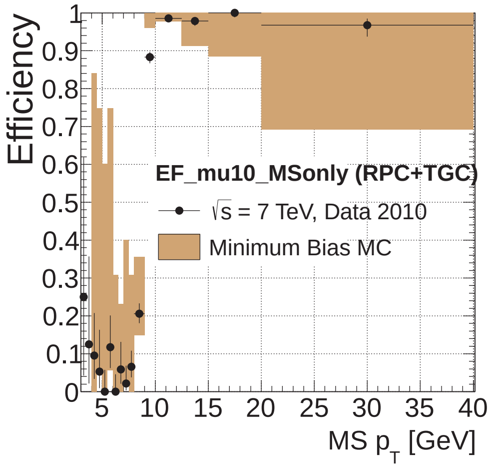

(c) *The EF_mu10_MSonly trigger.*

Figure 3.5: *The EF turn-on curves for* ***EF_mu4_MSonly****,* ***EF_mu6_MSonly*** *and* ***EF_mu10_MSonly*** *trigger . The efficiency is estimated relative to the L2 trigger and with respect to the offline Muon Spectrometer track p_T.*

$\lvert\eta\rvert$ **bin**	p_T **thresholds (GeV)**					
	mu4_MSonly		mu6_MSonly		mu10_MSonly	
	L2	**EF**	**L2**	**EF**	**L2**	**EF**
$[0.00, 1.05]$	3.0	3.93	5.8	5.88	9.8	9.77
$(1.05, 1.50]$	2.5	3.91	5.8	5.81	9.5	9.67
$(1.50, 2.00]$	2.5	3.88	5.8	5.78	9.6	9.62
$(2.00, 2.50]$	2.5	3.88	5.6	5.76	9.7	9.57

Table 3.5: *The L2 and Event Filter p_T thresholds applied for each of the combined triggers that are tested. Numbers taken from [122].*

100% efficiency, well in accordance with the Monte Carlo expectation. However, for the Event Filter it is observed that the plateau does not reach this value. In fact, the turn-on curve reaches a peak at the top of the slope, but a trend, in which for higher-p_{T} values the efficiency consistently drops, is observed. This is not the same effect as the statistical fluctuations observed in figures 3.4 and 3.5. This has been attributed to the absence of the alignment constants at this level of the trigger reconstruction which leads to an erroneous measurement of the p_{T} [125].

Residual distribution and algorithm resolution

The performance of an individual algorithm can be assessed by comparing the value of the transverse momentum at the trigger level with the one measured from the offline reconstruction. We use the following residual relation:

$$r = \frac{1/p_{\mathrm{T}}^{offline} - 1/p_{\mathrm{T}}^{trigger}}{1/p_{\mathrm{T}}^{trigger}}, \tag{3.2.4}$$

where the $p_{\mathrm{T}}^{offline}$ is the offline reconstructed transverse momentum and $p_{\mathrm{T}}^{trigger}$ is the transverse momentum as measured by the respective trigger algorithm. The residual distribution typically has a gaussian shape, as for example in figure 3.7 where the L2 `muComb` p_{T} residual is shown for the range of 6-8 GeV. Fitting a gaussian function on the resulting plots determines the mean of the residual distribution while the sigma provides the achieved resolution of the respective trigger algorithm with respect to the offline. In figure 3.8 the resulting residual mean and resolution is shown for each of the `muFast`, `muComb` and `TrigMuonEF` algorithms. For the latter, the combined measurement is used.

The result on the residuals of the `muFast` algorithm (figure 3.8(a)) shows a significant offset of the mean of the residual for the end-cap regions, consistent in both data and Monte Carlo. This is because the measurement exhibits large tails towards negative values. These are the result of the complex and inhomogeneous magnetic field regions of the end-caps which is only approximated for the determination of a track's p_{T}. Naturally, the resolution is also affected resulting in much higher values than in the RPC. Generally, the agreement between Monte Carlo and data is observed to be good indicating that the simulation describes these effects sufficiently well. The inclusion of the combined track is expected to provide a measurement at the trigger level which is closer to the expected offline reconstructed result. The result on the `muComb` algorithm (figure 3.8(b)) shows indeed values close to zero but with large deviation at low energy muons. Nevertheless, it is evident that the achieved resolution is considerably improved The differences that are shown to exist between Monte Carlo and data, indicate the need for a better understanding of the momentum scale of the algorithms. Finally, the `TrigMuonEF` result (figure 3.8(c)) shows an even better reconstruction performance by the Event Filter which is expected as the offline and the Event Filter reconstruction share the same algorithms. It should be noted that at the EF a larger difference in the resolution is observed between Monte Carlo and data. This, as has been said, is attributed to the absence of proper calibration constants at the EF combined triggers.

3.3 Data-driven trigger efficiency measurement

Estimating the efficiency with which a trigger is selecting events, is an important step in every analysis that requires knowledge on the exact amount of collected data. In the previous section the efficiency measurements presented were estimated by counting the number of muons that were passing a given trigger threshold and comparing it with the total number of candidates.

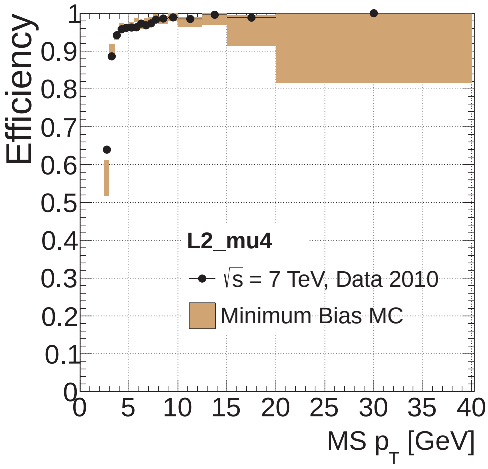

(a) *The L2_mu4 trigger.*

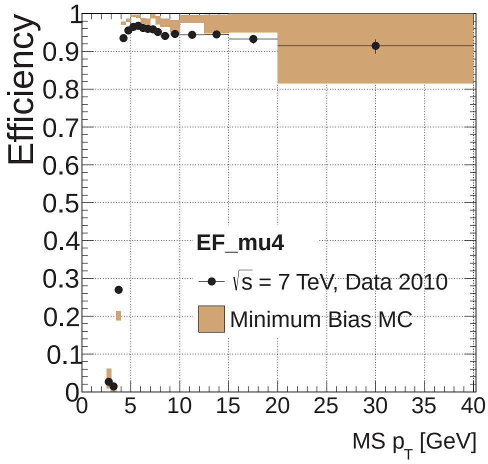

(b) *The EF_mu4 trigger.*

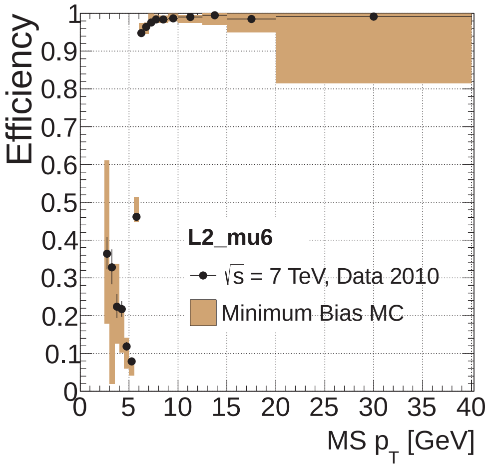

(c) *The L2_mu6 trigger.*

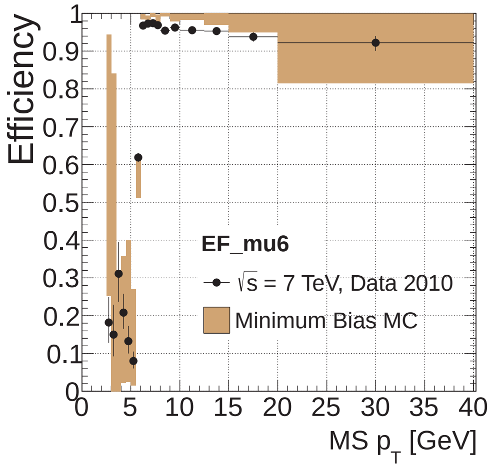

(d) *The EF_mu6 trigger.*

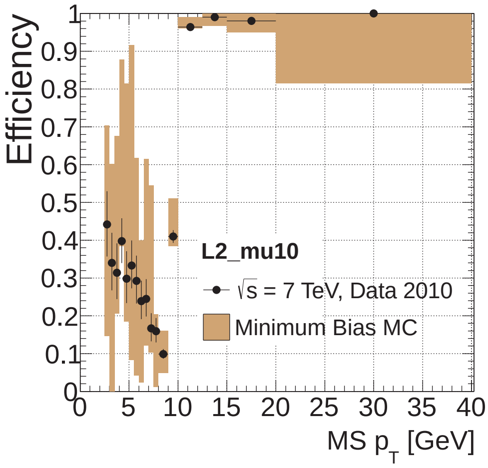

(e) *The L2_mu10 trigger.*

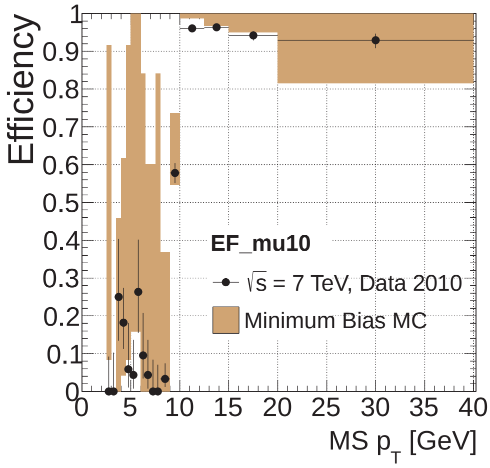

(f) *The EF_mu10 trigger.*

Figure 3.6: *The L2 and EF turn-on curves for* `mu4` *(a,b),* `mu6`*(c,d) and* `mu10`*(e,f) triggers. For the L2, the efficiency is estimated relative to the L2 Muon Spectrometer trigger and with respect to the offline combined track* p_{T}*. For the EF, the efficiency is estimated relative to the L2 combined trigger and with respect to the offline combined track* p_{T}*.*

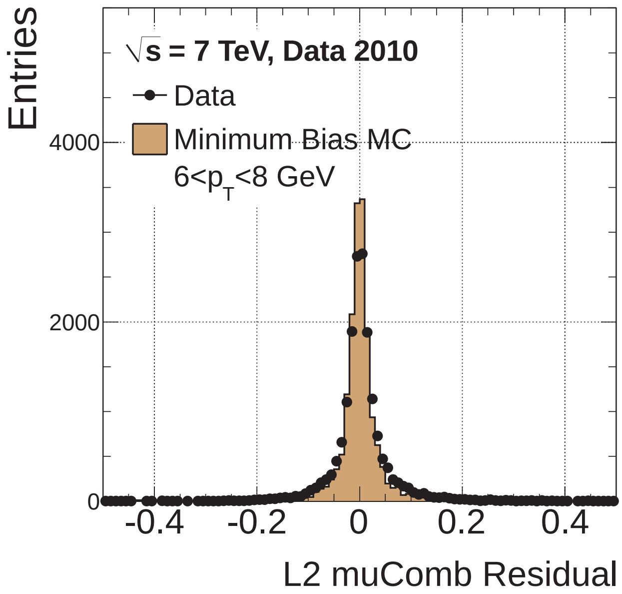

Figure 3.7: *Residual distribution of the transverse momentum calculated with equation 3.2.4 using as $p_{\mathrm{T}}^{offline}$ the measurement for the combined offline track and as $p_{\mathrm{T}}^{trigger}$ the measurement from the* `muComb` *algorithm.*

This approach, which is the easiest, is only possible when the events are unbiased from any kinematic cuts. In practice, as the instantaneous luminosity of the accelerator increases, the events that are written out are based on stricter trigger requirements and may be significantly biased. In this case, the easiest approach is to use Monte Carlo samples and apply the estimate directly to the analysis of interest. However, it is preferable to use data-driven techniques to avoid systematical uncertainties related with the simulation. Several data-driven methods exist:

- **Orthogonal triggers:** With this method the events are first selected based on a chain of algorithms A and are subsequently used to determine the efficiency of a second chain of algorithms B. For the measurement to be unbiased, A and B must be completely uncorrelated so that their efficiencies follow the relation $\epsilon_{A+B} = \epsilon_A \cdot \epsilon_B$. The following then holds:

$$N_A = \epsilon_A \cdot N_{all} \qquad \text{and}$$
$$N_{A+B} = \epsilon_B \cdot \epsilon_A \cdot N_{all} \; ,$$

  with N_{all} being the total number of events under consideration, N_A being the number of events left after using trigger A, and N_{A+B} when applying both trigger A and B. The efficiency of trigger B is then simply given by:

$$\epsilon_B = \frac{N_{A+B}}{N_A}.$$

  An important advantage of the orthogonal triggers method is that it can be applied on complex final states that have many different physics objects as these events may easily end-up in various physics streams. An example is the $t\bar{t}$ semi-leptonic events where one can trigger on the multiplicity and the high-p_{T} of the jets and subsequently measure the single-lepton trigger efficiency.

- **Tag-and-probe:** This method relies on collecting a sample of double-object final states where these objects are of the same kind. For example, such physics processes are the

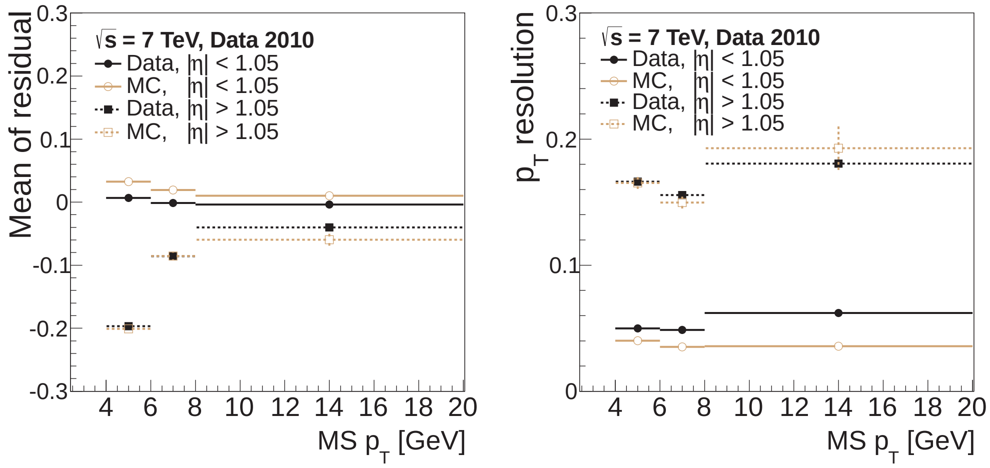

(a) *L2* `muFast` *distributions*

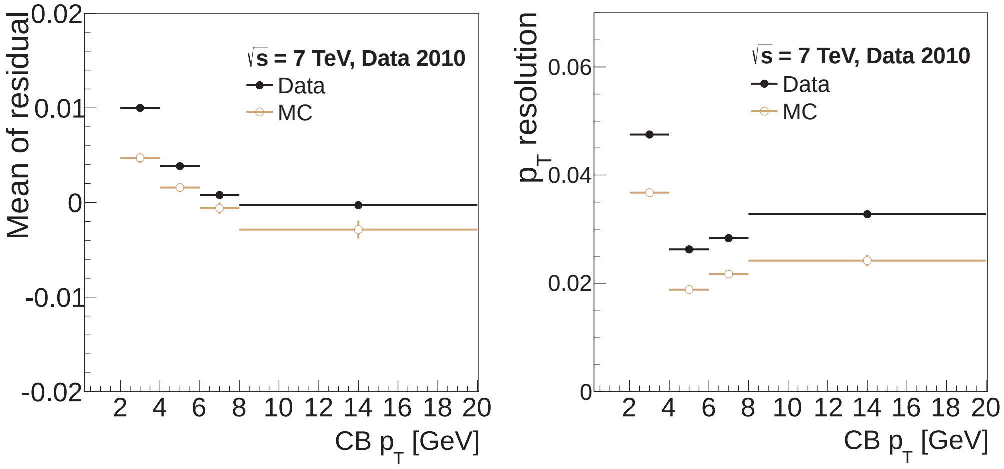

(b) *L2* `muComb` *distributions*

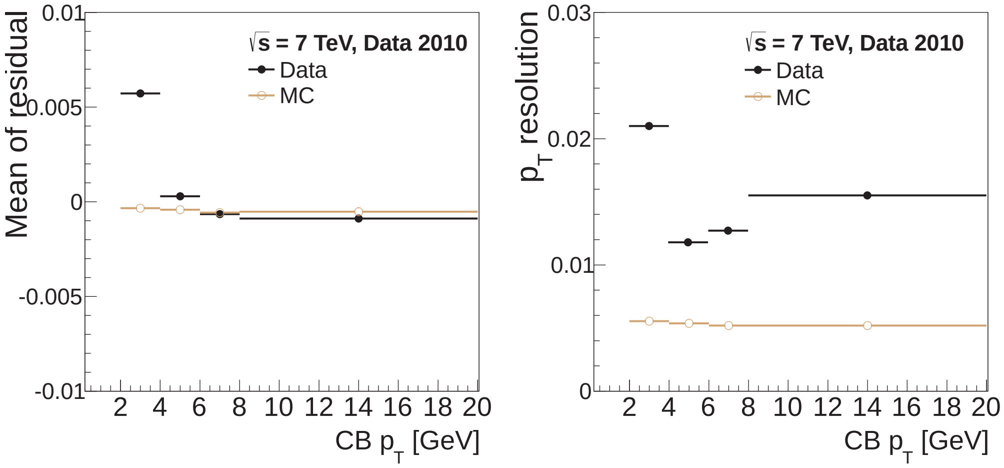

(c) *EF* `TrigMuonEF` *distributions*

Figure 3.8: *The residual mean (left) and the resolution (right) for different trigger algorithms as estimated by fitting the result on equation 3.2.4 at different* p_{T} *ranges. For the* `TrigMuonEF` *the combined track measurement is used.*

Z decay and the J/ψ decay which both result into two charged leptons which are also kinematically correlated. In this case, the signature is identified based on the two leptons and by estimating the invariant mass of the mother particle. However, only one of the leptons is used to trigger the events while the other is used to determine the trigger efficiency.

- **Bootstrap:** The bootstrap method requires the knowledge of a trigger's turn-on curve behavior, trigger A (ϵ_A), and provides an estimate on the efficiency of a second trigger, trigger B (ϵ_B), which has a higher threshold than A. Both triggers should be of the same type and events triggered by B must be triggered by A as well. The efficiency of B can be estimated with the following:

$$\epsilon_B = \epsilon_A \cdot \left[\frac{\epsilon_B}{\epsilon_A}\right],$$

where the fraction $[\epsilon_B/\epsilon_A]$ is equivalent to the ratio of events N_B/N_A and therefore is estimated by counting the corresponding event yield. Namely, those that passed trigger B, and therefore A as well, are divided by the total of those that passed trigger A. The main advantage of the bootstrap method is that it can provide an estimate of the efficiency for triggers with significantly high thresholds that would typically be used for rare physics signatures. Its reliance on the knowledge of the behavior of trigger A is important but this behavior can be determined with the use of a tag-and-probe technique.

From the above methods, the tag-and-probe is the one that is exploited the most as it uses physics signatures that are abundantly produced by the LHC. In the rest of this section this method is discussed in more detail and is applied on a dataset collected during 2010.

3.3.1 Description of the tag-and-probe method

As mentioned previously, the tag-and-probe (T&P) method is based on selecting an event sample that contains two correlated objects of the same type. Here, we apply this method to Z events that decay to two muons, namely:

$$Z \to \mu^+\mu^-.$$

These events provide energetic muons that are well isolated and kinematically very similar to muons originating from $t\bar{t}$ leptonic decays. The latter are of interest in this thesis as they are considered for the cross-section measurement presented in the next chapters.

The method can be summarized as follows. Events are selected at the trigger level by requiring the trigger, which is of interest for the measurement, to have fired; the trigger should have a multiplicity requirement of at least one and a p_{T} threshold that is consistent with what is expected from a Z decay. At the offline level, two muons of opposite charge are required to be present, both satisfying the same set of kinematic cuts. Combined, they should have an invariant mass within a mass-window around the true Z mass. If di-muon invariant mass is compatible with the Z mass, one of the muons is required to have fired the trigger and is then flagged as the 'tag'. The fact that events are selected with the trigger that is examined ensures that at least one of the muons fulfills this requirement. Subsequently, the second muon is considered as the 'probe' and the trigger efficiency can be examined by checking whether it has fired the trigger as well.

Mathematically we can formulate the method by forming two event samples. The first sample is after the tag selection where at least one muon is required to have passed the trigger:

$$N_{1\mu} = \epsilon_{1\mu}^{trig} \cdot \epsilon_{sel} \cdot N_{all}, \tag{3.3.1}$$

where ϵ_{sel} is the selection efficiency of the events based on the offline cuts and includes the reconstruction efficiency of the Z boson, $\epsilon_{1\mu}^{trig}$ is the efficiency with which the trigger selects these events by requiring at least one muon to have fired, and N_{all} is the total number of events under consideration.The second sample is after requiring that the probe muon has also passed the trigger, thus:

$$N_{2\mu} = \epsilon_{2\mu}^{trig} \cdot \epsilon_{sel} \cdot N_{all}, \tag{3.3.2}$$

where $\epsilon_{2\mu}^{trig}$ is again the efficiency with which these events are triggered based on both muons having passed the trigger requirements.

The efficiencies $\epsilon_{1\mu}^{trig}$ and $\epsilon_{2\mu}^{trig}$ are not equivalent but are related to the absolute trigger efficiency (ϵ_{trig}), which is of interest as explained in the next paragraph. Seen as a probability per event, in which two muons exist (μ_1 and μ_2), the parameters $\epsilon_{1\mu}^{trig}$, $\epsilon_{2\mu}^{trig}$ can be written in the following form:

$$\begin{aligned} P_{1\mu} &= P(\mu_1, \bar{\mu_2}) + P(\bar{\mu_1}, \mu_2) + P(\mu_1, \mu_2), \\ P_{2\mu} &= P(\mu_1, \mu_2). \end{aligned} \tag{3.3.3}$$

where $P(\mu_1, \bar{\mu_2})$ is the probability with which μ_1 is accepted by the trigger when μ_2 is rejected, $P(\bar{\mu_1}, \mu_2)$ where μ_1 is rejected while μ_2 is accepted, and $P(\mu_1, \mu_2)$ is the probability where both are accepted. These can be written as follows:

$$\begin{aligned} P(\mu_1, \bar{\mu_2}) &= P(\mu_1) \cdot [1 - P(\mu_2)], \\ P(\bar{\mu_1}, \mu_2) &= P(\mu_2) \cdot [1 - P(\mu_1)], \text{ and} \\ P(\mu_1, \mu_2) &= P(\mu_1) \cdot P(\mu_2). \end{aligned} \tag{3.3.4}$$

where $P(\mu_1)$ and $P(\mu_2)$ are the probabilities of μ_1 or μ_2 respectively to pass the trigger requirement and which are equivalent. Therefore, following from the equations 3.3.3 and 3.3.4 we can write:

$$\begin{aligned} P_{1\mu} &= \epsilon_{1\mu}^{trig} = 2 \cdot \epsilon_{trig} - \epsilon_{trig}^2, \\ P_{2\mu} &= \epsilon_{2\mu}^{trig} = \epsilon_{trig}^2. \end{aligned} \tag{3.3.5}$$

By substituting the result of the equations 3.3.5 to equations 3.3.1 and 3.3.2 we have the following relation for the absolute trigger efficiency:

$$\epsilon_{trig} = \frac{2 \cdot N_{2\mu}}{N_{1\mu} + N_{2\mu}}. \tag{3.3.6}$$

The result of equation 3.3.6 is equivalent with what we would obtain by simply counting the rate of probes that successfully pass the trigger criteria over the total number of probes, namely:

$$\epsilon_{trig} = \frac{N_{\text{triggered probes}}}{N_{\text{all probes}}}. \tag{3.3.7}$$

In this case, it should be taken into account that when a probe is successful in firing the trigger, the event has two possible permutation of tag and probe muons. Both of these cases must be considered in order to avoid the bias due to the selection of the tag.

3.3.2 Data sample and event selection for the T&P

The data sample used for performing this measurement is not the same as the one in section 3.2.1. A number of interventions were made after the first data were collected, which improved the performance of the trigger system. In addition, the higher luminosity in later periods provided a larger number of events in subsequent periods. The data sample that is used contains events that were recorded with the detector fully operational from period E4 up to and including the end of period F, and is estimated to a total of 2.04 pb^{-1}; see table 3.6.

Period	$\int \mathcal{L}dt$ (nb^{-1})	Date (in 2010)
E (4-7)	510	6^{th} August - 18^{th} August
F (1-2)	1530	19^{th} August - 30^{th} August
All Periods	2040	

Table 3.6: *Total integrated luminosity registered by ATLAS for the data periods included in the T&P analysis in this thesis.*

Event selection

The selection of events for the T&P analysis starts by requiring the events to have passed the `EF_mu10_MSonly` trigger chain. This is also the trigger for which the efficiency will be measured as it was chosen as the primary trigger for the $t\bar{t}$ analyses that involve a muon in their final states. In the following chapters of this thesis (where the $t\bar{t}$ cross-section measurement is discussed), this trigger was used for the periods from E4 until F. A positive decision on the `EF_mu10_MSonly` implies that the corresponding L2 trigger (`L2_mu10_MSonly`) and L1 item (`L1_MU0`) have also given a positive response, the final efficiency is therefore cumulative for all the trigger levels.

At the offline level, for identifying the Z decays, each event must successfully pass the following requirements:

- A primary vertex reconstructed with at least three tracks associated with it in order to reject the non-collision background.
- The number of accepted reconstructed muons must be exactly two ($N_\mu = 2$) and they must be of opposite charge.

Not all muons are considered in the above selection. Each muon must fulfill the following requirements:

- Muons must be reconstructed by the `MuID` reconstruction and be classified as *"tight"* with a combined track. The "tight" classifications requires the muon to fulfill the logical `OR` of having a `MuID` combined track, having a `MuID` standalone track for when $|\eta| > 2.5$ and having a `MuGirl` extended track. The explicit requirement in our selection for a combined track refines this definition, aiming to increase the purity of the final sample. The muon reconstruction and its track quality definitions are also discussed in the following chapter, in section 4.1.2, and in more detail under the context of the $t\bar{t}$ cross-section analysis.
- The quality of the Inner Detector track of the combined muon must also be ensured. This requires a set of cuts to be applied, namely:
  i. A hit on the B-layer of the Inner Detector is required, unless the muon track has passed an un-instrumented or dead-area of this sub-detector.

ii. The number of hits in the Pixel layers plus the number of crossed dead pixel sensors must be $N_{Pixel} + N_{dead,Pixel} > 1$.
iii. The number of hits in the SCT layers plus the number of crossed dead SCT sensors must be $N_{SCT} + N_{dead,SCT} > 5$.
iv. The number of Pixel and SCT layers traversed by the track but with no hits (holes) must be, $N_{holes,Pixel} + N_{holes,SCT} < 2$.
v. Lastly, for the region that is covered by the TRT, if we define:

$$N_{TRT} = N_{TRT}^{hits} + N_{TRT}^{outliers},$$

then we require that:

$$\text{for } |\eta| < 1.9 : N_{TRT} > 5 \text{ and } \frac{N_{TRT}^{outliers}}{N_{TRT}} < 0.9,$$
$$\text{for } |\eta| \geq 1.9 : \frac{N_{TRT}^{outliers}}{N_{TRT}} < 0.9 \text{ only if } N_{TRT} > 5.$$

- The transverse momentum of the muon must be $p_{\mathrm{T}} > 20$ GeV. This requirement puts the muon far from the turn-on slope and within the expected plateau of the trigger's turn-on curve.
- It should lie within $|\eta| < 2.5$, which is the acceptance of the Inner Detector.
- Lastly, the muon should be well isolated and this is ensured by the following requirements:
  i. The calorimetric and tracking isolation parameters should both be less than 4 GeV. The definition of these parameters stipulates that a cone with an opening angle of 0.3 in $\eta - \phi$ space around the muon track is defined. For the calorimetric isolation, the energy deposited on the calorimeter within the cone and excluding the muon itself should be less than 4 GeV. Similarly, the tracking isolation, estimates the scalar sum of the p_{T} of all tracks within the cone and, excluding the muon, requires that is less than 4 GeV. Both isolation variables are also discussed in the next chapter in section 4.1.2 as they are also used for the cross-section analysis.
  ii. The distance of the muon with respect to the closest reconstructed jet with a $p_{\mathrm{T}} > 20$ GeV must be $\Delta R(\mu, \text{closest jet}) > 0.4$. Reconstructed jets are created with the `anti-`$k_{\perp}$ [126] using a jet size of 0.4 and are calibrated with the `EMJES` scheme [127]. The jet reconstruction and calibration is discussed in greater detail in the next chapter in section 4.1.3.

The definitions for both muons and jets in this selection are motivated by the selection that is applied for the $t\bar{t}$ cross-section measurement that is described in the following chapters.

After identifying the muon sample, the tag and the probe muons are specified

- **Tag:** For an offline reconstructed muon to be considered a tag, it must be matched to a trigger object that satisfies the `EF_mu10_MSonly` threshold. The matching requirement is $\Delta R < 0.3$.
- **Probe:** For the second muon in the event to be considered as a probe, the reconstructed di-muon invariant mass must give a result compatible with the Z boson mass pole. In particular, it must hold that $|M_{\mu^+\mu^-} - M_Z| \leq 12.5$ GeV, where the M_Z is 91.1876 ± 0.0021 [53]. The choice of the 12.5 GeV threshold is made such that the acceptance window is roughly ten times the decay width of the boson ($\Gamma_Z = 2.4952$ GeV [53]), thus reducing significantly the probability of a true Z boson to be excluded because its mass is found deviated from the lineshape's peak.

The above selection selects an almost pure sample of Z bosons as is also evident by the invariant mass distribution of the muon pair which is shown in figure 3.9. The agreement with Monte Carlo is good, indicating that any background contributions is negligible. A total of 1114 probes are collected from which 541 are found in the barrel region ($|\eta| < 1.05$) and 573 in the end-caps ($1.05 \leq |\eta| < 2.4$). The kinematic distributions of the probes are shown in figure 3.10 and again a good agreement with the Monte Carlo is observed.

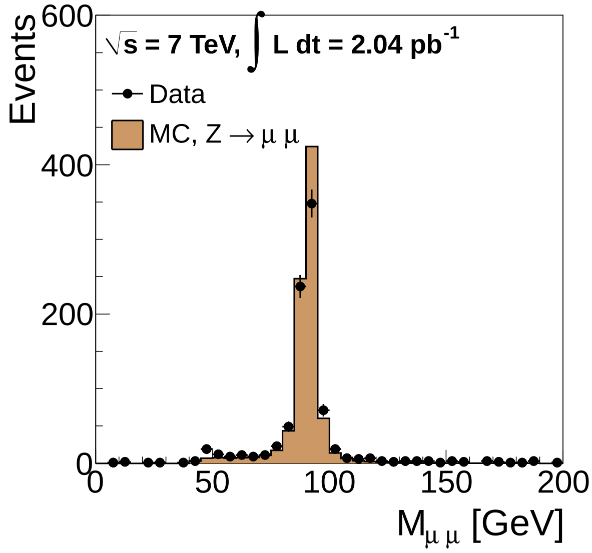

Figure 3.9: *Invariant mass distribution of the muon pair after the tag and probe event selection requirements. The Monte Carlo $Z \rightarrow \mu^+\mu^-$ is also drawn.*

3.3.3 Results

The efficiency of the `EF_mu10_MSonly` trigger as obtained by counting the probes that have fired this trigger is shown in table 3.7. We expect the difference between data and Monte Carlo to be caused by effects explained in section 3.2.2 such as the L2 LUT optimization.

In figure 3.11 the efficiency is shown with respect to p_{T}, η and ϕ. The data and Z boson Monte Carlo efficiency is obtained from the probe muons after applying the T&P method. It is clear that the amount of statistics does not leave room for a refined binning, however it still possible to observe the reduced plateau efficiency of the p_{T} distribution in the barrel, compared to the one measured in the end-caps, which is attributed to the complex geometry of the Muon Spectrometer in that pseudo-rapidity region; this is in agreement with the performance measurements presented earlier. The complex geometry also affects the η and ϕ distributions, with the most striking example in the negative ϕ region where the 'feet' of the detector are located. Overall, the data and Monte Carlo agreement is good and in certain bins where large fluctuation are observed, as in example in the region of $-0.8 < \eta < -0.6$. These are attributed to the limited statistics.

*Z **boson decays vs.** $t\bar{t}$ **decays***

An important question that arises after measuring the efficiency using Z decays, is whether this number is applicable to other physics processes as well. The events that are of interest in this thesis are the $t\bar{t}$ leptonic decays and the muons that originate from the W boson decay are expected also to be well isolated and in general kinematically equivalent to muons coming from Z bosons. However, $t\bar{t}$ events exhibit differences in their signature with respect to the Z boson events and most notably in their jet activity which is much higher. To make sure that the T&P analysis result is valid for $t\bar{t}$ events, the efficiency of muons originating from decaying

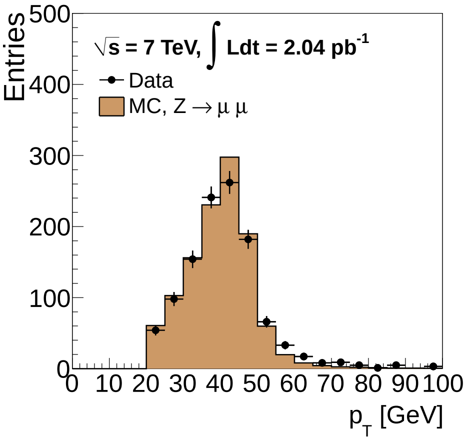

(a) *Transverse momentum (p_T).*

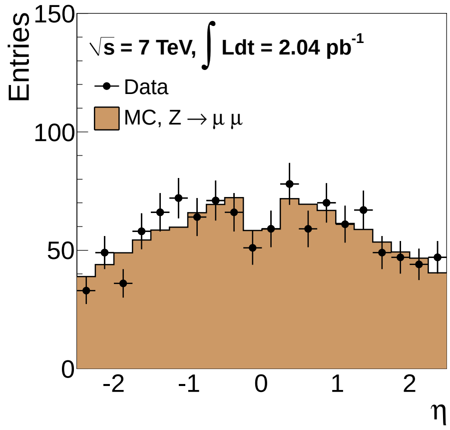

(b) *Pseudo-rapidity (η).*

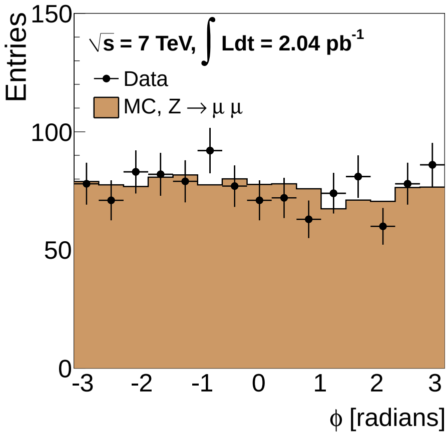

(c) *Azimuthal angle (ϕ).*

Figure 3.10: *The p_T, η and ϕ of the probe muons selected with the T&P selection requirements. A total of 1138 probes are collected.*

Detector Region	**Efficiency**	
	Monte Carlo	Data
Barrel ($\lvert\eta\rvert < 1.05$)	$75.02^{+0.12}_{-0.13}\%$	$70.05^{+1.94}_{-1.99}\%$
End-caps ($1.05 < \lvert\eta\rvert < 2.4$)	$93.61^{+0.09}_{-0.09}\%$	$90.92^{+1.15}_{-1.24}\%$
Full coverage ($\lvert\eta\rvert < 2.4$)	$84.33^{+0.08}_{-0.08}\%$	$80.79^{+1.16}_{-1.20}\%$

Table 3.7: *Overall trigger efficiency for* `EF_mu10_MSonly` *as obtained with the T&P method. The quoted uncertainties are statistical only.*

top quarks is also plotted in figure 3.11. As with the Z muons, these are also required to pass object selection requirements mentioned earlier. The agreement between the Z boson Monte Carlo and the $t\bar{t}$ is very good, suggesting that there is no need for further correction.

Application of the extracted efficiency to analyses

Finally, after determining the trigger efficiency with the described method, it must be applied on the analysis of interest. This usually happens not by directly applying it on the final

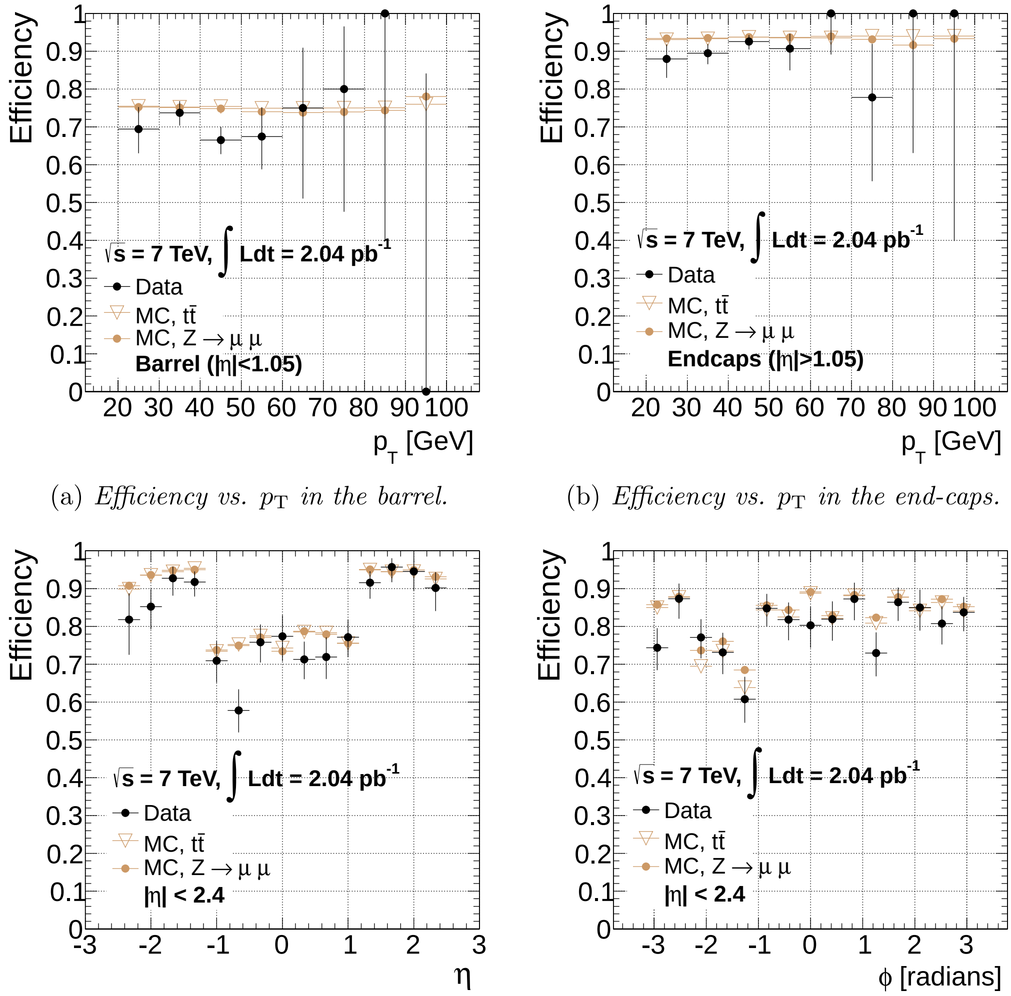

(a) *Efficiency vs.* p_T *in the barrel.* (b) *Efficiency vs.* p_T *in the end-caps.*

(c) *Efficiency vs.* η. (d) *Efficiency vs.* ϕ.

Figure 3.11: *Efficiency with respect to the probe muon's* p_T *in the barrel (a) and end-cap (b) regions as well as with respect to its* η*(c) and* ϕ *(d) co-ordinates. The estimate from Monte Carlo Z boson decays is plotted and also the efficiency as obtained by muons coming from* $t\bar{t}$ *decays.*

measurement but instead by expressing it in the form of a scale factor which is defined as follows:

$$SF = \frac{\epsilon_{data}}{\epsilon_{MC}}, \tag{3.3.8}$$

where ϵ_{data} is the efficiency as obtained from the data-driven method and ϵ_{MC} is the efficiency as obtained from the Monte Carlo. The main advantage of this is that one could simply take the uncertainty on the scale factor which is less sensitive to systematic variation than the efficiency itself. As will be discussed in chapter 6, this approach is preferred for the analysis performed in this thesis.

For the results shown above, the scale factor is expressed separately for the barrel and the end-cap regions; see table 3.8. The total systematic uncertainty quoted in the final result is taken after adding in quadrature the variation of the scale factor from each of the following sources:

Detector Region	Scale Factor
Barrel ($\|\eta\| < 1.05$)	$0.934^{+0.026}_{-0.027}(stat.)^{+0.012}_{-0.008}(syst.)$
End-caps ($1.05 < \|\eta\| < 2.4$)	$0.971^{+0.012}_{-0.013}(stat.)^{+0.010}_{-0.016}(syst.)$

Table 3.8: *Resulting trigger scale factors from T&P for the* `EF_mu10_MSonly` *trigger during the data periods E4-F2.*

- **Mass-window:** The choice of the 12.5 GeV mass-window is based on the decay width of the Z boson. We test the sensitivity of our result by changing the threshold by 2.5 GeV to both higher and lower values.
- **Offline-to-trigger matching:** Determining that an offline muon has fired the trigger, happens by matching it to a trigger object that passes these requirements. The choice of the matching threshold is tested by altering it by 0.2 both upwards and downwards.
- **Tag isolation criteria:** Lastly, the choice of the isolation criteria and their effects on the scale factor is examined in a rather conservative way by completely removing these requirements, namely the calorimetric and tracking isolation as well as the overlap removal with the close-by jet.

3.4 Summary

In this chapter the triggering of muon particles was thoroughly discussed. With the first data recorded by the detector it was possible to assess the performance of the muon trigger and identify problems that would help in the commissioning of the detector. All of the problems that were encountered have been addressed for the subsequent data taking periods. In addition, as the trigger system is the first event selection layer in an analysis, it is imperative that its efficiency is known during data-taking. With the increase of the instantaneous luminosity of the LHC, the selected events become biased by the selection of the trigger and therefore direct estimation of its efficiency is not possible. The tag-and-probe method provides a data-driven method that allows the measurement of the muon trigger efficiency also for muons that originate from $t\bar{t}$ decays. The result from this method was obtained and presented for the `EF_mu10_MSonly` trigger that was used during the data periods E4-F2 for the top-related analysis.

Chapter 4

Reconstruction and selection of top quark-pairs.

"High thoughts must have high language."

Aristophanes - c. 446 - c. 386

In chapter 2 the ATLAS detector layout and its readout system were described. Here we focus on those elements that are necessary for detecting top quark-pair events ($t\bar{t}$) where one top quark decays to a leptonic final state and the other hadronically to jets (single-lepton). The $t\bar{t}$ single-lepton topology is a busy and complex signature with many different physics objects that need to be reconstructed. As a result, almost all the different sub-detectors of ATLAS are involved for detecting these interesting events. In this chapter, section 4.1 presents the reconstruction techniques of the objects involved in the $t\bar{t}(e\nu_e)$ and $t\bar{t}(\mu\nu_\mu)$ topologies, namely those of electrons, muons, missing transverse energy, and jets[1]. Section 4.2 discusses corrections that are applied on reconstructed observables for improving the agreement between data and Monte Carlo. The sections 4.3 and 4.4 present the requirements that are applied at both the physics object-level and the event level for selecting the $t\bar{t}$ single-lepton events for our analysis. Lastly, section 4.5 introduces us to the cross-section measurement that is presented in greater detail in the forthcoming chapters.

4.1 Reconstruction of physics objects

This section describes how the raw detector signals are transformed by specific algorithms to meaningful physics objects. The calibration of those objects is also discussed. For various objects, such as jets, several reconstruction possibilities exist. In these cases, the focus is on the choices made for the analysis presented in the later chapters.

[1] The $t\bar{t}(\tau\nu_\tau)$ final state where the τ -lepton decays hadronically is not considered explicitly as it is a special case when it comes to isolating candidate events. On the other hand, the case where the τ-lepton decays into an electron or a muon is practically indistinguishable from the actual $t\bar{t}(e\nu_e)$ or $t\bar{t}(\mu\nu_\mu)$ final states and enters the signal distributions even though kinematically they may differ due to the presence of the produced neutrino. Naturally, these events are not excluded.

4.1.1 Electrons

Reconstruction

For electron detection both the Inner Detector (ID) and the Electromagnetic (EM) calorimeter are used. The standard reconstruction starts from the EM calorimeter where a sliding window algorithm identifies clusters of cells[2] with a size of 3×5 cells and with at least 2.5 GeV of deposited energy (seed clusters). The seed clusters are then matched to tracks from the Inner Detector forming electron candidates. Multiple tracks may be matched to the seed cluster and in this case the best-match is selected as the one with the smallest distance in $\Delta R = \sqrt{\Delta\eta^2 + \Delta\phi^2}$; priority is given to tracks that have silicon hits. For each electron candidate the initial seed cluster is again scanned with a sliding window algorithm of size 3×5 cells for the barrel region, or 5×5 cells for the end-cap region. Finally, the electron four-momentum is calculated from the combination of the best-match track and the reconstructed cluster, the energy is recomputed as the weighted average between the cluster's energy and the track's momentum while the η and ϕ coordinates are taken from the track information. Specifically for lower-p_{T} electrons a better reconstruction efficiency is achieved if the track is used as the starting point. In this case, the track is extrapolated to the EM calorimeter and its entry point is used as the seed for the cluster reconstruction. Both algorithms are restricted by the pseudo-rapidity coverage of the ID ($|\eta| \leq 2.5$).

Identification requirements

The reconstruction algorithms are very likely to provide electron candidates which should be accounted as background instead, e.g. converted photons or jets (faking electrons). Depending on the analysis, a refinement of the objects is necessary with the goal to decrease the background rate while keeping real electrons. Three sets of identification criteria are established which define the following electron collections (a more detailed description is presented in [128]):

- The *"loose"* electrons which are identified using calorimeter information only. The energy deposition of the electromagnetic shower on the first layer of the hadronic calorimeter (hadronic leakage) is evaluated as well as the shower-shape from the second layer of the EM calorimeter.
- The *"medium"* electrons which require both calorimeter and tracking information. Selection cuts are applied on top of the "loose" information and utilize also the first layer of the calorimeter for shower-shape estimates as well as ID track quality and matching criteria.
- Finally the *"tight"* electrons keep the same calorimeter cuts as for the "medium" electrons but require tighter track matching and quality cuts as well as a number of hits on the Pixel B-Layer and the TRT sub-detectors. In addition, electrons that are matched to converted photons are also rejected.

In figure 4.1 the binned efficiency is shown for each selection, as calculated from $Z \to e^+e^-$ simulated decays, with respect to the cluster's E_T and $|\eta|$. The efficiency is defined as the ratio of reconstructed signal electrons which pass the selection criteria and are matched to true electrons over the total number of true electrons. The apparent drop at $|\eta| > 1$ is attributed to the reduced tracking efficiency in the end-cap regions, where particles travel through more dead material, as well as to the lower efficiency in the transition region between barrel and

[2] The size of a cell is that of the middle layer cell and corresponds to $\Delta\eta \times \Delta\phi = 0.025 \times 0.025$.

	Efficiency (%)		Jet Rejection
	$E_T \geq 17$ GeV	$E_T \geq 20$ GeV	
	$t\bar{t}(e\nu_e)$	$Z \to e^+e^-$	Di-jet QCD
Loose	89.73 ± 0.04	94.68 ± 0.03	614.3 ± 1.5
Medium	87.20 ± 0.05	89.61 ± 0.03	4435 ± 30
Tight	75.26 ± 0.06	72.77 ± 0.03	$(4.9 \pm 0.1) \cdot 10^4$

Table 4.1: *The expected integrated efficiency for "loose", "medium" and "tight" electron selections for the $Z \to e^+e^-$ and $t\bar{t}$ events as estimated from Monte Carlo. The E_T cut applied in each of the MC samples is slightly different. The expected jet rejection rate is shown in the last column. Numbers taken from [128].*

end-cap of the EM calorimeter [128].

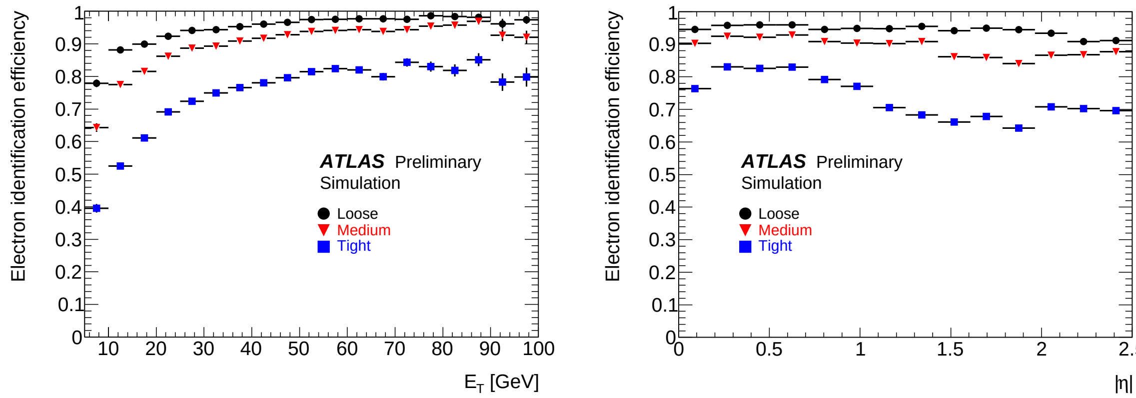

(a) *Efficiency vs. E_T*

(b) *Efficiency vs. $|\eta|$*

Figure 4.1: *Electron identification efficiency with respect to the cluster energy (a) and the absolute pseudo-rapidity values (b) for "loose", "medium" and "tight" selections as estimated from Monte Carlo. The efficiencies are calculated from a $Z \to e^+e^-$ sample using the tag-and-probe method. Plots taken from [128].*

Electrons originating from the Z boson decay are high-E_{T} and well isolated, similar to the electrons from the $t\bar{t}(e)$ decay. However, $t\bar{t}$ events have a large jet multiplicity and thus they are considered a more 'busy' environment. As a result, the probability of identifying a jet as an electron is increased. Table 4.1 shows the overall efficiency for the Z boson and the $t\bar{t}(e\nu_e)$ samples as well as the jet rejection rate which is calculated from QCD di-jet events. The jet rejection rate is defined as the ratio of the number of true jets in the sample over the number of electron candidates which are reconstructed and pass the selection criteria (fakes).

Isolation variables

Electron isolation cuts are explicitly added in the selection procedure if necessary. Two variables are defined, `etcone` and `ptcone`, which correspond to calorimetric and tracking isolation respectively [128]:

- The `etcone` corresponds to the reconstructed transverse energy on the calorimeter in a cone of opening angle of R_0 around the electron axis direction after excluding the intrinsic energy of the electron. The R_0 typical values, measured in the $\eta - \phi$ plane, range from 0.2 to 0.6. Naturally, the `etcone` variables are dependent on the p_T of the object and in addition they are affected by the pile-up and the underlying event activity. For these effects corrections can be applied as explained in [129].

- The `ptcone` corresponds to the scalar sum of transverse momentum of the tracks which are within a cone of $R_0 = 0.3$ around the electron. Specific requirements are placed for the tracks used in this case. Namely, all tracks must have $p_T \geq 1$ GeV, a hit at the inner layer of the Pixel detector as well as 7 hits on the SCT sub-detector. Lastly, both transverse and longitudinal impact parameters must have a value of at most 1 mm. Naturally, for this calculation neutral particles are not taken into account.

4.1.2 Muons

Reconstruction

The reconstruction of muons involves all layers of the detector. The Muon Spectrometer (MS) is the dedicated sub-detector for muon-finding but information from the Inner Detector (ID) as well as from the calorimeters is also exploited. Muon candidates are formed by any of the following identification strategies:

- *Standalone* muons (SA), which are reconstructed using only MS information and their track is extrapolated to the beam line in order to identify their trajectory and their impact parameter.
- *Combined* muons (CB), which are formed by combining the independently calculated tracks from the MS and the ID.
- *Segment-tagged* (ST) muons, which are ID-reconstructed muons for which the track is extrapolated to the MS and subsequently matched with straight-track segments.
- *Calorimeter-tagged* (CT) muons, which are ID-reconstructed muons that are extrapolated to the calorimeters.

For each of the above categories various algorithms are employed which are not necessarily mutually exclusive. Two major reconstruction chains exist in ATLAS, commonly referred to as 'collections', the `STACO` collection (or chain 1) and the `MuID` collection (or chain 2). For the analysis presented in this thesis the `MuID` collection is preferred as it provides a slightly better overall efficiency for high-p_T muons which is also relatively constant in each of the different pseudo-rapidity regions of the detector [130, 131].

In the `MuID` collection the SA muons are found by the `MOORE` [120] algorithm and the extrapolation of their tracks to the vertex is handled by `MuIDStandalone` [132]. Forming of CB muons is performed by `MuIDCombined` [132] where a global refit of ID tracks from `NewTracking` and SA tracks from `MOORE` is done. Segment-tagged muons are also reconstructed from two algorithms, namely the `MuGirl` [133] where a full refit is done between the seed ID track and the associated SA track, and the `MuTagIMO` which also uses ID track seed and associates it with `MOORE` segments.

The overall reconstruction efficiency for CB muons is measured from data with a tag-and-probe technique based on $Z \rightarrow \mu^+\mu^-$ events and is found to have an average value of $0.958 \pm 0.001\%$ [131]. The deviation of the efficiency from the ideal 100% is largely due to the Muon Spectrometer acceptance which is not uniform in $\eta - \phi$. The various detector regions are depicted in figure 4.2. In figure 4.3 the reconstruction efficiency is shown for CB muons for the various regions as well as the dependence with respect to the pseudo-rapidity. Clearly,

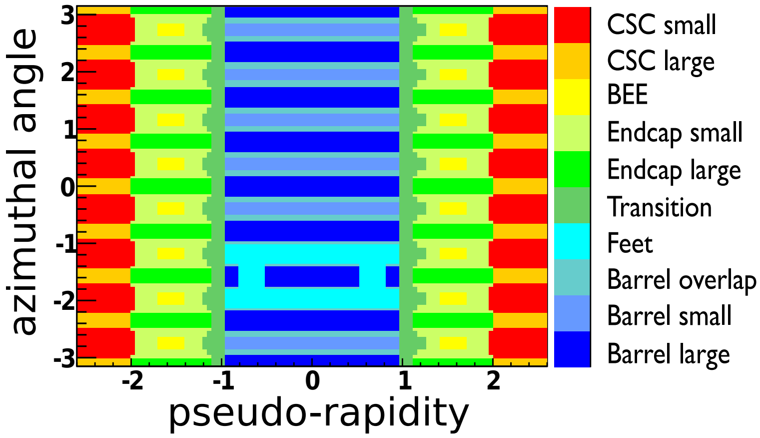

Figure 4.2: *The different detector regions with respect to $\eta - \phi$ coordinates.*

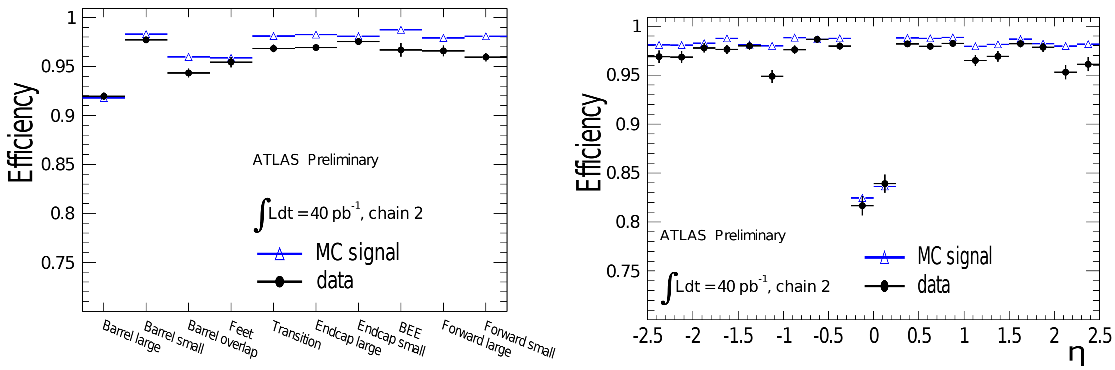

(a) *Efficiency vs. detector regions* (b) *Efficiency vs. η*

Figure 4.3: *The reconstruction efficiency (a) for each of the defined MS detector regions (b) as measured from $Z \to \mu^+\mu^-$ events using the tag-and-probe method. The muons probed are required to have $p_{\rm T} \geq 20$ GeV and lie within $|\eta| \leq 2.5$. The data are corrected for the background contribution. Plots taken from [131].*

the largest inefficiencies come from the 'large-barrel' stations, the 'feet' region and the 'barrel-overlap' region. The large dip in the 'large-barrel' region is because it covers the $\eta \approx 0$ area where a detector cabling hole exists, the dip in figure 4.3(b) justifies this effect; the 'barrel-overlap' region is also affected by the cabling hole. Similarly, the 'feet' region has less muon chambers in order to accommodate the structure for the detector's support, hence the quality of reconstruction is worse.

Improvements on the overall efficiency are achieved if ST muons are used together with CB muons [131, 105] since the former do not require a complete MS track and thus can increase the amount of successfully reconstructed muons. However, the trade-off for using ST algorithms is that the amount of non-prompt muons, e.g. muons coming from kaons or pions decaying in-flight, is significantly increased [105].

Quality definitions

Similar to the electron case, muons are categorized with respect to the quality of the reconstruction with a set of predefined selection requirements based on the algorithms used for the reconstruction. For muons in the `MuID` collection the categories are [134]:

- The *"tight"* muons, which are all the `MuID` combined muons and the `MuGirl` muons with

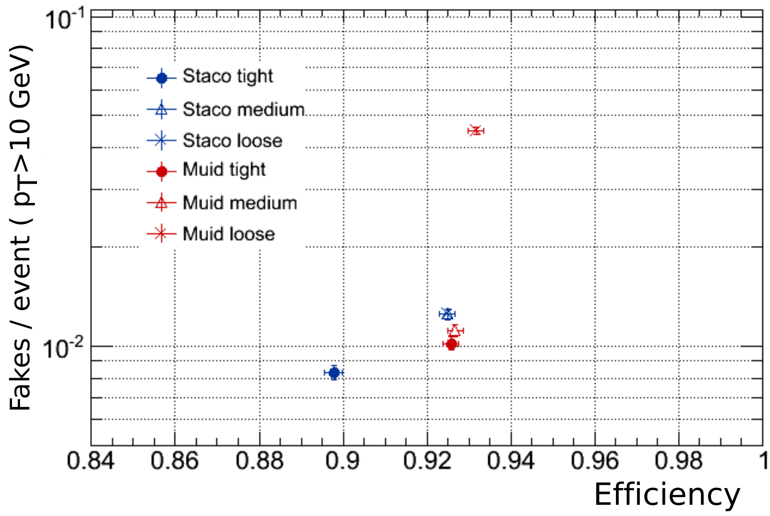

Figure 4.4: *The muon fake rate per event (purity) with respect to the efficiency for the various MuID (red) and STACO (blue) quality definitions as calculated for muons with $p_T \geq 10$ GeV. Plot from [136].*

a successful combined fit.

- The *"medium"* muons, which are all muons with a successful standalone fit.
- The *"loose"* muons, which are all the muons found by segment-tagging algorithms and have Inner Detector tracks with silicon hits associated.
- Lastly, the *"very loose"* muons in which all muons that are reconstructed by `MuTagIMO` with only TRT seeds are included.

The requirements are inclusive for increasing tightness of the reconstruction quality e.g. "loose" muons contain "medium" and "tight" muons as well. In figure 4.4 the efficiencies of the quality definitions for `MuID` (red) are shown with respect to the relevant fake rate. It is clearly seen that for tighter requirements the fake rate is significantly reduced with a small trade-off to the overall efficiency. For completeness the `STACO` (blue) collection categories are also seen, for which the definitions are described in [135].

Isolation variables

As in the electron case, the calorimetric (`etcone`) and tracking (`ptcone`) isolation parameters are defined for muons [131]. The definitions of the variables are the same as before. The `etcone` variable gives the transverse energy deposited in the calorimeter in a cone of opening angle of 0.3 or 0.4 around the muon and after correcting for the muon energy loss. The `ptcone` variable is the scalar sum of the transverse momentum of particle tracks that reside within a cone of 0.3 or 0.4 around the muon axis.

4.1.3 Jets

At the LHC conditions the proton collisions result in an immense production of quarks and gluons which either come from the hard scattering or from the initial and final state radiation. These particles carry color charge and as a result of color confinement they cannot exist freely. Subsequently they hadronize[3] into a bunch of colorless and collimated stream of particles, usually hadrons, which can simply be seen as a jet.

For the identification of $t\bar{t}(\ell\nu_\ell)$ events, the jets are of particular importance since they can be used to directly reconstruct the hadronically decaying top quark mass. Detection

[3] With the exception of the top quark which decays much faster.

and reconstruction of jets is a challenging process that involves mainly the hadronic and electromagnetic calorimeters and from an experiment's point of view it can be split into three major ingredients: the input to the jet reconstruction, the jet finding (clustering) algorithm and the calibration that is used to correct the final jet energy back to the parton level.

Inputs to jet reconstruction

The inputs to jet reconstruction are the four-momentum elements that are used by a clustering algorithm to form a jet. Although at the Monte Carlo level it is straightforward to use stable particles, [4] with real data this is not possible and the calorimeter energy depositions must be utilized. Two main options exist in ATLAS, the *topological clusters* and the *calorimeter towers* [137]. Calorimeter towers are constructed by splitting the calorimeter in bins of fixed size of $\Delta\eta \times \Delta\phi = 0.1 \times 0.1$. All cells that lie within a bin and for the whole depth of the calorimeter are combined together to form a single four-vector object. The amount of energy that each cell contributes depends on the fraction of the cell that falls within the bin. The reconstructed energy at this level is at the electromagnetic scale, that is to say it corresponds only to the energy deposited from electromagnetic showers. Cells with no signal also take part in the reconstruction and therefore calorimeter towers maybe formed by using also noisy cells[5]. Given that no noise-suppression is applied, calorimeter towers can often result into having negative energies. When a negative energy tower is built it is typically combined with neighboring positive energy towers in order to cancel the effect. However, it is not unlikely especially in the presence of pile-up to have towers with significantly large negative energy where the above procedure is ineffectual and thus not being able to avoid the presence of negative energy towers.

A topological cluster on the other hand takes advantage of the fine granularity of the detector. It is a dynamically growing cluster of cells that is formed starting from a seed cell with a high signal-to-noise ratio. Once a cell is found that fulfills the requirement of $|E_{cell}|/\sigma_{cell}^{noise} > 4$ it serves as a seed, where the σ_{cell}^{noise} depends on the exact position of the cell in the calorimeter. At the next step, all cells neighboring the seed are added if they have $|E_{cell}|/\sigma_{cell}^{noise} > 2$. This continues for all neighbors of the neighbors as long as the requirement is fulfilled every time. The growing of the cluster stops when no cell passing the $2\sigma_{cell}^{noise}$ excess is found, where at this point all cells surrounding the cluster are also added. By construction, topological clusters are a noise-suppressed input since by taking the absolute value requirement the positive noise is on average cancelled by the negative noise effects. Thus this method is inherently dependent on the noise modeling of the detector. However, negative energy clusters are possible to emerge especially in the presence of large noise fluctuations. In this case those clusters are completely withdrawn from the reconstruction.

In an alternative approach a combination of the above two techniques can be made forming topological towers [138]. Topological towers are again tower objects of size $\Delta\eta \times \Delta\phi = 0.1 \times 0.1$ where only cells that belong to a topological cluster are combined. The benefit of this method is a noise-suppressed input that keeps a fixed geometrical size and therefore does not rely on the cluster-making algorithm.

[4] Typically, all particles with a decay length of more than 10mm excluding neutrinos and muons that result as decay products after the hadronisation of the partons.

[5] Calorimeter noise comes from the inherent electronic noise of the detector or from depositions due to pile-up activity, or from both. The noise modeling results in a gaussian distribution centered around zero and as such negative energy cells may exist.

Jet clustering

Clustering algorithms are assigned the task to collect the input objects and decide which and how they are going to be recombined in order to form a jet. Being a challenging field, many approaches have been implemented but two major algorithm classes can be distinguished, the *cone* algorithms and the *sequential recombination* algorithms.

In ATLAS, a fixed-size and seeded version of the cone algorithm has been extensively used in the past. It starts by first assembling all the input objects into a list with decreasing transverse momentum. A seed is then selected as the highest p_{T} object, with the lowest acceptable threshold being at the energy of 1 GeV. All other objects that are within $\Delta R \leq R_{cone}$ in the $\eta - \phi$ space from the seed are clustered together to form a jet. An iterative procedure is used thereafter, where the direction of the new jet becomes the central point and the objects around it are then re-clustered; the recalculation of the jet continues until its direction is considered stable. With the above approach it is possible that jets share the same constituents. As a result, a split-merge procedure is applied under which it is decided whether to merge two jets or split them by giving the overlapping constituents to the one of the highest p_{T}.

A significant problem with all common cone algorithms is that they are considered collinear and infrared unsafe hence they cannot be trusted for multi-jet systems. However, in a more advanced implementation, the Seedless Infrared Safe cone algorithm or `SISCone+` [139], these issues are resolved. A complete description of collinear and infrared safety effects is given in [140].

On the other hand, sequential recombination algorithms by construction do not suffer from the above issues. In ATLAS the main algorithm generally defines the following parameters which are calculated for each of the input objects i:

$$d_{ij} = min(k_{Ti}^{2p}, k_{Tj}^{2p}) \frac{(\Delta R)_{ij}^2}{R^2} \ , \tag{4.1.1}$$

$$d_{iB} = k_{Ti}^{2p}. \tag{4.1.2}$$

The k_T variable refers to the transverse momentum of the object, ΔR_{ij} to the $\eta - \phi$ distance of two objects i and j, R is a measure of the jet size and the parameter p is the power of the energy scale. In practice, d_{ij} is the distance variable between two objects and d_{iB} is the distance variable between an object and the beam; for all the input objects the d_{ij} and d_{iB} are calculated and are put in a list. If the smallest entry of the list belongs to a d_{ij} category then i and j are combined into a single object and the distances are re-evaluated. If, however, it belongs to a d_{iB} category then the object is considered a jet and is removed from the list. This procedure continues until no objects remain in the list.

The jets used in this thesis follow the above clustering scheme where the parameter p is set to -1, referring to the `anti-`$k_{\perp}$ algorithm [126]. The main advantage, except from being infrared and collinear safe, is that it usually results in regular jet boundaries. In particular, it is by construction that the softer p_{T} particles will cluster with their neighboring hard p_{T} particles before they cluster with themselves. As a result, in the vicinity $\Delta R_{ij} \leq R$ of a single hard particle all soft candidates will be absorbed within the cone of size R. Although, typically this algorithm would require a significant amount of time, with the `FastJet` implementation this is drastically reduced [141].

Figure 4.5 shows the reconstruction efficiency of jets in the $t\bar{t}(e\nu_e)$ or $t\bar{t}(\mu\nu_\mu)$ topology with respect to the p_{T} of the mother quark (light-quark or b-quark). Events are preselected, requiring at least three jets of $p_{\mathrm{T}} \geq 40$ GeV or higher and at least one more with $p_{\mathrm{T}} \geq 20$ GeV or higher. All jets with $p_{\mathrm{T}} \geq 20$ GeV are considered and they are flagged as matched if they reside within $\Delta R \leq 0.3$ from the quark. The `anti-`$k_{\perp}$ algorithm with jet size $R = 0.4$ is

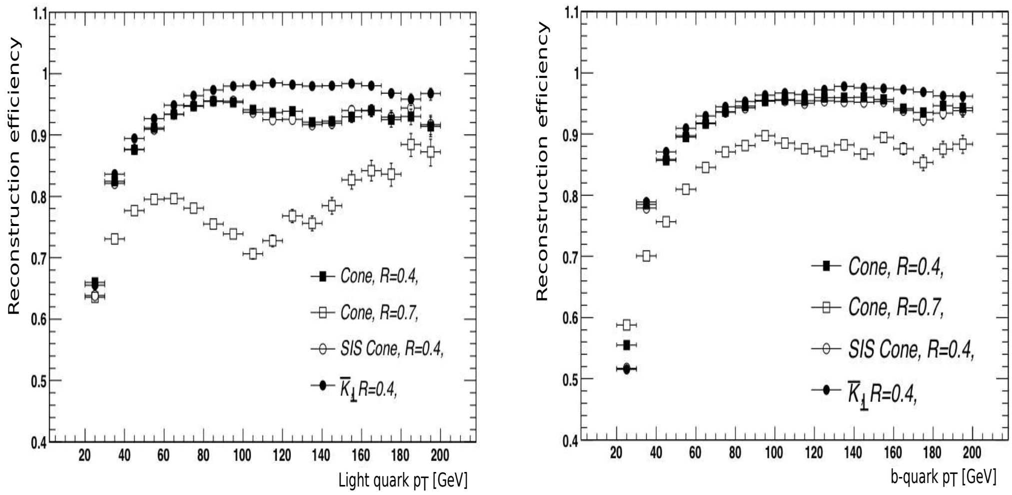

(a) *Jets from light quarks* (b) *Jets from bottom quarks*

Figure 4.5: *Reconstruction efficiency of light-quark (a) and b-quark (b) induced jets formed by the different algorithms, as a function of the p_{T} of the quarks. The* `anti-`$k_{\perp}$ *algorithm is denoted as $\bar{K}_{\perp}$. Plots taken from [142].*

compared with the cone jet finder of ATLAS as well as with the `SISCone` algorithm. The large drop in efficiency of the cone jet finder with $R = 0.7$ for light quark p_{T} above 80 GeV is identified as an effect of the reconstruction which fails to identify a single jet at these energies and with the given R parameter. For the jets originating from b-quarks the effect is much less profound because typically these jets are more narrow. Evidently, the `anti-`$k_{\perp}$ achieves always a higher reconstruction efficiency.

Using the `anti-`$k_{\perp}$ algorithm, the different calorimeter inputs are compared in terms of the jet resolution performance using Monte Carlo simulations. Figure 4.6 shows the evolution of the jet resolution for each input case and for three different luminosity scenarios: the no pile-up case, a low luminosity scenario with a large bunch-spacing (425 ns) that corresponds to an early running period and a higher luminosity one with a nominal bunch-spacing (25 ns) that refers to a mid-term running period. The vertical axis shows the σ_R/R, where $R = p_{\mathrm{T}}^{reco}/p_{\mathrm{T}}^{true}$, and the distribution is plotted against p_{T}^{true}. All jets are matched to true jets using a $\Delta R \leq 0.3$ requirement.

The conclusion that can be drawn from these plots is that using the topological clusters a better resolution is achieved in all scenarios. However, at the higher luminosity the performance is very similar with the topological towers which in fact show to be less affected by the increase in the pile-up activity.

Jet calibration

The energy deposited in the calorimeters corresponds to the energy of the showers. Eventually, the energy and the momentum of the jets must correspond to the hadronic scale and as a result a correction must be applied. This is an essential, yet challenging, step in the jet reconstruction and can take place either at the calorimeter reconstruction level, by correcting each input object to the hadronic scale and then letting the jet clustering algorithm act on them (local calibration), or at the jet reconstruction level, where jets are built from the input objects at their electromagnetic scale and afterwards they are adjusted as a whole (global

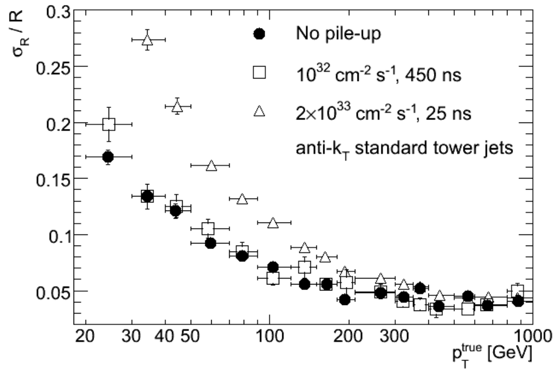

(a) *Calorimeter Towers*

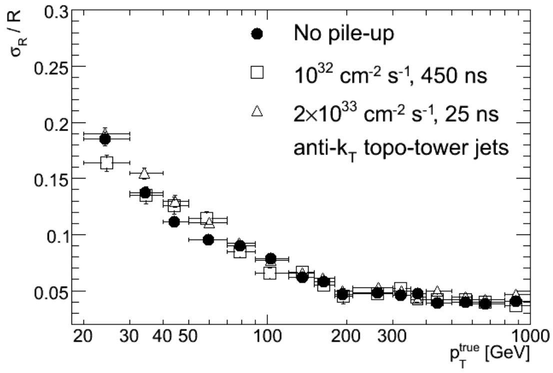

(b) *Topological Towers*

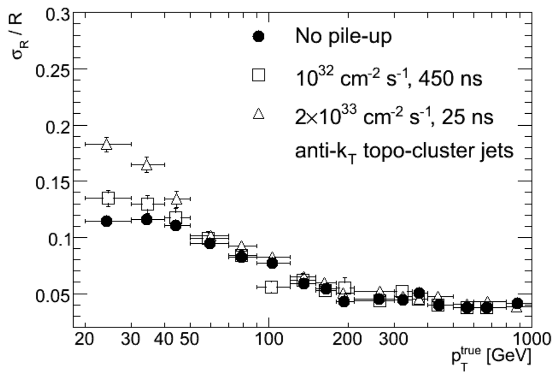

(c) *Topological Clusters*

Figure 4.6: *Jet resolution comparison using the* `anti-`$k_\perp$ *algorithm with jet size* $R = 0.4$ *for the three different inputs variables and for three different luminosity scenarios as measured from Monte Carlo. Plots taken from [143].*

calibration). However, corrections do not only involve the hadronic energy deposition, but also effects from dead material in the detector, from energy leakage due to escaping particles or from losses due to reconstruction effects. All these are included in the jet calibration step.

A number of different methods are available for ATLAS [138] that are meant to be complementary for the understanding of the systematic uncertainties. However, as the research in this thesis takes place in the beginning of the data-taking era of the experiment, a simple yet robust method is used, the `EMJES` calibration [127]. This method corrects each jet depending on its transverse momentum and pseudo-rapidity and it gives a straighforward evaluation of the related systematic uncertainties. More advanced methods at the time of this thesis were still under commissioning.

The `EMJES` method has three major steps:

- First, the energy is corrected at the electromagnetic level for the pile-up activity in the event. The correction factors are derived by estimating from minimum bias data the average jet energy and the average towers per jet with respect to the number of primary vertices and the η of the jet.
- Second, the jet direction is corrected so that it points to the primary vertex of the event and not to the detector's geometrical center as it is by default.
- Last, a correction is applied in both the energy and direction of the jet using factors ob-

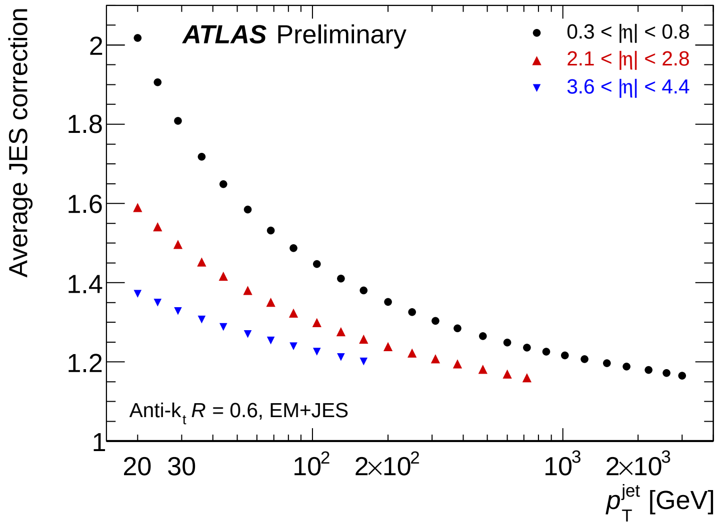

Figure 4.7: *The average jet energy scale correction applied with respect to the p_T of the jet after the calibration is applied. Plot taken from [127].*

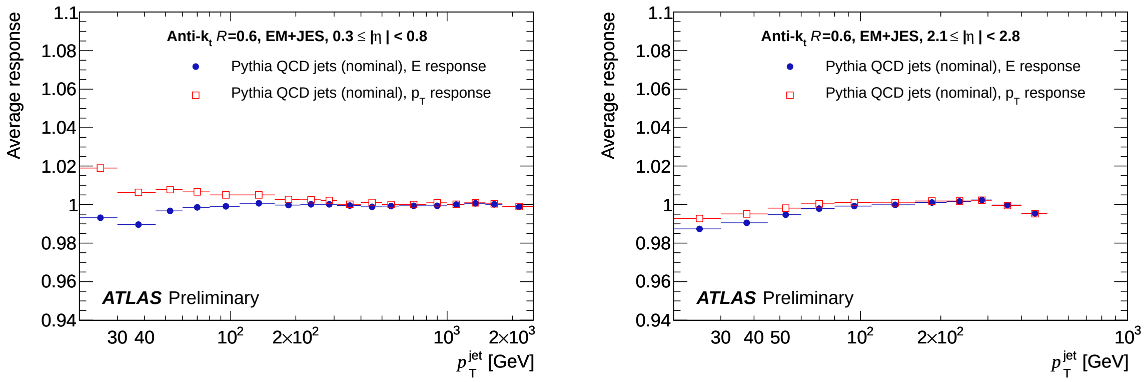

(a) *Barrel* (b) *End-caps*

Figure 4.8: *The jet p_T and E response after the* `EMJES` *calibration is applied as calculated from Monte Carlo samples. Plots taken from [127].*

tained from Monte Carlo samples in which the reconstructed jet kinematics are compared with the true particle jets.

In figure 4.7 the average jet energy scale correction is shown with respect to the jet transverse momentum for three different calorimeter regions, while in figure 4.8 the ratio of the measured energy after the calibration step over the true jet energy with respect to the calibrated jet p_T is plotted. All jets used in these plots are coming from inclusive QCD Monte Carlo events and are reconstructed using the $\texttt{anti-}k_\perp$ algorithm with a jet size of $R = 0.6$ on topological clusters. For the jet response plots the deviations from unity, when observed, suggest a failure of restoring the kinematics of the calibrated jet to that of the particle jet. The main reason for this is that the same correction factor is applied in both the transverse momentum and the energy of the jet. Naturally, for when the jet mass is found to be non-zero and deviated from the true jet mass the correction only on the energy and pseudo-rapidity of the jet is not sufficient as it leads to a bias of its p_T. In addition to the above, the calibration algorithm assumes that all jet constituents should receive the same average compensation when deriving the calibration constants; this is not always the case.

4.1.4 B-jet finding

Top quarks decay predominantly into a W boson and a b-quark. As a result, being able to tag the jets that come from b-quarks provides a great tool in $t\bar{t}$ signal selection and eventually increases the signal-to-background ratio.

Identification of those jets is possible either by exploiting the relatively long lifetime of the B-meson or baryon ($\sim$ 1.5 ps) that the b-quark hadronizes to, or by identifying its decay products. In the former case, the resulting hadron travels a measurable distance from the primary vertex (PV) before it decays to other particles, creating a secondary vertex (SV) which can be distinguished in the inner tracker. In the latter case, when the hadron decays leptonically, the resulting charged lepton (electron or muon) can be utilized since due to the hard fragmentation and the high mass of its parent particle ($\geq$ 5 GeV) it carries a relatively large transverse momentum and its track can be associated to the jet axis. Naturally, the Inner Detector and the calorimeters are the main detectors that take part in the process of B-jet finding.

A large number of algorithms are employed for measuring observables that are related to the above properties, but two major categories can be distinguished: the spatial taggers and the soft-lepton taggers. For the latter case, because the taggers utilize only properties of the resulting lepton, the efficiency of the algorithm is intrinsically limited by the branching ratio of the leptonic decay of the b-hadron. Hence, they suffer from a significant loss of statistics which is important at the early stages of the experiment. Consequently, they are not taken into account here and one can refer either to the b-tagging section of [137] or to [144] for more information. The spatial taggers on the other hand utilize information both from the lifetime of the hadron and the displaced vertex and several approaches have been considered for the initial running period.

Impact parameter taggers

One category of spatial taggers is dedicated in measuring the signed transverse (d_0) and the signed longitudinal (z_0) impact parameters (IP) of selected tracks. The former is defined as the closest distance between the track and the PV when projected in the $r-\phi$ plane, while the latter is defined as the z-coordinate of the track when projected to the $r-\phi$ plane. Typically, tracks originating from b-jets have larger positive values of d_0 and z_0 while the tracks that originate from lighter quarks are equally distributed around zero. The significance of these parameters, namely d_0/σ_{d_0} and z_0/σ_{z_0} are usually used as they give more discriminating power. Figure 4.9 shows an example of the transverse IP significance of selected tracks that are associated with b-jets, c-jets or lighter quark jets, as calculated from a sample of $t\bar{t}$ events.

Examples of taggers that take advantage of the impact parameter observables and are considered in the early data-taking are the `TrackCounting` [145] and the `JetProb` [137] algorithms.

Secondary vertex reconstruction taggers

The other category of spatial taggers exploits information after the secondary vertex is fully reconstructed. The SV reconstruction first selects tracks that can be associated with a given jet depending on a ΔR threshold from the jet axis. Track-pairs are then formed using all tracks that satisfy $L_{3D}/\sigma_{L_{3D}} > 2$, where L_{3D} is the distance between the PV and the closest point of the track, and $\sigma_{L_{3D}}$ is its associated error. This requirement ensures that tracks originating from the PV are excluded from the search. Subsequently, all pairs are combined into a vertex and a fit is performed. If the fit satisfies a given χ^2 threshold, the vertex is kept as long as

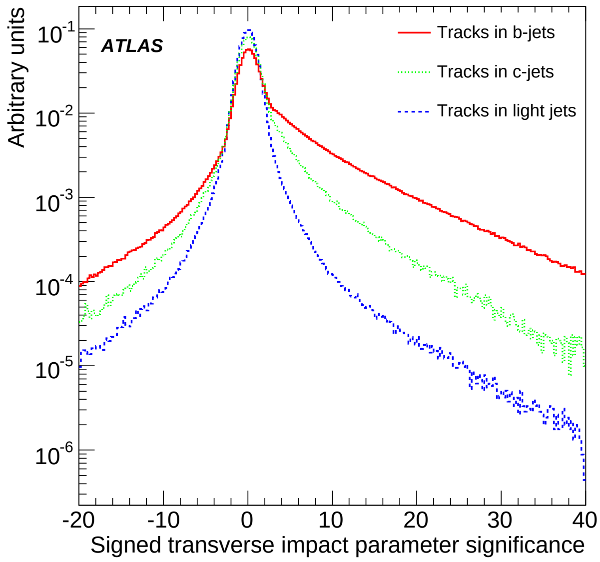

Figure 4.9: *The signed transverse impact parameter significance of tracks which are associated with b, c or lighter quark induced jets from a sample of Monte Carlo $t\bar{t}$ decays. Plot taken from [137].*

it is not likely to originate from K_s or Λ decays, or $\gamma \to e^+e^-$ conversions. Otherwise, the procedure is repeated after it removes the track with the largest χ^2 contribution.

Three observables can be defined after a secondary vertex is found:

- The invariant mass of all tracks in the vertex.
- The ratio of the energy sum of all tracks associated to the vertex over the energy sum of all tracks associated to the jet.
- The number of track-pairs that are used in the vertex.

As shown in figures 4.10 all of the above parameters are expected to have higher values for b-jets than for light jets and usually they are exploited in one of two ways: by retrieving information from the 2D-histogram of the first two variables and the 1D-histogram of the last (`SV1` tagger), or by retrieving information from the 3D-histogram of all the observables (`SV2` tagger) [137]. However, with this approach a significant amount of statistics is required and at the early stages of the experiment this leads to a large statistical uncertainty.

An alternative method instead of using the previous observables simply takes the signed decay length significance (L/σ_L), where the decay length (L) corresponds to the three-dimensional distance of the secondary vertex from the primary vertex. This algorithm which is named `SV0` is also considered for the early data-taking period [144].

In table 4.2, the selection purity as well as the rejection factors for light-jets and c-jets is shown for the 50% efficiency working point for the three algorithms that are considered for the early data taking period. The jet rejection factor is defined as the inverse of the tagging efficiency for the particular type of jets, namely $RF_{jet} = \frac{1}{\epsilon_{tag}} = N_{jet}/N_{jet}^{tagged}$.

The choice of the 50% efficiency is driven by the requirement to keep the statistics as high as possible while keeping low the fake rate. All jets that satisfy the $p_{\mathrm{T}} \geq 15$ GeV and $|\eta| \leq 2.5$ requirements are used. In the analysis presented hereafter the `SV0` algorithm is used since it has the largest purity and highest rejection factor.

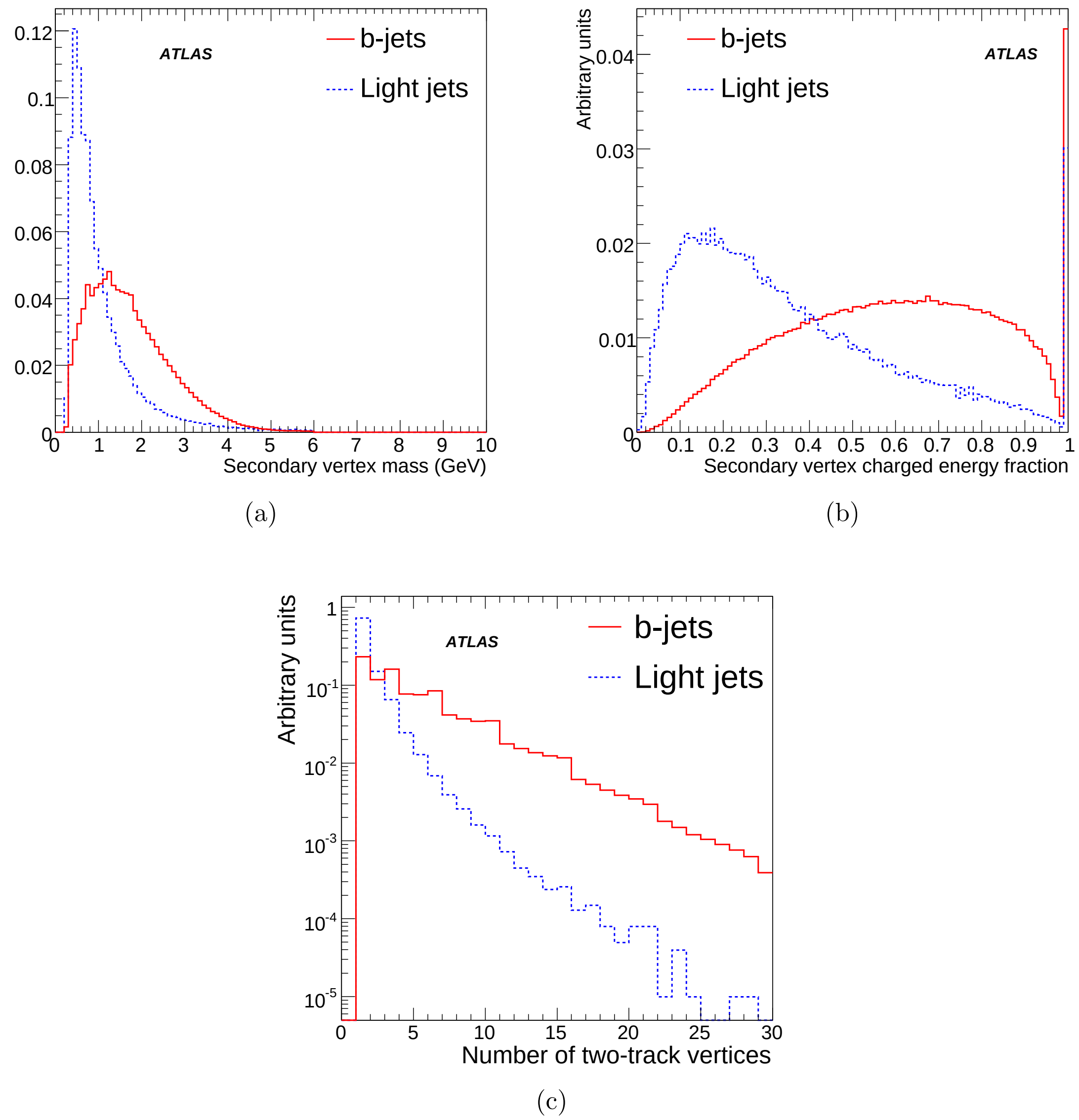

Figure 4.10: *The secondary vertex reconstructed mass (a) and charged tracks energy fraction (b), and the number of track-pairs used in the reconstruction (c). The distributions are obtained from $t\bar{t}$ Monte Carlo events. Plots taken from [137].*

	b-jet efficiency (%)	Purity(%)	Rejection factor		
			Light-jet	c-jet	τ-jet
`JetProb`	50.7	92.7	130	9	29
`TrackCounting`	50.2	92.5	140	8	34
`SV0`	50.1	93.9	271	9	38

Table 4.2: *Comparison of the purity and the rejection factors (RF) for each of the considered b-tagging algorithms at the 50% b-jet efficiency working point. Numbers estimated from Monte Carlo and taken from [146].*

4.1.5 Missing transverse energy - $E_{\mathrm{T}}^{\mathrm{miss}}$

In single-lepton $t\bar{t}$ decays a large part of the event's energy is carried away by the neutrino. This energy is not directly measurable since neutrinos do not leave a trace on any of the detector's components. However, it is possible to reconstruct the energy associated to all non-interacting particles in the event, by using the momentum conservation principle and balance the contribution of the other objects in the event. The "missing" energy, as it is referred, will correspond to the vector sum of the momenta of all non-interacting particles. It is easily perceived that this is not possible in the longitudinal direction where the exact initial momentum of the interacting partons is not known. Instead, the transverse $(x - y)$ plane is used as it can be assumed that in this direction the partons' momentum is zero, hence the missing transverse energy is calculated. This is then given by the following:

$$E_{\mathrm{T}}^{\mathrm{miss}} = \sqrt{(E_x^{miss})^2 + (E_y^{miss})^2}\ , \tag{4.1.3}$$

and the azimuthal angle (ϕ) of the vector is given by:

$$\tan\phi^{miss} = \frac{E_y^{miss}}{E_x^{miss}}. \tag{4.1.4}$$

Reconstruction

The $E_{\mathrm{T}}^{\mathrm{miss}}$ reconstruction sums up the deposited energy in the calorimeters (E^{Calo}) together with the energy of the muons (E^{Muon}) and in addition it corrects for the energy that is lost due to the inactive material in the cryostat region between the electromagnetic and the hadronic calorimeters (E^{Cryo}). The following relation holds for each of the two directions in the $x - y$ plane:

$$E_{x,y}^{miss} = -(E_{x,y}^{Calo} + E_{x,y}^{Muon} + E_{x,y}^{Cryo}), \tag{4.1.5}$$

where the minus sign is taken because of the energy conservation.

The calorimeter term

For the calorimeter term, in order to achieve noise-suppression, only cells that belong to topological clusters are used, although in this case all identified clusters are taken into account and not only the ones used in the jet reconstruction. A calibration scheme is also applied at the cell level.

This term can be refined into the individual contributions of the various objects that deposit energy in the calorimeters, e.g. electrons, jets etc. In this way a better calibration can be applied, based on the identified object, that replaces the previous. The assignment of cells to each reconstructed object is done by first identifying the latter and then moving back to the calorimeter components it traverses. It is possible that cells are shared between terms, in this case a priority list must be defined to avoid double counting of energy.

The cryostat term

The cryostat term in equation 4.1.5 effectively calculates the jet energy loss while it traverses the region between the two calorimeters. It is given by:

$$E_{x,y}^{Cryo} = \sum_{jets} E_{jet_{x,y}}^{Cryo} \tag{4.1.6}$$

where,

$$E_{jet}^{Cryo} = w^{Cryo}\sqrt{E_{EM3} \times E_{HAD}}. \tag{4.1.7}$$

The w^{Cryo} corresponds to a calibration weight, while the E_{EM3} and E_{HAD} are the amount of jet energy deposited to the third layer of the electromagnetic calorimeter and to the first layer of the hadronic calorimeter, respectively. The inclusion of the cryostat term is very important as for high-p_{T} jets it accounts for a 5% of its total energy [147].

The muon term

Lastly, the muon term takes into account the p_{T} of muons that reside within $|\eta| \leq 2.7$. For the region $|\eta| \leq 2.5$, only combined muons are accounted for, namely muons with a Muon Spectrometer track matched to an Inner Detector detector track, while for $|\eta| > 2.5$, where there is no Inner Detector coverage, muons from the Muon Spectrometer are used. Irrespectively of the region, the transverse momentum measurement that is used in the muon term is taken from the Muon Spectrometer component. The reason for this is that the energy deposition in the calorimeter is already included at the $E^{Calo}_{x,y}$ term and if combined muons where to be used then this would lead to double-count the energy loss.

4.2 Monte Carlo correction factors

One of the most important aspects in an experiment is the correct description of the detector performance by the Monte Carlo simulated events. Using well known physics processes it is possible to assess the level of agreement between data and Monte Carlo and apply corrections accordingly. For the results shown in the rest of the thesis the following corrections have been applied at the object reconstruction level by default[6].

4.2.1 Electron energy scale and resolution

Resonances such $Z \to e^+e^-$ or $J/\psi \to e^+e^-$ are used to determine the energy scale of electrons and correct the electromagnetic cluster energy [148]. Typically, the reconstructed invariant mass peak is required to match the well-known resonance line-shape of the respective particle. The extracted scale is quantified by the dimensionless parameter α as a function of pseudo-rapidity, and subsequently the correction is applied on data events, for each identified electron, using the following relation:

$$E_{new} = \frac{E}{1+\alpha}. \tag{4.2.1}$$

The values of α are shown in figure 4.11.

Both Z boson events and J/ψ events are examined in the di-electron final state with respect to their invariant mass distribution. Although for the latter the agreement between data and Monte Carlo is shown to be very good, for the Z boson events significant discrepancies have been observed. This effect is attributed to the modeling of the constant term in the electron energy resolution ($\sigma_E/E \approx 10\%/\sqrt{E} \oplus 1\%$) as it is the main contributing factor at the high electron energy region. As a result, a correction is applied to each electron in the Monte Carlo samples by smearing its energy according to new constant terms which have shown to achieve a good agreement. More details on the results for re-scaling and smearing the electrons can be found in [149].

[6]Unless stated otherwise within the text.

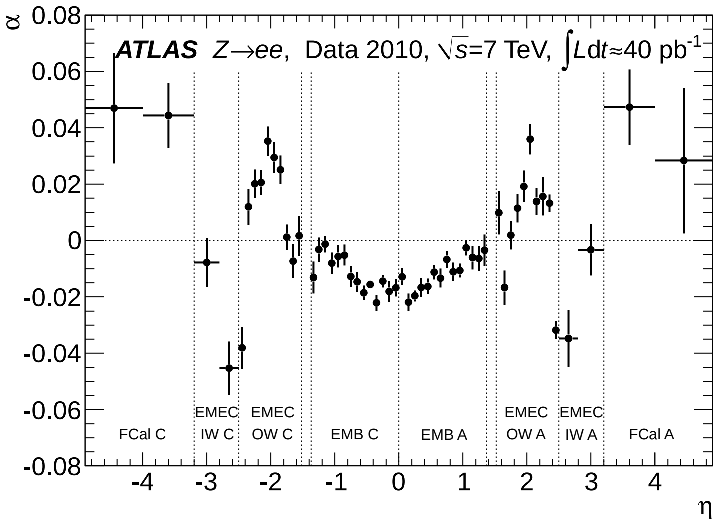

Figure 4.11: *The dimensionless electron energy scale parameter (α) as a function of pseudo-rapidity measured from $Z \to e^+e^-$ decays. Plot taken from [148].*

4.2.2 Muon momentum scale and resolution

Studies performed with the first data have shown discrepancies on the reconstructed Z boson invariant mass, obtained from di-muon events, when comparing to the Monte Carlo. This is attributed to inaccurate modeling of the material budget and the alignment of the different sub-detectors which affect the estimation of the muon's momentum and resolution. In order to improve the agreement the following smearing term is applied on each muon on the Monte Carlo:

$$\left(\frac{1}{p_{\mathrm{T}}}\right)_s = \frac{1}{C_1} \times \left(\frac{1}{p_{\mathrm{T}}}\right)_{MC} \times (1 + G(0,1) \times C_2)\,, \tag{4.2.2}$$

where $\left(\frac{1}{p_{\mathrm{T}}}\right)_s$ is the muon curvature after the smearing, $(\frac{1}{p_{\mathrm{T}}})_{MC}$ is the muon curvature before the smearing, and C_1 and $C2$ are the momentum scale and resolution smearing terms respectively. The function $G(0,1)$ corresponds to a gaussian with mean $\mu = 0$ and width $\sigma = 1$ which is used to randomly generate a number. Both the C_1 and C_2 are tuned based on the Z boson line-shape and are binned in different η bins.

For combined muons, the Inner Detector and the Muon Spectrometer components are treated independently. Once the smeared p_{T} is estimated for each component, a weighted average is taken for its expected resolution. This is done because the Inner Detector and the Muon Spectrometer components contribute in a different way to the combined muon's resolution, depending to a large extend on the the total momentum of the muon. A detailed discussion of the muon momentum scale and resolution can be found here [150].

4.2.3 Jet energy resolution

The jet resolution term is written in the following form:

$$\frac{\sigma_{p_{\mathrm{T}}}}{p_{\mathrm{T}}} = \frac{N}{p_{\mathrm{T}}} \otimes \frac{S}{\sqrt{p_{\mathrm{T}}}} \otimes C, \tag{4.2.3}$$

where N is a term that parametrizes noise fluctuations and offset energy from multiple pile-up activity (noise term), S parametrizes stochastic fluctuations in the energy measured from the hadronic shower (stochastic term), and C parametrizes constant fluctuations (constant term).

Using di-jet QCD events the energy resolution of jets was examined directly from data and a good agreement was in general observed [151]. However minor corrections are still applied to the Monte Carlo to further improve their description of data. The transverse momentum of each jet is corrected by a scale value following the relation:

$$(p_{\mathrm{T}})_s = (p_{\mathrm{T}})_{MC} \times (1 + G(0, S)), \tag{4.2.4}$$

where $(p_{\mathrm{T}})_{MC}$ and $(p_{\mathrm{T}})_s$ are the p_{T} of the jet before and after the smearing, and $G(0, S)$ is a gaussian random number generator with a mean of zero and a width taken from S, the smearing term. The S is typically obtained from look-up tables and it depends on the p_{T} and the rapidity (y) of the jet.

4.2.4 Heavy flavor composition in W+jets events

The composition of W+jets events in the Monte Carlo includes those events with jets induced by heavy flavor quarks, namely $Wb\bar{b}$, $Wc\bar{c}$ and Wc; extra jets from lighter quarks may also be present in these event types. The exact heavy flavor fraction in those events is not known with good accuracy as it depends on the heavy flavor Parton Distribution Functions (PDFs) and for this reason a better approximation is obtained using a data-driven approach. The method estimates the fraction of b-tagged events in the kinematic region where exactly two jets are identified; it is explained in detail in [152]. The result shows that no correction for Wc events is required but the simulation underestimates the fraction of $Wb\bar{b}$ and $Wc\bar{c}$ by 30% and therefore a per event scale factor should be applied.

4.2.5 Flavor tagging

For analyses that depend on event selection based on the identification of b-jets, the calibration of the flavor tagging algorithms is an important step. The b-tagging efficiencies for the `SVO` tagger have been measured in data using an enriched $b\bar{b}$ di-jet sample where a significant muon content is observed. In addition, the mis-tag rate, namely the rate at which light flavored jets are mistakenly seen as b-jets, is also examined for `SVO`. Further details on these methods can be found in [144].

The comparison of the data-driven measurements with the Monte Carlo shows differences which are parametrized in the form of scale factors. These scale factors are applied on the Monte Carlo in order to improve the agreement with the data and they depend on the flavor of the jet (b-jet, c-jet or light jet) as well as on its p_{T} and η. Summarizing, the scale factor for b-jet tagging efficiency is given by:

$$SF_{tagged}(p_{\mathrm{T}}, |\eta|) = \frac{\epsilon^{data}(p_{\mathrm{T}}, |\eta|)}{\epsilon^{MC}(p_{\mathrm{T}}, |\eta|)}. \tag{4.2.5}$$

While the scale factor for b-jets that are not tagged is given by:

$$SF_{not-tagged}(p_{\mathrm{T}}, |\eta|) = \frac{1 - SF_{tagged}(p_{\mathrm{T}}, |\eta|)\epsilon^{MC}(p_{\mathrm{T}}, |\eta|)}{1 - \epsilon^{MC}(p_{\mathrm{T}}, |\eta|)}. \tag{4.2.6}$$

The above formulation is also used for c-jets that are either tagged or not-tagged with the only difference that the estimated uncertainty in the scale factors is doubled. Lastly, and in addition to the above, a scale factor for the mis-tag rate of light jets is obtained. A complete list of the values of the scale factors for the `SVO` tagger at the 50% working point, which is of interest for this thesis, is provided in table 4.3.

p_{T}range (GeV)	b-tagging Scale Factor	Mis-tag rate Scale Factor	
		$\lvert\eta\rvert < 1.2$	$1.2 < \lvert\eta\rvert < 2.5$
20-25	0.872 ± 0.208	1.19 ± 0.43	1.36 ± 0.49
25-40	0.925 ± 0.105	1.36 ± 0.35	1.39 ± 0.32
40-60	0.942 ± 0.074	1.03 ± 0.19	1.20 ± 0.19
60-75	0.947 ± 0.102	1.07 ± 0.12	1.01 ± 0.22
75-90	0.947 ± 0.150	idem	idem
90-140	0.947 ± 0.200	0.95 ± 0.15	1.01 ± 0.19
140-200	idem	1.05 ± 0.14	0.99 ± 0.28
200-300	idem	1.29 ± 0.30	0.92 ± 0.60
300-500	idem	0.85 ± 0.51	1.70 ± 1.35

Table 4.3: *Scale factors for the tagging efficiency of b-jets and the mis-tag rate of light jets. The scale factor for the tagging efficiency of c-jets is the same but with a double uncertainty. All numbers correspond to the* 50% `SV0` *tagger working point. Numbers taken from [153].*

4.3 "Good" object definitions

To increase the quality of the $t\bar{t}$ single-lepton signature the reconstructed objects are required to pass a number of precise identification criteria which are based on the characteristics of the $t\bar{t}$ topology. The selected objects are defined as "good" and the event selection is applied later on these.

"Good" electrons

Selecting good electrons is essential for the search in the $t\bar{t}(e\nu_e)$ channel. The electron must satisfy the following requirements:

- Be reconstructed by the algorithms presented in section 4.1.1.
- Be identified as a tight electron. This is motivated by the fact that although the efficiency of signal electrons drops to 75%, the expected fake rate and consequently the background acceptance is significantly decreased.
- Must lie within $|\eta_{cluster}| \leq 2.47$, where $\eta_{cluster}$ is the pseudo-rapidity of the calorimeter cluster, but if it falls within $1.37 < |\eta_{cluster}| < 1.52$ it is rejected. The upper limit of $|\eta_{cluster}| \leq 2.47$ is set because of the acceptance of the Inner Detector which is up to $|\eta| \leq 2.5$ and is an essential part of the reconstruction algorithms. The small difference between the actual cut and the ID acceptance is because the pseudo-rapidity of the electron is not coming from the reconstructed track but from the calorimeter. On the other hand, the rejected region corresponds to uninstrumented parts of the detector which are not well modeled in the Monte Carlo.
- Be isolated. The calorimetric isolation parameter (`etcone`) is used in this case (see section 4.1.1) with an R_0 parameter set to 0.2. The energy deposition in the calorimeter and within the defined cone should not exceed 4 GeV.
- Finally, the electron should have transverse energy (E_T) of at least 20 GeV.

The above criteria take into account the distinct characteristics of electrons that result from the W decay in a $t\bar{t}$ event. However, detector problems such as: dead or non-nominal high-voltage regions, channels with very high noise which are masked by the reconstruction or dead front-end boards, must also be taken into account. For this reason, dedicated $\eta-\phi$ maps of the calorimeters are created for each data-taking run where such problems are documented. For each electron the cluster coordinates ($\eta_{cluster}, \phi_{cluster}$) are checked in the map and a decision is made on whether it will be rejected or not. This is applied not only in data but also in Monte Carlo to get a better agreement. For the electrons selected here the map corresponding to the highest integrated luminosity is used.

"Good" jets

Motivated by the performance comparisons shown in section 4.1.3, all jets that are considered in this analysis use as input topological clusters and are reconstructed with the `anti-`$k_\perp$ algorithm with an R parameter of 0.4. In addition, as mentioned above, the `EMJES` calibration scheme is used. At the software level these jets are denoted as `AntiKt4TopoEMJets`.

For the definition of a good jet, the following requirements are applied:

- It does not overlap within $\Delta R \leq 0.2$ with a "good" electron. The coordinates used for the electron are taken from its track component ($\eta_{track} - \phi_{track}$) and for the jet they are obtained before applying the calibration ($\eta_{em} - \phi_{em}$). However, for each electron only one jet, the closest, is removed.
- Unless the top quark-pair is boosted, the jets are produced in the central region of the detector since they are the result of the decay of a heavy object. Thus, it is required that the jet lies within $|\eta| \leq 2.5$.
- Lastly, the transverse momentum is required to be $p_{\mathrm{T}} \geq 20$ GeV.

In addition to the above cuts, a good jet is flagged as b-tagged if the weight assigned to it by the `SV0` algorithm is greater than 5.82. This weight corresponds to the working point of 50% efficiency as shown in section 4.1.4.

"Good" muons

As mentioned in section 4.1.2 all muons used in this thesis come from the `MuID` collection. Specifically for the analysis presented here, a good muon should:

- Be a tight muon. As shown in figure 4.4 the tight requirements select muons with an efficiency above 90% and have a better fake rejection.
- Be a combined `MuID` muon. Hence, `MuGirl` muons are not considered in this analysis.
- The muon must satisfy the quality requirements for the Inner Detector track quality which include the detector status during data-acquisition. Documented in detail in [154].
- It must be within $|\eta| \leq 2.5$ which is the Inner Detector's acceptance region.
- The muon must be isolated. Both calorimetric and tracking isolation is used in this case (see section 4.1.2). For both terms, the cone parameter is set at 0.3 and the energy content within the cone should not exceed 4 GeV.
- To improve the isolation and to avoid selecting mainly QCD events in which a b-quark decayed leptonically, any muon that is within $\Delta R \leq 0.4$ from a jet with $p_{\mathrm{T}} \geq 20$ GeV is rejected.
- Lastly, the transverse momentum of the muon must be at least 20 GeV.

$E_{\mathrm{T}}^{\mathrm{miss}}$ *definition*

The $E_{\mathrm{T}}^{\mathrm{miss}}$ reconstruction used in this thesis uses the definition given earlier with a refined calorimeter term which is derived as follows:

$$E_{x,y}^{Calo} = E_{x,y}^{RefElec} + E_{x,y}^{RefPhoton} + E_{x,y}^{RefTau} + E_{x,y}^{RefJet} + \\ + E_{x,y}^{RefSoftJet} + E_{x,y}^{RefMuon} + E_{x,y}^{CellOut}, \quad (4.3.1)$$

where the parameters refer respectively to the contribution from electrons, photons, muons that deposit energy in the calorimeter, taus that decay hadronically, jets with $p_{\mathrm{T}} \geq 20$ GeV, soft jets with $5 \leq p_{\mathrm{T}} \leq 20$ GeV, and finally calorimeter cells that reside within the topological cluster but do not contribute to any of the above objects. The inclusion of the last term is proven to give a better absolute $E_{\mathrm{T}}^{\mathrm{miss}}$ value and a better resolution [147].

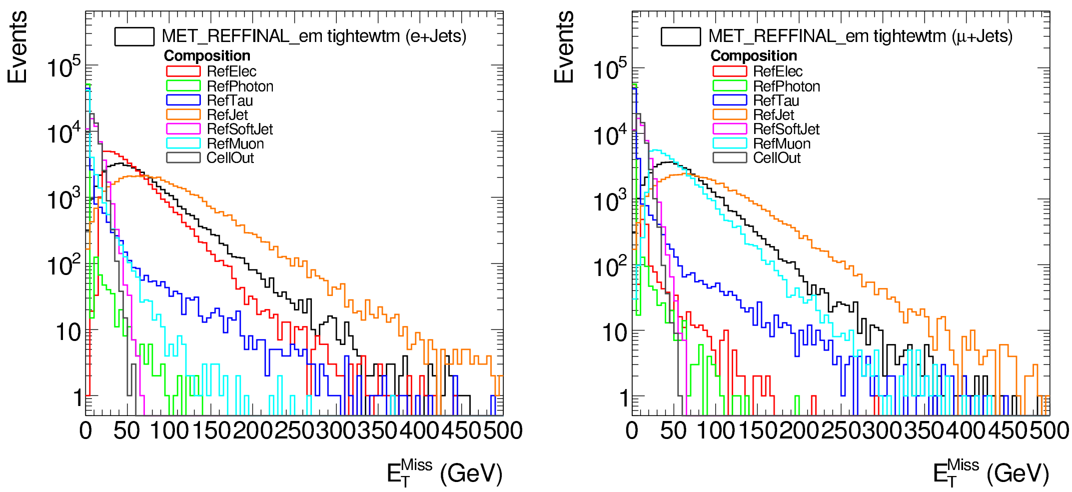

(a) *Electron channel* (b) *Muon channel*

Figure 4.12: *The total $E_{\mathrm{T}}^{\mathrm{miss}}$ and the E^{Calo} term components for single-lepton $t\bar{t}$ events. Plots taken from [155].*

A detailed description of the object selection requirements as well as the relevant calibration schemes that are used for the calorimeter term in this thesis are documented in [155]. Figure 4.12 shows the components of the calorimeter term together with the total $E_{\mathrm{T}}^{\mathrm{miss}}$ measurement - denoted as `MET_REFFINAL_em_tightewtm` - for $t\bar{t}(e)$ and $t\bar{t}(\mu)$ events as calculated for this thesis.

4.4 Baseline top quark-pair event selection

For each of the $t\bar{t}(e)$ or $t\bar{t}(\mu)$ final states we apply certain requirements. These involve: the online selection criteria, namely the trigger used for accepting the events to be registered in the data sample; the data quality criteria, which are requirements related with the status of the detector and which affect the object reconstruction; the analysis requirements, which are based on the object definitions given in section 4.3 and are motivated by the topology of the events.

4.4.1 Data sample

As mentioned already in 3.2.1, the data recorded by ATLAS are separated in periods and further into sub-periods. Because the 2010 physics run was the very first physics data-taking of ATLAS, it served to a large extend for commissioning and understanding of the detector. For the $t\bar{t}$ measurement, the data from sub-period E4 and after are used as earlier periods suffer from technical shortcomings that are difficult to treat in the analysis. However, the data content of the excluded periods does not represent a significant fraction of the data. The integrated luminosity that was registered by the detectors is shown in table 4.4. The relative uncertainty on the integrated luminosity collected is measured in [156] and is found to be $\pm 3.4\%$. For the present analysis only data from the electron and the muon streams are used and the total events that are processed are about 16.8 million from the first and around 13.5 million from the second stream.

Period	$\int \mathcal{L} dt$ (pb^{-1})
A-E3	0.75
E4-E7	0.51
F (1-2)	1.53
G (1-6)	5.53
H (1-2)	6.99
I (1-2)	20.73
All Periods	36.05
excl. A-E3	35.30

Table 4.4: *Total integrated luminosity registered by ATLAS in 2010 with respect to the various data-taking periods.*

4.4.2 Trigger selection

The first step in the selection procedure of a data sample is to require that the events have been accepted by a certain trigger. From all the distinctive characteristics of the $t\bar{t}$ single-lepton topology, the simplest and most straightforward approach is to use a single-lepton trigger for each of the channels that are analyzed. One of the main considerations in the decision of a trigger is its energy or transverse momentum threshold. Having a threshold as low as possible increases the overall acceptance of the signal. However, this decision depends largely on the instantaneous luminosity delivered by the LHC which, as it increases, also increases the rate of the triggers; if the threshold is too low, triggers might need to be pre-scaled[7]. In addition, it must also be considered that not all the possibilities can be exploited at the beginning of the experiment. For example, leptons coming from $t\bar{t}$ are also expected to be well isolated with no jet activity around their trajectory. However, using such isolation criteria at the trigger level requires a better understanding and calibration of the detector. In the following, the triggers used for each of the channels of this analysis are discussed.

[7] A pre-scaled triggered performs the same task as a normal trigger with the only difference that it will allow a fraction of the total events to be accepted. For example a pre-scale of 1000 for a trigger will only give a positive decision for 1 out of 1000 fired events.

Electron channel

For the $t\bar{t}(e)$ channel the `Egamma` stream is used and the selection trigger is `EF_e15_medium` which is used consistently in both Monte Carlo and data. This trigger follows the chain:

$$\texttt{L1\_EM10} \rightarrow \texttt{L2\_e15\_medium} \rightarrow \texttt{EF\_e15\_medium}.$$

At the L1, at least one calorimeter cluster with at least 10 trigger counts is required, where 1 trigger count corresponds to approximately 1 GeV in the calorimeters. At the L2, the electron is required to have an $E_T \geq 15$ GeV and at the Event Filter, where a better resolution can be achieved, it must still pass the 15 GeV threshold but also be identified as a "medium" electron. The identification requirements for "medium", as well as for "loose" and "tight", at the trigger level are not exactly the same as in the offline reconstruction; they are documented in [157].

Table 4.5 shows the integrated efficiency for each trigger level as calculated using the tag-and-probe method on identified $Z \rightarrow e^+e^-$ events [157]. The overall trigger efficiency for an electron of $E_T > 20$ GeV is well close to 100%.

Trigger	**Efficiency** (%)	
	Data	**Simulation**
`L1_EM10`	$99.90 \pm 0.03(stat.) \pm 0.02(syst.)$	$99.995 \pm 0.001(stat.)$
`L2_e15_medium`	$99.60 \pm 0.06(stat.) \pm 0.05(syst.)$	$99.699 \pm 0.004(stat.)$
`EF_e15_medium`	$98.97 \pm 0.09(stat.) \pm 0.09(syst.)$	$99.445 \pm 0.006(stat.)$

Table 4.5: *Integrated efficiency for each trigger level of the* `e15_medium` *chain at* $E_T >$ 20 GeV, *using tag-and-probe on* $Z \rightarrow ee$ *events. Numbers taken from [157].*

Muon channel

For the $t\bar{t}(\mu)$ channel the `Muon` stream data are used and three different triggers are utilized, each corresponding to a different data-taking period. In section 3.1 a detailed description of the muon online reconstruction was given. From period E4 until and including period F the `EF_mu10_MSonly` trigger is used. The chain followed is:

$$\texttt{L1\_MU0} \rightarrow \texttt{L2\_mu10\_MSonly} \rightarrow \texttt{EF\_mu10\_MSonly}.$$

At the L1, the trigger item uses the 'open' road configuration, thus a pass-through threshold of approximately 4 GeV is effectively applied. At the L2, the trigger uses the `muFast` algorithm (see section 3.1.2) to reconstruct the track, while at the Event Filter the result is more refined with the use of the `TrigMuonEF` algorithm but without using the `Combiner` step (see section 3.1.3). The event is accepted if at each level the muon satisfies the momentum threshold requirement that were given in table 3.4. For the periods G1 to G5 the `EF_mu13` trigger is used following the chain:

$$\texttt{L1\_MU0} \rightarrow \texttt{L2\_mu13} \rightarrow \texttt{EF\_mu13}.$$

The Level-1 trigger is the same as as before. At the HLT the Inner Detector information is used and a combined track is fitted. For the L2 trigger the `muComb` algorithm is used and for the Event Filter the `TrigMuonEF` including the `Combiner` step. The transverse momentum thresholds applied at L2 and Event Filter are showed in table 4.6

Lastly, from period G6 and until the end of the 2010 proton-proton collisions the trigger used is `EF_mu13_tight` which is similar to the `EF_mu13` with the exception that at Level-1 it is seeded by `L1_MU10`. Most of the statistics used in the analysis are collected during this

$\lvert\eta\rvert$ bin	p_T threshold (GeV)	
	Level-2	**Event Filter**
$[0.00, 1.05]$	12.6	12.67
$(1.05, 1.50]$	12.2	12.55
$(1.50, 2.00]$	12.2	12.49
$(2.00, \infty)$	12.4	12.46

Table 4.6: *Level-2 and Event Filter p_T thresholds with respect to $\lvert\eta\rvert$ for the* `mu13` *chain. Numbers taken from [122].*

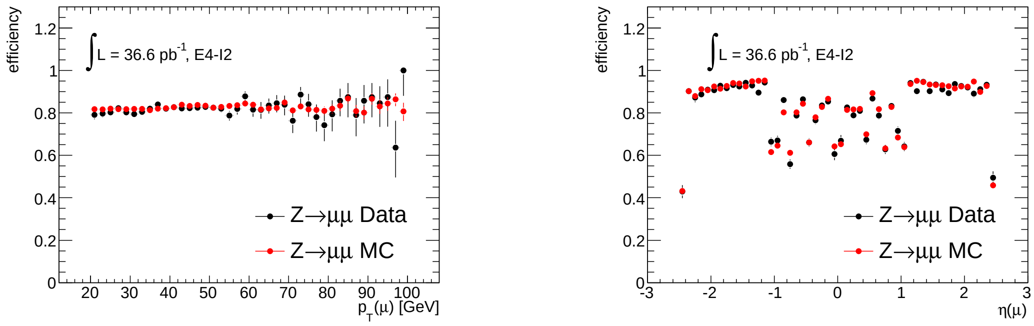

(a) *Efficiency vs. p_T*

(b) *Efficiency vs. η*

Figure 4.13: *Muon trigger efficiency distributions with respect to the muon p_T (a) and the pseudo-rapidity (b) calculated with tag-and-probe from $Z \to \mu^+\mu^-$ events. The result is overlaid with the Monte Carlo. Plots taken from [148].*

period, thus in order to retain simplicity only the `EF_mu13_tight` is used for the Monte Carlo samples. The efficiency of these triggers has been extracted using the tag-and-probe method on $Z \to \mu^+\mu^-$ events. This method has been discussed in detail in section 3.3 where the results of the study on the `EF_mu10_MSonly` trigger were shown. Here we use the results as obtained from the analysis documented in [148]. Figure 4.13 shows the efficiency binned as a function of p_T and η. A good agreement between data and Monte Carlo is evident.

4.4.3 Offline event selection

Before an event is evaluated for the physics analysis cuts, it must fulfill certain requirements that take into account the machine conditions and the quality of the reconstructed data. These data-quality cuts are:

- **Non-collisions background cut:** To reject events that are not related to a collision, a reconstructed primary vertex is required with at least 5 tracks associated to it.
- **Jet-cleaning cut:** The quality of the jet reconstruction is ensured with a set of cuts which are referred to as "jet-cleaning" and are documented in detail in [158]. These guarantee that out-of-time activity or defects in the calorimeters during data-taking do not affect the analysis. The event is eventually rejected if a jet with $p_T \geq 20$ GeV is flagged as `LooseBad`. This particular cut is not applied in Monte Carlo.
- **Electron-muon overlap cut:** Finally, an event is rejected when a "good" electron and a "good" muon, but without the muon-jet overlap removal step (see section 4.3), are

identified as sharing the same Inner Detector track.

If the event is not rejected by the data-quality cuts it is tested against the following cuts, which also classify the event as belonging to the electron channel (e-channel) or to the muon channel (μ-channel):

- **Trigger cut:** The electron or the muon Event Filter trigger must have passed for the event. The relevant triggers are presented in section 4.4.2.
- **Charged lepton cut:** Exactly one "good" lepton, either an electron or a muon must be identified. In addition, the lepton needs to be matched with the corresponding Event Filter object using a ΔR cut in $\eta - \phi$ space of 0.15. The electron is matched using the calorimeter coordinates ($\eta_{cluster} - \phi_{cluster}$) with the Region-of-Interest of the trigger, while the muon matches its reconstructed track with the track of the trigger object.

One of the most prominent backgrounds are the QCD multi-jet final states due to their large cross-section. Naturally, these topologies do not result in energetic and isolated leptons but given the large number of events it is possible that a considerable amount of them survives the trigger and charged lepton requirements. To reduce this background two observables can be used: the reconstructed $E_{\mathrm{T}}^{\mathrm{miss}}$ component of the events and the transverse mass of the W boson ($M_{W,T}$). The former is motivated by the presence of the energetic neutrino in $t\bar{t}$ final states which results in a peak at high $E_{\mathrm{T}}^{\mathrm{miss}}$ values. The latter exploits the fact that the leptonically decaying W boson in the $t\bar{t}$ events can be probed by its decay products. The $M_{W,T}$ is defined by the following:

$$M_{W,T} = \sqrt{(E_{\mathrm{T}}^{\mathrm{miss}} + p_{\mathrm{T},\ell})^2 - \sum_{i=x,y} (E_i^{\mathrm{miss}} + p_{i,\ell})^2} \; . \tag{4.4.1}$$

The discriminating power of these observables is shown in figure 4.14 where they are plotted for the QCD multi-jet and the $t\bar{t}$ samples after applying the trigger and charged lepton requirements for the μ-channel. In addition, figure 4.15 shows the two-dimensional $E_{\mathrm{T}}^{\mathrm{miss}} - M_{W,T}$ plot for both channels after the trigger and charged lepton cuts. Utilizing these two observables the following cuts are applied at the analysis level:

- **$E_{\mathrm{T}}^{\mathrm{miss}}$ cut:** For the e-channel the missing transverse energy component is required to be $E_{\mathrm{T}}^{\mathrm{miss}} > 35$ GeV while for the μ-channel it is $E_{\mathrm{T}}^{\mathrm{miss}} > 25$ GeV.
- **W boson transverse mass cut:** For the μ-channel the measurement of $M_{W,T}$ is summed with the $E_{\mathrm{T}}^{\mathrm{miss}}$ to form the *triangular* cut; the cut requires $E_{\mathrm{T}}^{\mathrm{miss}} + M_{W,T} >$ 60 GeV. For the e-channel no triangular cut is used but it is still required that $M_{W,T} >$ 25 GeV.

The considered single-lepton $t\bar{t}$ final states have four jets in their final topology with two originating from the hadronization of a b-quark. Additional jets can be produced through initial or final state radiation (ISR/FSR). This is different from the leptonically decaying W+jets events where jets are exclusively produced by ISR/FSR. In addition, jets in $t\bar{t}$ events being the product of the decay of heavy particles have on average higher transverse momenta. In figure 4.16 the $t\bar{t}$ and W+jets are compared in the μ-channel for their "good" jet content in terms of multiplicity and of the p_{T} of the fourth highest-p_{T} "good" jet. Evidently, the $t\bar{t}$ is dominant in higher multiplicities and high transverse momenta. Therefore the following cuts can be applied which also define the signal region of the analysis:

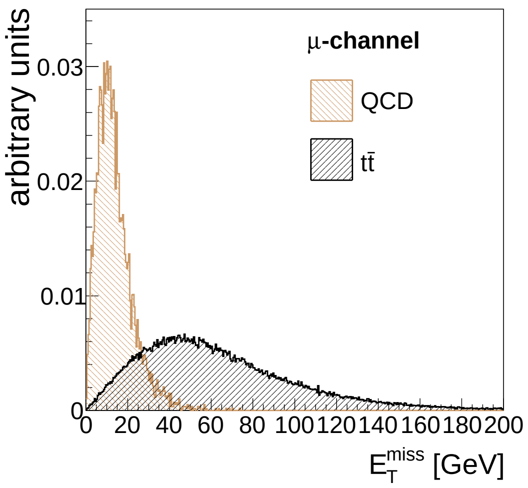

(a) E_T^{miss} *component* (b) *W boson transverse mass*

Figure 4.14: *Comparison of $t\bar{t}$ events with the QCD multi-jet events after the trigger and charged lepton cuts in the μ-channel. The reconstructed E_T^{miss} component (a) and the $M_{W,T}$ (b) are shown. The behavior also holds for the e-channel cuts. Histograms normalized to unit area.*

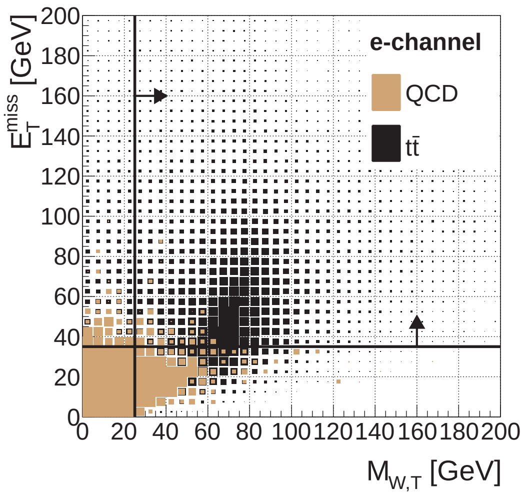

(a) *e-channel* (b) *μ-channel*

Figure 4.15: *E_T^{miss} versus $M_{W,T}$ for the e-channel (a) and the μ-channel after trigger and lepton requirements. The triangular cut is defined by the sum of these two variables. In this analysis it is used for the μ-channel. The lines with the arrows indicate the phase space that is selected.*

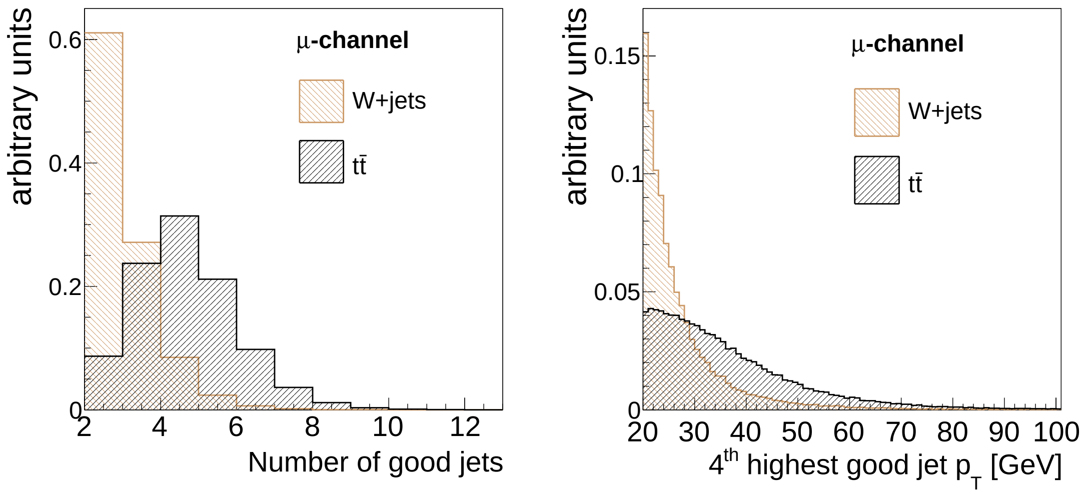

(a) (b)

Figure 4.16: *The "good" jet multiplicity (a) and the p_{T} of the fourth highest-p_{T} jet (b) in the $t\bar{t}$ and W+jets events. The trigger and charged lepton requirements for the μ-channel selection are applied as well as a preselection of at least two good jets. The results are similar for the e-channel cuts. Histograms are normalized to unit area.*

- **Jet cut:** The event must have at least four good jets with $p_{\mathrm{T}} \geq 25$ GeV.
- **b-jet cut:** At least one good jet with $p_{\mathrm{T}} \geq 25$ GeV must be identified as a b-jet, that is to say it must have a weight of 5.85 from the `SV0` algorithm. This weight corresponds to the 50% efficiency working point, see section 4.1.4.

4.4.4 Cut-flow

In table 4.7 the cut-flow is given for each channel and for each Monte Carlo sample for all but the jet cuts[8]. Clearly, the charged lepton cut as well as the missing transverse energy and the transverse W mass cuts reduce significantly the QCD background. On the other hand, the rest of the background processes, which can easily provide an isolated lepton, are affected less and in particular the W+jets which still contributes significantly. Table 4.8 shows the surviving Monte Carlo and data events after applying the jet cut broken down into two bins: one where at least one jet is b-tagged, which corresponds to the signal region, and one where no b-tagged jet exists. The combination of the two bins defines the pre-tagged sample. The background contribution, and especially the W+jets events, is largely reduced in the signal region ($N_{j,25} \geq 4$, $N_{bj,25} \geq 1$) and the signal-to-background ratio (S/B), as given purely by the Monte Carlo, is at 4.7 for the μ-channel and 5.7 for the e-channel. For the pre-tagged sample the S/B is only 0.7 for the μ-channel and 0.8 for the e-channel, highlighting the importance of b-tagging.

[8]It should be reminded that the QCD Monte Carlo that are used are heavily filtered as discussed in the first chapter, and the filters are effectively cancelled out only at the last steps of the event selection procedure.

μ-channel

	Trigger & Data Quality cuts	Charge Lepton cut	$E_{\mathrm{T}}^{\mathrm{miss}}$ cut	Triangular cut
$t\bar{t}$	1172.5±2.0	624.6±1.8	545.3±1.7	522.3±1.7
W+**jets**	225296±143	172272±128	144261±117	143641±116
Z+**jets**	37991±57	15297±37	6036±24	5721±23
Single-top	360.8±0.7	210.0±0.8	177.3±0.7	170.0±0.7
Dibosons	418.6±0.8	218.0±0.7	170.5±0.6	164.5±0.6
QCD	$2.5 \cdot 10^6 \pm 3.0 \cdot 10^3$	19519±259	1906±80	333.7±34.1
Data	$4.818 \cdot 10^6$	323024	187246	181042

e-channel

	Trigger & Data Quality cuts	Charge Lepton cut	$E_{\mathrm{T}}^{\mathrm{miss}}$ cut	$M_{W,T}$ cut
$t\bar{t}$	1031.6±2.0	568.9±1.7	429.1±1.5	377.5±1.4
W+**jets**	220692±142	131356±104	52370±65	51736±65
Z+**jets**	34565±55	16984±39	655.0±7.6	234.2±4.5
Single-top	315.1±0.7	183.0±0.8	124.3±0.6	113.2±0.6
Dibosons	431.5±0.2	183.7±0.6	100.4±0.4	93.0±0.4
QCD	317293±1060	5229±141	366.2±37.3	113.4±20.9
Data	$8.119 \cdot 10^6$	372085	68101	63881

Table 4.7: *Event cut-flow from left to right for the Monte Carlo samples and the collected data. All numbers correspond to 35.3 pb^{-1} of integrated luminosity and all uncertainties are due to statistics.*

	μ-channel		**e-channel**	
	$N_{j,25} \geq 4$		$N_{j,25} \geq 4$	
	$N_{bj,25} = 0$	$N_{bj,25} \geq 1$	$N_{bj,25} = 0$	$N_{bj,25} \geq 1$
$t\bar{t}$	70.7±0.6	193.5±1.0	51.3±0.5	136.7±0.8
W+**jets**	270.1±3.1	25.5±0.9	160.4±2.0	14.7±0.6
Z+**jets**	21.6±1.2	2.9±0.4	18.8±1.2	2.1±0.3
Single-top	5.2±0.1	9.1±0.1	3.8±0.1	6.7±0.1
Dibosons	3.4±0.1	0.0±0.0	2.2±0.1	0.2±0.0
QCD	14.3±7.1	3.5±3.4	19.9±8.7	0.1±0.1
Total MC	385.3±7.9	234.5±3.7	256.4±9.1	160.5±1.1
Data	373	234	239	157

Table 4.8: *Event yields of the two channels after all the cuts including the jet cut, separated in an exclusive zero b-jets bin and an inclusive one b-jet bin. All numbers correspond to 35.3 pb^{-1} of integrated luminosity and all uncertainties are due to limited statistics.*

4.5 A preamble to the cross-section analysis

The cross-section analysis performed in this thesis will be presented in detail in chapter 6. However, some key aspects upon which the analysis depends are presented here.

The following general relation holds for any cross-section calculation:

$$\sigma = \frac{N_{signal}}{\int \mathcal{L}dt \cdot \epsilon_{signal}} \ , \tag{4.5.1}$$

where the N_{signal} is the number of identified signal events, $\int \mathcal{L}dt$ is the integrated luminosity and ϵ_{signal} is the selection efficiency of the signal events. In the most straight-forward method, the number of signal events can be extracted by subtracting from the collected data the expected background contribution (cut-and-count):

$$N_{signal} = N_{observed} - N_{background} \ ,$$

where the $N_{background}$ can be calculated by determining the normalization of each contributing process. For following this approach it is preferable to benefit from using a kinematic region where the S/B ratio is large so as to reduce the contribution on the uncertainty coming from $N_{background}$.

4.5.1 The template fit approach

A more evolved method is implemented for the analysis presented in this thesis. Firstly, an extended kinematic region is used that includes all events that pass the baseline selection but requiring at least three "good" jets with $p_{\mathrm{T}} \geq 25$ GeV. In this way, information from a significantly larger dataset is exploited, as opposed to the one from the signal region only. Based on this selection, four distinct regions are defined according to their jet multiplicity, all being mutually exclusive:

- Bin-30 : Exactly three jets ($N_{j,25} = 3$) with no b-jets ($N_{bj,25} = 0$).
- Bin-31 : Exactly three jets ($N_{j,25} = 3$) with at least one b-jet ($N_{bj,25} \geq 1$).
- Bin-40 : At least four jets ($N_{j,25} \geq 4$) with no b-jets ($N_{bj,25} = 0$).
- Bin-41 : At least four jets ($N_{j,25} \geq 4$) with at least one b-jet ($N_{bj,25} \geq 1$), which is the signal region defined previously.

Table 4.9 shows the event yields for the exclusive three-jet bins; the inclusive four-jet bins are already shown in 4.8.

The method, instead of simply relying on the counting of data events and subtracting the background, determines the contributions of both signal and background events, in each bin, from the data; practically constraining the result to the number of observed events. To achieve this, the signal and background are characterized by a single observable: the reconstructed invariant mass of the top quark. This is a straightforward choice considering that its distribution is expected to peak in the region of the true mass of the top providing a distinctive shape with respect to the shape of the expected background processes. Eventually, the shape of the observable is obtained individually for signal and background and each remains fixed to serve as template in the fitting procedure. The relative normalization between signal and background shapes becomes then the floating parameter.

	μ-channel		**e-channel**	
	$N_{j,25}=3$		$N_{j,25}=3$	
	$N_{bj,25}=0$	$N_{bj,25}\geq 1$	$N_{bj,25}=0$	$N_{bj,25}\geq 1$
$t\bar{t}$	53.6±0.5	103.8±0.7	38.2±0.4	76.3±0.6
W+jets	952.5±7.1	49.9±1.3	529.9±3.8	28.2±0.8
Z+jets	65.0±2.3	4.0±0.4	31.7±1.8	1.8±0.3
Single-top	12.8±0.2	17.6±0.2	9.1±0.1	12.2±0.2
Dibosons	13.8±0.2	1.2±0.05	8.3±0.1	0.7±0.03
QCD	28.4±7.1	3.6±3.6	27.0±10.0	11.5±6.7
Total MC	1126.1±10.3	180.1±3.9	644.2±10.8	130.7±6.8
Data	1027	213	594	173

Table 4.9: *Event yields of the two channels after all the cuts but with the jet cut requiring exactly three good jets. The events are separated in an exclusive zero b-jets bin and an inclusive one b-jet bin. All numbers correspond to* 35.3 *pb*$^{-1}$ *and all uncertainties are statistical only.*

Calculating the M_{jjj} observable

In the single-lepton topology the invariant mass of the top quark is derived from the hadronically decaying side of the event which, consisting of three jets, is fully reconstructable. However, given the increased jet multiplicity of $t\bar{t}$ events, especially due to ISR/FSR effects, it is possible to have several three-jet combinations and as a result further refinement is needed. Eventually, the M_{jjj} observable is created from those three jets that maximized the vector-sum of their transverse momenta. This choice is motivated by the fact that the top and anti-top quarks are created back-to-back in the transverse plane and any directional information must be retained in the daughter particles. Hence, the three jets originating from the hadronically decaying top are most likely to be boosted to the same direction, fulfilling the above requirement. In the present analysis, all "good" jets are taken into account for the above implementation. Figure 4.17 shows the M_{jjj} distributions for both channels after four "good" jets with $p_{\mathrm{T}} \geq 25$ GeV are requested and with at least one being identified as a b-jet.

4.5.2 The background contribution

From what discussed previously, it is evident that estimating the contribution of the background in the selected dataset is very important for any cross-section measurement. For the fit method, as it is followed in this thesis, the shape of the background is the crucial element.

Regardless of the choice, in the simplest approach the background can be estimated by employing the Monte Carlo samples. However, this also introduces large uncertainties for the following reasons:

- Firstly, as explained in greater detail in section 1.3.3, the cross-sections of the W+jets and QCD samples are known from theory with a significant uncertainty. Especially for the large jet multiplicity final states, the relevant normalization is not well known.
- Secondly, the estimated QCD cross-section is extremely large. As a result, the number of events produced does not exceed the equivalent of 10 pb^{-1} in integrated luminosity and subsequently the overall statistical uncertainty is large. Naturally, this affects also the shape of event-level observables since after the baseline cuts, which are shown earlier, only a handful of events remains which have typically large weights to account for the

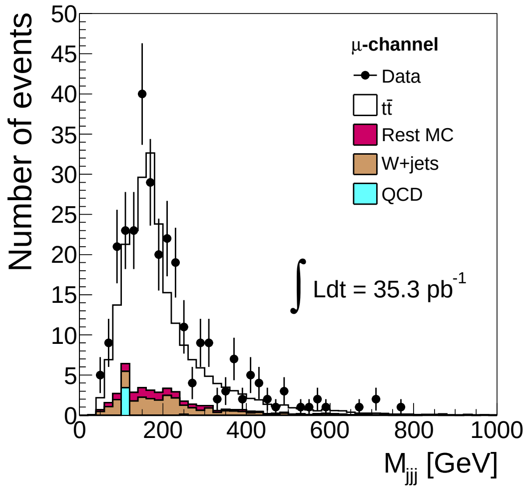

(a) *μ-channel*

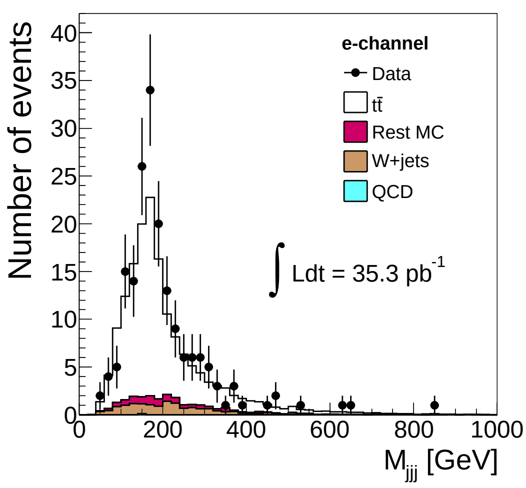

(b) *e-channel*

Figure 4.17: *The three-jet invariant mass observable in the signal region, namely the Bin-41 as described in the beginning of section 4.5.1. All other requirements of the baseline selection for $t\bar{t}$ events are applied.*

normalization.

- Lastly, both the QCD and W+jets samples are produced using the `AlpGen` generator. As this is a leading order generator the shape of observables cannot be trusted a priori. A systematic uncertainty must, therefore, be introduced.

Besides from the large uncertainties, the lack of understanding is clearly demonstrated when comparing the Monte Carlo to the data. Figure 4.18 shows the $E_{\mathrm{T}}^{\mathrm{miss}}$ and $M_{W,T}$ distributions for the μ-channel after requiring the trigger, the data-quality and the charged lepton cuts, as well as at least one jet with $p_{\mathrm{T}} \geq 20$ GeV and $|\eta| \leq 2.5$. The rest of the top selection specific cuts are not applied. It is clear that in the lower values of both distributions, a region where the QCD is expected to be prominent, the Monte Carlo underestimates the data. Additionally, a non-negligible discrepancy exists at the region of the Jacobian peak of the $M_{W,T}$ distribution, which suggests that the W+jets normalization is not accurate.

The aforementioned issues, related to the use of Monte Carlo, can effectively be evaded if we adapt a method in which these background contributions are estimated from the data itself. This also has the advantage that the statistical uncertainty can only but decrease as more data are collected. In the following chapter, a method is implemented to extract the background shape directly from the data. This shape is then used for the cross-section measurement that is presented in detail in chapter 6.

Normalization of QCD

The normalization of the QCD after applying the event selection for the single-lepton $t\bar{t}$ topologies can be evaluated with data-driven methods. Typically, such methods are used for estimating the cross-section with the cut-and-count approach and in our analysis, as it will be presented, they are not needed since the total background normalization is the result of the fit. However, we do make use of these methods in order to provide an initial estimate of the background contribution of the QCD in parameters that serve as input to our fit, therefore reducing the dependance on Monte Carlo QCD. Two methods are implemented:

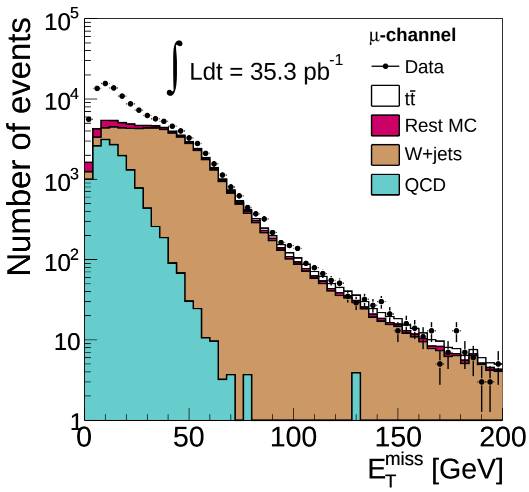

(a) *Missing transverse energy*

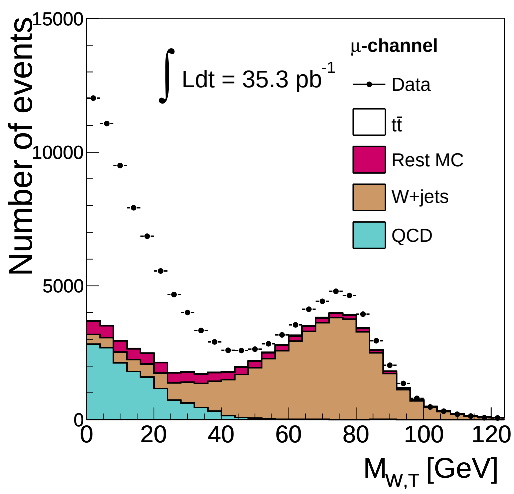

(b) *Transverse W mass*

Figure 4.18: *The $E_{\mathrm{T}}^{\mathrm{miss}}$ and $M_{W,T}$ distributions comparison between Monte Carlo and data showing significant discrepancy especially in the lower values. Events are selected using the trigger, data-quality and charged lepton cuts, for the μ-channel and with at least one jet within $|\eta| \leq 2.5$ being above 20 GeV.*

- The **matrix method**: Implemented for the μ-channel. The QCD that is identified as signal in the μ-channel is mainly due to real muons that are coming from heavy flavor decays, hence they are not well isolated. The matrix method uses the intrinsic differences between the QCD muons and the isolated muons, such as the ones found from W or Z decays. Two samples are defined, one where the track isolation and calorimetric isolation criteria, as defined in section 4.3, are dropped (loose), and one where they are kept as in the "good" muon definition (tight). The following holds:

$$N_{sig}^{tight} = \frac{\epsilon_{sig}}{\epsilon_{sig} - \epsilon_{QCD}}(N^{tight} - \epsilon_{QCD} N^{loose}), \text{ and} \tag{4.5.2}$$

$$N_{QCD}^{tight} = \frac{\epsilon_{QCD}}{\epsilon_{sig} - \epsilon_{QCD}}(\epsilon_{sig} N^{loose} - N^{tight}), \tag{4.5.3}$$

  where N^{tight} and N^{loose} are the total amount of events in the tight and loose samples respectively, ϵ_{sig} and ϵ_{QCD} are the respective efficiencies for the selection of the two samples, and the final numbers N_{sig}^{tight} and N_{QCD}^{tight} are the events with a real isolated muon (signal) and with a non-isolated muon respectively. For the estimation of ϵ_{sig}, the tag-and-probe method on $Z \to \mu^+\mu^-$ decays is implemented, while the ϵ_{QCD} is calculated by measuring the ratio of tight events over loose events in a control region rich in QCD events and orthogonal to the final analysis sample which is then extrapolated to the signal region.
- The **template-fit method**: Implemented for the e-channel. The method uses a binned template likelihood fit on the $E_{\mathrm{T}}^{\mathrm{miss}}$ observable at the sideband region of $E_{\mathrm{T}}^{\mathrm{miss}} \leq 35$ GeV. The signal template is estimated from Monte Carlo, while the QCD template from a QCD-rich sample obtained after inverting the electron identification criteria. The selected electrons in this case (anti-electrons) would typically be accounted as jets in the baseline $t\bar{t}$ selection and consequently the $E_{\mathrm{T}}^{\mathrm{miss}}$ must be re-evaluated for the QCD-rich sample. The result of the fit in the sideband region is extrapolated to the signal region ($E_{\mathrm{T}}^{\mathrm{miss}} \geq 35$ GeV).

	μ-channel		**e-channel**	
	Pre-tagged	**Tagged**	**Pre-tagged**	**Tagged**
$N_{j,25} = 3$	121.4 ± 8.4	24.2 ± 3.4	62.0 ± 11.4	10.8 ± 8.6
$N_{j,25} \geq 4$	51.3 ± 5.6	13.0 ± 2.5	22.0 ± 8.0	8.6 ± 9.2

Table 4.10: *Data-driven estimates of QCD contribution per kinematic region after the baseline $t\bar{t}$ event selection for the μ-channel (matrix method) and e-channel (template fit method). Numbers taken from [159].*

Both the matrix and the template fit methods are documented in detail in [159]. The estimates on the QCD content for each is given in table 4.10.

4.6 Summary

In this chapter we discussed those ingredients that are needed to perform the $t\bar{t}$ cross-section measurement. We explained the reconstruction techniques for the various objects of interest and we highlighted the important parameters which allow us to efficiently select the $t\bar{t}(e)$ and $t\bar{t}(\mu)$ events. In addition, we presented the methodology, based on data-driven methods, for correcting certain parameters at the Monte Carlo level, hence improving the agreement between data and simulation. Subsequently, we showed and justified the requirements that were placed, at both particle-level and event-level, for selecting the events for our measurement. We separated the phase space of interest in four kinematic regions based on their “good” jets multiplicity, considering all events with three or more “good” jets, and whether they contain a b-tagged jet or not. In this way, we included, but kept exclusive, kinematic regions that are background dominated in order to utilize both the greater statistics and the background characteristics of the event sample. This is a necessary step for our cross-section measurement that is presented later on. We concluded the chapter with pointing out the importance of understanding the background contribution in our method. Our measurement has minimum reliance on the exact normalization of the background however the shape is regarded as an important element. The following chapter discusses a method with which the background shape is obtained from data, in view of the cross-section measurement that is presented in chapter 6.

Chapter 5

Data-driven background estimation

"Sine qua non" -
"Without which it could not be..."

Latin legal term

In view of the determination of the $t\bar{t}$ production cross-section that will be shown in the next chapter, we present here a method to estimate the background shape contribution for the fit variable (M_{jjj}) directly from data. As mentioned in section 4.5, the cross-section analysis we implement does not depend on the exact normalization of the background but it demands an accurate determination of the shape of the M_{jjj} distribution. The aim of our method is to obtain a sample where the background contribution is significantly increased and at the same time the signal is minimized. In addition, the following two points must be considered:

- Firstly, the extracted background shape must be kinematically equivalent to the expected background shape from the nominal selection.
- Secondly, the shape must be obtained from a statistically significant sample so that the related statistical uncertainty is minimized.

As shown in tables 4.8 and 4.9, after the cuts for selecting $t\bar{t}$ events are applied the background yield for each of the four regions (see section 4.5.1) consists of events from several different processes. The most dominant contribution is coming from the W+jets events where their yield ranges from 50% up to 90% of the total background. However, the QCD process also has an important role. Even though it is a non-prompt background, it has a large cross-section that still provides the second most important contribution in the final data sample. This is evident from the contributions as measured by the data-driven methods explained in section 4.5.2 and shown in table 4.10. As a result, it is expected that the W+jets and the QCD multi-jet processes will be the ones that play the most important role in the determination of the final shape of the M_{jjj} observable. In the following we develop a method that is based on the assumption that the shapes of these two processes are equivalent; we justify this assumption in the next section. If such a similarity holds we can use a single shape, derived from any of the two background, in order to describe the overall background contribution. As mentioned above, with this approach we need to make sure that the extracted shape will remain unaltered with respect to the original shape.

5.1 Comparison of W+jets and QCD multi-jet events

The assumption of the M_{jjj} shape similarity between W+jets and QCD multi-jet events stems from the fact that the two processes follow the same mechanism for associated jets production. Ignoring the intrinsic differences in the topology between the two processes, one can assume that since the mechanism is the same then the basic kinematic properties of the jets should show an identical behavior and consequently, any quantity derived solely from jets, as in the case of M_{jjj}, should also have the same behavior. In this section we compare those basic kinematic properties of the jets as well as the derived M_{jjj} quantity.

5.1.1 Jet kinematics and M_{jjj} shape

The basic kinematic quantities are compared at first by using the particle-jets from the Monte Carlo samples. Particle-jets are formed by running the corresponding jet clustering algorithm on the stable truth particles[1] excluding muons, neutrinos and other non-interacting particles. Here, the `anti-`$k_\perp$ algorithm is used with an $R = 0.4$. The comparison is performed between a combined W+jets sample where the W boson decays leptonically, and two combined QCD multi-jet samples, one with the jet-filter and one with the muon-filter applied (see section 1.4.2). In addition, special care is taken in the W+jets sample to identify jets that originate from energetic electrons ($W \rightarrow e\nu_e$) or hadronically decaying taus ($W \rightarrow \tau\nu_\tau$); we remove those jets from the comparison.

In figures 5.1 and 5.2, the distributions of transverse momentum (p_{T}), energy (E), pseudo-rapidity (η) and azimuthal angle (ϕ) of the jets are compared. To assist the comparison between the QCD and W+jets events a *relative difference* measure is used that is defined with the following relation:

$$\text{Relative Difference} = \frac{h_{QCD} - h_{W+jets}}{h_{QCD} + h_{W+jets}}, \tag{5.1.1}$$

where h_{QCD} and h_{W+jets} are the histograms for QCD and W+jets respectively. For all the distributions the jets are requested to be within $|\eta| \leq 4.9$ and have $p_{\mathrm{T}} \geq 20$ GeV or $p_{\mathrm{T}} \geq 25$ GeV depending on whether the muon or jet-filtered sample is used respectively. The transverse momentum cut is required in order to cancel biases that relate with the filtering of the QCD samples while the pseudo-rapidity cut corresponds to the actual acceptance of the detector's calorimeters.

$\eta - \phi$ *space*

In the $\eta - \phi$ space the agreement in predictions of the QCD and W+jets samples appears good for the complete ϕ range (figures 5.1(d) and 5.2(d)) but also for the central η region of $|\eta| \leq 2.5$ (figures 5.1(c) and 5.2(c)). However, a large relative difference is evident in the forward regions ($|\eta| > 2.5$) where a higher rate of produced jets in QCD events is observed compared with the one from W+jets events. This result is consistent in both the muon-filtered and the jet-filtered QCD, although, for the former there are additional effects that appear. Specifically, from figure 5.1 we observe dips in the η distribution of the muon-filtered QCD samples at $\eta \approx 0$ as well as in the region of $3.0 \geq |\eta| \geq 2.5$. Both of these effects are not physical but are attributed to the filter requirement of the particular sample which requires the presence of a true muon within $|\eta| \leq 2.8$ for these events. As the existence of the muon is naturally linked to the jet topology, being part of the jet's fragmentation process, any cut

[1] Where 'stable' refers to particles with a lifetime of at least 10 picoseconds.

on the muons affects also the distributions of the jets[2]. It should be noted that despite the discrepancy in the forward region, the jets with $\eta > 2.5$ are not considered in the baseline $t\bar{t}$ selection (see section 4.4.3) and consequently they do not take part in the reconstruction of the M_{jjj} observable.

p_{T} *and* E *content*

With respect to the energy content (figures 5.1(b) and 5.2(b)) and transverse momentum (figures 5.1(a) and 5.2(a)) of the jets, the comparison between W+jets and QCD multi-jet events shows small discrepancies. While for the larger part of the statistics the agreement is reasonable and statistically insignificant, there is a clear trend, especially in the p_{T} distributions, which results in differences at the tail region. In particular, it is observed that the W+jets events exhibit a higher content at the tail, thus indicating a higher rate of harder jets in comparison to the QCD events.

The M_{jjj} *distribution*

In figure 5.3 we show the M_{jjj} distribution calculated with jets that have $|\eta| \leq 2.5$. The shapes of W+jets and QCD events have sizeable discrepancies with the W+jets sample exhibiting a longer tail than the QCD one. This observation, which is visible in both truth and reconstructed level, can be explained by the fact of the harder jet content of the W+jets events, as discussed earlier. Figure 5.4 shows the highest-p_{T} particle-jet (leading-jet) from the three-jet set that forms the M_{jjj} observable and clearly for the W+jets sample this jet is more energetic; similar result holds also for the second and third highest-p_{T} jets of the set.

Summarizing the above observations we conclude that, without taking into account the $t\bar{t}$ baseline selection cuts, the shape of M_{jjj} shows non-negligible differences between W+jets and QCD multi-jet events. We attribute these differences to the jet energy content of the events where the W+jets are shown to have a large content of jets at high-p_{T}. However, it must be noted that by not taking into account the baseline cuts for the $t\bar{t}$ selection, as discussed in the previous chapter, we implicitly ignore the differences that emerge due to the distinctive final state topology of the events. In particular, as it was discussed in section 1.3.3, the W+jets are characterized by the presence of the massive W which decays leptonically to an energetic charged lepton and a neutrino, while the QCD multi-jet events consist solely of jets. As we are only interested in the phase-space region that is selected after the $t\bar{t}$ selection requirements, we examine in the following section the behavior of M_{jjj} shape with respect to the $E_{\mathrm{T}}^{\mathrm{miss}}$ and $M_{W,T}$ cuts.

5.1.2 Effects from $E_{\mathrm{T}}^{\mathrm{miss}}$ and $M_{W,T}$ cuts

As discussed in section 4.4.3, the $E_{\mathrm{T}}^{\mathrm{miss}}$ and $M_{W,T}$ observables are exploited in the $t\bar{t}$ baseline selection because of their rejection power against QCD events, which in turn results to an increased signal-to-background ratio. The presence of the charged lepton and the neutrino in the final state of the W+jets implies that the distributions of the two observables are very different in comparison with the ones obtained from the QCD. This is indeed depicted in figures 5.5 and 5.6 where the variables are plotted at the reconstruction level. For the $E_{\mathrm{T}}^{\mathrm{miss}}$ distribution no cuts are applied while for the $M_{W,T}$ distribution an identified “good” charged lepton is required (see section 4.3); as is evident, the requirement of a “good” charged lepton

[2]For example, in the case of the $\eta \approx 0$ dip the muons are undetected due to the reduced acceptance of the Muon Spectrometer in that region, caused by the cabling ‘hole’ of the detector, and as a result the event is rejected. On the other hand, the dip in $3.0 \geq |\eta| \geq 2.5$ is caused by the η cut of the filter.

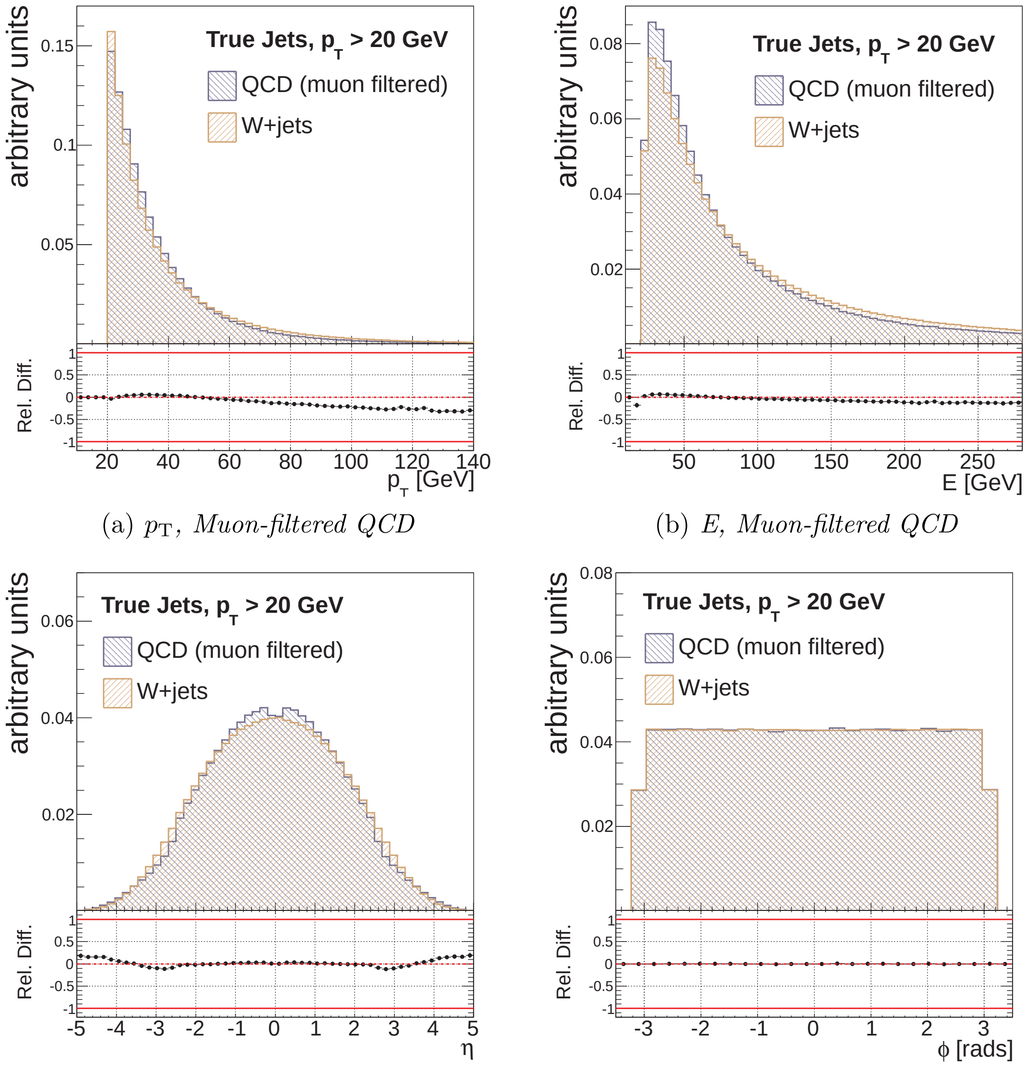

(a) p_{T}, *Muon-filtered QCD* (b) E, *Muon-filtered QCD*

(c) η, *Muon-filtered QCD* (d) ϕ, *Muon-filtered QCD*

Figure 5.1: *Comparison of basic kinematic variables between W+jets and QCD multi-jet muon-filtered Monte Carlo samples. Histograms normalized to unit area.*

significantly reduces the absolute amount of surviving QCD events.

The $E_{\mathrm{T}}^{\mathrm{miss}}$ distribution for the W+jets events clearly shows a pair of peaks: one at low energies which is related to the detector response on the visible reconstructed objects and a second one at high energies that suggests the existence of the energetic neutrino. On the other hand, the same distribution for QCD events, as expected, shows only the lower energy peak, thus being dependent on the reconstructed jets in the events. In a similar way, the $M_{W,T}$ distribution, for the W+jets, has a peak at the true mass of the W boson, while for the QCD events the values closer to zero are favored. Naturally, when a cut is placed in either the $E_{\mathrm{T}}^{\mathrm{miss}}$ or $M_{W,T}$ observables, the selected W+jets events are driven by their leptonic side. On the contrary, QCD events depend entirely on the energy of the jets.

To examine how the selection requirements affect the M_{jjj} shape, a comparison is made for different thresholds of $E_{\mathrm{T}}^{\mathrm{miss}}$ and $M_{W,T}$. Figures 5.7 and 5.8 show the M_{jjj} distributions of QCD (jet-filtered and muon-filtered respectively) and W+jets events for the various thresholds.

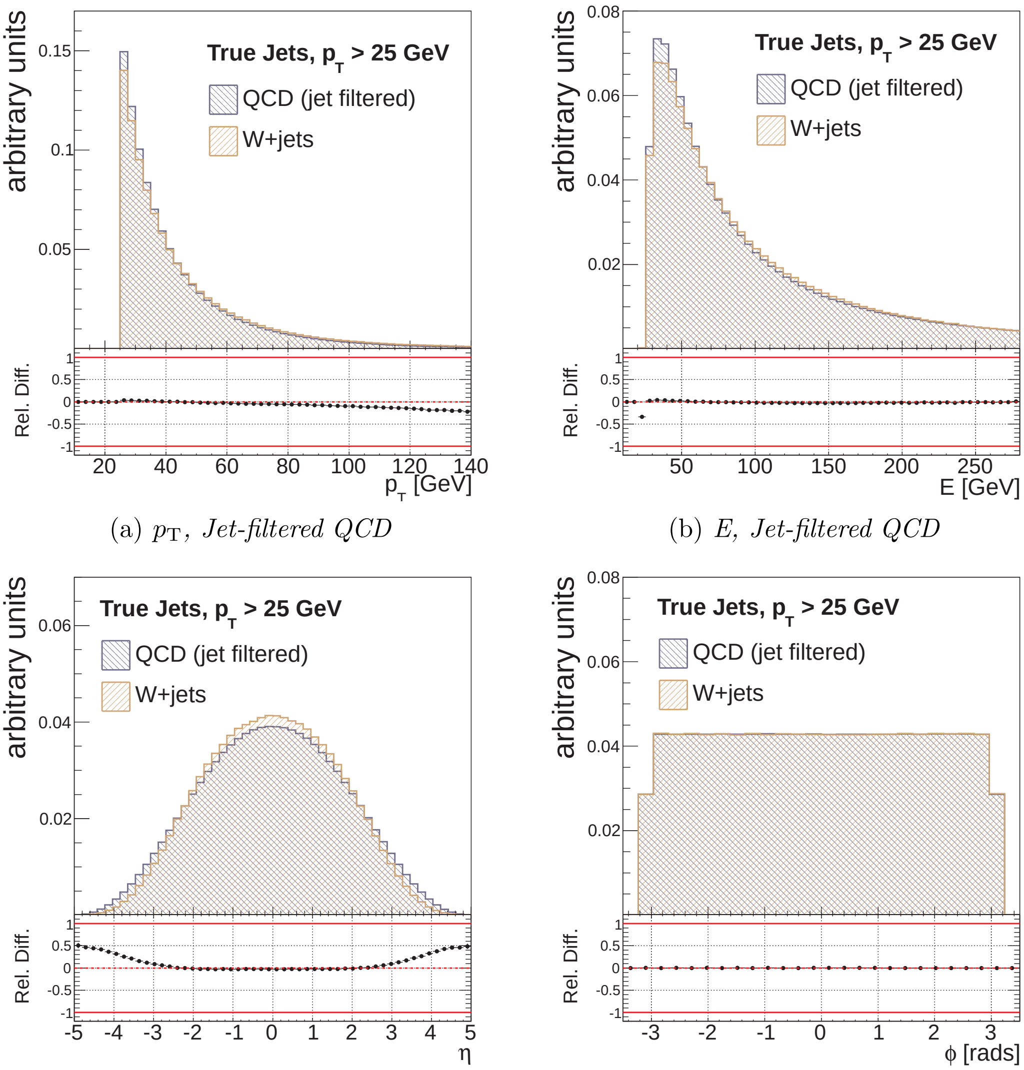

(a) p_{T}, *Jet-filtered QCD* (b) E, *Jet-filtered QCD*

(c) η, *Jet-filtered QCD* (d) ϕ, *Jet-filtered QCD*

Figure 5.2: *Comparison of basic kinematic variables between W+jets and QCD multi-jet jet-filtered Monte Carlo samples. Histograms normalized to unit area.*

As before, for the comparison with the $E_{\mathrm{T}}^{\mathrm{miss}}$ there are no other cuts applied while for the comparison with the $M_{W,T}$ a charged "good" lepton is required. However, for the QCD events the lepton cut greatly reduces the number of surviving events which in addition to the implicit requirement of at least three jets that are needed to make up the M_{jjj} makes the comparison unfeasible. To overcome this in a way that the M_{jjj} would remain unaffected the isolation cuts from the "good" lepton definition are dropped, namely the `etcone` and `ptcone` cuts.

It is observed that the W+jets shape is only slightly affected with increasing $E_{\mathrm{T}}^{\mathrm{miss}}$ thresholds (figures 5.7(b) and 5.8(b)), but remains unaltered for any of the different $M_{W,T}$ cuts (figures 5.7(d) and 5.8(d)). On the other hand, as seen in figures 5.7(a) and 5.8(a), the shape of the QCD events changes significantly, especially when the $E_{\mathrm{T}}^{\mathrm{miss}}$ cut increases.

Employing the relative difference measure as defined in 5.1.1, the W+jets and QCD are compared with each other after each of the $E_{\mathrm{T}}^{\mathrm{miss}}$ and $M_{W,T}$ thresholds is applied. This way we aim to identify a working point at which the shape differences between W+jets and QCD

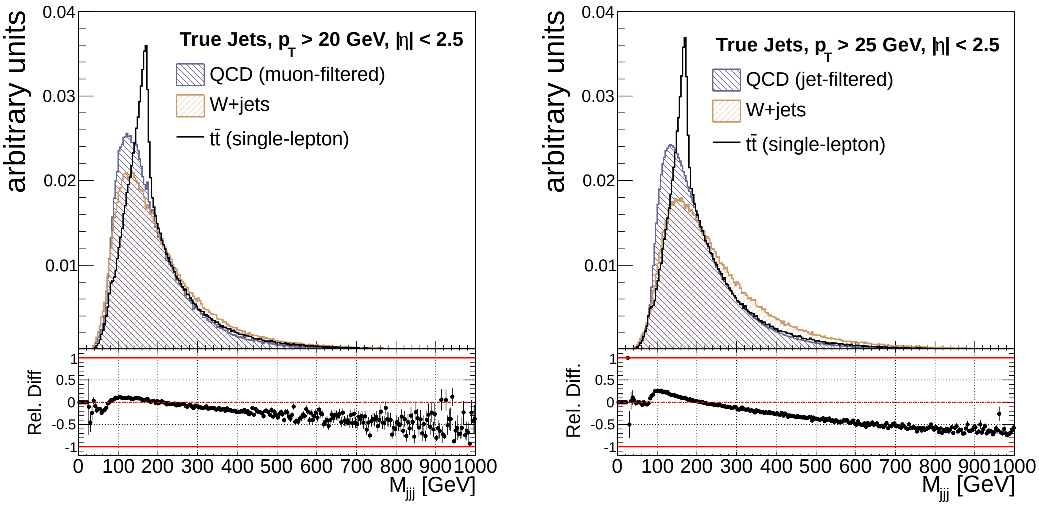

(a) *Truth-level comparison.*

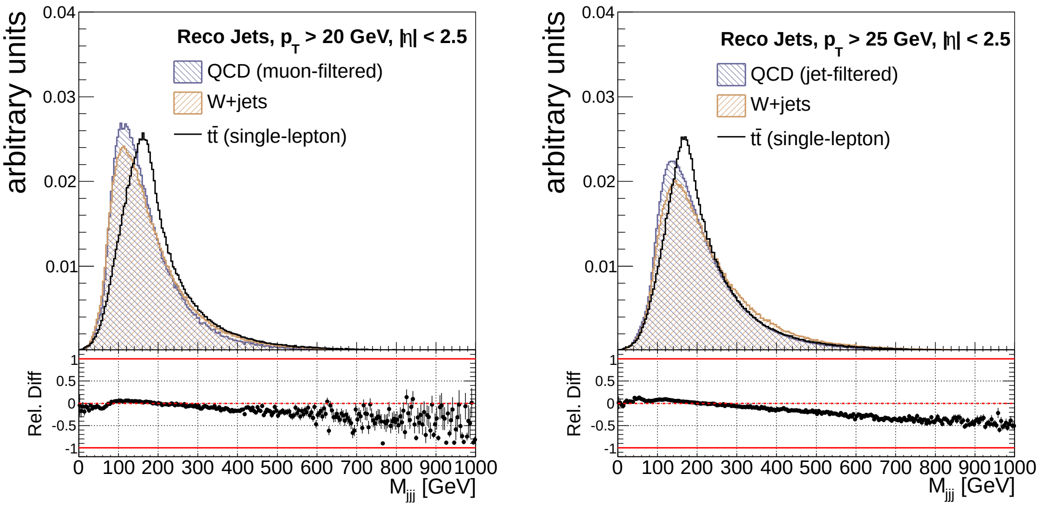

(b) *Reconstruction-level comparison.*

Figure 5.3: *Three-jet invariant mass distributions of W+jets and QCD multi-jet events using truth-level particle-jets (a) and reconstructed jets (b). On the left, the comparison with the jet-filtered QCD is shown and on the right with the muon-filtered ones. The $t\bar{t}$ semi-leptonic distribution is shown for completeness. All histograms are normalized to unit area.*

events are minimized. The results are shown in figures 5.9 and 5.10 for the QCD jet-filtered and muon-filtered samples respectively.

For the $E_{\mathrm{T}}^{\mathrm{miss}}$ cut an excellent agreement between the shapes is achieved between 30 and 40 GeV, when comparing with the jet-filtered samples, and between 20 and 30 GeV, when comparing with the muon-filtered samples. This is in good agreement with the cuts that are applied in the baseline selection, namely $E_{\mathrm{T}}^{\mathrm{miss}} \geq 35$ GeV for the e-channel, where the jet-filtered QCD sample is relevant, and $E_{\mathrm{T}}^{\mathrm{miss}} \geq 25$ GeV for the μ-channel, where the muon-filtered QCD sample is relevant. On the other hand, for the $M_{W,T}$, for all thresholds between 10 and 40 GeV, the shapes show a good agreement irrespectively of the sample used.

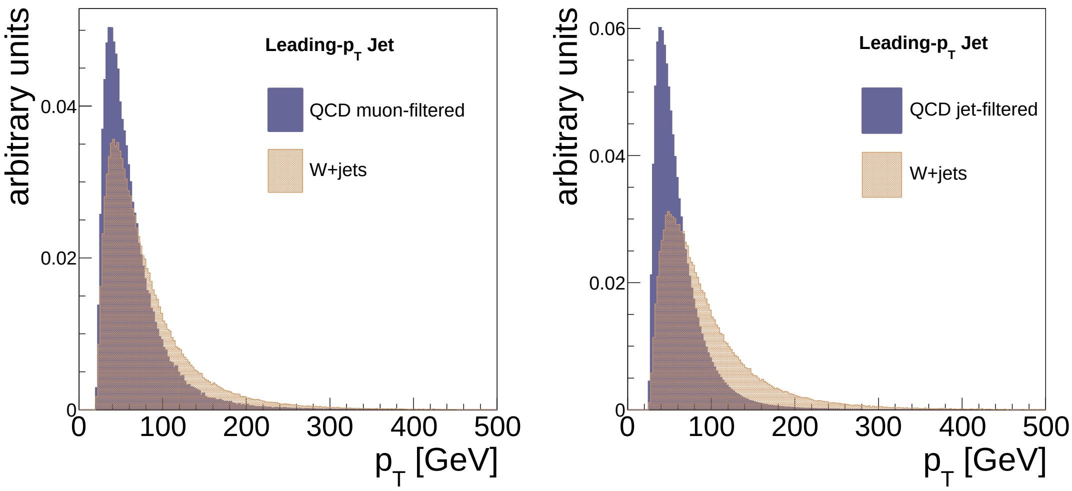

(a) (b)

Figure 5.4: *The p_T distributions of the highest-p_T particle-jets that make up the M_{jjj} observable for W+jets and QCD events. In (a), the comparison is made with the muon-filtered QCD sample, hence jets are selected with $p_T \geq 20$ GeV and in (b) the jet-filtered QCD sample is used so the jet p_T cut is set to 25 GeV. Histograms normalized to unit area.*

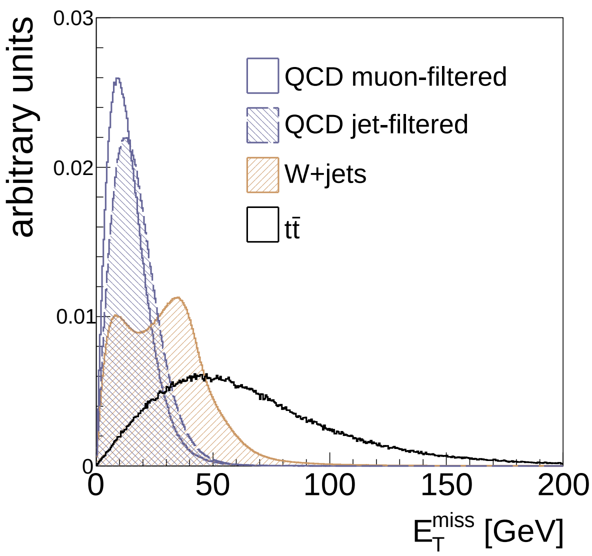

Figure 5.5: *The reconstructed E_T^{miss} distribution of W+jets and QCD multi-jet events with no cuts applied. The $t\bar{t}$ semi-leptonic events are shown for completeness. The discrepancy between the QCD samples is due to their different filtering. Histograms normalized to unit area.*

5.1.3 Conclusions

Following from our observation that the W+jets and QCD multi-jet events dominate the background after applying the $t\bar{t}$ event selection, we tried to justify our assumption that the M_{jjj} shape produced by each of the two samples is the same. This would facilitate the data-driven method because a single shape, obtained by any of the two processes, would suffice for describing the background.

Initially, we compared the kinematic distributions of the jets from both processes, at the truth level, and we showed that, although to a large extend the distributions are equivalent, differences are observed especially at the p_T tails and in the forward η regions. Also, when comparing the M_{jjj} shape, before any cuts are applied, the two processes show even more sig-

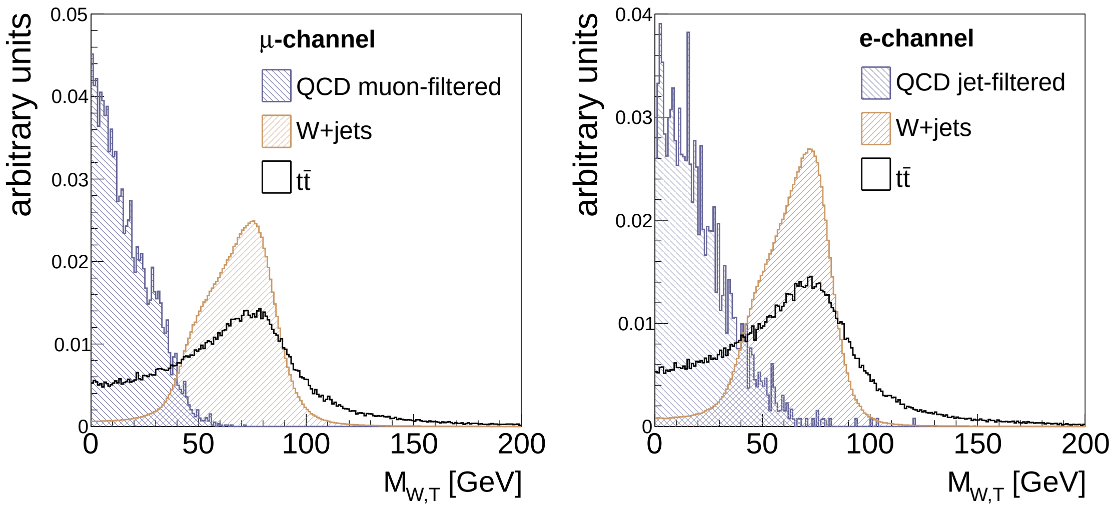

(a) *μ-channel* (b) *e-channel*

Figure 5.6: *Comparison of the $M_{W,T}$ observable based on "good" lepton selection criteria for W+jets, QCD multi-jet and $t\bar{t}$ semi-leptonic events. Histograms normalized to unit area.*

nificant discrepancies due to the higher jet p_{T} content of W+jets. However, we demonstrated that this shape is affected differently in the two processes when $E_{\mathrm{T}}^{\mathrm{miss}}$ and $M_{W,T}$ requirements are applied. Especially, for the different $E_{\mathrm{T}}^{\mathrm{miss}}$ thresholds the shape of the QCD events appears to be particularly sensitive, which is attributed to the fact that QCD events with higher jet energies are selected. Eventually, we showed that at the thresholds applied in the $t\bar{t}$ selection (see section 4.4.3), a reasonable match between the shape of the QCD and W+jets events is achieved. Therefore, we use this observation to develop the data-driven method for extracting the background shape; this is presented in the following section.

5.2 The data-driven method and application on data

As mentioned earlier, the obtained shape must be both statistically significant and kinematically equivalent to the shape after the baseline selection. By having established the similarity of the shape between W+jets and QCD in the given kinematic region it is now possible to focus only on one of the two processes in order to extract its shape. In the following, the choice that is made is to enhance the QCD content of the final selection. This is motivated by the following two characteristics of those events:

- The large production cross-section which results in sufficient statistics.
- The absence of energetic and isolated leptons in their final state which effectively provides a foothold for controlling the contamination from the signal as well as from other backgrounds.

5.2.1 Enhancing QCD content

The main consideration for enhancing the QCD content on the final dataset is to rely as much as possible on the original baseline selection for the analysis as shown in section 4.4. This way, possible biases that may be introduced on the extracted shape by altering or using different

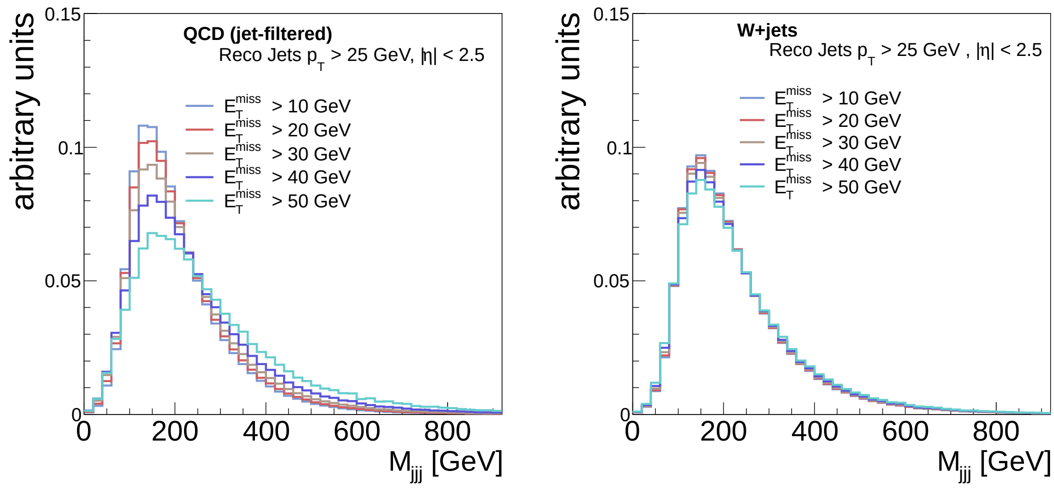

(a) *M_{jjj} vs. $E_{\mathrm{T}}^{\mathrm{miss}}$ thresholds, QCD jet-filtered* (b) *M_{jjj} vs. $E_{\mathrm{T}}^{\mathrm{miss}}$ thresholds, W+jets*

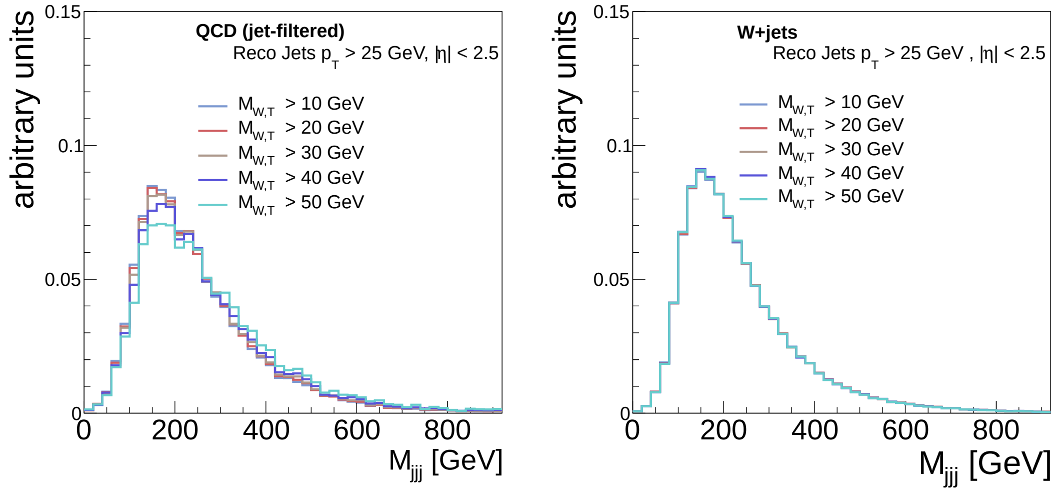

(c) *M_{jjj} vs. $M_{W,T}$ thresholds, QCD jet-filtered* (d) *M_{jjj} vs. $M_{W,T}$ thresholds, W+jets*

Figure 5.7: *The M_{jjj} distribution for different $E_{\mathrm{T}}^{\mathrm{miss}}$ and $M_{W,T}$ thresholds for both W+jets and the QCD jet-filtered events. An* ***electron*** *requirement is applied for calculating $M_{W,T}$. Histograms are normalized to unit area.*

cuts can be minimized or even completely avoided.

Given that the shape of the M_{jjj} observable is derived only by the jet content of the event, it is straightforward to consider that the least invasive action is to alter the lepton requirement in the selection. In addition, as it is obvious from table 4.7, the QCD events suffer a significant loss of statistics of up to three orders of magnitude when the charged lepton cut is applied, while at the same time the rest of the processes are only halved. The following cuts are applied at the event level:

- The triggers used to select events are kept the same as in the baseline selection (see section 4.4.2). The analysis channels (e-channel or μ-channel) will be defined by the trigger used.
- The *non-collision background*, *jet-cleaning* and *electron-muon overlap* requirements, as explained in section 4.4.3, are also applied.

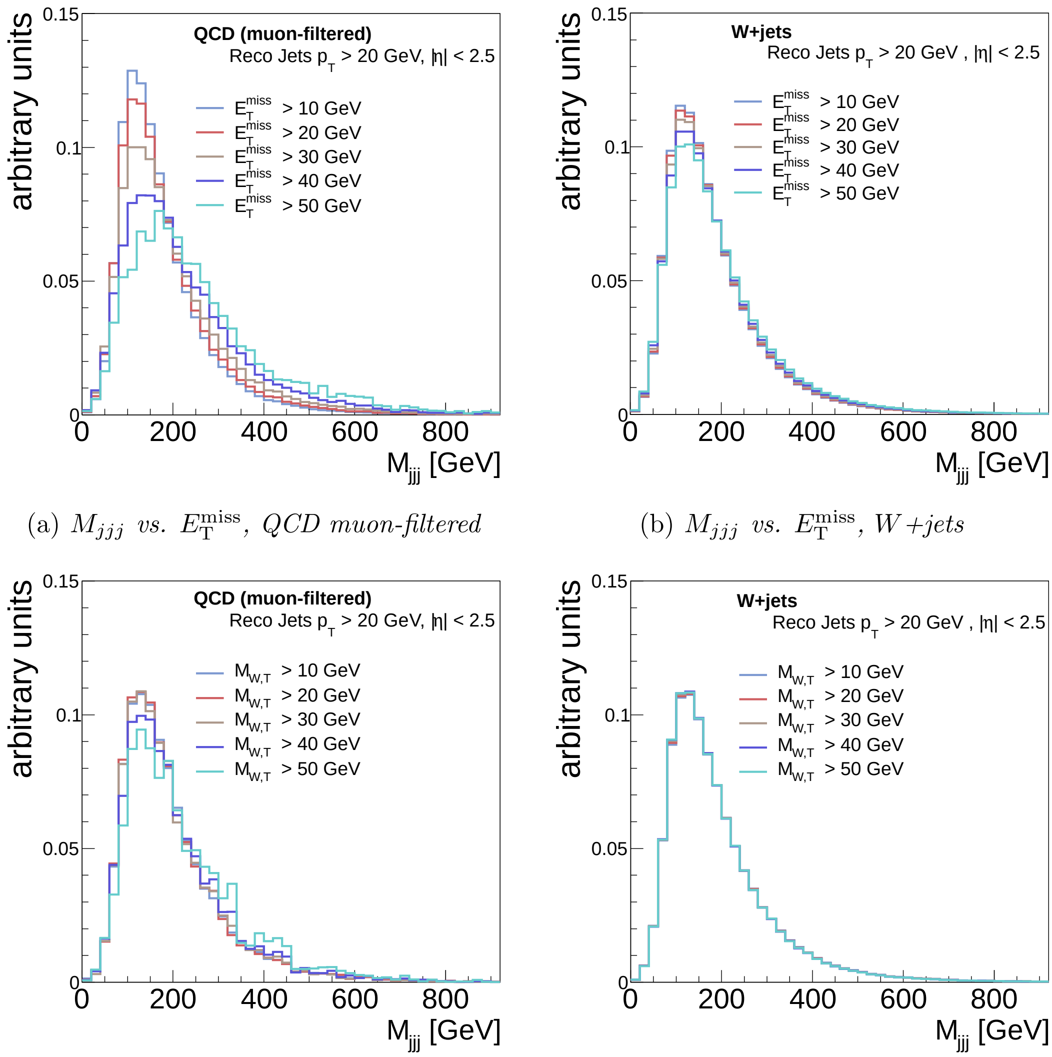

(a) M_{jjj} *vs.* $E_{\mathrm{T}}^{\mathrm{miss}}$*, QCD muon-filtered* (b) M_{jjj} *vs.* $E_{\mathrm{T}}^{\mathrm{miss}}$*, W+jets*

(c) M_{jjj} *vs.* $M_{W,T}$*, QCD muon-filtered* (d) M_{jjj} *vs.* $M_{W,T}$*, W+jets*

Figure 5.8: *The* M_{jjj} *distribution for different* $E_{\mathrm{T}}^{\mathrm{miss}}$ *and* $M_{W,T}$ *thresholds for both W+jets and the QCD muon-filtered events. A* ***muon*** *requirement is applied for calculating* $M_{W,T}$*. Histograms are normalized to unit area.*

- For the e-channel: $E_{\mathrm{T}}^{\mathrm{miss}} \geq 35$ GeV and $M_{W,T} \geq 25$ GeV. The threshold values are the same as in the baseline selection.
- For the μ-channel: $E_{\mathrm{T}}^{\mathrm{miss}} \geq 25$ GeV and $M_{W,T} + E_{\mathrm{T}}^{\mathrm{miss}} \geq 60$ GeV. The threshold values are the same as in the baseline selection.
- For both channels: exactly zero "good" leptons are required in the final topology. The definitions of "good" muons and "good" electrons is already given in section 4.3.

For the calculation of $M_{W,T}$ (see equation 4.4.1) there is, by definition, a requirement for a charged lepton to exist. Given that we reject events with "good" charged leptons, different candidates must be defined. Although with the selection criteria mentioned above we expect that the final event sample will be dominated by QCD events, we have kept the requirement for a lepton trigger to have fired. As a result, the final event sample will contain objects

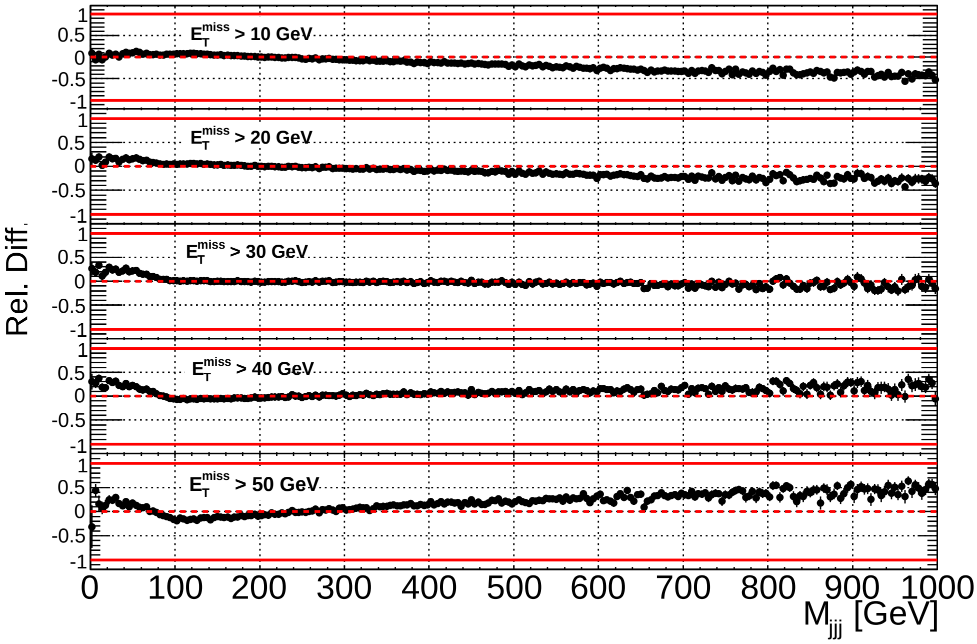

(a) *Comparison of M_{jjj} shape for different $E_{\mathrm{T}}^{\mathrm{miss}}$ thresholds. No other cuts applied.*

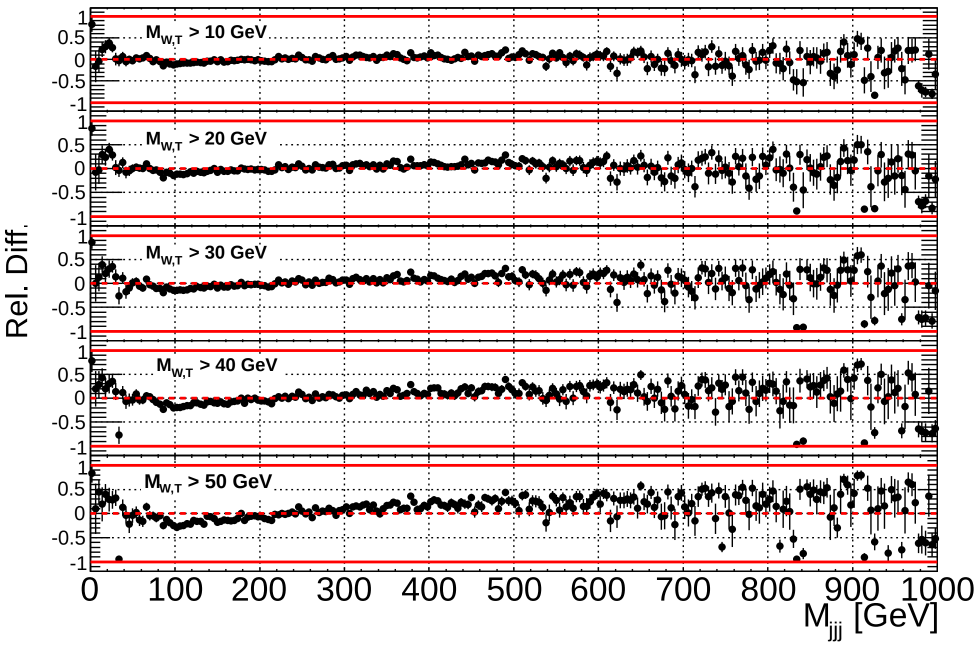

(b) *Comparison of M_{jjj} shape for different $M_{W,T}$ thresholds. For the e-channel an electron requirement is applied (see section 4.4.3).*

Figure 5.9: *Comparison of W+jets and QCD (jet-filtered) M_{jjj} distributions for various $E_{\mathrm{T}}^{\mathrm{miss}}$ (a) and $M_{W,T}$ (b) thresholds. The relative difference measure is used (equation 5.1.1).*

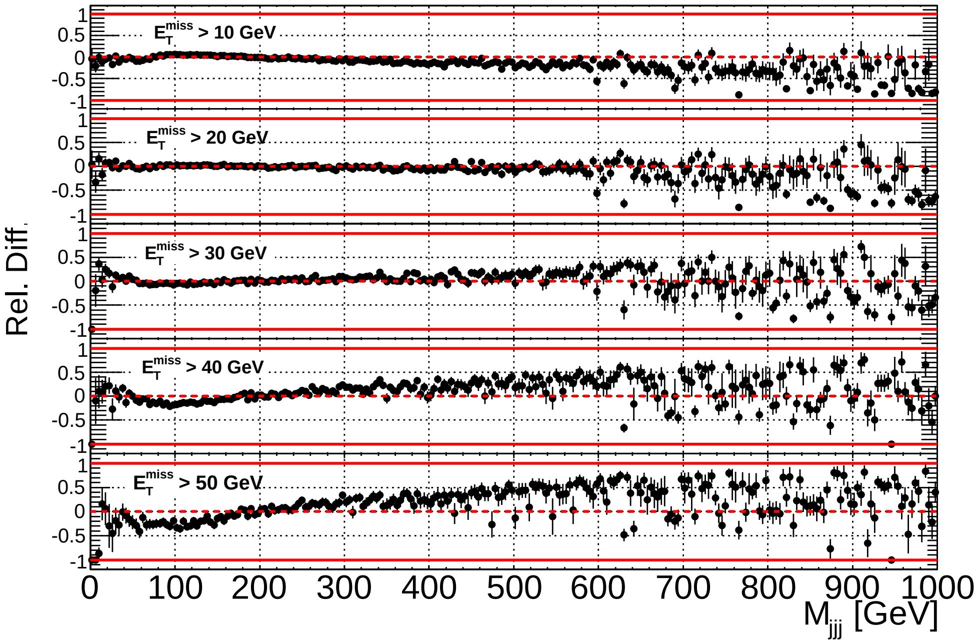

(a) *Comparison of M_{jjj} shape for different $E_{\mathrm{T}}^{\mathrm{miss}}$ thresholds. No other cuts applied.*

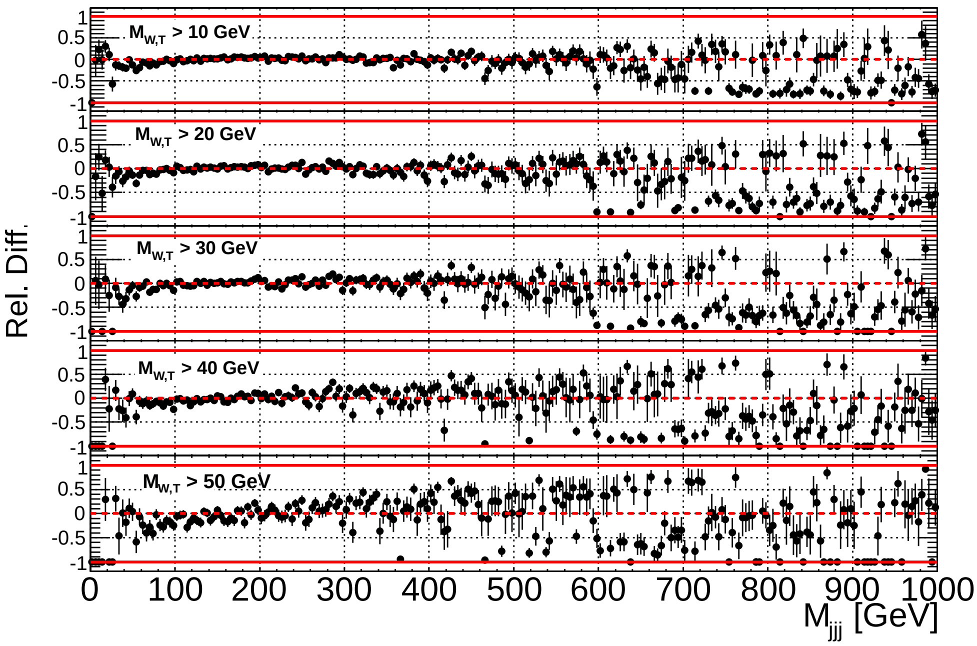

(b) *Comparison of M_{jjj} shape for different $M_{W,T}$ thresholds. For the μ-channel a muon requirement is applied (see section 4.4.3).*

Figure 5.10: *Comparison of W+jets and QCD (muon-filtered) M_{jjj} distributions for various $E_{\mathrm{T}}^{\mathrm{miss}}$ (a) and $M_{W,T}$ (b) thresholds. The relative difference measure is used (equation 5.1.1).*

that, at the trigger level, have been identified as leptons. These objects may be non-prompt muons or electrons, or jets identified as electrons. We utilize this information and we define the following:

Triggered muons: Combined muons reconstructed with `MuId` algorithm and flagged as *tight*, with $p_{\mathrm{T}} \geq 5$ GeV, $|\eta| \leq 2.5$ and that are matched to the corresponding selection trigger.

Triggered electrons: Electrons reconstructed with the algorithms presented in 4.1.1, with $E_{\mathrm{T}} \geq 5$ GeV, $|\eta_{cluster}| \leq 2.5$ excluding the crack region $1.37 \leq |\eta_{cluster}| \leq 1.52$ and that are matched to the corresponding selection trigger.

Multiple triggered muons and electrons may exist in an event and so, to avoid ambiguity on which lepton to be used, further refinement is made. For the μ-channel the QCD events triggered by the muon are likely to contain a non-prompt muon. The probability of more than one non-prompt muons to exist in these events is not expected to be large and therefore for simplicity we require exactly one triggered muon ($N_{\mu}^{triggered} = 1$). The $M_{W,T}$ is eventually derived from the single triggered muon and the $E_{\mathrm{T}}^{\mathrm{miss}}$ of the event. For the e-channel the selection is different. In addition to non-prompt electrons, there is also a large probability of jets to be identified as electrons by the trigger, namely "fake" electrons. Given that also the jet multiplicity is large in QCD events, it is not unlikely that more than one jet has fired the respective trigger. In this case, the strict requirement that was applied for the μ-channel may lead to a significant loss of statistic and for this reason we require at least one triggered electron instead ($N_{e}^{triggered} \geq 1$). The triggered electron that is eventually used for the $M_{W,T}$ calculation is the one that is most isolated. The isolation is measured in this case with the calorimetric isolation term (`etcone`) with $R_0 = 0.2$ (see section 4.1.1). The one with the lowest value is taken.

As a last step in the selection procedure for enhancing the QCD content of the dataset, the jets in the selected events must be redefined. The reason for this is that since the triggered, most isolated, electron is used in the selection requirements, which happens implicitly due to the cut on $M_{W,T}$, it must then be avoided to be taken into account for the M_{jjj} calculation. The jets that are used thereafter are defined by the following:

"Qcd" jets: Jets with $p_{\mathrm{T}} \geq 20$ GeV and $|\eta| \leq 2.5$ that are reconstructed with the `anti-`$k_{\perp}$ algorithm having $R = 0.4$ (using as input topological clusters) and are calibrated with the `EMJES` scheme. These requirements are the same as in baseline selection (see section 4.3). If $dR(jet, electron) \leq 0.2$ the jet is removed. The calculation of the dR uses for the electron coordinates its track coordinates (η_{track},ϕ_{track}) and for the jet the coordinates before the calibration (η_{em},ϕ_{em}).

In table 5.1 the event count is shown for each of the different jet multiplicities that are of interest in our analysis calculated for the Monte Carlo samples and the data, with the former being normalized to 35.3pb^{-1}. All numbers are obtained after the QCD-enchancing cuts have been applied. As expected, the number of surviving QCD events is much larger than the total contribution of the rest of the processes with its fraction being close to or above 90%.

5.2.2 Shape comparisons on Monte Carlo

With the QCD-enhancing cuts that were discussed in the previous section, a statistically significant data sample is collected that consists almost completely of QCD multi-jet events.

μ-channel

	$N_{j,25}=3$		$N_{j,25}\geq 4$	
	$N_{bj,25}=0$	$N_{bj,25}\geq 1$	$N_{bj,25}=0$	$N_{bj,25}\geq 1$
$t\bar{t}$ **(leptonic)**	16.3±0.3	30.5±0.4	30.5±0.4	85.0±0.6
$t\bar{t}$ **(hadronic)**	0.8±0.1	1.45±0.2	10.8±0.5	31.2±0.8
W**+jets**	424.7±3.7	21.3±0.7	148.2±2.2	14.1±0.6
Z**+jets**	20.9±1.4	0.8±0.3	9.0±0.9	0.25±0.15
Single-top	4.4±0.1	5.7±0.1	3.4±0.1	5.9±0.1
Dibosons	0.2±0.01	0.01±0.002	0.06±0.005	0.005±0.001
QCD	6603.5±151.2	3953.8±116.6	3807.4±115.3	2724.8±94.2
Total MC	7070.8±151.2	4013.5±116.6	4009.4±115.3	2861.2±94.2
Data	11489	5621	6080	3923

e-channel

	$N_{j,25}=3$		$N_{j,25}\geq 4$	
	$N_{bj,25}=0$	$N_{bj,25}\geq 1$	$N_{bj,25}=0$	$N_{bj,25}\geq 1$
$t\bar{t}$ **(leptonic)**	13.5±0.2	24.9±0.3	22.6±0.3	57.3±0.5
$t\bar{t}$ **(hadronic)**	0.1±0.0	0.3±0.1	2.7±0.2	6.2±0.4
W**+jets**	563.9±4.4	22.2±0.8	177.8±2.4	12.9±0.6
Z**+jets**	28.8±1.6	0.9±0.3	14.2±1.1	1.1±0.3
Single-top	3.8±0.1	4.8±0.1	2.3±0.1	3.5±0.1
Dibosons	0.3±0.0	0.0±0.0	0.1±0.0	0.0±0.0
QCD	7881.1±171.4	519.1±43.6	6197.3±149.7	662.8±48.1
Total MC	8491.54±171.5	572.2±43.6	6416.9±149.7	743.8±48.1
Data	12601	1089	5471	790

Table 5.1: *Event count after applying the QCD-enhancing cuts, as listed in 5.2.1. Monte Carlo normalized to* $35.3pb^{-1}$ *of integrated luminosity. All uncertainties are statistical.*

However, it still needs to be verified that the M_{jjj} shape of the extracted data sample remains unaffected with respect to the background shape after the $t\bar{t}$ baseline cuts.

In figure 5.11(a) we compare the shape of W+jets Monte Carlo after the baseline cuts with the one obtained after the QCD-enhancing cuts. In order to minimize the statistical fluctuations, the comparison is made on the inclusive data sample, namely with at least three-jets ("qcd" or "good") and without requiring a b-tag. The agreement is indeed remarkable showing that the QCD-enchaning cuts do not affect the M_{jjj} shape. Figure 5.11(b) shows the same comparison but including all the contributing background processes. A good agreement is again evident with only minor fluctuations at the tails of the distributions. It should be noted that a direct comparison with only the QCD samples is not possible. This is due to the small amount of available statistics of the sample which results to only a handful of events with very large weights after the $t\bar{t}$ baseline cuts are applied.

5.2.3 Distributions on data

Having showed that the QCD-enhancing cuts achieve a shape for the background that resembles the original shape from the baseline analysis we apply the method on the collected data.

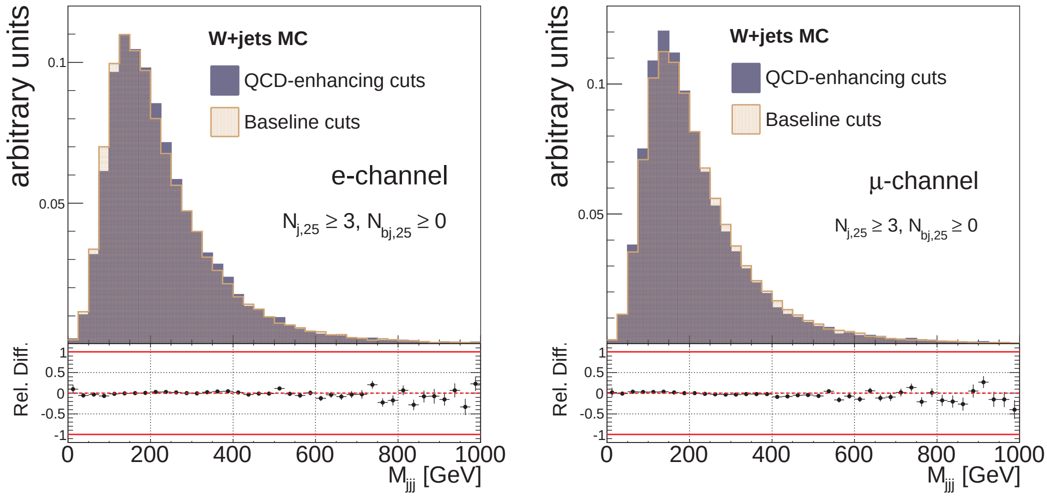

(a) *W+jets Monte Carlo, e-channel (left) and μ-channel (right)*

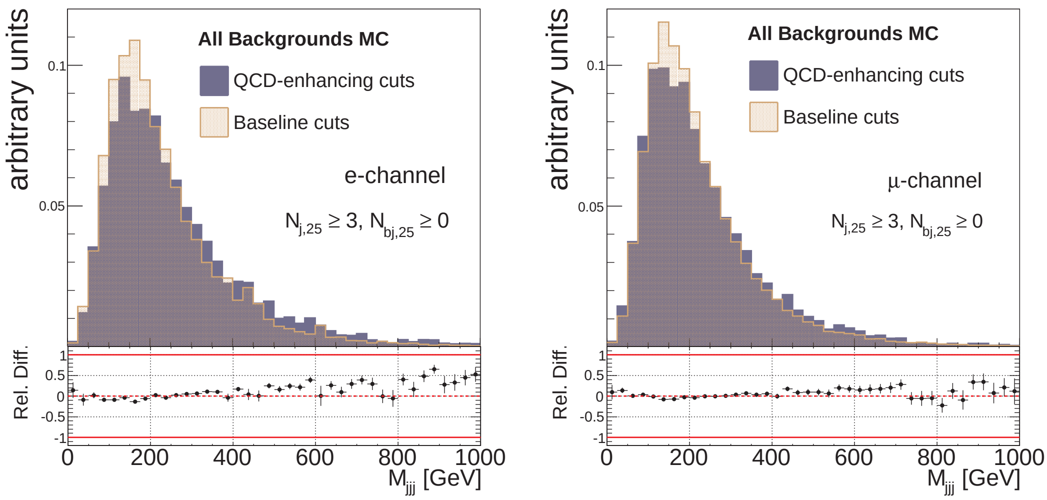

(b) *Inclusive background (MC), e-channel (left) and μ-channel (right)*

Figure 5.11: *Comparison of M_{jjj} shape between baseline and QCD-enhancing cuts. In (a) only W+jets MC is used and in (b) the inclusive MC background. Histograms normalized to unit area.*

At first the M_{jjj} distribution is compared between the data after the QCD-enhancing cuts and the full Monte Carlo background after the $t\bar{t}$ baseline cuts are applied. The result of the comparison is shown in figures 5.12 and 5.13 for the electron and the muon channels respectively. Also, the selected events are now separated in the four distinct kinematic regions. For the muon channel the agreement is shown to be very good with only large fluctuation at the tails which are attributed to the limited statistics in that region. This agreement, indicates that a good description of the data from the Monte Carlo exists. For the electron channel a good agreement is also observed, for most kinematic regions, but with larger fluctuations at the tails, mostly prominent at the tagged $N_{j,25} \geq 4$ region. The only significant discrepancy appears at the no-tag $N_{j,25} = 3$ region. This reflects the benefit of using a data-driven method since, having established that the QCD-enhancing cuts do not bias the original M_{jjj} shape, we can be confident that the description of the shape by the data is more accurate than the one from the Monte Carlo.

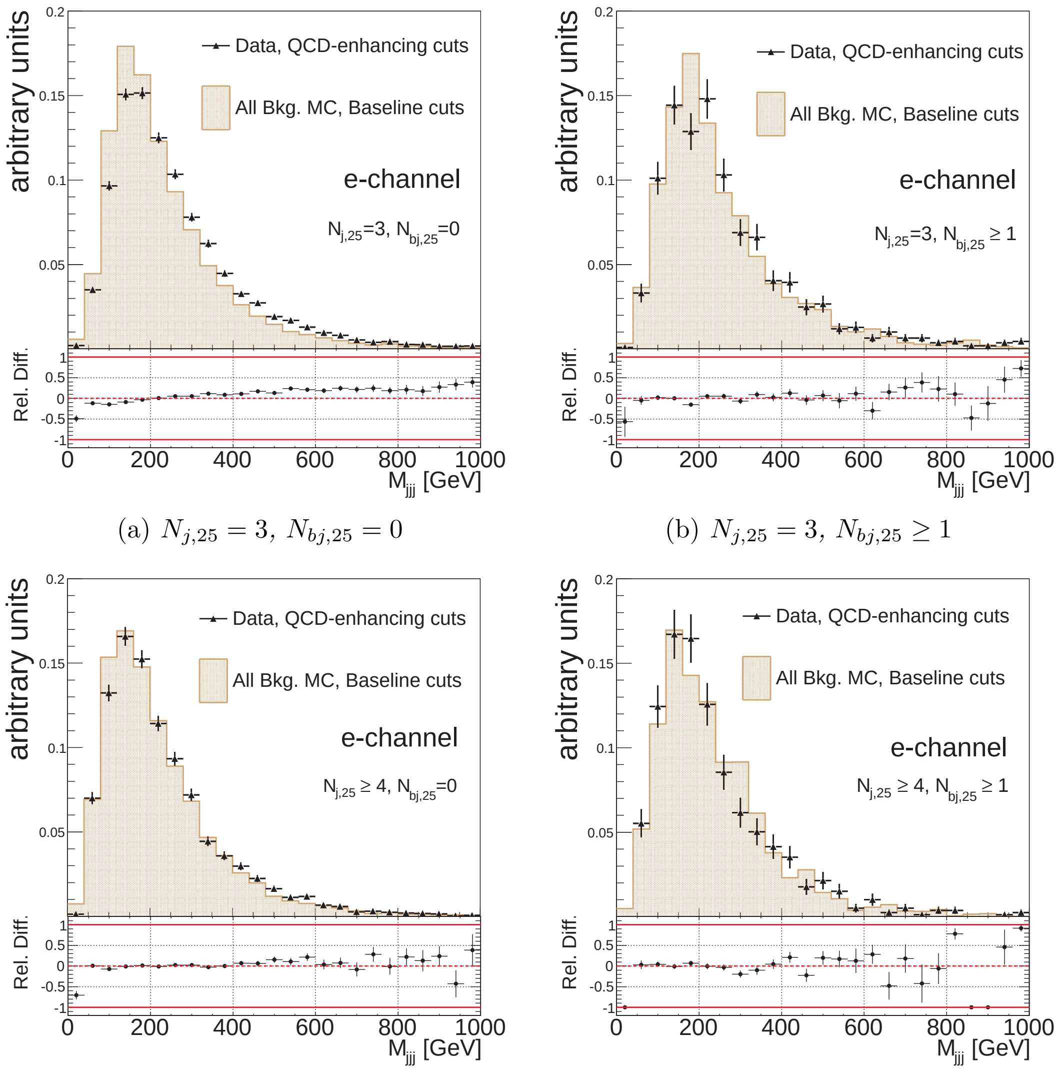

(a) $N_{j,25} = 3,\ N_{bj,25} = 0$ (b) $N_{j,25} = 3,\ N_{bj,25} \geq 1$

(c) $N_{j,25} \geq 4,\ N_{bj,25} = 0$ (d) $N_{j,25} \geq 4,\ N_{bj,25} \geq 1$

Figure 5.12: *Comparison of the data-driven shape, extracted with the QCD-enhancing cuts, and the inclusive background Monte Carlo shape after the baseline cuts for each of the four bins in the e-channel. The normalized to 35.3 pb^{-1} contribution of each background process is shown in tables 4.8 and 4.9. Histograms normalized to unit area.*

In addition, we make a comparison of the the data and the Monte Carlo after applying the QCD-enhancing cuts. Given that in both cases the surviving sample is dominated by QCD events this comparison essentially checks how well the Monte Carlo QCD shape is described. Naturally, because the Monte Carlo normalization is expected to be inaccurate, we normalize the simulated events to the exact number of data events. In figure 5.14 the result is shown for each channel. It is evident that the level of agreement is very good even though at the tails of the distributions fluctuations appear; these are attributed to the limited statistics in that region.

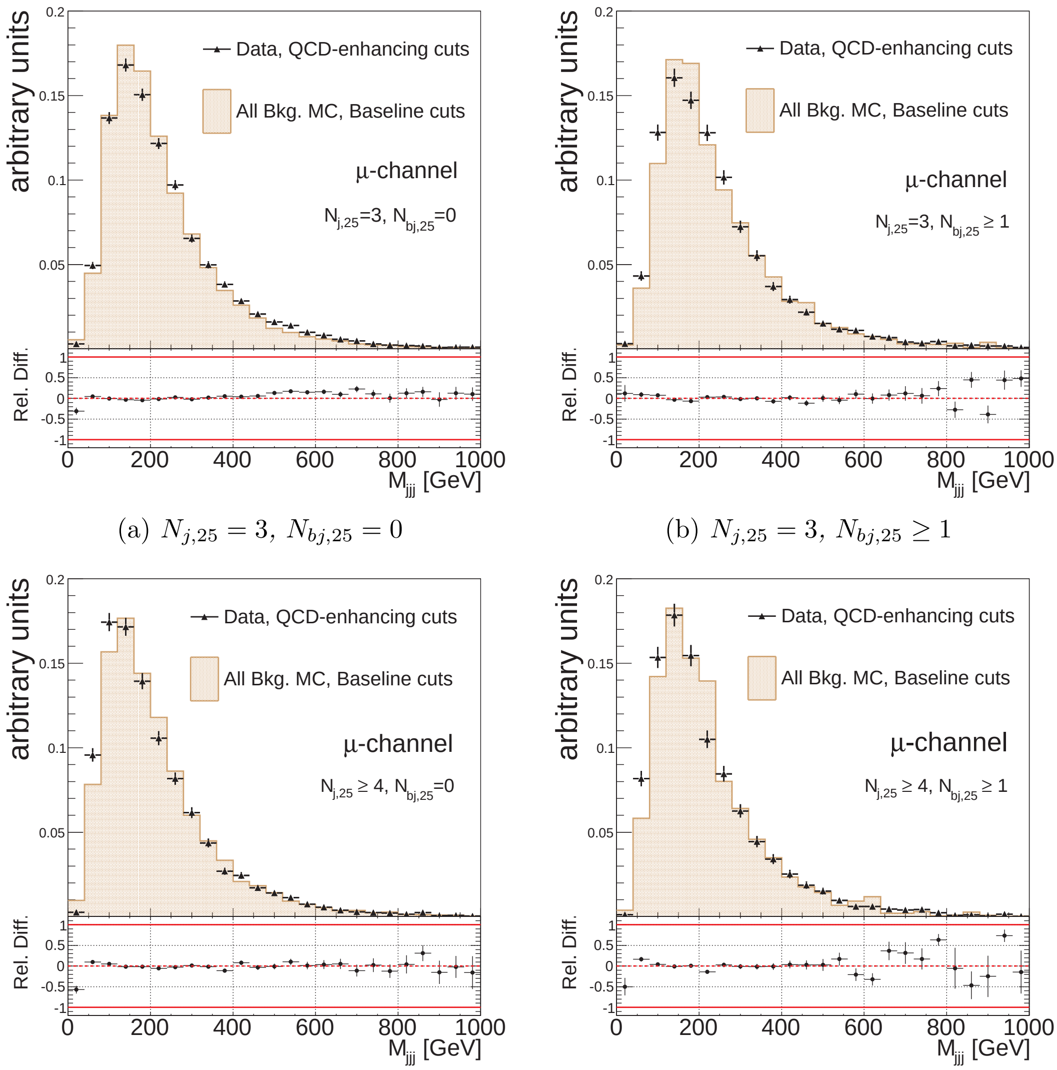

(a) $N_{j,25} = 3,\ N_{bj,25} = 0$

(b) $N_{j,25} = 3,\ N_{bj,25} \geq 1$

(c) $N_{j,25} \geq 4,\ N_{bj,25} = 0$

(d) $N_{j,25} \geq 4,\ N_{bj,25} \geq 1$

Figure 5.13: *Comparison of the data-driven shape, extracted with the QCD-enhancing cuts, and the inclusive background Monte Carlo shape after the baseline cuts for each of the four bins in the μ-channel. The normalized to 35.3 pb^{-1} contribution of each background process is shown in tables 4.8 and 4.9. Histograms normalized to unit area.*

5.3 Summary

In this chapter we discussed the possibility of extracting the background shape, on the M_{jjj} observable, in a data-driven way, so that it can be used for our cross-section template fit method later on (see chapter 6). The approach we followed takes advantage of the fact that we are interested in the shape of the background only and not on the exact normalization; this will be left a free parameter in our fit. As our observable depends on the jet content and topology of the events we simply choose to reverse the lepton requirement in the baseline analysis, while leaving the rest of the selection cuts the same. This is important because we showed that M_{jjj} shape of the QCD events mainly, and secondarily of the W+jets, depends on the $E_{\mathrm{T}}^{\mathrm{miss}}$ and $M_{W,T}$ threshold requirements. For the kinematic region that is of interest for the $t\bar{t}$ analysis, we show that the applied baseline thresholds give a good shape agreement

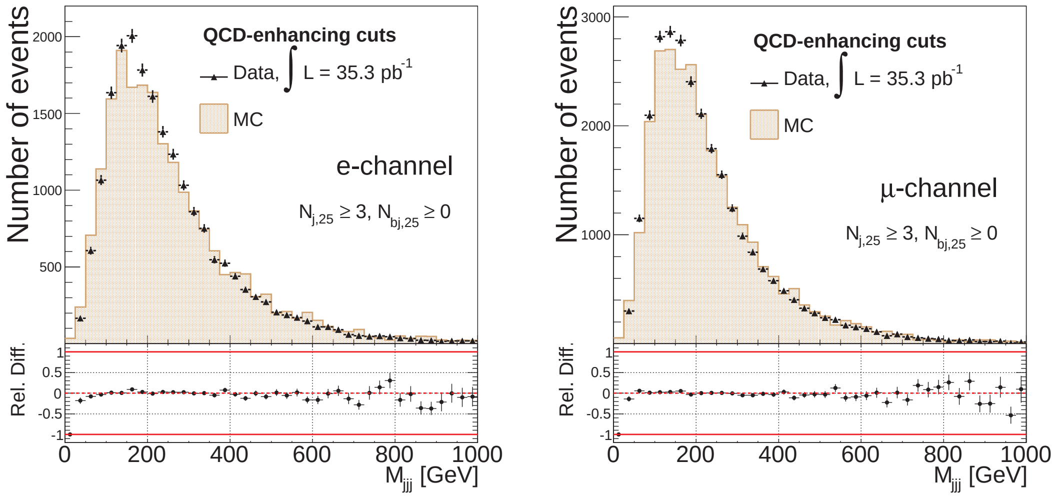

(a) *e-channel* (b) *μ-channel*

Figure 5.14: *Data distribution after applying QCD enhancing cuts. The Monte Carlo distribution is normalized to the number of data events.*

between QCD and W+jets events.

As a cross-check, we compared the W+jets samples between the baseline cuts and the QCD-enhancing cuts. At the inclusive kinematic region, namely $N_{j,25} \geq 3$ and $N_{bj,25} \geq 0$, the statistics are still considerable. We observed that the agreement on the shape between the two cut requirements is remarkable, suggesting that the change of cuts should not affect this background. The same comparison when adding the full background list is again very good but with a small discrepancy at the higher invariant masses ($M_{jjj} > 500$ GeV). We will account for this in the systematic uncertainties of our fit method which we present in the next chapter.

Chapter 6

Top-quark pair production cross-section at $\sqrt{s} = 7$ TeV

"Big results require big ambitions."

Heraclitus of Ephesus
c. 535 BC - c. 475 BC

In this chapter we present the measurement of the inclusive production cross-section of top quark-pair events that are produced in 7 TeV center-of-mass energy of proton-proton collisions in the ATLAS detector. For this proton collision energy the theoretical prediction of the cross-section at NNLO approximation gives a value of $164.6^{+11.4}_{-15.8}$ pb (see [55]).

The measurement we present here uses the complete 2010 dataset recorded by ATLAS corresponding to a total of 35.3 pb^{-1} of integrated luminosity (see section 4.4.1). The method we develop relies on the identification of the single-lepton $t\bar{t}$ events in the $t\bar{t}(e)$ and $t\bar{t}(\mu)$ final states, however in the final event sample we make no distinction from other leptonically decaying channels that may be seen as signal e.g. $t\bar{t}(\tau)$ or di-leptonic flavors. Therefore, for deriving the cross-section from the number of identified signal events (N_{signal}) we use equation 4.5.1 in the following form:

$$\sigma_{t\bar{t}} = \frac{N_{signal}}{\int \mathcal{L}dt \cdot BR \cdot \epsilon_{t\bar{t}}} \ , \tag{6.0.1}$$

where $\epsilon_{t\bar{t}}$ is the selection efficiency for $t\bar{t}$ events at any of the leptonic final states and BR corresponds to the branching ratio of our signal events. To estimate the branching ratio we take the branching ratio of $W \to \ell\nu_\ell$ decays to be 0.108 per leptonic flavor or 0.324 for all flavors inclusive [53]. This suggests that the hadronically decaying W boson has a total ratio of 0.676. Since we include all but the fully-hadronic $t\bar{t}$ channel, the branching ratio in equation 6.0.1 will be:

$$BR = 1 - 0.676 \cdot 0.676 = 0.543 \ .$$

In section 6.1 we discuss the estimation of parameter $\epsilon_{t\bar{t}}$ and how we utilize the data-driven scale factors. Section 6.2 presents our simultaneous template fit method. We discuss the general formulation of the method and we provide the list of parameters categorized in those which are obtained from the Monte-Carlo and those which are extracted from data-driven methods. We also discuss the constraints we placed in certain parameters. In section 6.3 we validate the method by applying it on the Monte Carlo and we also perform ensemble and linearity tests. In section 6.4 we present the result by applying the method on the collected

Kinematic Region	Selection efficiency (%)	
	μ-channel	e-channel
$N_{j,25} = 3$, $N_{bj,25} = 0$	1.707 ± 0.009	1.216 ± 0.008
$N_{j,25} = 3$, $N_{bj,25} \geq 1$	3.306 ± 0.013	2.430 ± 0.011
$N_{j,25} \geq 4$, $N_{bj,25} = 0$	2.251 ± 0.010	1.634 ± 0.009
$N_{j,25} \geq 4$, $N_{bj,25} \geq 1$	6.612 ± 0.027	4.353 ± 0.021

Table 6.1: *The $t\bar{t}$ selection efficiency for each of the kinematic regions that are used for the cross-section calculations. The numbers are estimated from the Monte Carlo shown in tables 4.8 and 4.9. The notation is explained in section 4.5.1.*

data sample and in section 6.5 we discuss the relevant systematic uncertainties. Lastly, in section 6.6 we present the measurement based on the combination of the $t\bar{t}(\mu)$ and $t\bar{t}(e)$ channels. The necessary extension on the fit formulation is also explained.

6.1 The $\epsilon_{t\bar{t}}$ estimate and data-driven scale factors

The value of the $t\bar{t}$ selection efficiency ($\epsilon_{t\bar{t}}$), present in equation 6.0.1, can be described as the product of all the individual efficiencies of the selection cuts and of the geometrical acceptance of the detector (A_g). We write it in the following way :

$$\epsilon_{t\bar{t}} = \epsilon_{trig} \cdot \epsilon_{\ell,reco} \cdot \epsilon_{\ell,id} \cdot \epsilon_{other} \cdot A_g \tag{6.1.1}$$

where A_g the geometrical acceptance of the detector, ϵ_{trig} is the efficiency of the trigger selection, $\epsilon_{\ell,reco}$ is the efficiency on the lepton reconstruction, $\epsilon_{\ell,id}$ is the efficiency on the lepton identification, ϵ_{other} is the product of all other efficiencies, namely the jet identification and reconstruction as well as the b-jet identification. Typically, the overall $\epsilon_{t\bar{t}}$ value is estimated from Monte Carlo. Using the results shown in tables 4.8 and 4.9 we get the $\epsilon_{t\bar{t}}$ for each of the kinematic regions of interest for this analysis; the results are shown in table 6.1 and the notation of the kinematic regions are explained section 4.5.1. With this approach systematic variations must be taken into account for each of the terms.

Alternatively, estimates for certain terms can also be obtained from the data itself. For this analysis, data-driven methods are used for the trigger (see also section 3.3), and the lepton reconstruction and identification efficiency terms. The results of these calculations can be compared with the equivalent Monte Carlo ones using scale factors:

$$SF = \frac{\epsilon^{data}}{\epsilon^{MC}} \ . \tag{6.1.2}$$

In this case, the $\epsilon_{t\bar{t}}$ can be corrected to the data-driven estimate and can be re-written as follows:

$$\epsilon_{t\bar{t}} = (\epsilon^{MC}_{trig} \cdot \epsilon^{MC}_{\ell,reco} \cdot \epsilon^{MC}_{\ell,id} \cdot \epsilon^{MC}_{other} \cdot A_g) \cdot (SF_{trig} \cdot SF_{\ell,reco} \cdot SF_{\ell,id}) \tag{6.1.3}$$

The terms that are included in the ϵ_{other} are not corrected at this level but instead systematic variations are taken into account; systematics of the method are discussed in section 6.5.

6.1.1 Trigger scale factors

Trigger scale factors are estimated using the tag-and-probe method on $Z \to \ell\ell$ events, where ℓ stands for electrons or muons. The muon tag-and-probe was introduced in chapter 3. For the electron trigger also $W \to e\nu_e$ events are used. A detailed description of the method and the results corresponding to the dataset used in this analysis is given in [148, 157] for the electron trigger and in [148].

As mentioned already in section 4.4.2, the electron trigger that is used is the `EF_e15_medium`, which shows a 99% efficiency with a plateau at $E_T \geq 20$ GeV. The result on its scale factor is:

$$SF_{trig,e} = 0.995 \pm 0.005(stat. + syst.) \; , \tag{6.1.4}$$

and is taken uniformly in the whole η and ϕ range that is of interest for this analysis.

For the muon, the triggers used are the `EF_mu10_MSonly`, `EF_mu13` and `EF_mu13_tight`, each for a certain period of the data-taking (see section 4.4.2), a single scale factor however is computed for the total of the selected data. Due to the complexity on the geometry of the Muon Spectrometer, disagreements between data and Monte Carlo have been observed especially with respect to different η and ϕ areas. Therefore the scale factor is separated into ten bin regions as shown in table 6.2. The value of the scale factor at each bin is shown in table 6.3. Although a generally good agreement between Monte Carlo and data is observed, namely the value of the scale factor is close to 1, still fluctuations between the regions are observed justifying the separation into different bins.

Bin Name	**η range**	**ϕ range**
EC	$\|\eta\| > 1.05$	-
B1P1	[-1.05,0.60],	[-π,5π/16] or [11π/16,π]
B1P2	[-1.05,0.60] or [-0.60,-0.50] or [-0.50,0.20] or [0.30,0.60]	[5π/16,π/2]
B1P3	[-1.05,0.60]	[π/2,11π/16]
B2P1	[-0.60,0.60]	[-π,5π/16] or [11π/16,π]
B2P2	[-0.50,-0.40] or [0.20,0.30]	[5π/16,π/2]
B2P3	[-0.60,0.60]	[π/2,11π/16]
B3P1	[0.60,1.05]	[-π,5π/16] or [11π/16,π]
B3P2	[0.60,1.05]	[5π/16,π/2]
B3P3	[0.60,1.05]	[π/2,11π/16]

Table 6.2: *The ten bins in $\eta - \phi$ space for which the muon trigger scale factor is estimated. The first columns give a name for each bin for simplicity. See [148]*

6.1.2 Lepton reconstruction and identification scale factors

In a the same way as with the trigger scale factors the lepton reconstruction and identification scale factors are estimated. For both electrons and muons the tag-and-probe technique is used on $Z \to ee$ [148, 160] or $Z \to \mu\mu$ [148] events respectively. For the electrons, the identification efficiency estimation also uses W events [160] which are combined statistically with the Z boson decay events.

The muon scale factor estimates are calculated independently, but are provided as a single number. No kinematic dependence is given and the value of the scale factor is provided uniformly in $\eta - \phi$ coordinates:

$$SF_{\mu,reco,id} = 0.999 \pm 0.002(stat.) + 0.003(syst.) \; . \tag{6.1.5}$$

It is evident that the agreement between data and Monte-Carlo is very good, while the expected uncertainty is also very low.

Bin Name	Scale Factor ($SF_{trig,\mu}$)
EC	$0.987^{+0.001}_{-0.001}$(syst.) $\pm\, 0.003$(stat.)
B1P1	$1.026^{+0.003}_{-0.002}$(syst.) $\pm\, 0.010$(stat.)
B1P2	$0.919^{+0.007}_{-0.000}$(syst.) $\pm\, 0.017$(stat.)
B1P3	$0.952^{+0.002}_{-0.003}$(syst.) $\pm\, 0.030$(stat.)
B2P1	$1.009^{+0.001}_{-0.002}$(syst.) $\pm\, 0.006$(stat.)
B2P2	$0.657^{+0.010}_{-0.000}$(syst.) $\pm\, 0.050$(stat.)
B2P3	$0.906^{+0.000}_{-0.004}$(syst.) $\pm\, 0.019$(stat.)
B3P1	$1.005^{+0.002}_{-0.003}$(syst.) $\pm\, 0.010$(stat.)
B3P2	$0.843^{+0.000}_{-0.013}$(syst.) $\pm\, 0.053$(stat.)
B3P3	$1.046^{+0.011}_{-0.009}$(syst.) $\pm\, 0.029$(stat.)

Table 6.3: *Muon trigger scale factor as estimated for each of the ten $\eta - \phi$ bins. Numbers from [148].*

Similarly, the electron scale factor is also evaluated uniformly in η and ϕ range with a value of:

$$SF_{e,reco} = 1.000 \pm 0.015(stat. + syst.)\ . \tag{6.1.6}$$

For the identification however, the estimation is separated in different η areas and for different E_T ranges. Together with the identification, the isolation efficiency of electrons is measured. Detailed descriptions on the above measurements are documented in [148, 160]. The combined result of identification and isolation efficiencies is shown in table 6.4, separated in the different kinematic regions. Only very small fluctuations are observed in between $E_T - \eta$ regions.

$SF_{e,id,iso}$

	$\eta \in$			
E_T **(GeV)**	$[-2.47, 2.01]$	$[-2.01, -1.52]$	$[-1.37, -0.8]$	$[-0.8, 0]$
20-25	0.917 ± 0.082	0.946 ± 0.084	0.968 ± 0.083	0.907 ± 0.082
25-30	0.960 ± 0.028	0.990 ± 0.032	1.013 ± 0.029	0.949 ± 0.027
30-35	0.998 ± 0.027	1.029 ± 0.030	1.053 ± 0.027	0.987 ± 0.025
35-40	0.996 ± 0.024	1.027 ± 0.028	1.051 ± 0.025	0.985 ± 0.023
40-45	0.998 ± 0.025	1.029 ± 0.029	1.053 ± 0.026	0.987 ± 0.024
>45	1.007 ± 0.033	1.038 ± 0.037	1.062 ± 0.034	0.995 ± 0.032

$SF_{e,id,iso}$

	$\eta \in$			
E_T **(GeV)**	$[0, 0.8]$	$[0.8, 1.37]$	$[1.52, 2.01]$	$[2.01, 2.47]$
20-25	0.912 ± 0.082	0.970 ± 0.082	0.961 ± 0.086	0.953 ± 0.086
25-30	0.955 ± 0.027	1.016 ± 0.028	1.006 ± 0.038	0.998 ± 0.036
30-35	0.993 ± 0.025	1.056 ± 0.026	1.046 ± 0.037	1.037 ± 0.035
35-40	0.991 ± 0.023	1.054 ± 0.024	1.044 ± 0.035	1.035 ± 0.034
40-45	0.993 ± 0.024	1.056 ± 0.024	1.046 ± 0.036	1.037 ± 0.034
>45	1.002 ± 0.032	1.065 ± 0.033	1.055 ± 0.042	1.046 ± 0.041

Table 6.4: *Electron identification and isolation scale factors as estimated with respect to different η and E_T ranges. Numbers from [160].*

6.2 Simultaneous template fit method

A key element of the method we present here is that an extended dataset is utilized that includes also areas of the phase-space that are dominated by background events. In particular all events with at least three "good" jets with $p_{\mathrm{T}} \geq 25$ GeV are considered. This dataset is subsequently separated in four distinctive kinematic regions based on their overall jet multiplicity and the b-jet multiplicity, these regions have already been defined in section 4.5.1.

Compared to a cut-and-count method where Monte Carlo or data-driven background estimates would be subtracted by the collected data in a given signal region ,the fit approach we implement has two main advantages. Firstly, a higher-statistics sample is made available for the cross-section measurement by including background-dominated regions. Secondly, exactly because of the inclusion of these regions it is possible to parametrize the method in such a way that strong constraints can be placed to the background normalization. The information from background-dominated areas can subsequently be translated to the signal region.

In our method we first characterize independently the signal and the background contributions with functional templates that are obtained from the shape of their M_{jjj} distributions. We then perform an extended likelihood fit on the observed data simultaneously in all regions keeping the shape of the templates fixed and their relative normalization free to float.

Formulation

Mathematically, the method is described by a set of four equations, one for each of the kinematic regions that are of interest. The total number of events within each region is given by:

$$N_{obs}^{i,j} = \varepsilon_S^{i,j} N_S^i T_S^{i,j} + \varepsilon_B^{i,j} N_B^i T_B^{i,j} \ , \tag{6.2.1}$$

where the subscript S refers to signal and B to background events and the i and j superscripts denote the jet multiplicity ($i = 3$ or $i \geq 4$) and b-jet multiplicity ($j = 0$ or $j \geq 1$) respectively[1]. The parameters that appear in the formula are:

- The event tagging rate ($\varepsilon^{i,j}$) of the background or signal events in the i-th jet multiplicity and j-th b-jet multiplicity region.
- The template function ($T^{i,j}$), built from the shape of the M_{jjj} distribution for signal or background, at the i-th jet multiplicity and j-ith b-jet multiplicity region.
- The total number of signal or background events ($N_{S,B}^i$) in the i-th jet multiplicity region.
- The total number of observed events ($N_{obs}^{i,j}$) in the i-th jet multiplicity and j-ith b-jet multiplicity region.

These are described in greater detail in the following paragraphs and a summary is shown in table 6.6 at the end of this section.

6.2.1 Template Functions

The template functions are extracted by fitting the M_{jjj} distribution with a functional form. For the case of the background, the distribution is extracted in a data-driven way following the observations and the methodology presented in chapter 5. On the other hand the signal

[1]The $i = 3$ and $i \geq 4$ will also be referred to as 'three-jet' and 'four-jet' regions respectively. Similarly, the $j = 0$ and $j \geq 1$ will be referred to as the 'no-tag' and 'tagged' regions respectively, while for the case of $j \geq 0$ the term 'pre-tagged' is used.

templates are entirely taken from Monte Carlo. The following functional form is used to fit the background shapes:

$$f(x) = \begin{cases} \dfrac{\alpha}{\sqrt{2\pi}} e^{-\frac{(x-x_0)^2}{2\sigma^2}} & , \text{if } x < x_0 + \dfrac{1}{2\gamma}\sigma^2 \\ \dfrac{\beta}{\sqrt{2\pi}} e^{-\frac{(x-x_0)}{2\gamma}} & , \text{if } x \geq x_0 + \dfrac{1}{2\gamma}\sigma^2 \end{cases} , \tag{6.2.2}$$

which translates to a gaussian on the left-hand side of the M_{jjj} distribution and an exponential to the right-hand side. Parameters α and β define the normalization of the function, x_0 is the position of the peak of the distribution, σ is the width of the gaussian and γ is the inverse of the exponential falling rate. The left and right-hand side of the function are distinguished by a cross-over point (x_c) which is estimated by requiring the function to be continuous, hence the following must hold:

$$\begin{aligned} f(x = x_c)_{left} &= f(x = x_c)_{right} \quad , \text{and} \\ \left.\frac{df_{left}}{dx}\right|_{x=x_c} &= \left.\frac{df_{right}}{dx}\right|_{x=x_c} . \end{aligned}$$

A direct consequence of this is that the normalization parameters in each part of the function are related by the following:

$$\beta = \alpha e^{\frac{\sigma^2}{8\gamma}} ,$$

therefore reducing the independent fit parameters by one. For the case of the signal templates, the above function is again used but with an additional gaussian introduced to the model. This extra gaussian parametrizes the expected top quark signal peak.

Figure 6.1 shows the fitted distributions of signal (first and third lines) and background (second and fourth lines) for the μ-channel (top two lines) and e-channel (bottom two lines) respectively. Once the parameters are determined, the template function is formed and is kept fixed in formula 6.2.1.

6.2.2 Event Tagging Rates

For each jet multiplicity region an efficiency parameter is defined that represents the number of signal (background) events with at least one "good" jet of $p_{\mathrm{T}} \geq 25$ GeV being identified as a b-jet (hence having a weight from the `SVO` tagger of at least 5.85) divided by the total number of signal (background) events in the given region. The following, thus, holds:

$$\varepsilon_X^{i,1} = \frac{N_X^{i,1}}{N_X^i} , \tag{6.2.3}$$

where X denotes either the signal (S) or background (B) events. This parameter is introduced in formula 6.2.1 as the event tagging rate and it holds by definition that $\varepsilon^{i,1} = 1 - \varepsilon^{i,0}$.

For the signal events the tagging rates ($\varepsilon_S^{4,1}$, $\varepsilon_S^{3,1}$) are determined from the Monte Carlo sample and are introduced in the fit as fixed parameters. On the other hand, the tagging rates for the background are introduced through $\varepsilon_B^{3,1}$ and a scale factor that translates the rate from the three-jet region to the four jet region ($SF_{3\to4}$), hence the following holds:

$$\varepsilon_B^{4,1} = SF_{3\to4}\varepsilon^{3,1} . \tag{6.2.4}$$

In this formulation the $SF_{3\to4}$ parameter is estimated from the Monte Carlo while the $\varepsilon^{3,1}$ term is free to float. We prefer the use of the scale factor, instead of just simply taking $\varepsilon_B^{4,1}$

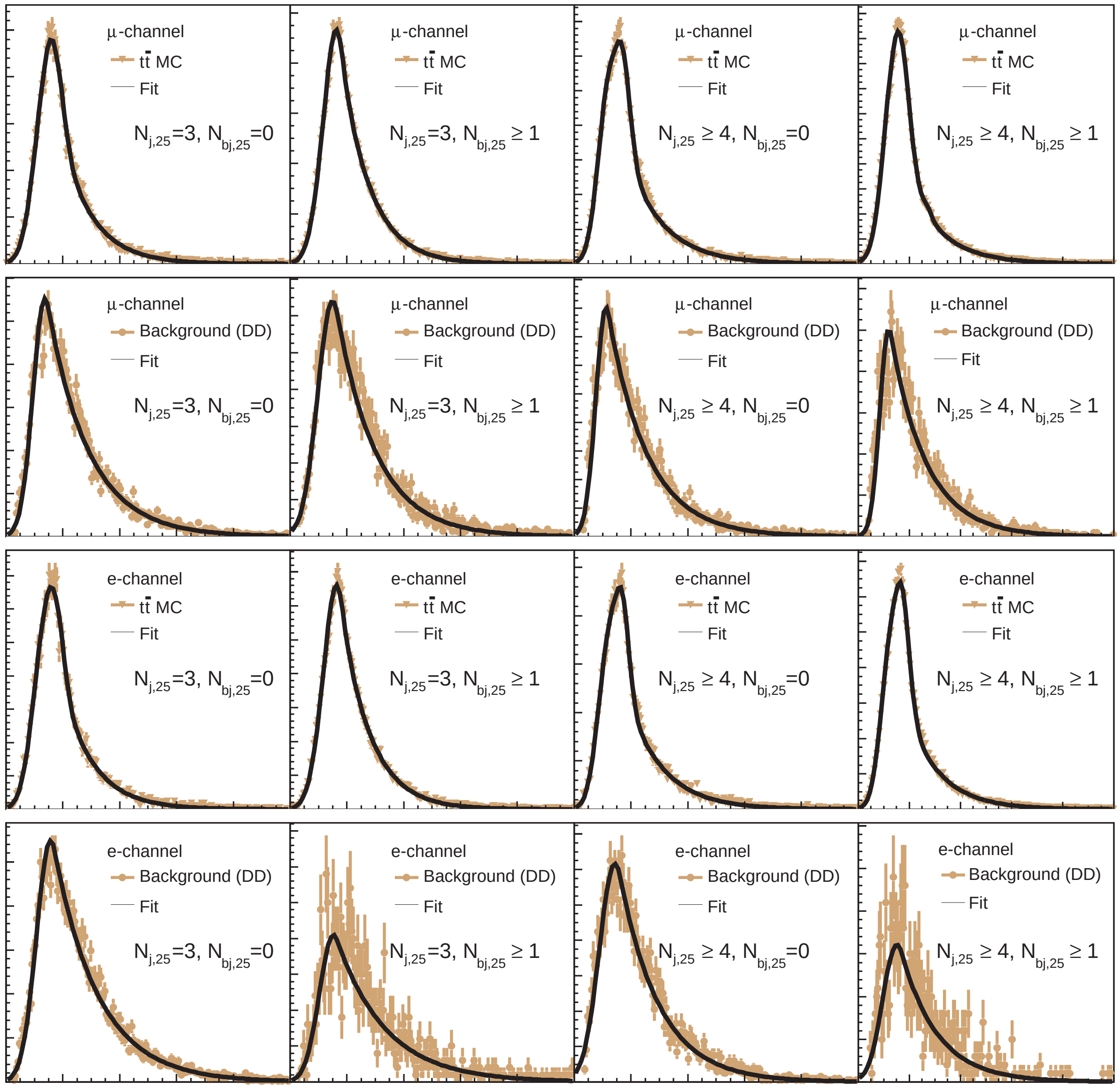

Figure 6.1: *Functional fit of M_{jjj} distributions: the x-axis corresponds to the value of M_{jjj} in the range [0,1000] GeV while the y-axis gives the normalization (number of events) which is not relevant for the extraction of the shape. The bin width is set at 5 GeV. In the first and second lines the μ-channel is shown, signal and background respectively, and in the third and fourth lines the e-channel, also signal and background respectively. The four columns correspond to the kinematic regions of interest, from left to right: $N_{j,25} = 3$ & $N_{bj,25} = 0$, $N_{j,25} = 3$ & $N_{bj,25} \geq 1$, $N_{j,25} \geq 4$ & $N_{bj,25} = 0$, $N_{j,25} \geq 4$ & $N_{bj,25} \geq 1$. The background distributions are all obtained using the data-driven method (see chapter 5) while the signal ones are taken from Monte Carlo.*

from Monte Carlo, because, as it is a ratio of the respective efficiencies, it is less sensitive in systematic effects.

In order to improve the fit method with respect to the expected systematic uncertainties on the background parametrization, a gaussian term on $\varepsilon^{3,1}$ is applied; this is explained in the next paragraph.

The constraint on $\varepsilon^{3,1}$

We define the following relation for the $\varepsilon^{3,1}$ term:

$$\varepsilon_B^{3,1} = \varepsilon_B^{2,1} SF_{2\to3} \ , \tag{6.2.5}$$

where the $\varepsilon_B^{2,1}$ corresponds to the event tagging rate of background events at the exclusive two-jet bin, namely events with exactly two "good" jets of $p_{\mathrm{T}} \geq 25$ GeV, and the $SF_{2\to3}$ is a factor that translates the rate of background events to the corresponding three-jet region, similar to the $SF_{3\to4}$.

The $SF_{2\to3}$ factor is entirely obtained from Monte Carlo. On the other hand, the $\varepsilon_B^{2,1}$ has the advantage that it corresponds to a kinematic region which is expected to be dominated by background events. Thus, it can be calculated from the observed data events with only requiring a correction for the expected signal contamination which is introduced from the Monte Carlo. It holds that :

$$\varepsilon_B^{2,1} = \frac{N_{obs}^{2,1} - N_{t\bar{t}}^{2,1}}{N_{obs}^{2} - N_{t\bar{t}}^{2}} \ , \tag{6.2.6}$$

where N_{obs}^{2} and $N_{t\bar{t}}^{2}$ is the number of pre-tagged data and Monte Carlo $t\bar{t}$ events respectively, while $N_{obs}^{2,1}$ and $N_{t\bar{t}}^{2,1}$ is the subsets of events that are tagged. The corresponding yields for each channel are shown in table 6.5. The estimate of $\varepsilon_B^{2,1}$ now depends mainly on the available data statistics and the description of the signal events by the Monte Carlo which is substantially more accurate than the background estimates as it is simulated by a next-to-leading order generator.

Having calculated $\varepsilon_B^{2,1}$ from 6.2.6, the $\varepsilon^{3,1}$ enters the fit as gaussian constrained parameter with a central value that is obtained from equation 6.2.5 and with a width taken equal to the uncertainty that comes from the $\varepsilon_B^{2,1}$ term. The reason for this is to disentangle the uncertainty that is entirely Monte Carlo based, like in the case of the $SF_{2\to3}$, as it will be taken into account for the calculation of the systematics later on. The uncertainty of $\varepsilon_B^{2,1}$ is driven by the data statistics and the description of the simulation which affects the acceptance of $t\bar{t}$ events (systematic). The systematic part is obtained by calculating the $t\bar{t}$ contribution for each of the variated Monte Carlo samples that are used for the systematic checks and comparing the value with the one from the reference Monte Carlo. Subsequently, all the deviations are added in quadrature and are combined with the statistical uncertainty giving a total of 17.8% for the e-channel and 14.9% for the μ-channel parameter.

6.2.3 Jet multiplicity ratio

In the template fit as described by 6.2.1, the parameters N_S^3, N_S^4, N_B^3 and N_B^4 are left free to float. They can be connected to the total number of signal or background events with the following relations:

$$\begin{aligned} N_X^3 &= \epsilon_X^3 N_X \text{ and similarly} \\ N_X^4 &= \epsilon_X^4 N_X \ , \end{aligned} \tag{6.2.7}$$

Parameter	μ-channel	e-channel
N^2_{obs}	4677	2534
$N^{2,1}_{obs}$	271	131
$N^2_{t\bar{t}}$	69.9	52.2
$N^{2,1}_{t\bar{t}}$	38.9	29.6

Table 6.5: *Event yields in the two-jet region for data (N^2_{obs}, $N^{2,1}_{obs}$) and $t\bar{t}$ Monte Carlo ($N^2_{t\bar{t}}$, $N^{2,1}_{t\bar{t}}$) events.*

where X refers to signal (S) or background (B) events and N_X is the total number of the given type of events. Similarly to the event tagging rates, the parameters ϵ^3_X and ϵ^4_X are defined as the rates of having three-jet or four-jet events of a given type, irrespectively of the content of b-tagged jets. We can parametrize these rates with in the following way:

$$\epsilon^3_X = \frac{1}{1+R_X} \text{ and} \tag{6.2.8}$$

$$\epsilon^4_X = \frac{R_X}{1+R_X} \ , \tag{6.2.9}$$

where R_X is the ratio of the number of four-jet events over the number of three-jet events, namely:

$$R_X = \frac{N^4_X}{N^3_X} \ . \tag{6.2.10}$$

The better description of the signal Monte Carlo events allows for the R_S parameter to be known with a better accuracy. Since we make no assumption on the total number of signal events we can take advantage of this and apply a gaussian constraint on R_S. The central value of the constrained parameter is obtained from Monte Carlo, while its deviation is calculated as the quadratic sum of all systematic variations and is taken as the width of the gaussian. The variations are obtained by comparing the value from the reference Monte Carlo with the value that is extracted by performing a fit with the R_S unconstrained on the variated Monte Carlo (pre-fit). The uncertainty estimate is 30.3% for the e-channel and 22.5% for the μ-channel. For the background events the relationship between N^3_B and N^4_B is also parametrized by R_B but no constrain is applied.

A summary of the parameters that are present in the fit is given in table 6.6.

6.3 Validation of the fit

We validate the fit method by applying it on the nominal Monte Carlo samples treating the latter as "data" (pseudo-data). Naturally, no data-driven approach is used and the parameters that are given as input correspond to an ideal description of the data by the Monte Carlo. This also includes the background templates, which should follow the data as they are obtained in a data-driven way, and therefore are re-computed from the combination of the Monte Carlo samples. The constrained parameters obtain their gaussian central values likewise and their width remains the same as shown in the previous section. Each of the fitted free parameters is compared using the relation:

$$\delta_x = \frac{x_{fit} - x_{input}}{x_{input}} \ ,$$

Fit Parameter	Type	Comments
$T_B^{3,0}, T_B^{3,1}, T_B^{4,0}, T_B^{4,1}$	Data-driven	Fixed shape templates. See chapter 5.
$T_S^{3,0}, T_S^{3,1}, T_S^{4,0}, T_S^{4,1}$	Monte Carlo	Fixed shape templates.
$\epsilon_S^{3,1}$, $\epsilon_S^{3,0}$	Monte Carlo	Constrained with $\epsilon_S^{3,0} = 1 - \epsilon_S^{3,1}$
$\epsilon_S^{4,1}$, $\epsilon_S^{4,0}$	Monte Carlo	Constrained with $\epsilon_S^{4,0} = 1 - \epsilon_S^{4,1}$
$\epsilon_B^{3,1}$, $\epsilon_B^{3,0}$	Gaussian constraint	Central value from $\epsilon_B^{3,1} = \epsilon^{2,1} SF_{2\to3}$, width from $\epsilon_B^{2,1}$ uncertainty. Constrained with $\epsilon_B^{3,0} = 1 - \epsilon_B^{3,1}$
$\epsilon_B^{4,1}$, $\epsilon_B^{4,0}$	Derived	$\epsilon_B^{4,1} = \epsilon^{3,1} SF_{3\to4}$. Connected with $\epsilon_B^{4,0} = 1 - \epsilon_B^{4,1}$,
$SF_{3\to4}$	Monte Carlo	
N_S^3, N_S^4	Free	Connected with $R_S = N_S^4/N_S^3$, R_S is constrained with a gaussian term.
N_B^3, N_B^4	Free	Connected with $R_B = N_B^4/N_B^3$, R_B is free.

Table 6.6: *List of the parameters that are involved in the fit (see equation 6.2.1).*

	μ-channel	**e-channel**
x	δ_x	
N_S	-0.0059	-0.0082
N_B	0.0005	0.0005
R_S	0.0083	0.0041
R_B	-0.0016	0.0013
$\epsilon_B^{3,1}$	0.0037	0.0087

Table 6.7: *Relative difference of fitted value versus input value for each of the floating parameters of the fit. The results are obtained from a single fit on the Monte Carlo samples (validation fit).*

where x_{input} is the true value of the parameter, which is also given as initial value to the fit, and x_{fit} is the resulting fitted value. The result of the validation fit is summarized in table 6.7 where it is shown that δ_x is very close to unity for all parameters, demonstrating a good behavior of the fit.

Ensemble test

In order to ensure that the fit is not biasing the result, we perform an ensemble test of 10000 pseudo-experiments (PSEs) for each channel. Each PSE is generated from the shape of the expected distributions, it corresponds to an integrated luminosity of 35.3 pb^{-1} and the normalization of signal and background at each bin is randomized following Poisson statistics. Each PSE is subsequently fitted and the result of the fit is stored. We determine the bias on N_S and N_B by calculating their *pull* distributions, where the pull is defined as:

$$pull = \frac{N_{real} - N_{fit}}{\sigma_{fit}} \ , \tag{6.3.1}$$

where N_{real} is the number of the generated number of events, N_{fit} is the number of events that the fit estimates and σ_{fit} is the uncertainty that is returned by the fit. A standard normal distribution is expected and therefore the resulting pulls are fitted with a gaussian function. In case the mean of the gaussian is larger (smaller) than zero, a negative (positive) bias is observed. Figures 6.2(a) and 6.2(b) show the results of the pulls for the μ-channel and the e-channel respectively and in all cases the resulting gaussian parameters are within expectations.

Linearity test

As a last check we perform a linearity test for different input cross-sections. We create variations of the Monte Carlo samples where the signal is re-weighted such that it corresponds to the different cross-sections, starting from 120 pb. up to and including 220 pb. in steps of 10 pb. The background samples remain the same. As before, we perform an initial fit and subsequently 2000 PSEs are drawn for each variation of the Monte Carlo. The resulting N_S are then fitted with a gaussian function and the mean is used to evaluate the fitted cross-section.

The sigma of the gaussian is divided by the square root of the total number of PSEs and is used as the error on the estimate. Figure 6.2(c) shows the estimated cross-section with respect to the input cross-section. A first degree polynomial of the form $y = \alpha + \beta x$ is used to fit the points and, as expected, the y-intercept point α is close to zero and the slope parameter β close to one; this is consistent in both channels.

6.4 Application on Data

Following the description given in section 6.2, we give as input to the fit the M_{jjj} template shapes (as calculated in section 6.2.1), the parameters that are taken from the Monte Carlo and are kept fixed (namely the signal tagging rates and the background scaling factor $SF_{3\to4}$), and lastly the constrained gaussian terms. Table 6.8 summarizes the values of these parameters.

The resulting M_{jjj} distributions from the fit are shown in figure 6.3 for the μ-channel and in figure 6.4 for the e-channel. The number of signal and background events that is estimated from the fit is shown in table 6.9. The quoted uncertainty is statistical and is obtained by performing 2000 PSEs; the relevant distributions for the number of signal events are shown in figure 6.5.

It is evident that the agreement of the fits to the data is very good for all the kinematic regions defined and for both channels. As expected, the 3-jet and 4-jet regions are completely dominated by background in the no-tag bin, while in their tagged bins it is considerably reduced. This highlights the importance of b-tagging for selecting signal events. The apparent difference in the yield of background between muon and electron channel is due to the different cuts applied in the two channels, namely with respect to the selection based on $E_{\mathrm{T}}^{\mathrm{miss}}$ and $M_{W,T}$ cuts.

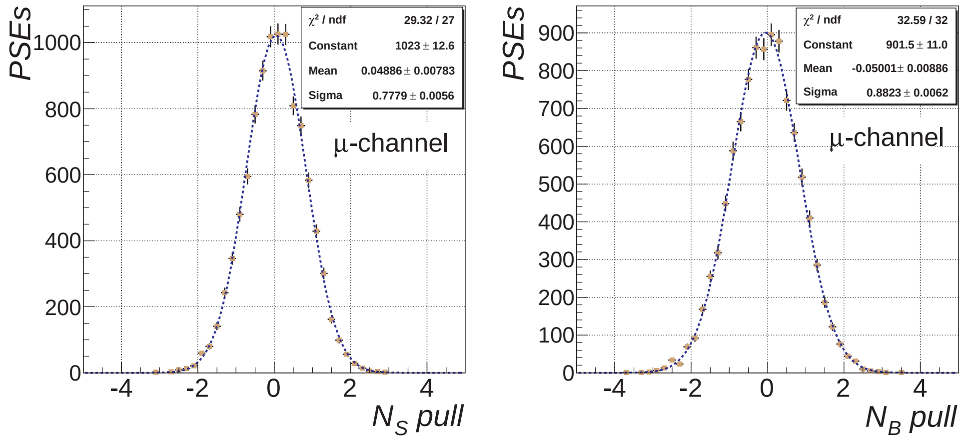

(a) *μ-channel: N_S (left) and N_B (right) pull distributions.*

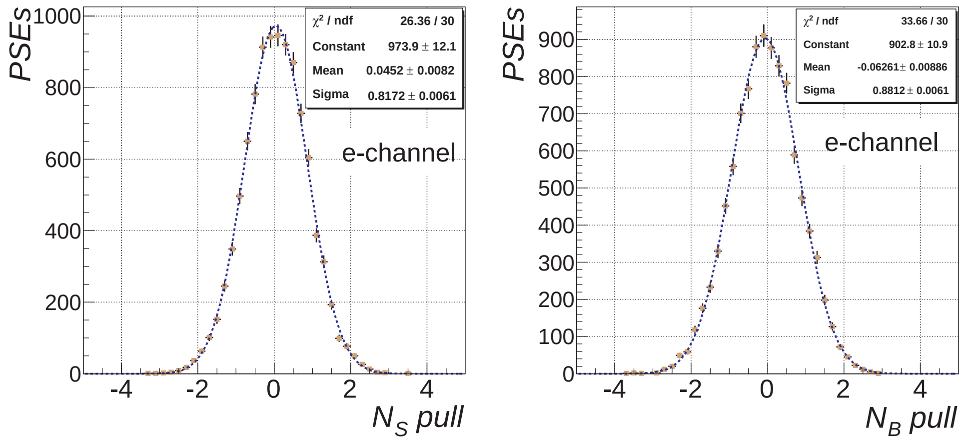

(b) *e-channel: N_S (left) and N_B (right) pull distributions.*

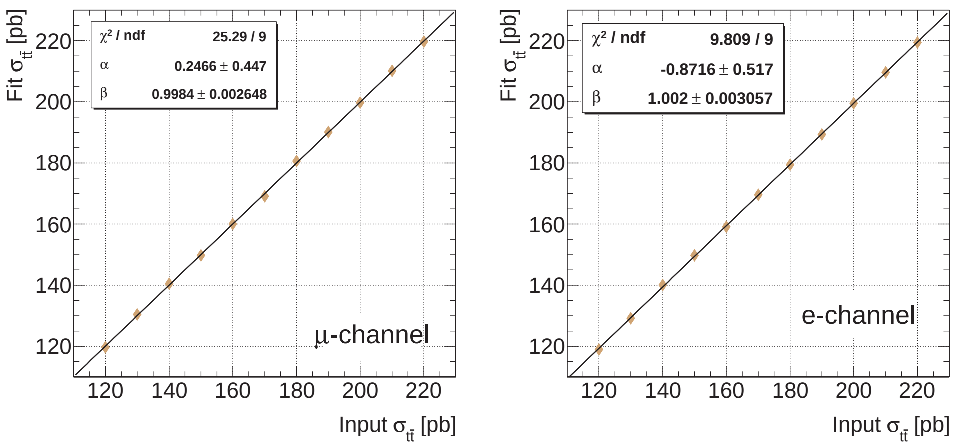

(c) *Linearity test for μ-channel (left) and for e-channel (right)*

Figure 6.2: *The pull distributions of N_S and N_B, drawn from an ensemble test of 10000 PSEs, are shown for the μ-channel (a) and for the e-channel (b). In addition, the linearity test performed for different input signal cross-sections is shown in (c) for both channels: the μ-channel (left) and the e-channel (right). The points from the linearity test are fitted with a first degree polynomial.*

	μ-channel		e-channel	
	Values of Monte Carlo fixed terms			
$\varepsilon_S^{3,1}$	0.6603		0.6668	
$\varepsilon_S^{4,1}$	0.7321		0.7273	
$SF_{3\to4}$	1.6699		1.7895	
	Gaussian-constrained terms			
	Value	**Uncertainty**	**Value**	**Uncertainty**
$\varepsilon_B^{3,1}$	0.0918	± 0.0137	0.0700	± 0.0125
R_S	1.6792	± 0.3778	1.6405	± 0.4971

Table 6.8: *Input values of parameters that are given as input to the fit. The $\varepsilon_S^{3,1}$, $\varepsilon_S^{4,1}$ and $SF_{3\to4}$ are kept fixed while $\varepsilon_B^{3,1}$ and R_S are given as gaussian constraints. A detailed description is given in sections 6.2.2 and 6.2.3.*

	μ-channel	e-channel
N_S	386.9 ± 35.7	392.1 ± 55.8
N_B	1451.1 ± 48.1	769.0 ± 59.7

Table 6.9: *Number of signal and background events as calculated by applying the simultaneous template fit on the 35.3 pb^{-1} of $\sqrt{s} = 7$ TeV proton-proton collision data. The uncertainties are statistical and estimated from running 2000 PSEs.*

6.5 Systematic uncertainties

This section discusses the various sources of systematic uncertainties (systematics) that need to be taken into account in our cross-section calculation. The method we mainly follow depends on comparing the nominal Monte Carlo result with the result from variated versions of the simulation. The variation depends on the evaluated systematic source and typically corresponds to $\pm 1\sigma$ uncertainty. We re-run the fit for each systematic check treating the variated samples as pseudo-data. It should be noted that the advantage of obtaining the background shape with a data-driven way is apparent now since we do not need to take it into account as a source of uncertainty. Therefore, for each systematic variation we re-evaluate the background templates based on the pseudo-data background distributions.

In the following, the Monte Carlo samples assume a top quark mass equal to 172.5 GeV. This choice is consistent with the current world average [53] but we do not assign a systematic for it. The reason is that for small deviations around this value the cross-section is expected to behave linearly. Likewise, we make an assumption for the branching ratio used in equation 6.0.1. We use the value of $BR = 0.543$, which is extracted as describe in the beginning of this chapter, and we conventionally assign no uncertainty to it. In fact, the contribution of the uncertainty is $< 1\%$ [53].

6.5.1 Lepton trigger, reconstruction and identification

The data-driven estimates of efficiencies, and consequently their scale factors, are not free from uncertainties and as a result they must be propagated to the final cross-section result. The values of the scale factor together with their uncertainties were already shown in section 6.1. It should be mentioned that because some scale factors are given with respect to kinematic

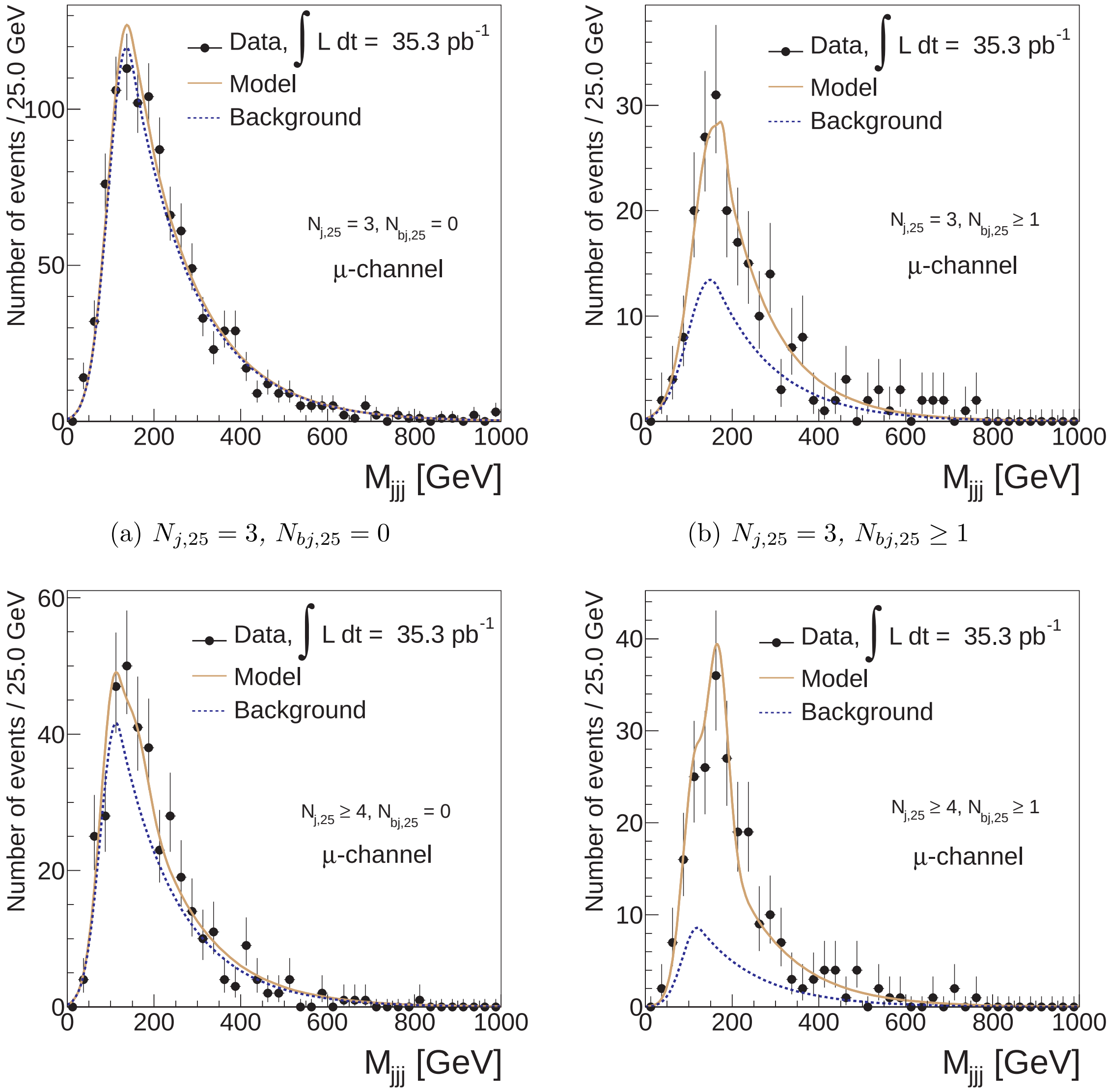

(a) $N_{j,25} = 3,\ N_{bj,25} = 0$

(b) $N_{j,25} = 3,\ N_{bj,25} \geq 1$

(c) $N_{j,25} \geq 4,\ N_{bj,25} = 0$

(d) $N_{j,25} \geq 4,\ N_{bj,25} \geq 1$

Figure 6.3: *The M_{jjj} distributions after applying the simultaneous template fit on the 35.3 pb^{-1} of $\sqrt{s} = 7$ TeV proton-proton collision data. The single-lepton top quark pair μ-channel selection is applied (section 4.4.3).*

ranges, they are not applied directly on the cross-section formula (equation 6.0.1) but are rather given as weights, event by event, depending on the kinematics of the identified lepton. The systematic variations are treated in a similar way by adjusting the weight accordingly.

The uncertainty on our analysis is evaluated by re-running the fit model on the variated Monte Carlo and comparing the results with the nominal case. Since these systematics are not expected to alter the shape of the backgrounds but only their acceptance, the background templates do not need to be re-evaluated. We find a modest 4% uncertainty for the e-channel and 1.5% for the μ-channel. The result is symmetrical in positive and negative deviations since almost all of the scale factors are given with a symmetrical uncertainty.

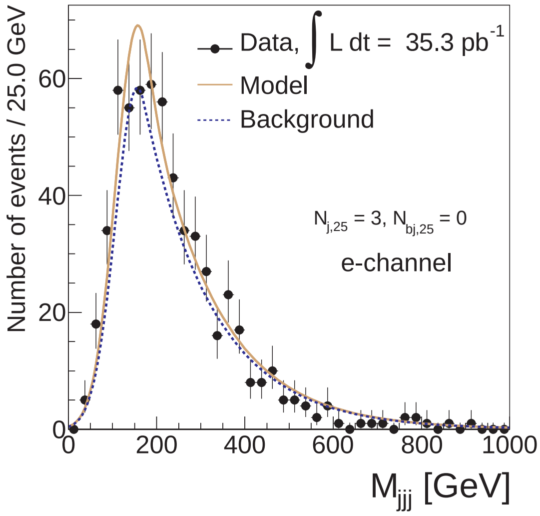

(a) $N_{j,25} = 3,\ N_{bj,25} = 0$

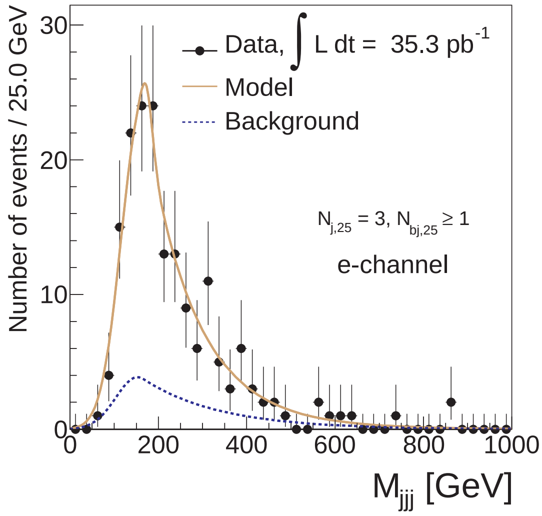

(b) $N_{j,25} = 3,\ N_{bj,25} \geq 1$

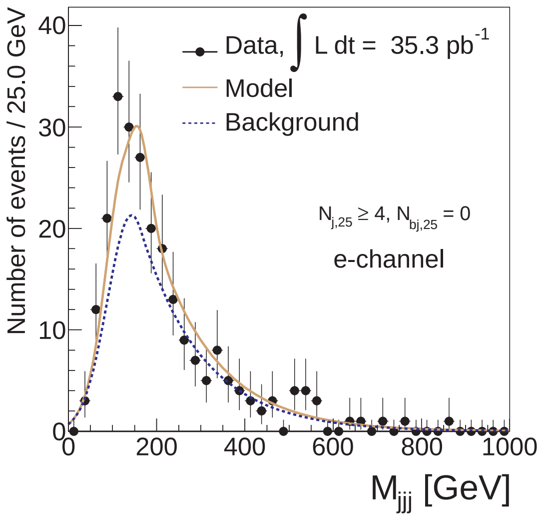

(c) $N_{j,25} \geq 4,\ N_{bj,25} = 0$

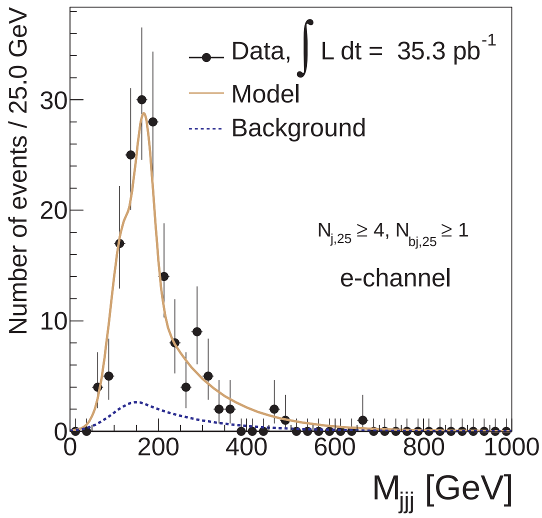

(d) $N_{j,25} \geq 4,\ N_{bj,25} \geq 1$

Figure 6.4: *The M_{jjj} distributions after applying the simultaneous template fit on the 35.3 pb^{-1} of $\sqrt{s} = 7$ TeV proton-proton collision data. The single-lepton top quark pair e-channel selection is applied (section 4.4.3).*

6.5.2 Lepton energy scaling and resolution smearing

In sections 4.2.1 and 4.2.2 the correction factors that are applied on the electrons and muons respectively for improving the agreement between Monte Carlo and data were given. For both muons and electron the energy scaling and resolution is applied by default on the nominal Monte Carlo but naturally their related uncertainties must be taken into account. The implementation is similar as before where the correction factors are given as a weight on event by event and their uncertainties are accounted by adjusting the weight. Likewise, the estimation of the final uncertainty on the cross-section is obtained by comparing the nominal Monte Carlo with their variated versions. We find that for the electron channel the contribution is relatively small at about $+1.3/-1.2\%$ and even smaller for the muon channel, at $\pm 0.4\%$.

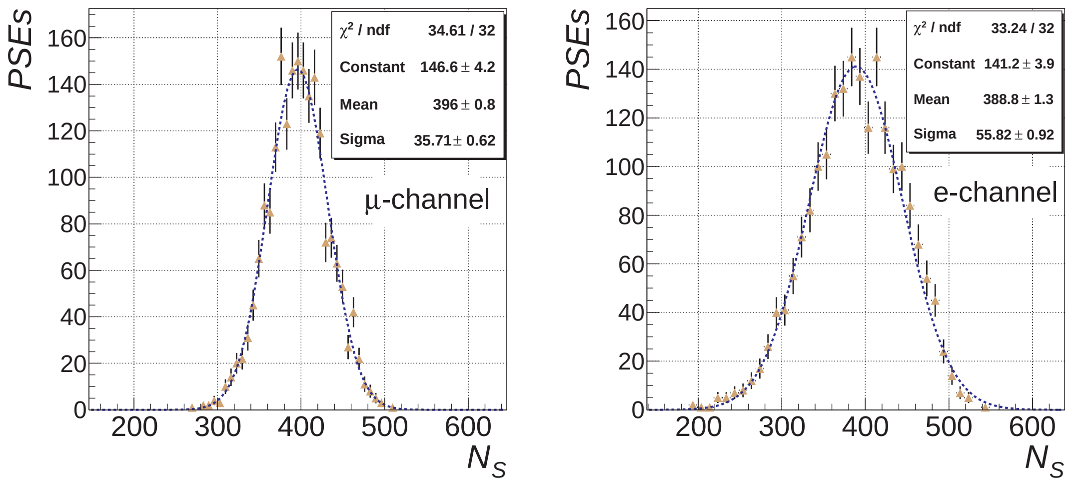

(a) *μ-channel* (b) *e-channel*

Figure 6.5: *Distributions of N_S from 2000 PSEs ran after the fit to the data. The fitted gaussian sigma is taken as the statistical uncertainty on the signal events.*

6.5.3 Jet energy scale

One of the uncertainties that is expected to be more prominent comes from the jet energy scale corrections (JES). The various sources of uncertainty on the JES are estimated from a combination of in-situ measurements of the single hadron response, either from data or pion test-beam measurement, and systematic variations of Monte Carlo samples. The total uncertainty is given per jet depending on its transverse momentum and pseudo-rapidity. The following systematic sources are considered:

- Detector effects such as distortions and un-instrumented material which are evaluated by testing different geometry models.
- The calorimeter cluster noise for topological clusters which is varied with a $\pm 10\%$.
- The Monte Carlo modeling used in event generation.
- The "non-closure" of the jet calibration step (see section 4.1.3).
- Effects from multiple interaction within one event (pile-up).

The result of each particular source are documented in detail in [161, 162]. For isolated jets reconstructed with the `anti-`$k_\perp$ and with $R = 0.4$, and calibrated with the `EMJES` scheme, the JES systematic uncertainty as a function of p_T and η is shown in table 6.10. To the above calculations a conservative approach is taken for accounting close-by activity by adding 5% to each jet for when a second jet with $p_T > 10$ GeV resides within $\Delta R \leq 0.6$ [163].

In this analysis, each jet in the Monte Carlo is varied by its 1σ variation, upwards or downwards, creating two different samples. After running the fit on the two variations we compare their results with the one obtained from the nominal case. The uncertainty we find for the e-channel is considerably high at $+5.3/-6.2\%$ and slightly lower for the μ-channel at $+4.2/-5.8\%$.

η region	Maximum fractional JES uncertainty		
	$p_T^{jet} = 20$ GeV	$p_T^{jet} = 200$ GeV	$p_T^{jet} = 1.5$ TeV
$0.0 < \|\eta\| < 0.3$	4.1%	2.3%	3.1%
$0.3 < \|\eta\| < 0.8$	4.3%	2.4%	3.3%
$0.8 < \|\eta\| < 1.2$	4.3%	2.5%	3.5%
$1.2 < \|\eta\| < 2.1$	5.2%	2.6%	3.6%
$2.1 < \|\eta\| < 2.8$	8.2%	2.9%	
$2.8 < \|\eta\| < 3.2$	10.1%	3.5%	
$3.2 < \|\eta\| < 3.6$	10.3%	3.7%	
$3.6 < \|\eta\| < 4.5$	13.8%	5.3%	

Table 6.10: *The maximum JES systematic uncertainties for isolated jets, reconstructed with* `anti-`$k_\perp$ *(R=0.4) and calibrated with* `EMJES`*, as estimated from Monte Carlo. Numbers taken from [162].*

6.5.4 Jet energy resolution

In section 4.2.3 the jet energy resolution (JER) correction was discussed. The smearing is applied by default on the nominal Monte Carlo in order to improve the agreement with the data. Running the fit model on the smeared sample, which is used as the reference sample throughout the analysis, we compare the result with the one from the non-smeared simulation. This is taken as the systematic uncertainty due to the JER corrections and it amounts to $\pm 1.9\%$ for the e-channel and $\pm 1.8\%$ for the μ-channel.

6.5.5 Jet reconstruction efficiency

In a similar way as with the lepton reconstruction efficiency, the jet reconstruction efficiency is defined ($\epsilon_{jet,reco}$). The $\epsilon_{jet,reco}$ is measured for calorimeter jets, which are used in this analysis, with respect to track jets, namely jets that are built solely from charged particle track information obtained by the Inner Detector; track jet reconstruction and performance is documented in [164]. The method typically relies on matching a jet, which is identified in the calorimeters, with a jet reconstructed at the Inner Detector. Since the two reconstruction methods depend on different techniques, due to the different input parameters, they also have different systematic sources allowing for complementarity.

For the jets used in our analysis (`anti-`$k_\perp$), both Monte Carlo and data samples are used in order to extract the $\epsilon_{reco,jet}$. Comparison between them shows very small differences and within the uncertainty limits, especially for calorimeter jets with $p_{\mathrm{T}} \geq 20$ GeV, hence no scale factor is assigned [165]. For the uncertainty a conservative approach is followed where the 2%, at maximum, residual difference between data and Monte Carlo is propagated to our calculation. This is implemented by randomly rejecting a 2% of jets and comparing the fit result with respect to the nominal Monte Carlo. We find that the cross-section result deviates by $\pm 2.8\%$ and $\pm 3.3\%$ for the e-channel and μ-channel respectively.

6.5.6 b-tagging calibration

Section 4.2.5 discussed the corrections applied to the jets with respect to the b-jet identification. The respective scale factors are applied by default on a jet-by-jet basis in the form of event weights; they are shown in tables 4.3. Similarly to the corrections for the leptons and the jet resolution smearing, the corresponding uncertainties need to be propagated to the final analysis. We take the $\pm 1\sigma$ variations of the scale factors to obtain the upward and the downward fluctuations. We compare the fit result from the variated samples with the one from the nominal Monte Carlo and we obtain the respective uncertainty. The uncertainty is found to be considerable, at $+3.3/-4.9\%$ for the electron channel and $+3.5/-4.2\%$ for the muon channel.

6.5.7 Heavy flavor composition in W+jets events

The composition of W+jets from b-jets, c-jets or light jets can be an important source of uncertainty as it can affect the value of the event tagging rates and as a consequence the parameters $SF_{2\to3}$ and $SF_{3\to4}$ which are used in the fit.

The Monte Carlo is corrected at the exclusive two-jet bin for its $Wb\bar{b}$ and $Wc\bar{c}$ fractions. This correction is associated with a 50% uncertainty for the $Wb\bar{b}$ and $Wc\bar{c}$, fully correlated between the two processes. In addition, a 40% uncertainty is associated to the uncorrected Wc fraction. These uncertainties are derived according to the data-driven method as documented in [152]. For extrapolating from the two-jet bin to the three-jet and four-jet bin we use a conservative approach based on results from Monte Carlo studies and therefore an additional 20% per bin is linearly added for all cases. The $Wb\bar{b}$ and $Wc\bar{c}$ are again taken as fully correlated. The final result of the uncertainty is found to be particularly large with $+5.5/-5.8\%$ at the e-channel and $+7.5/-5.8\%$ at the μ-channel.

6.5.8 Normalization of the background

The normalization of the background becomes an input to the fit through the use of the $SF_{2\to3}$ and $SF_{3\to4}$ scale factors, where the first enters via the constrained parameter $\varepsilon_B^{3;1}$ and the second is estimated from Monte Carlo and remains fixed. Since these parameters are ratios of event tagging rates we do not expect large variation due to the overall normalization of the background, nevertheless we still test the dependence for the QCD normalization and the sum of the rest of the backgrounds (except the W+jets).

QCD normalization

As mentioned in section 4.5.2 we do not rely on the Monte Carlo samples for QCD estimates but we use the event numbers as obtained from the data-driven methods documented in [159]. These numbers are extracted also per kinematic region and with respect to the number of b-tagged jets, therefore accounting for knowledge on heavy flavor composition. The data-driven results are given in table 4.10 along with their uncertainties. The uncertainties are propagated to our analysis by varying the Monte Carlo samples accordingly and, as before, comparing the fit result with the one from the nominal Monte Carlo. We find that the electron channel deviates at $+1.4/-0.6\%$ while the muon channel at only $+0.3/-0.1\%$, indeed a very small contribution.

Other backgrounds

Other contributing backgrounds are the single-top, the di-bosons and the Z+jets. Their normalization is taken from the respective Monte Carlo samples and therefore any uncertainty involved should be related with their theoretical prediction. For the Z+jets a conservative approach of variating the normalization by 100% is used. This takes into account the uncertainty with respect to the jet multiplicity as well as the heavy flavor content. For the di-bosons a variation of 5% is taken, motivated by the theoretical uncertainty on the generator cross-section [166]. Similarly, the single-top is variated by 10% to account for the expected theoretical uncertainty [167]. The combined uncertainty for both channels is found to be very small, at the order of 0.1% and therefore omitted from the calculation.

6.5.9 Template systematics

Systematics from data-driven method

We should account for systematics that originate from the template parametrization. First we consider the data-driven method for the background templates. As discussed in section 5.2.2, the Monte Carlo comparison of the background shapes obtained after the baseline $t\bar{t}$ cuts and the QCD-enhancing cuts have a good agreement. We account for the possibility of mis-modeling by comparing the nominal fit result, taken after applying the QCD-enhancing cuts on the data, with the fit result after using background templates that are derived from Monte Carlo; we perform the comparison with both `AlpGen` generated and `Sherpa` generated W+jets samples and we take the maximum deviation as the uncertainty. The final result, which is symmetrized, is $\pm 4.1\%$ and $\pm 3.5\%$ for the electron and the muon channels respectively.

Systematic from functional parametrization

In addition, as discussed in section 6.2.1 the template functions are obtained by doing a binned fit of the distributions with the function as given in equation 6.2.2. Naturally, the cross-section calculation is incurred by the choice of the functional form and the bin-size selected for the fit. We test the dependence on the functional form by substituting the function templates with binned templates obtained directly from the histograms and we re-run the fit comparing the result with the one from the nominal case. For the bin-size we re-calculate the templates with three different bin sizes, 1 GeV/bin, 5 GeV/bin and 20 GeV/bin and we take the 5 GeV/bin as our nominal case. We perform the fit for each version of the templates and we take the maximum deviation from the nominal case as the uncertainty. The two uncertainties are eventually added in quadrature and we find that the overall uncertainty is $\pm 1.2\%$ for either of the two channels.

6.5.10 Initial and final state radiation

An important source of uncertainty comes from the modeling of the initial and final state radiation (ISR and FSR respectively) of the signal Monte Carlo. The ISR/FSR parameters affect significantly the acceptance of the signal as they alter the jet multiplicity as well as the jet transverse momentum.

For the analysis presented here, the ISR and FSR uncertainty is determined by varying the relevant parameters of the underlying event tuning, such as the momentum scale, the Λ_{QCD} and the parton radiation cut-off mass. We use a leading-order signal simulation, the `AcerMC`, combined with `Pythia` for which six variated samples exist: maximum ISR, maximum FSR, minimum ISR, minimum FSR, maximum ISR and FSR, and minimum ISR and FSR. We run the fit on the nominal `AcerMC` signal, after re-evaluating the signal templates, and then we compare the result with all of the above variations. The final uncertainty is taken from the maximum positive and the maximum negative difference. We find a significant contribution of $+3.8/-4.8\%$ at the electron channels and of $+4.3/-5.2\%$ at the muon channel.

It should be noted that we do not use a next-to-leading order signal variation. The reason is that no final recommendation exists within ATLAS on how to vary ISR and FSR on next-to-leading order generators.

6.5.11 Parton distribution functions

The choice of a Parton Distribution Function (PDF) for the event generation of the Monte Carlo gives rise to another source of uncertainty. For the analysis presented in this thesis the signal is produced using the CTEQ6.6 PDF while other samples are produced using MSTW08 [48] and NNPDF2.0 [168]. The treatment of the uncertainties follows the recommendations as reported by the PDF4LHC working group, documented in [169]. In principle, the uncertainty is evaluated for each of the three PDFs and for which error PDF sets exist. The error PDF sets have their PDF parameters varied upwards or downwards. For CTEQ exist 44 sets while for MWST are 42 and 100 for the NNPDF. The analysis must be repeated for each of those PDF. Practically, the samples are not re-generated with new PDFs but are re-weighted using the following:

$$w = \frac{P_{var}(x_1, f_1, Q) \cdot P_{var}(x_2, f_2, Q)}{P_{nom}(x_1, f_1, Q) \cdot P_{nom}(x_2, f_2, Q)} , \tag{6.5.1}$$

where P_{var} and P_{nom} are the variated and the nominal PDF set respectively, f_1 and f_2 are the flavors of the scattering partons while x_1 and x_2 are their fractional momenta. Finally, Q is the momentum transfer in the event.

The total uncertainty for each PDF family is obtained in the following way: for the CTEQ variations by using a symmetric Hessian calculation, for the MWST an asymmetric Hessian calculation and for the NNPDF is taken as the standard deviation of the variations. The final uncertainty is the linear combination of the three families. The PDF uncertainty affects mainly the acceptance of the events and the change on the template shapes is expected to be negligible. The result gives $\pm 1.7\%$ deviation for each of the two channels.

6.5.12 Signal generator, parton shower and fragmentation modeling

To test the dependance of the fit on the choice of the signal next-to-leading order simulation, we compare the result of the nominal Monte Carlo validation fit, which uses the `MC@NLO` event generator coupled with `HERWIG` for the hadronization, with the result obtained by using the `POWHEG` event generator using the same hadronization model. The found result yields a $\pm 2.6\%$ uncertainty for the e-channel and a $\pm 1.7\%$ uncertainty for the μ-channel.

In addition, we test the dependance on the hadronization model by comparing the result from using the `POWHEG/HERWIG` signal sample with the one estimated from using the `POWHEG/Pythia` version. In this case, since the first is taken as the nominal Monte Carlo the signal templates must be re-calculated accordingly. We find $\pm 1.2\%$ for the e-channel and $\pm 0.3\%$ for the μ-channel.

6.5.13 Multiple interaction activity (pile-up)

In our analysis we use the Monte Carlo samples without correcting for the pile-up activity to match the one seen from data. We account for this by assigning a systematic in the following way. We create a separate version of Monte Carlo samples in which the events are re-weighted such that they match the data expectation. The weight is applied on event-by-event basis according to the number of vertices with at least 5 tracks associated to each of them. It applies for all events in either the μ-channel or e-channel with at least three "good" jets with $p_{\mathrm{T}} \geq 25$ GeV. The relevant value of the weight is seen in table 6.11 and are obtained from [170].

Number of vertices	Weight
1	1.9290
2	1.3025
3	0.8380
4	0.6225
5	0.4635
≥ 6	0.4345

Table 6.11: *Weight applied on the Monte Carlo variation for pile-up systematic estimation. The value of the weight depends on the number of vertices that are found in the simulated event and have more than 5 tracks associated with them. Numbers taken from [170].*

The result of the fit from the nominal Monte Carlo is compared with the one taken from the variated samples and the final uncertainty is extracted. A considerable contribution of $\pm 5.8\%$ for the electron channel and $\pm 5.5\%$ for the muon channel is found.

6.5.14 Luminosity

The uncertainty on the luminosity is taken to be 3.4% and is based on the selected sample as already discussed in section 4.4.1. This value is obtained from [156] and the major contribution comes from the bunch charge product $n_1 \cdot n_2$, where n_1 and n_2 are the proton population in the colliding bunch of beam 1 (clockwise) and beam 2 (anti-clockwise) respectively. We translate this uncertainty to the cross-section uncertainty by varying it accordingly in equation 6.0.1.

6.6 Combination of channels

The events selected with the $t\bar{t}$ baseline selection are completely orthogonal between the electron and the muon channel; this is ensured by the charged lepton requirement, as explained in section 4.4.3. It is trivial, therefore, to combine the two channels into a single fit and take advantage from a higher statistics sample. In addition, we can obtain a single result for our analysis which can simplify the comparison with other methods that estimate the $t\bar{t}$ production cross-section.

In principle, the merging of the two channels can be achieved by simply selecting events and substituting the charged lepton requirement in one channel with the logical `OR` of the two charged lepton requirements. This would provide a single dataset from which we can estimate the signal templates as well as the values of the parameters that enter the fit, both those that are fixed from Monte Carlo and those that are constrained. However, the templates would need to be re-calculated. Specifically, an adjustment on the QCD-enhancing cuts for the extraction of the background shape is required, as well as additional validation of the method, which may increase the complexity of the method. Therefore, we do not follow this approach.

The method we use is to form a single likelihood from the two independent likelihoods of each channel, effectively using a total of eight distinct kinematic regions. The parameters for each channel remain the same, hence their respective initial values as well as the templates can be kept the same as for the individual channel fits. The total number of signal events can now be parametrized in the following way:

$$N_{S,e} = \varepsilon_{S,e} N_S \text{ and}$$
$$N_{S,\mu} = \varepsilon_{S,\mu} N_S \ , \tag{6.6.1}$$

where $\varepsilon_{S,e}$ and $\varepsilon_{S,\mu}$ correspond to the selection efficiency for each channel with respect to the total signal events obtained from their combination, hence $N_{S,e}$ and $N_{S,\mu}$ is the signal events found in each channel. In a similar way to what happen in section 6.2.3 the efficiencies can be written as follows:

$$\varepsilon_{S,e} = \frac{RC_S}{1 + RC_S} \text{ and} \tag{6.6.2}$$
$$\varepsilon_{S,\mu} = \frac{1}{1 + RC_S} \ , \tag{6.6.3}$$

where RC_S is the ratio of the number of signal events found by the e-channel likelihood over the number of signal events found by the μ-channel likelihood. Thus:

$$RC_S = \frac{N_{S,e}}{N_{S,\mu}} \ . \tag{6.6.4}$$

For the fit the RC_S is left free to float. In the same way as described above we define RC_B as the ratio on the number of background events found by each channel. The RC_B is also left free to float.

The calculation of the cross-section from the extracted number of signal events is the same as given in equation 6.0.1 with all but the $t\bar{t}$ selection efficiency parameter ($\epsilon_{t\bar{t}}$) remaining the same. The latter now corresponds to the following:

$$\epsilon_{t\bar{t}} = \epsilon^{e}_{t\bar{t}} + \epsilon^{\mu}_{t\bar{t}} \ , \tag{6.6.5}$$

where $\epsilon^{e}_{t\bar{t}}$ and $\epsilon^{\mu}_{t\bar{t}}$ are the $t\bar{t}$ selection efficiencies for each individual channel. Because the selection cuts between the two channels are mutually exclusive, it is ensured that $\epsilon^{e}_{t\bar{t}} + \epsilon^{\mu}_{t\bar{t}} \leq 1$, since in the opposite case it would be unphysical. The additional advantage of this approach is that there is no need to re-calculate the scale factors, presented in section 6.1, for the trigger and the lepton reconstruction and identification.

The application of the above methodology on the data yields the result that is shown in table 6.12. After the combination of the channels, the treatment of the systematics can be done in the same way as presented in section 6.5.

	Channel combination
N_S	782.1 ± 59.6
N_B	2216.9 ± 68.0

Table 6.12: *Number of signal and background events as calculated by applying the channel-combined simultaneous template fit on the the 35.3 pb^{-1} of $\sqrt{s} = 7$ TeV proton-proton collision data. The uncertainties are statistical and estimated from running 2000 PSEs.*

6.7 Summary and discussion

The methodology for extracting the $t\bar{t}$ production cross-section was presented, including the explanation for the treatment of systematics. Thus far, the result of the fitted signal events was shown in table 6.9 (section 6.4) for the fit on the individual channels and in table 6.12 (section 6.6) for the channel combination fit.

From the extracted number of signal events we can use equation 6.0.1. The total luminosity, already discussed in section 4.4.1, is 35.3 pb^{-1} and the branching ratio for normalizing to the total $t\bar{t}$ cross-section is taken as $BR = 0.543$ [53]. The $t\bar{t}$ signal efficiency before the scale factor corrections are shown in table 6.1 (section 6.1) for the respective kinematic regions. Combining them on an event-by-event basis with the scale factors shown in sections 6.1.1 and 6.1.2 we obtain an efficiency of 9.76% for the e-channel and of 13.15% for the μ-channel. The final result of the cross-section measurement using the simultaneous template fit method is shown in table 6.13 for the individual channel fits and their combination. The uncertainties that are taken into account are summarized in table 6.14.

	$t\bar{t}$ **cross-section,** $\sigma_{t\bar{t}}$ (pb)
e**-channel**	$209.6 \pm 29.8(stat.)^{+27.9}_{-30.4}(syst.)^{+7.3}_{-6.9}(lumi.)$
μ**-channel**	$153.5 \pm 14.1(stat.)^{+20.1}_{-20.6}(syst.)^{+5.4}_{-5.1}(lumi.)$
Combination	$178.1 \pm 13.5(stat.)^{+23.0}_{-24.6}(syst.)^{+6.2}_{-5.9}(lumi.)$

Table 6.13: *The $t\bar{t}$ cross-section from proton-proton collisions delivered by the LHC at $\sqrt{s} = 7$ TeV as estimated from the simultaneous template fit method on a total of 35.3 pb^{-1} dataset, corresponding to the 2010 ATLAS recorded dataset.*

With the measurement presented here a test of QCD is provided at an energy regime that was previously unexplored. Figure 6.6 shows the measurement made in this thesis in comparison with the theoretical expectations at NLO and (approximated) NNLO as estimated for a top quark mass of 172.5 GeV using the tool documented in [171]. Measurements from the Tevatron experiments, DØ and CDF, have shown at lower center-of-mass energies the good agreement between theory and experiment [172, 173, 174, 175]. It is evident that a good agreement with the theory is observed well within the limits of the estimated uncertainties.

Discussion

The analysis presented in this thesis covers an important milestone for the experiment. Not only it shows the great ability of the detector in identifying complex topologies in an immense background but it also illustrates that even with a small amount of data such measurements can be made with an acceptable total uncertainty. The method employed here, takes advantage of a greater kinematic region thus increasing the necessary statistics. However, the important novelty is that a largely data-driven approach is followed where the background normalization is part of the fit, thus resulting in reducing the expected systematic uncertainties.

Naturally, more data will improve the statistical uncertainty but more importantly they will also provide a better understanding of the detector. A number of systematics can be therefore improved, namely the scale factors for trigger, reconstruction and identification of objects, the jet energy scale treatment which follows a largely conservative approach, similarly the b-tagging uncertainty which also depends on the amount of available data for calibrating the b-tagging algorithms. All these uncertainties are based An extension of the method can also be implemented such that it increases the number of kinematic regions, isolating parts of the phase space with a much greater signal-over-background ratio, e.g. separating the inclusive tagged regions to an exactly one b-tagged and an inclusive two b-tagged bins. This approach can increase the number of equations and therefore allow to parametrize also the b-tagging efficiency within the model.

It is important to highlight that the analysis presented in this thesis has provided a measurement of the inclusive $t\bar{t}$ cross-section. Even though the result shows a good agreement between theory and experiment, it cannot be inferred that this agreement holds for the complete $t\bar{t}$ phase-space. As an example, a $t\bar{t}$ resonance signal may be present in the data e.g. due to gauge bosons which couple strongly to the top quark [176]. In this case, this signal will show as an excess in the $t\bar{t}$ invariant mass spectrum. Naturally, such theories cannot be excluded unless they are probed by the experiment. With the larger data sample that ATLAS is collecting will allow a more accurate measurement of the inclusive $t\bar{t}$ cross-section which will pave the way for the measurement of the differential cross-section and the discovery of such processes. What is considered our signal today is simply our background for future discoveries.

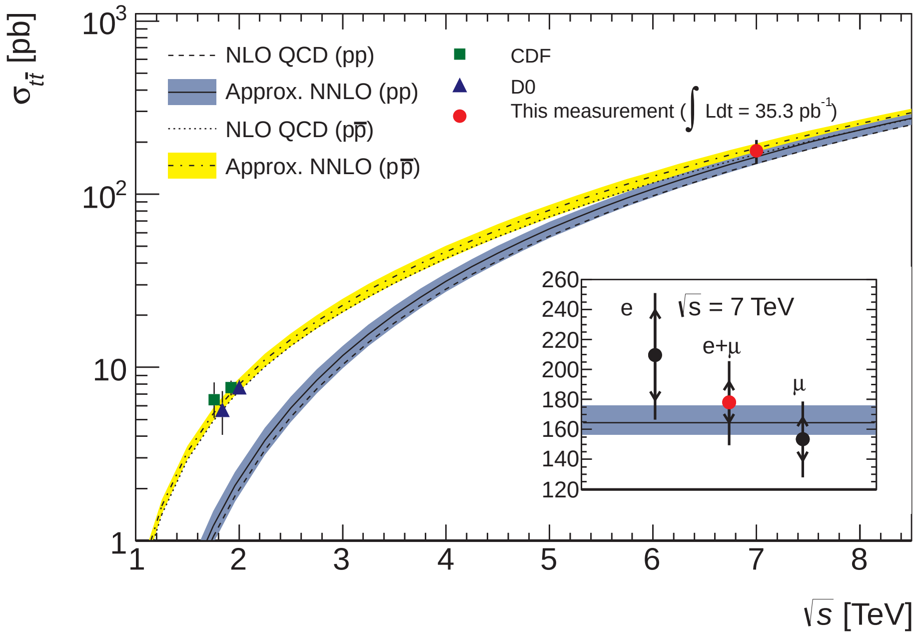

Figure 6.6: *The inclusive $t\bar{t}$ production cross-section as estimated by theory (for $M_{top} = 172.5$ GeV) with respect to the center-of-mass energy of $p-p$ and $p-\bar{p}$ collisions (lines) [171], the measurements made from CDF, DØ during Run-I and Run-II of the Tevatron collider (square and triangle points) [174, 172, 175, 173] and the measurement performed in this thesis (circle point) with $\int \mathcal{L}dt = 35.3$ pb^{-1} of proton-proton collisions delivered by the LHC to the ATLAS detector. The error-bar region in between the arrows indicates the contribution of the statistical uncertainty only.*

Source	$\Delta\sigma/\sigma$ (%) e-channel	μ-channel	Combination
Statistical	± 14.2	± 9.2	± 7.6
Systematics			
Object selection			
Lepton trigger, reconstruction & identification SF	± 4.0	± 1.5	± 2.5
Lepton energy scaling & resolution smearing	$+1.3/-1.2$	± 0.4	$+1.4/-1.3$
Jet energy scale	$+5.3/-6.2$	$+4.2/-5.8$	$+4.6/-6.0$
Jet energy resolution	± 1.9	± 1.8	± 1.9
Jet reconstruction efficiency	± 2.8	± 3.3	± 3.1
b-tagging calibration	$+3.3/-4.9$	$+3.5/-4.2$	$+3.5/-4.5$
Monte Carlo description			
W+jets heavy flavor content	$+5.5/-5.8$	$+7.5/-5.8$	$+6.4/-5.8$
Signal ISR/FSR	$+3.8/-4.8$	$+4.3/-5.2$	$+4.1/-5.1$
PDF	± 1.7	± 1.7	± 1.7
NLO generator	± 2.6	± 1.7	± 1.9
Parton shower	± 1.2	± 0.3	± 0.6
Pile-up activity	± 5.8	± 5.5	± 5.6
QCD normalization	$+1.4/-0.6$	$+0.3/-0.1$	$+0.5/-0.2$
Templates			
Data-driven method	± 4.1	± 3.5	± 3.7
Functional parametrization	± 1.2	± 1.2	± 1.2
Sum systematics	$+13.3/-14.5$	$+13.1/-13.4$	$+12.9/-13.8$
Statistical + Systematics	$+19.5/-20.3$	$+16.0/-16.2$	$+15.0/-15.8$
Int. Luminosity	$+3.5/-3.3$	$+3.5/-3.3$	$+3.5/-3.3$

Table 6.14: *Summary of uncertainties on the $t\bar{t}$ production cross-section for the individual channel fits and the combined channel fit.*

Bibliography

[1] C. C. W. Taylor, *The Atomists, Leucippus and Democritus: a text and translation with commentary by C. C. W. Taylor.*, University of Toronto Press, 1999.

[2] M. Gell-Mann, *Symmetries of Baryons and Mesons.*, Phys. Rev. **125** (1962) 1067.

[3] M. Gell-Mann, *A schematic Model of Baryons and Mesons.*, Phys. Lett. **B**(8) (1964) 214.

[4] G. Zweig, *An SU(3) Model for Stron Interaction Symmetry and its Breaking*, CERN Report No. 182/TH. 01 (1964) .

[5] G. Zweig, *An SU(3) Model for Stron Interaction Symmetry and its Breaking II*, CERN Report No. 419/TH. 12 (1964) .

[6] E.D. Bloom *et al.*, *High-Energy Inelastic e-p Scattering at* 6^o *and* 10^o*.*, Phys. Rev. Lett. **23** (1969) 930.

[7] M. Breidenbach *et al.*, *Observed Behavior of Highly Inelastic Electron-Proton Scattering.*, Phys. Rev. Lett. **23** (1969) 935.

[8] TASSO Collaboration, *Evidence of Planar Events in* e^+e^- *Annihilation at High Energies.*, Phys. Lett. **B**(86) (1979) 243.

[9] PLUTO Collaboration, *Jet analysis of the Y(9.46) decay into charged hadrons*, Phys. Lett. **B**(82) (1979) 3.

[10] MARK-J Collaboration, *Discovery of Three-Jet Events and a Test of Quantum Chromodynamics at PETRA.*, Phys. Rev. Lett. **43** (1979) 830.

[11] JADE Collaboration, *Observation of planar three-jet events in* e^+e^- *annihilation and evidence of gluon bremsstrahlung.*, Phys. Lett. **B**(91) (1980) 142.

[12] D. Gross and F. Wilczek, *Asymptotically Free Gauge Theories. I*, Phys. Rev. **D**(8) (1973) .

[13] D. Gross and F. Wilczek, *Ultraviolet Behavior of Non-Abelian Gauge Theories.*, Phys. Rev. Lett. **30** (1973) .

[14] H. D. Politzer, *Asymptotic freedom: An approach to Strong Interactions.*, Physics Reports **14** (1974) .

[15] E. Fermi, *Tentativo di una teoria dei raggi* β*.*, Ricerca Scientifica (1933) .

[16] S. Weinberg, *A Model of Leptons*, Phys. Rev. Lett. **19** (1967) 1264.

[17] S.L Glashow, *Partial-symmetries of weak interactions*, Nucl. Phys. **22** (1961) 579.

[18] Jeffrey Goldstone, Abdus Salam, and Steven Weinberg, *Broken Symmetries*, Phys. Rev. **127** (1962) 965.

[19] P.W. Higgs, *Broken Symmetries, Massless Particles and Gauge Fields*, Phys. Lett. **12** (1964) 132.

[20] P.W. Higgs, *Broken Symmetries and the Masses of Gauge Bosons*, Phys. Rev. Lett. **13** (1964) 508.

[21] P.W. Higgs, *Spontaneous Symmetry Breakdown without Massless Bosons*, Phys. Lett. **145** (1966) 1156.

[22] M. Kobayashi and T. Maskawa, *CP-Violation in the Renormalizable Theory of Weak Interactions*, Prog. Theor. Phys. **49** (1973) 652.

[23] S.W. Herb *et al.*, *Observation of a Dimuon Resonance at 9.5 GeV in 400 GeV Proton-Nucleus Collisions*, Phys. Rev. Lett. **39** (1977) 252.

[24] F. Abe *et al.*, *Observation of Top Quark Production in $p\bar{p}$ Collisions with the Collider Detector at Fermilab*, Phys. Rev. Lett. **74** (1995) 2626, `arXiv:hep-ex/9503002v2`.

[25] S. Abachi *et al.*, *Observation of the Top Quark*, Phys. Rev. Lett. **74** (1995) 2632, `arXiv:hep-ex/9503003v1`.

[26] UA1 Collaboration, *Experimental observation of isolated large transverse energy electrons with associated missing energy at $\sqrt{s} = 540$ GeV*, Phys. Lett. B **122** (1983) 103.

[27] The UA2 Collaboration, *Observation of single isolated electrons of high transverse momentum in events with missing transverse energy at the CERN $p\bar{p}$ collider*, Phys. Lett. B **122** (1983) 476.

[28] `http://www.atlas.ch/news/2012/latest-results-from-higgs-search.html`

[29] `http://cms.web.cern.ch/news/observation-new-particle-mass-125-gev`

[30] Gerard 't Hooft and M. J. G. Veltman, *Regularization and Renormalization of Gauge Fields*, Nucl. Phys. **B**(44) (1972) 189.

[31] S. N. Bose, *Plancks Gesetz und Lichtquantenhypothese*, Zeithschrift fuer Physik **26** (1924) 178.

[32] A. Einstein, *Quantentheorie des einatomigen idealen Gases*, Sitzungsberichte der Preussischen Akademie der Wissenschaften **1** (1925) 3.

[33] E. Fermi and A. Zannoni (transl.), *Sulla quantizzazione del gas perfetto monoatomico - On the Quantization of the Monoatomic Ideal Gas*, Rendiconti Lincei **3** (1926) 149, `arXiv:cond-mat/9912229`.

[34] P. A. M. Dirac, *On the Theory of Quantum Mechanics*, Proceedings of the Royal Society **Series A**(112) (1926) 661.

[35] E. Noether and M. A. Tavel, *Invariante Variationsprobleme*, Gott. Nachr. (1918) 235.

[36] E. Noether and M. Tavel, *Invariant Variation Problems*, Transp. Theory Statist. Phys. **1** (1971) 186, `arXiv:physics/0503066`.

[37] H1 Collaboration, *Measurement and QCD Analysis of Neutral and Charged Current Cross Sections at HERA*, Eur. Phys. J. **C**(30) (2003) 1, `hep-ex/0304003`.

[38] H1 Collaboration, *Measurement of $F_2^{c\bar{c}}$ and $F_2^{b\bar{b}}$ at High-Q^2 using the H1 Vertex Detector at HERA.*, Eur. Phys. J. **C**(40) (2005) 349, `hep-ex/0411046`.

[39] H1 Collaboration, *Measurement of $F_2^{c\bar{c}}$ and $F_2^{b\bar{b}}$ at Low Q^2 and x using the H1 Vertex Detector at HERA.*, Eur. Phys. J. **C**(45) (2006) 23, `hep-ex/0507081`.

[40] H1 Collaboration, *Measurement of $D^{*\pm}$ Meson Production and F_2^c in Deep-Inelastic Scattering at HERA*, Phys. Lett. **B**(528) (2002) 199, `hep-ex/01080391`.

[41] ZEUS Collaboration, *Measurement of high-Q^2 charged current cross-sections in e^+p deep inelastic scattering at HERA*, Eur. Phys. J. **C**(32) (2003) 1, `hep-ex/0307043`.

[42] ZEUS Collaboration, *Measurement of $D^{*\pm}$ production and the charm contribution to F_2 in Deep-Inelastic Scattering at HERA.*, Eur. Phys. J. **C**(12) (2000) 35, `hep-ex/9908012`.

[43] NuTeV Collaboration, *Precise measurement of neutrino and anti-neutrino differential cross-section.*, Phys. Rev. **D**(74) (2006) , `hep-ex/0509010`.

[44] FNAL E866/NuSea Collaboration, *Improved Measurement of the $\bar{d}/\bar{u}$ Asymmetry in the Nucleon Sea.*, Phys. Rev. **D**(64) (2001) , `hep-ex/0103030`.

[45] ZEUS Collaboration, *Inclusive jet cross-section in the Breit frame in neutral current deep inelastic scattering at HERA and determination of alpha$_s$.*, Phys. Lett. **B**(547) (2002) 164, `hep-ex/0208037`.

[46] ZEUS Collaboration, *Inclusive-jet and di-jet cross-section in deep inelastic scattering at HERA.*, Nucl. Phys. **B**(765) (2007) 1, `hep-ex/0608048`.

[47] H1 Collaboration, *Measurement of Inclusive Jet Production in Deep-Inelastic Scattering at High-Q^2 and Determination of the Strong Coupling.*, Phys. Lett. **B**(653) (2007) 134, `0706.3722 [hep-ex]`.

[48] A. D. Martin, W. J. Stirling, R. S. Thorne, and G. Watt, *Parton distributions for the LHC*, Eur. Phys. J. C (2009) 189, `arXiv:0901.0002v3 [hep-ph]`.

[49] J. M. Campbell, J. W. Huston, and W. J. Stirling, *Hard Interactions of Quarks and GLuons: A Primer for LHC Physics*, Rept. Prog. Phys. **70** (2007) 80, `arXiv:hep-ph/0611148`.

[50] S.L Glashow, J. Iliopoulos, and L. Maiani, *Weak Interactions with Lepton-Hadron Symmetry*, Phys. Rev. **D**(2) (1970) 1285.

[51] J. J. Aubert *et al.*, *Experimental Observation of a Heavy Particle J*, Phys. Rev. Lett. **33**1404.

[52] J. Augustin *et al.*, *Discovery of Narrow Resonance in e^+e^- Annihilation*, Phys. Rev. Lett. **33** (1974) 1406.

[53] K. Nakamura *et al.*, *The Review of Particle Physics*, J. Phys. G: Nucl. Part. Phys. **37**(075021) (2011) .

[54] S. Moch and P. Uwer, *Theoretical status and prospects for top-quark pair production at hadron colliders*, Phys. Rev. D **78** (2008) 034003, `arXiv:0804.1476 [hep-ph]`.

[55] U. Langenfeld, S. Moch, and P. Uwer, *New results for $t\bar{t}$ production at hadron colliders*, To appear in the proceedings of 17th International Workshop on Deep-Inelastic Scattering and Related Subjects (DIS 2009), Madrid, Spain, 26-30 Apr 2009 (2009) , `arXiv:0907.2527 [hep-ph]`.

[56] P.M. Nadolsky, N.-L. Lai, Q.-H. Cao, Joey Huston, J. Pumplin, D. Stump, W.-K. Tung, and C.-P. Yuan, *Implications of CTEQ global analysis for collider observables*, Phys. Rev. D **78** (2008) 013004, `arXiv:0802.0007v3 [hep-ph]`.

[57] W. Bernreuther, *Top quark physics at the LHC*, 2008, `arXiv:0805.1333v1 [hep-ph]`.

[58] J.R. Incandela, A. Quadt, W. Wagner, and D. Wicke, *Status and Prospects of Top-Quark Physics*, 2009, `arXiv:0904.2499v1 [hep-ex]`.

[59] `http://www-d0.fnal.gov/Run2Physics/top/top_public_web_pages/top_feynman_diagrams.html`

[60] C. F. Berger, Z. Bern, L. J. Dixon, F. Febres Cordero, D. Forde, T. Gleisberg, H. Ita, D. A. Kosower, and D. Maitre, *Precise Predictions for W+4 Jet Production at the Large Hadron Collider*, Phys. Rev. Lett. **106** (2011) , `arXiv:1009.2338 [hep-ph]`.

[61] H. Ita, Z. Bern, L. J. Dixon, F. Febres Cordero, D. A. Kosower, and D. Maitre, *Precise Predictions for Z+4 Jets at Hadron Colliders*, 2011.

[62] N. Kidonakis, *Next-to-next-to-leading-order collinear and soft gluon corrections for t-channel single top quark production.*, Phys. Rev. **D**(83) (2011) 091503, `arXiv:1103.2792`.

[63] N. Kidonakis, *Two-loop soft anomalous dimensions for single top quark associated production with a W^- or H^-.*, Phys. Rev. **D**(82) (2010) 054018, `arXiv:1005.4451`.

[64] N. Kidonakis, *NNLL resummation for s-channel single top quark production.*, Phys. Rev. **D**(81) (2010) 054028, `arXiv:1001.5034`.

[65] J. M. Butterworth, E. Dobson, U. Klein, B.R. Mellado Garcia, T. Nunnemann, J. Qian, D. Rebuzzi, and R. Tanaka, *Single Boson and Diboson Production Cross Sections in pp Collisions at $\sqrt{s} = 7$ TeV.*, `ATL-COM-PHYS-2010-695`.

[66] U. Langenfeld, S. Moch, and P. Uwer, *Measuring the running top-quark mass*, Phys. Rev. D **80** (2009) 054009, `arXiv:0906.5273v2 [hep-ph]`.

[67] A. Sirlin, *Radiative corrections in the $SU(2) \times U(1)$ theory: A simple renormalization framework*, Phys. Rev. D **22** (1980) 971.

[68] ALEPH Collaboration and DELPHI Collaboration and L3 Collaboration and OPAL Collaboration and SLD Collaboration and LEP Electroweak Working Group and SLD Electroweak Heavy Flavour Groups, *Precision electroweak measurements on the Z resonance.*, Phys. Rep. **427** (2006) 257.

[69] J. Z. Bai, *Measurements of the Cross Section for $e^+e^- \rightarrow$ Hadrons at Center-of-Mass Energies from 2 to 5 GeV.*, Phys. Rev. Lett. **88** (2002) .

[70] T. van Ritbergen and R. G. Stuart, *Complete 2-loop quantum electrodynamic contributions to the muon lifetime in the Fermi model.*, Phys. Rev. Lett. **82** (1999) 488.

[71] `http://lepewwg.web.cern.ch/LEPEWWG/`

[72] T. Sjöstrand, S. Mrenna, and P. Skands, *PYTHIA 6.4 Physics and Manual*, JHEP **0605** (2006) 026, `arXiv:hep-ph/0603175v2`.

[73] G. Corcella, I.G. Knowles, G. Marchesini, S. Moretti, K. Odagiri, P. Richardson, M.H. Seymour, and B.R. Webber, *HERWIG 6.5: an event generator for Hadron Emission Reactions With Interfering Gluons (including supersymmetric processes)*, JHEP **0101** (2001) 010, `arXiv:hep-ph/0011363v3, arXiv:hep-ph/0210213v2`.

[74] T. Gleisberg, S. Hoeche, F. Krauss, M. Schoenherr, S. Schumann, F. Siegert, and J. Winter, *Event generation with SHERPA 1.1*, JHEP **0902** (2009) 007, `arXiv:0811.4622v1 [hep-ph]`.

[75] S. Frixione, P. Nason, and B.R. Webber, *Matching NLO QCD and Parton Showers in Heavy Flavour Production*, JHEP **0308** (2003) 007, `arXiv:hep-ph/0305252v2`.

[76] S. Frixione and B.R. Webber, *Matching NLO QCD computations and parton shower simulations*, JHEP **0206** (2002) 029, `arXiv:hep-ph/0204244v2`.

[77] P. Torrielli and S. Frixione, *Matching NLO QCD computations with PYTHIA using MC@NLO*, 2010, `arXiv:1002.4293v2 [hep-ph]`.

[78] M.L. Mangano, M. Moretti, F. Piccinini, and M. Treccani, *Matching matrix elements and shower evolution for top-quark production in hadronic collisions*, JHEP **0701** (2007) 013, `arXiv:hep-ph/0611129v1`.

[79] B.P. Kersevan and E. Richter-W as, *The Monte Carlo Event Generator AcerMC version 3.5 with interfaces to PYTHIA 6.3, HERWIG 6.5 and ARIADNE 4.1*, `arXiv:hep-ph/0405247v1`.

[80] M.L. Mangano, M. Moretti, F. Piccinini, R. Pittau, and A. Polosa, *ALPGEN, a generator for hard multiparton processes in hadronic collisions*, JHEP **0307** (2003) 001, `arXiv:hep-ph/0206293v2`.

[81] Stefano Frixione, Paolo Nason, and Carlo Oleari, *Matching NLO QCD computations with Parton Shower simulations: the POWHEG method*, JHEP **11** (2007) 070, `arXiv:0709.2092v1 [hep-ph]`.

[82] J. M. Butterworth, Jeffrey R. Forshaw, and M .H. Seymour, *Multiparton interactions in photoproduction at HERA*, Z. Phys. **C72** (1996) 637, `arXiv:hep-ph/9601371`.

[83] V.N. Gribov and L.N. Lipatov, *Deep inelastic ep scattering in perturbation theory*, Sov. J. Nucl. Phys **15** (1972) 428.

[84] L.N. Lipatov, *The parton model and perturbation theory*, Sov. J. Nucl. Phys **20** (1975) 94.

[85] G. Altarelli and G. Parisi, *Asymptotic freedom in parton language*, Nucl. Phys. B **126** (1977) 298.

[86] Y. Dokshitser, *Calculation of the Structure Functions for Deep Inelastic Scattering and e^+e^- Annihilation by Perturbation Theory in Quantum Chromodynamics*, Sov. Phys. JETP **46** (1977) 641.

[87] V.V. Sudakov, *Vertex parts at very high-energies in quantum electrodynamics*, Sov. Phys. JETP **30** (1956) 65, see also: arXiv:hep-ph/0312336v1.

[88] M.L. Mangano, http://home.fnal.gov/~mrenna/tuning/nov2002/mlm.pdf and https://mlm.web.cern.ch/mlm/talks/lund-alpgen.pdf.

[89] M.L. Mangano, M. Moretti, and R. Pittau, *Multijet matrix elements and shower evolution in hadronic collisions: $Wb\bar{b} + n$ jets as a case study*, Nucl. Phys. B **632** (2002) 343, arXiv:hep-ph/0108069v1.

[90] C.D. White, S. Frixione, E. Laenen, and F. Maltoni, *Isolating Wt production at the LHC*, arXiv:0908.0631v1 [hep-ph].

[91] J. Pumplin *et al.*, *New Generation of Parton Distributions with Uncertainties from Global QCD Analysis*, JHEP **07** (2002) 012, arXiv:hep-ph/0201195v3.

[92] Lyndon Evans and Philip Bryant, *LHC Machine*, JINST **3** (2008) S08001.

[93] The ATLAS Collaboration, *The ATLAS experiment at the CERN Large Hadron Collider*, JINST **3** (2008) S08003.

[94] The ALICE Collaboration, *The ALICE experiment at the CERN Large Hadron Collider*, JINST **3** (2008) S08002.

[95] The CMS Collaboration, *The CMS experiment at the CERN Large Hadron Collider*, JINST **3** (2008) S08004.

[96] The LHCb Collaboration, *The LHCb detector at the CERN Large Hadron Collider*, JINST **3** (2008) S08005.

[97] http://linac2.home.cern.ch/linac2/sources/source.htm

[98] Gerhard A. Schuler and Torbjörn Sjöstrand, *Hadronic diffractive cross sections and the rise of the total cross section*, Phys. Rev. D **49** (1994) 2257.

[99] https://lpc.web.cern.ch/lpc/

[100] The ATLAS Collaboration, *Alignment Performance of the ATLAS Inner Detector Tracking System in 7 TeV proton-proton collisions at the LHC*, ATLAS-CONF-2010-067.

[101] The ATLAS Collaboration, *Performance of the ATLAS Silicon Pattern Recognition Algorithm in Data and Simulation at $\sqrt{s} = 7$ TeV*, ATLAS-CONF-2010-072.

[102] The ATLAS Collaboration, *Performance of the Missing Transverse Energy Reconstruction and Calibration in Proton-Proton Collisions at a Center-of-Mass Energy of 7 TeV with the ATLAS Detector*, ATLAS-CONF-2010-057.

[103] The ATLAS Collaboration, *Electron performance measurements with the ATLAS detector using the 2010 LHC proton-proton collision data*, 1110.3174 [hep-ex].

[104] P. F. Giraud and C. Amelung and F. Bauer, *Muon alignment plots*, ATL-COM-PHYS-2011-460.

[105] The ATLAS Collaboration, *Muon reconstruction Performance*, ATLAS-CONF-2010-064.

[106] The ATLAS Collaboration, *Dimuon composition in ATLAS at 7 TeV* , ATLAS-CONF-2011-003.

[107] The ATLAS Collaboration, *Performance of the ATLAS Trigger in 2010 running at the LHC*, ATL-COM-DAQ-2011-009.

[108] https://twiki.cern.ch/twiki/bin/view/AtlasPublic/TriggerOperationPublicResults

[109] Nicoletta Garelli on behalf of ATLAS TDAQ Collaboration, *Operating the ATLAS data-flow system with the first LHC collisions*, Journal of Physics: Conference Series **331**(022007) (2011) .

[110] ATLAS Collaboration, *Technical Design Report: Level-1 Trigger*, ATLAS TDR-012.

[111] A. Di Mattia *et al.*, *A muon trigger algorithm for Level-2 feature extraction*, ATL-DAQ-2000-036.

[112] A. Di Mattia, S. Falciano, and A. Nisati, *The implementation of the muFast algorithm in the new PESA framework*, ATL-DAQ-2003-021.

[113] ATLAS Collaboration, *Technical Design Report: High-Level Trigger, Data Acquisition and Controls*, ATLAS TDR-016.

[114] https://twiki.cern.ch/twiki/bin/viewauth/Atlas/MuonTriggerDocLvl2muIsol

[115] https://twiki.cern.ch/twiki/bin/viewauth/Atlas/MuonTriggerDocLvl2muTile

[116] I. Gaines, S. Gonzalez, and S. Qian, *Implementation of an Object Oriented Track Reconstruction Model into Multiple LHC Experiments*, Proceedings, Padova 2000.

[117] D. Candlin, R. Candlin, and S. Qian, *Update of an Object Oriented Track Reconstruction Model into Multiple LHC Experiments*, Proceedings, Beijing 2001.

[118] J.Baines and others, *B-Physics Event Selection for the ATLAS High-Level Trigger*, ATL-DAQ-2000-031.

[119] https://twiki.cern.ch/twiki/bin/viewauth/Atlas/MuonTriggerDocTrigMuonEF

[120] D. Adams, K.A. Assamagan, M. Biglietti, G. Carlino, G. Cataldi, F. Conventi, A. Farilla, Yu Fisyak, S. Goldfarb, E. Gorini, T. Lagouri, K. Mair, L. Merola, A. Nairz, A. Poppleton, M. Primavera, S. Rosati, J.T. Shank, S. Spagnolo, L. Spogli, G.D. Stavropoulos, M. Verducci, and T. Wenaus, *Track reconstruction in the ATLAS Muon Spectrometer with MOORE*, ATL-SOFT-2003-007.

[121] N. Lavesson and L. Lönnblad, *A Muon Identification and Combined Reconstruction Procedure for the ATLAS Detector*, IEEE Trans. Nucl. Sci. **51**(6) (2004) 3030.

[122] https://atlas-trigconf.cern.ch/

[123] T. Hayakawa, *Detailed performance study of ATLAS endcap muon trigger with beam collision*, JINST **5** (2010) C11010.

[124] A. Di Mattia, *Online Muon Reconstruction in the ATLAS Muon Spectrometer at the Level-2 stage of the Event Selection*, Proceedings of the *IEEE Nuclear Science Symposium*, 2011.

[125] M. A. Owen for the Muon Signature Group, *ATLAS Trigger Workshop 2010: Muon HLT Status and Issues*, Presentation, 2010.

[126] M. Cacciari, G.P. Salam, and G. Soyez, *The anti-k_T jet clustering algorithm*, JHEP **0804** (2008) 063, `arXiv:0802.1189v2 [hep-ph]`.

[127] The ATLAS Collaboration, *Jet energy scale its systematic uncertainty in proton-proton collisions at $\sqrt{s} = 7$ TeV with ATLAS 2010 data*, `ATLAS-CONF-2011-032`.

[128] The ATLAS Collaboration, *Expected electron performance in the ATLAS experiment*, `ATL-PHYS-PUB-2011-006`.

[129] `https://twiki.cern.ch/twiki/bin/view/AtlasProtected/PAUcaloIsolationTool`

[130] The ATLAS Collaboration, *Determination of the muon reconstruction efficiency in ATLAS at the Z resonance in proton-proton collisions at $\sqrt{s} = 7TeV$*, `ATLAS-CONF-2011-008`.

[131] The ATLAS Collaboration, *Muon reconstruction efficiency in reprocessed 2010 LHC proton-proton collision data recorded with the ATLAS detector*, `ATLAS-CONF-2011-063`.

[132] D. Fassouliotis, T. Lagouri, A. Poppleton, S. Robins, G.D. Stavropoulos, and I. Vichou, *Muon Identification using the MUID package*, `ATL-COM-MUON-2003-003`.

[133] `http://twiki.cern.ch/twiki/bin/viewauth/Atlas/MuGirl`

[134] `https://twiki.cern.ch/twiki/bin/view/AtlasProtected/MuidMuonCollection`

[135] `https://twiki.cern.ch/twiki/bin/view/AtlasProtected/QualityDefinitionStaco`

[136] `https://twiki.cern.ch/twiki/bin/view/AtlasProtected/MuonCombinedQualityDocumentation`

[137] The ATLAS Collaboration, *Expected performance of the ATLAS experiment: detector, trigger and physics*, CERN-OPEN-2008-020 (2008) , `arXiv:0901.0512v4 [hep-ex]`.

[138] The ATLAS Collaboration, *Properties of Jets and Inputs to Jet Reconstruction and Calibration with the ATLAS Detector Using Proton-Proton Collisions at $\sqrt{s} = 7$ TeV*, `ATLAS-CONF-2010-053`.

[139] G.P. Salam and G. Soyez, *A practical Seedless Infrared-Safe Cone jet algorithm*, JHEP **0705** (2007) 086, `arXiv:0704.0292v2 [hep-ph]`.

[140] M. H. Seymour, *Jet shapes in hadron collisions: Higher orders, resummation and hadronization*, Nucl. Phys. **B513** (1998) 269, `arXiv:9707338 [hep-ph]`.

[141] G.P. Salam and M. Cacciari, *Dispelling the N**3 myth for the k(t) jet-finder*, Phys. Lett. **B641** (2006) 57, `arXiv:0512210 [hep-ph]`.

[142] N. Ghodbane, *Performance of Jet Algorithms for the Top Quark Physics at the ATLAS Experiment*, `ATL-PHYS-INT-2009-087, ATL-COM-PHYS-2009-432`.

[143] `https://twiki.cern.ch/twiki/bin/view/AtlasProtected/TowerNoiseSuppression`

[144] B. Alvarez, H. Bachacou, V. Boisvert, J. Boudreau, N. Bousson, L. Cerrito, B. Clement, B. Cooper, T. Delemonte, J. Donini, L. Feligioni, F. Filthaut, F. Garberson, S. Guindon, B. Guo, R. Goncalo, C. Helsens, F. Hirsch, J. Holzbauer, A. Juste, C. Kendziorra, A. Khanov, K. Kroeninger, C. Liu, C. Lapoire, A. Lucotte, M. zur Nedden, G. Oakham, M. Pinamonti, B. Pope A.J. Polli, F. Rizatdinova, M. Rose, M. Saleem, R. Schwienhorst, J. Schwindling, E. Shabalina, P. Sinervo, P. Skubic, K. Suruliz, M. Talby, N. Tannour, L. Vacavant, B. Walsh, J. Wang, J. Yu, and T. Golling, *B-tagging for top physics analyses with early ATLAS data at* $\sqrt{s} = 7$ TeV, `ATL-PHYS-INT-2010-133`.

[145] Th. Goepfert, *Counting Signed Impact Parameter based b-tagging algorithm with ATLAS*, `ATL-COM-PHYS-2008-254`.

[146] `https://twiki.cern.ch/twiki/bin/view/AtlasProtected/BTaggingBenchmarks`

[147] The ATLAS Collaboration, *Measurement of Missing Transverse Energy*, `ATL-PHYS-PUB-2009-000`.

[148] N. Benekos, K. Benslama, S. Caughron, V. Dao, F. Derue, J. Erdmann, V. Ferrara, P. Ferrari, L. Ferrari, I. Fleck, S. Heim, A. Henrichs, S. Hasegawa, K. Khandanyan, B. Kaplan, A. Krasznahorkay, J.R. Lessard, T. McLaughlan, Y. Ming, Y. Okumura, J. Palmer, A.J. Poll, O. Rosenthal, P. Ryan, A. Roe, R. Schwienhorst, T. Theveneaux-Pelzer, H. Zhu, L. Cerrito, G. Salamanna, and K. Ikematsu, *Lepton trigger and identification for the Winter 2011 top quark analyses*, `ATL-COM-PHYS-2011-123`.

[149] `https://twiki.cern.ch/twiki/pub/AtlasProtected/EnergyScaleResolutionRecommendations/summary_rel16.pdf`

[150] The ATLAS Collaboration, *ATLAS Muon Momentum Resolution in the First Pass Reconstruction of the 2010 p-p Collision Data at* $\sqrt{s} = 7$ *TeV*, `ATLAS-CONF-2011-046`.

[151] G. Romeo and A. Schwartzman and R. Piegaia and T. Carli and R. Teuscher, *Jet Energy Resolution from In-Situ Techniques with the ATLAS Detector Using Proton-Proton Collisions at a Center of Mass Energy* $\sqrt{s} = 7$ *TeV*, `ATLAS-CONF-2011-240`.

[152] B. Alvarez, V. Boisvert, B. Clement, B. Cooper, T. Delemonte, J. Donini, L. Feligioni, A. Ferretto Parodi, F. Filthaut, B. Guo, T. Golling, R. Goncalo, M. Hirose, F. Hirsch, L. Heinrich, J. Holzbauer, C. Jung, C. Kendziorra, A. Khanov, J. Kvita, C. Liu, A. Lucotte, F. Parodi, A.J. Poll, F. Rizatdinova, M. Rose, L. Rossi, M. Saleem, R. Schwienhorst, P. Sinervo, C. Schiavi, K. Suruliz, M. Talby, N. Tannoury, B. Walsh, J. Wang, and C. Weydert, *b-jet Tagging for Top Physics: Performance studies, Calibrations and Heavy Flavor Fractions*, `ATL-COM-PHYS-2011-124`.

[153] `https://twiki.cern.ch/twiki/bin/view/AtlasProtected/Analysis16`

[154] `https://twiki.cern.ch/twiki/bin/view/AtlasProtected/MCPAnalysisGuidelinesRel16`

[155] S. Cabrera Urban, M.J. Costa, N. Ghodbane, I.M. Nugent, S. Adomeit, J.F. Arguin, C. Bernius, D. Boumediene, J. Brau, D. Cinca, C. Doglioni, C. Escobar, K. Flavia Loureiro, D. Gillberg, J. Godfrey, Z. Greenwood, P. Haefner, D. Hellmich, J. Kroseberg, H. Liao, A.C. Martyniuk, D. Lopez Mateos, S. Marti i Garcia, R. Moles, M. Moren Llacer, A. Mc Carn, M. Neubauer, H. Okawa, D. O'Neil, D. Pallin, T. Perez, M.A. Pleier, S. Protopopescu, R. Rajagopalan, J. Schovancova, A. Schwartzman, J. Searcy, A. Taffard, Y. Takahashi, M. Tomoto, M.F. Watson, and U. K. Yang, *Jets, Missing*

Transverse Energy and Taus for Top Physics Analyses in Release 16 with the 2010 Dataset, ATL-COM-PHYS-2011-132.

[156] The ATLAS Collaboration, *Updated Luminosity Determination in pp Collisions at* $\sqrt{s} =$ 7 TeV *using the ATLAS detector*, ATLAS-CONF-2011-011.

[157] H.S. Bansil, E.F.Berglund, J. Bracinik, J.T. Childers, D. Damazio, V. Dao, O. Davignon, X.A. Del Popolo, M. Dieli, M.Goebel, A. Hamilton, D. Hayden, S. Heim, K. Heine, T. Kono, Z. Liang, F. Monticelli, P.R. Newman, A. Ruiz Martinez, G. Siragusa, R. Stamen, A. Tricoli, M. Wielers, and H. Zhang, *Performance of the Electron and Photon Trigger in p-p Collisions at* $\sqrt{s} = 7$ TeV, ATL-COM-DAQ-2011-008.

[158] M. Baak, M. Petteni, and N. Makovec, *Data-quality Requirements and Event Cleaning for Jets and Missing Transverse Energy Reconstruction with the ATLAS Detector in Proton-Proton Collisions at a Center-of-Mass Energy of* $\sqrt{s} = 7$ *TeV*, ATLAS-COM-CONF-2010-038.

[159] B. Abi, M. Bosman, V. Dao, L. Fiorini, K. Gellerstedt, C. Helsens, A. Henrichs, U. Husemann, J. Juste, C. Lange, A. Leyko, A. Lister, L. Mir, J. Nadal, M. Owen, M. Pinamonti, F. Rizatdinova, A. Roe, M. Saleem, E. Shabalina, J. Sjolin, and V. Vorwerk, *Misidentified lepton backgrounds to top quark-pair production for Moriond 2011 analysis*, ATL-COM-PHYS-2011-144.

[160] O. Arnaez, D. Froidevaux, M. Aharrouche, J. Alison, E. Berglund, R. Bernhard, A. Bocci, V. Dao, F. Ellinghaus, F. Derue, M. Fiascaris, S. Heim, F. Hubaut, L. Iconomidou-Fayard, N. Kerschen, J. Kretzschmar, Z. Liang, D. Liu, K. Lohwasser, J. Maurer, G. Pasztor, R. Pottgen, E. Richter-Was, A. Robichaud-Veronneau, T. Theveneaux-Pelzer, RD. Schaffer, E. Schmidt, M. Teinturier, and H. Zhu, *Electron efficiency measurements using ATLAS 2010 data at* $\sqrt{s} = 7$ *TeV : Supporting note for the 2010 egamma paper*, ATL-COM-DAQ-2011-008.

[161] The ATLAS Collaboration, *ATLAS Calorimeter Response to Single Isolated Hadrons and Estimation of the Calorimeter Jet Scale Uncertainty*, ATLAS-CONF-2011-028.

[162] The ATLAS Collaboration, *Jet energy scale and its systematic uncertainty in proton-proton collisions at* $\sqrt{s} = 7$ *TeV in ATLAS 2010 data*, ATLAS-CONF-2011-032.

[163] K. Terashi, *Close-by Jet Effects on Jet Energy Scale Calibration in pp Collisions at* $\sqrt{s} = 7$ *TeV* , ATLAS-COM-CONF-2011-060.

[164] A. S. B. Butler, *Track-Jet Reconstruction and Performance*, ATL-PHYS-INT-2010-040.

[165] J. F. Arguin, D. E. Boumediene, M. Bondioli, G. Cortiana, M. J. C. Mezquita, C. Cowden, P. O. DeViveiros, C. Doglioni, J. Erdmann, J. Ferrando, A. Gaponenko, N. Ghodbane, C. Issever, H. Liao, P. Kovesarki, K. Kroeninger, B. Lemmer, J-R. Lessard, M. A. Losada, S. Marti i Garcia, K. L. Mattioli, M. M. Llacer, R. Nisius, H. Okawa, M. Petteni, R. Piegaia, S. Psoroulas, G. Romeo, F. Ruhr, F. Spano, D. Urbaniec, D. Lopez Mateos, S. Adomeit, O. Biebel, M-A. Pleier, J. Kroseberg, D. Hellmich, U. Yang, A. Martyniuk, and D. Pallin, *Jet selection for top physics*, ATL-PHYS-INT-2010-134.

[166] J. M. Campbell and R. K. Ellis, *An update on vector boson pair production at hadron colliders*, Phys. Rev. D **60** (1999) 113006, arXiv:hep-ph/9905386.

[167] J. Campbell, R. K. Ellis, and F. Tramontano, *An update on vector boson pair production at hadron colliders*, Phys. Rev. D **70** (2004) 094912, `arXiv:hep-ph/0408158`.

[168] R. D. Ball *et al.*, *A first unbiased global NLO determination of parton distributions and their uncertainties*, Nucl. Phys. B **838** (2010) 136.

[169] M. Botje, J. Butterworth, A. Cooper-Sarkar, A. de Roeck, J. Feltesse, S. Forte, A. Glazov, J. Huston, R. McNulty, T. Sjoestrand, and R. S. Thorne, *The PDF4LHC Working Group Interim Recommendations*, `arXiv: 1101.0538 [hep-ph]`.

[170] `https://twiki.cern.ch/twiki/bin/view/AtlasProtected/TopSystematicUncertainties2010`

[171] M. Aliev *et al.*, *HATHOR: HAdronic Top and Heavy quarks crOss section calculatoR*, Computer Physics Communincations **182** (2011) 1034, `arXiv:1007.1327 [hep-ph]`.

[172] The D0 Collaboration, *$t\bar{t}$ production cross-section in $p\bar{p}$ collisions at $\sqrt{s}$ = 1.8 TeV*, Phys. Rev. D **67** (2003) 012004.

[173] The D0 Collaboration, *Measurements of the $t\bar{t}$ Cross Section in the lepton+jets Channel with 4.3 fb^{-1}*, D0 Conference Note (2010) .

[174] The CDF Collaboration, *Measurement of the $t\bar{t}$ Production Cross Section in $p\bar{p}$ Collisions at $\sqrt{s} = 1.8$ TeV*, Phys. Rev. D **64** (2001) 032002.

[175] The CDF Collaboration, *Measurement of the Top Cross Section in the Lepton + Jets Channel Using Simultaneous Kinematic Fits with 2.7 fb^1 of CDF Data*, CDF Conference Note (2010) .

[176] C. T. Hill and E. H. Simmons, *Strong Dynamics and Electroweak Symmetry Breaking*, Phys. ept. **381** (2003) 235, `hep-ph/0203079`.

Summary

The Standard Model is the cornerstone theory for Particle Physics that describes matter particles and the interactions between them. As a result of its robust mathematical formulation it allows for detailed and precise quantitative predictions to be made. However, although it has been a very successful theory until this day, many questions remain unanswered. The Large Hadron Collider was built with the goal to address many of these questions. Being the world's most energetic particle collider by smashing protons together at an outstanding center-of-mass energy of 7 TeV (8 TeV in 2012; 13 TeV expected in 2014), the LHC gives the possibility to explore regions of the phase-space that were previously uncharted. In other words, it enables physicists to test the Standard Model even further but also pave the way to new discoveries.

Motivation

In this thesis, we presented a first measurement of the top quark pair production cross-section using data delivered by LHC and recorded with the ATLAS detector. The motivation behind this cross-section analysis is summarized on the following:

i. To test Quantum Chromodynamics and establish the validity of the Standard Model at the collision energy of the LHC.
ii. To challenge the experiment with identifying a complex signature under an enormous background of processes, gaining in parallel a better understanding of the detector.
iii. To provide a footing for analyses that explore models Beyond the Standard Model and which consider the top quark pair production as a background to their signal.

Triggering on events

One of the most important aspects of the analysis process was to select the appropriate sample of events. This selection is typically separated into the online and the offline selection stages.

The online selection, also known as *triggering*, is performed at quasi-realtime by specialized algorithms (triggers) which run once the collision products are recorded by the different sub-detectors. Events that get rejected by all algorithms are deleted immediately, while events that are accepted by at least one algorithm are stored to mass-storage for further processing in the offline analysis. The triggering of events has the disadvantage that it imposes a selection efficiency to the final measurement which must be measured accurately. On the other hand, it is absolutely necessary in order to protect the detector's data-taking process from the immense rate of incoming events, most of which are of no interest. In the cross-section measurement, for each of the channels, $t\bar{t}(\mu)$ or $t\bar{t}(e)$, we chose a single-lepton trigger, muon or electron respectively, with a requirement on the minimum transverse momentum (p_{T}) of the lepton.

With the first data collected, starting from April 2010 and until July 2010, we assessed the performance of the *muon* trigger hardware and software by examining a subset of the single-lepton triggers. These performance checks were made based on an inclusive sample where

only the presence of a muon was required and no other kinematic cuts were applied. This was possible because of the low luminosity of the LHC during the first stages of the experiment.

We measured the turn-on curves, namely the efficiency of the trigger with respect to the p_{T} of the muons, where the efficiency is defined as the ratio of the number of selected and triggered muons over the total number of selected muons. Also we measured the resolution of the algorithms by fitting the residual distribution for different p_{T} regions. The residual is measured by comparing the relative difference between the offline estimate for the muon's p_{T} with the estimate from the respective trigger algorithm. The resulting plots showed a good performance of the trigger and in most cases a reasonable agreement between data and Monte Carlo. For those cases that discrepancies were observed, all of which indicated a worse performance than expected, the issues were identified and solutions were provided with the priority towards maximum efficiency.

In addition to the performance measurements, we also presented a methodology for estimating the trigger efficiency directly from data, for when the data are kinematically biased. The study focused on the most commonly used method, the tag-and-probe, which was also utilized for the cross-section measurement. We showed that it is possible to measure the efficiency in an unbiased way by identifying $Z \to \mu\mu$ candidates based on a single muon trigger (tag) and counting the number of times the second muon was actually triggered by the system (probe).

Analyzing the sample

After events are selected by the trigger, the sample was refined even further using specific kinematic cuts. These cuts were motivated by the expected final state signature of the single-lepton $t\bar{t}$ events and their goal was to increase the signal-to-background ratio.

With the top quark almost exclusively decaying into a W boson and a bottom quark (b-quark), the $t\bar{t}(\mu)$ and $t\bar{t}(e)$ topologies, which were considered the signal for this analysis, are characterized by one W boson decaying leptonically ($W \to \ell\nu_\ell$) and one decaying hadronically ($W \to q\bar{q}$). Therefore, the signal events contain an energetic charged lepton (electron or muon) and its neutrino partner, two jets from light quark hadronization, and two jets induced from b-quark hadronization; extra jets maybe produced as the result of initial and final state radiation, namely emissions of gluons or photons radiating immediately before and after the collision. The hadronization process, is a consequence of the properties of the strong force which does not allow quarks or gluons to be free. Therefore, the resulting quarks in the $t\bar{t}$ topology, form hadrons which further decay resulting in a narrow cone of particles, the *jet*. The b-jets are a powerful selection tool because b-quarks form exclusively B-hadrons. The B-hadrons in turn have a relatively long lifetime (approximately 1.6 pico-seconds) which allows the observation of a secondary interaction vertex, and therefore the *tagging* of the jet.

Considering these characteristics, it is also evident that identifying the complex $t\bar{t}$ topology is a test for the detector's performance since almost all of the detection technologies are used. Electrons use tracking and calorimetry, muons tracking and muon spectrometry, jets depend on calorimetry while b-jets also utilize tracking techniques, and the neutrino's energy component is extracted by measuring the energy offset, required to balance the total observed transverse energy, using all detector's components.

The template fit method

For the cross-section analysis, the final sample was separated into four exclusive kinematic regions. These regions were distinguished by their high-p_{T} jet multiplicities in the exactly-three jets and the at-least-four jets regions, and according to the number of identified b-jets in the exactly-zero b-jets (no-tag) and the at-least-one b-jets (tagged) region.

The method that was implemented for the cross-section measurement depended on two elements: the *b-tagging rates* at each jet multiplicity region, and the *shape-templates* of the *hadronic top mass* observable in each of the four kinematic regions. These parameters were estimated for both signal and background but with the latter ones being derived by using, primarily, data-driven techniques. In the end, we fitted for the relative normalization of signal and background in each region and from the number of signal events we obtained the final cross-section measurement.

The hadronic top mass observable was derived by identifying the top quark with the hadronic final state, namely the one with its W boson decaying hadronically. This eventually forms a three-jet signature. Due to the large number of jets that are typically found, the best candidate was considered as the three-jet combination with the vector sum of the jet's p_{T} maximized. From the three jets the invariant mass (M_{jjj}) was estimated.

In order to minimize simulation dependance, and therefore systematic effects, the templates for the background were extracted in a data-driven way. The method followed was based on increasing the QCD multi-jet content by simply reverting the lepton requirements. With all other selection cuts left the same, we showed that the M_{jjj} shape is unbiased by this change and equivalent to the shape when obtained by the usual cuts. Subsequently, we showed that the normalization of the sample was greatly increased in favor of the background processes and with minimal contamination from the signal.

Results and outlook

The final results of the fit showed that the experimental measurement for proton-proton collisions at $\sqrt{s} = 7$ TeV is in good agreement with the theoretical expectations. This is evident from figure 1 where the results from the measurement on both channels, as well as their combination, are shown.

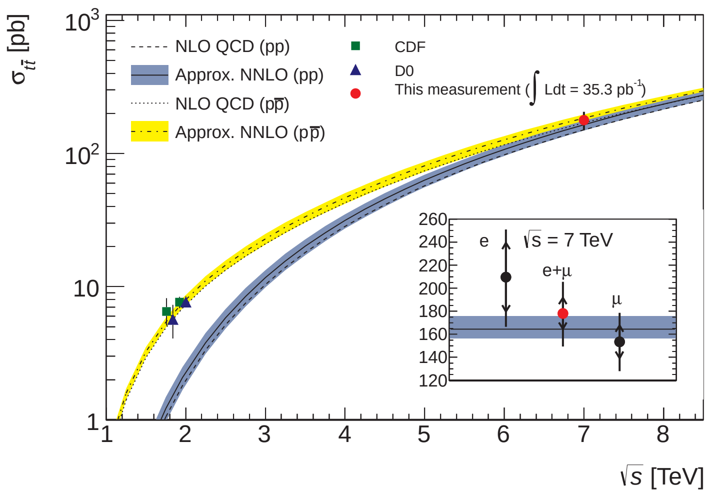

Figure 1: *The $t\bar{t}$ production cross-section as estimated by theory (assuming $M_{top} =$ 172.5 GeV) with respect to the center-of-mass energy of $p-p$ and $p-\bar{p}$ collisions (lines), the measurements made from CDF, DØ of the Tevatron collider (square and triangle points) and the measurement performed in this thesis (circle points) with $\int \mathcal{L}dt = 35.3$ pb^{-1} of $p-p$ collisions delivered by the LHC to the ATLAS detector. The error-bar region in between the arrows indicates the contribution of the statistical uncertainty only.*

The total uncertainty achieved is regarded as competitive, considering the limited amount of statistics, indicating the spectacular capabilities of the detector. With respect to possible improvements on the method, more data accumulated by the detector will definitely reduce the statistical uncertainty but will also allow for better calibration and more efficient data-driven techniques to be applied. In addition, the simulation can be optimized with respect to new findings, allowing for better treatment of the systematic uncertainties.

Naturally, the exciting discovery by ATLAS and CMS of a boson that is consistent with the Higgs boson, draws the attention of the scientific community and of the public as well. However, discoveries such as these can only be made once a good understanding of the detector is achieved and once the known Standard Model processes have been tested. From this point of view, the cross-section measurement of the $t\bar{t}$ is an important milestone as it serves a purpose for both of the above reasons.

Samenvatting

Het Standaard Model is de basistheorie voor deeltjesfysica. Het beschrijft de interacties tussen de elementaire deeltjes van materie en door de jaren heen is het zeer succesvol gebleken in deze taak. De theorie voorspelde onder andere het bestaan van nieuwe fundamentele deeltjes, zoals het $W^{\pm}$, het Z en de top-quark. Echter, het Standaard Model wordt niet beschouwd als een complete theorie, omdat veel vragen nog niet worden beantwoord door dit model. De Large Hadron Collider is gebouwd met als doel deze vragen te onderzoeken en te beantwoorden. Als 's werelds meest energetische deeltjesversneller –protonen worden op elkaar gebotst met de enorme energie van 7 TeV (8 TeV in 2012, 13 TeV verwacht in 2014)– maakt de LHC experimenten mogelijk die regio's in de fase-ruimte verkennen die voorheen niet in kaart konden worden gebracht. Met andere woorden, het stelt fysici in de gelegenheid het Standaard Model nog verder te testen, maar het maakt ook de weg vrij naar geheel nieuwe ontdekkingen.

Motivatie

In dit proefschrift hebben we een eerste meting van de werkzame doorsnede van top-quark paarproductie gedaan, met behulp van gegevens van de botsingen in de LHC, gemeten met de ATLAS-detector. Het doel achter deze analyse van de werkzame doorsnede is:

i. Om Quantum Chromodynamica te testen en de geldigheid van het Standaard Model op de botsingsenergie van de LHC vast te stellen.
ii. Om het ATLAS-experiment te testen op de mogelijkheden op het identificeren van een complexe botsingssignatuur in een enorme hoeveelheid achtergrondprocessen.
iii. Om een houvast te bieden voor de analyses die modellen te verkennen buiten het Standaard Model, waarvoor top-quark paarproductie een achtergrond vormt.

Triggering op de gebeurtenissen

Een van de belangrijkste aspecten van de analyse was het selecteren van de geschikte set botsingsdata. Deze selectie wordt meestal gescheiden in de 'online' en 'offline' selectiefases.

De online-selectie, ook wel bekend als *triggering*, wordt uitgevoerd door gespecialiseerde algoritmes (triggers) die starten zodra de subdetectoren botsingsproducten hebben geregistreerd. Botsingen *events* die worden afgewezen door alle algoritmes worden onmiddellijk verwijderd, terwijl de events die worden geaccepteerd door ten minste één algoritme worden opgeslagen in massa-opslagsystemen voor verdere verwerking in de offline analyse. Het triggeren van events heeft als nadeel dat het een selectie-efficiëntie oplegt aan de uiteindelijke meting, die op zijn beurt nauwkeurig gemeten moet worden. Aan de andere kant is het absoluut noodzakelijk voor de werking van de opslagsystemen om de gegevens te filteren en zo te beschermen tegen enorme hoeveelheden events, waarvan de meeste toch niet van belang zijn.

Voor het meten van de werkzame doorsnede hebben we gekozen voor een 'single-lepton' trigger voor zowel het muon- als het elektronkanaal ($t\bar{t}(\mu)$ of $t\bar{t}(e)$, respectievelijk), met daarop een voorwaarde voor de minimale transversale impuls (p_{T}) van het lepton.

Met de eerste gegevens, verzameld van april 2010 tot en met juli 2010, hebben we de prestaties van de *muon* trigger hard- en software gemeten, door het bekijken van een aantal single-lepton triggers. Deze controles werden uitgevoerd op basis van een dataset waar alleen de aanwezigheid van een muon vereist was, zonder deze kinematische eisen op te leggen. We hebben de zogenaamde *turn-over curves*, de efficiëntie van de trigger ten opzichte van de p_T van de muonen, gemeten. En daarnaast hebben we de resolutie van de algoritmes in verschillende p_T gebieden gemeten door het afschatten van de residueverdeling. Uit de resulterende plots bleek een goede prestatie van de trigger en een redelijke overeenkomst tussen de meetgegevens en simulatie. De waargenomen verschillen zijn allemaal geïdentificeerd en we hebben oplossingen verstrekt die voorrang geven aan een maximale efficiëntie. Ten slotte hebben we een methode voor het schatten van de trigger-efficiëntie met data-gedreven technieken *data-driven methods* gepresenteerd. Data-gedreven technieken voor het afschatten van de efficiëntie zijn noodzakelijk in gevallen waarbij een meetafwijking door kinematische effecten kan worden verwacht. We hebben de *tag-and-probe* methode, die is gebaseerd op de identificatie van $Z \to \mu\mu$ kandidaten, onderzocht. In deze methode eisen we dat de events zijn geselecteerd door een single-muon trigger (tag) om vervolgens het aantal keren dat het tweede muon daadwerkelijk getriggerd was te tellen (probe).

Het analyseren van de dataset

Nadat events zijn geselecteerd door de trigger, hebben we de dataset verder gereduceerd door specifieke kinematische snedes in te voeren. Deze snedes zijn gebaseerd op de verwachte signatuur van de single-lepton ttbar events en het doel hiervan is om de verhouding van signaal tot achtergrond te verhogen.

Omdat de top-quark in bijna alle gevallen vervalt in een W boson en een bottom-quark, vormen de $t\bar{t}(\mu)$ en $t\bar{t}(e)$ topologieën, het signaal in deze analyse, het resultaat van één W boson dat leptonisch vervalt en één Wboson dat hadronisch vervalt. Daarom bevatten signaal events dus een energetisch, geladen lepton (elektron of muon), de neutrinopartner van het lepton, twee jets afkomstig van gehadroniseerde (lichte) quarks, en twee jets afkomstig van b-quarks die uitsluitend B-hadronen vormen. Naast deze objecten kunnen er extra jets worden geproduceerd als gevolg van straling van de begin- of eindproducten van de botsing (initial state radiation; ISR, final state radiation; FSR). De b-jets zijn een sterk instrument in de selectie, omdat de lange levensduur van B-hadronen (ongeveer 1,6 picoseconden) een secundaire interactievertex kan vormen en het zo goed mogelijk maakt om ze te identificeren.

De identificatie van de complexe $t\bar{t}$ topologie is een uitdagende taak is voor de detector. Aangezien alle techologieën gebruikt worden voor dit type events, worden hiermee effectief alle mogelijkheden van de detector getest. Voor elektronen maken we gebruik van tracking en calorimetrie, voor muonen van tracking en muon-spectrometrie. Voor jets wordt ook calorimetrie gebruikt, en tracking is nodig voor b-jets. Als laatste kunnen we de energiecomponent van de neutrino vinden door het meten van de energieafwijking, de balans van de totale waargenomen energie in de transversale richting die wordt gemeten met behulp van alle detectorcomponenten.

De template-fit methode

Voor de analyse van de werkzame doorsnede wordt een zogenaamde template-fit (sjabloon-fit) toegepast. We scheiden de dataset in vier exclusieve kinematische regio's; ten eerste door het aantal hoge p_T jet in de 'exact-drie' jets en de 'tenminst-vier' jets regio's, en aan de hand van het aantal geïdentificeerde b-jets in de 'exact-nul' b-jets (no-tag) en de 'tenminst-één b-jet (tagged) regio. De fit maakt gebruik van twee elementen: de *b-tagging rates* bij elke jet multipliciteit regio, en de *vorm-sjablonen* van de *hadronische top-quark massa*, in elk van de vier kinematische gebieden. Al deze parameters zijn zowel voor signaal als achtergrond bepaald, maar voor de de laatstgenoemde uit data-gedreven technieken. Uiteindelijk hebben we gefit voor de relatieve verhouding van signaal en achtergrond in elk gebied en van het aantal signaal events hebben we de totale werkzame doorsnede van top-quark paarproductie kunnen bepalen.

We hebben de hadronische top-quark massa verkregen door het vinden van de top-quark met een hadronische eindtoestand, namelijk diegene waarbij het W boson hadronisch vervalt. De hadronisch vervallende top-quark resulteert in drie jets. Vanwege het grote aantal jets die gewoonlijk in events worden gevonden, is de beste kandidaat gedefinieerd als de drie-jet combinatie waarbij de vectorsom van de jet p_{T} maximaal is. Van deze drie jets wordt dan de invariante massa (M_{jjj}) geschat.

Voor het verkrijgen van het sjabloon van de achtergrond hebben we een methode ontwikkeld die de QCD multi-jet bijdrage vergroot door eenvoudigweg alleen de lepton-eisen om te draaien. Alle andere snedes op de dataset blijven onveranderd. We hebben laten zien dat de vorm van M_{jjj} niet verandert onder deze aanpassing, door het te vergelijken met de dataset die onder normale omstandigheden is verkregen. Vervolgens hebben we aangetoond dat het aantal events in de dataset aanzienlijk verhoogd is ten voordele van de achtergrondprocessen en er maar een minimale bijdrage van het signaal overblijft.

Resultaten en vooruitzichten

Uit de definitieve resultaten van de fit bleek dat de experimentele meting voor proton-proton botsingen bij $\sqrt{s} = 7$ TeV in goede overeenstemming is met de theoretische verwachtingen. Dit blijkt uit figuur 1 waarbij de resultaten van de meting van beide onderzochte kanalen en voor de combinatie wordt weergegeven.

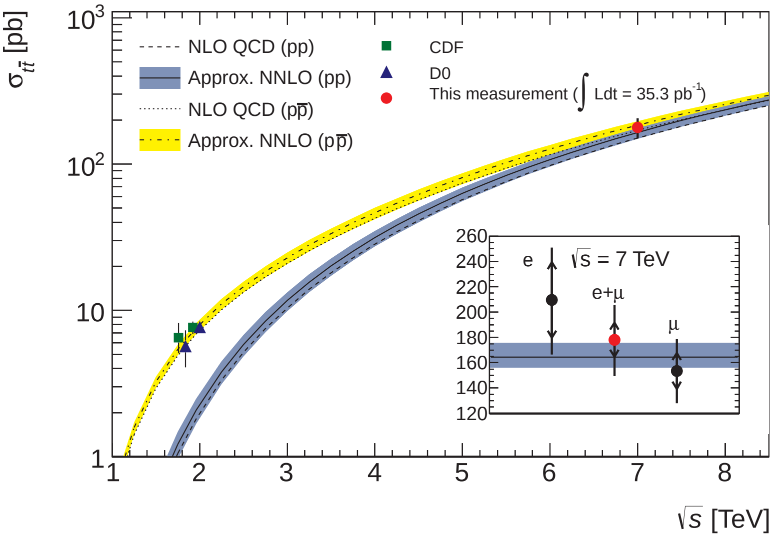

Figure 1: *De $t\bar{t}$ productie werkzame doorsnede zoals voorspeld door de theorie (in de veronderstelling $M_{top} = 172.5$ GeV) ten opzichte van de energie van $p-p$ en $p-\bar{p}$ botsingen (lijnen), de metingen gedaan door CDF, DØ van de Tevatron versneller (vierkant en driehoekpunten) en de meting verricht in dit proefschrift (cirkels) met $\int \mathcal{L}dt = 35.3$ pb^{-1} van $p-p$ botsingen geleverd door de LHC aan de ATLAS detector. De foutenmarges tussen de pijlen geeft de statistische bijdrage aan de onzekerheid weer.*

De vermelde onzekerheid op deze meting wordt beschouwd als gelijkwaardig aan de andere metingen, wat gezien de in vergeljiking beperkte hoeveelheid aan botsinggegevens aangeeft dat de mogelijkheden van de detector spectaculair zijn. Met betrekking tot mogelijke verbeteringen van de meetmethode: meer gegevens verzameld door de detector helpen zeker om de statistische onzekerheid te verkleinen maar zorgen ook voor betere ijkingen en toepassing van efficiëntere data-gedreven technieken. Bovendien kan de simulatie geoptimaliseerd worden met de kennis die is verkregen met meer data, waardoor de systematische onzekerheden beter in de hand kunnen worden gehouden.

Acknowledgments

So this is it! The book we all know as "The Thesis". Not so much of a distant goal anymore, I think it's not an understatement to say that this book wraps many sleepless nights, days of malnutrition and a bunch of missed opportunities for socializing. Nevertheless, what you are holding is the result of a truly amazing period, a period that starts from a bit further back than just the beginning of the PhD. Looking back to this journey there is a number of extraordinary, brilliant, spectacular people that, with one way or the other, have kept me going.

First and foremost, I wish to thank my promotor Stan Bentvelsen. Not only because he gave me the opportunity to work for the ATLAS experiment, but also because his enthusiastic approach and constructive discussions have been a constant encouragement and an inspiration throughout these years. A big thank you also to my supervisor Pamela Ferrari, because she accepted to be my supervisor when I needed one and because she showed me how to cope with *the job* when the 'real' data were coming.

A special thanks to Sander Klous for being my supervisor in my MSc and for enduring to this role until midway the PhD. He is a true mentor and I have learnt a lot from him, both in physics and 'real' life issues. His advices have truly helped. I am also grateful to him for jumping in again and reading this thesis at its last stages, I almost forgot the joy of reading your comments (and there is no irony in this sentence, I sincerely mean it).

A word of gratitude to Christos Eleftheriadis and Anastasios Liolios, as it was their inspiring lectures, back in the day at the Aristotle University of Thessaloniki, that motivated me to take the road of Particle Physics.

Having finished with the PhD, I can now say that sometimes it felt like extreme survival skills were needed in order to keep going. Luckily, there were a few people during this journey that made things a lot more easy. Hegoi Garitaonandia, it was a pleasure working with you. Thank you for being the driving force with your extreme work rate and for having a sense of humor when needed! Ido Mussche, thank you for all the fruitful discussions and for putting up with me barging into your office with every little question I had. Of course nothing would have been so easy (sic) with this thesis if it wasn't for the guidance of Marcel Vreeswijk and the help of Duc Bao Ta, Daniël Geerts and Hurng-Chun Lee. Jörg Mechnich, thank you for the countless times you helped me with coding, for all the discussions we had inside and outside physics, for the music we played - even though we could've played more... I am the one to blame, indeed - for the beers we drank, for sharing an office with me at CERN and later at Nikhef, and of course for withstanding my "blue" mood every now and then... Ma-Manouk Rijpstra, Manuel Kayl, Alex Koutsman, Alexander Doxiadis, Lisa Hartgring, Nicole Ruckstuhl, Gordon Lim, Corey Reed, John Ottersbach, Giuseppe Salamanna, Maria Tselengidou, Akis Gkaitatzis, thanks for all the coffee and lunch breaks and always being around, helping me to keep my sanity with one way or the other. A word of gratitude to Teus van Egdom and Ed van Willigen for dealing with my requests for all the unusual papers I needed from time to time; thank you!

Despite the long working hours there were many moments of bliss outside physics. Christian Mildner, Susanne Waaijers, Alexis Gillett, Chris White thanks for the tons of fun we had and for the good groovy music we created together, I truly hope we get the chance to share the stage once more in the future... Talking about music I, of course, can't forget "DATA?FAIL!", probably the hottest act in the Geneva region! Manu Turlay, with your endless creativity, and punk-face Rob Lambert, thank you for all the songs you wrote and for the invaluable experiences we shared on and off stage. George Kourkafas, a special mention to you as well! Our Mongol trip will happen... and that's all I had to say for now, the rest in Berlin! AC/DC thank you as well.

Georgios Bitios, thanks for all the Saturdays in Amsterdam with the legendary lentils-soup (...and now I know what you are thinking... "From all the things! The lentils-soup?"). Despoina Evangelakou, or should I say Dr. Evangelakou, I can't thank you enough for your support all these years... and it goes as far back as to the days of the MSc. Thank you, thank you, thank you! Andreas Stergiou and Dimitrios Korres, I understand that your awesomeness as flatmates had to be exported, but did it have to happen so early? California awaits ... Miłosz Panfil, thanks for all the good times in the house and I'm sorry I failed so much in learning even the basic Polish words... do widzenia.

Dimitris Palioselitis, or Dr. Dim, or Mister Music, or Chef Magnifique, the past years in the Netherlands have been awesome, thank you for all the music we played, all the cooking we did and all the discussions we had. Your friendship is irreplaceable! *So long, and thanks for all the fish!*

Tasos Zafeiriadis, Giorgos Fontaras, Theodor(e) Prousalis, Kostas Sortikos, Nikias Fontaras, Vasilis Christaras and Eva Kapravelou, thank you for all the times we met in Greece and you made me feel like no time has passed. The madrigalism crew of Christos Vavatsis, Georgios Pierrakos, Marios Kopsidis, Dimitris Panaritis and... Georgios Bitios (once more!) you have been the most reliable and trustworthy bunch of people and I love you for that!

Most of all I want to thank my family, Stamatis, Charoula and Olga. Σας ευχαριστὼ που πιστεὺετε σε εμὲνα και που συνεχὶζετε να με υποστηρὶζετε με κὰθε τρὸπο!

The very last words go to you Vily, because it is what comes next that motivates me all this time, and if it wasn't for your constant support and encouragement, this little book would still be blank pages. Thank you, καλὸ μου!

Menelaos Tsiakiris
Amsterdam - July 19, 2012